Quantum Pulse Shaping by Direct Temporal Phase Modulation

Laura Jayne Wright
St Cross College, Oxford

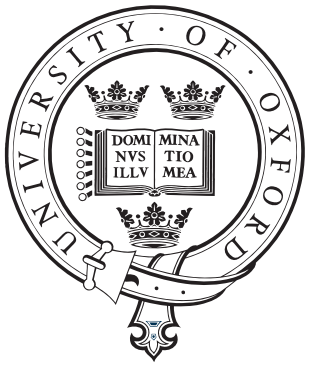

Submitted for the degree of Doctor of Philosophy
Hilary term 2015

Supervised by
Dr Brian J. Smith

Clarendon Laboratory
University of Oxford
United Kingdom

Quantum Pulse Shaping by Direct Temporal Phase Modulation

Laura Jayne Wright, St Cross College, Oxford

Submitted for the degree of Doctor of Philosophy, Hilary term 2015

Creating and controlling well-defined single-photon states is important for many quantum-enhanced technologies. Information can be encoded in any degree of freedom associated with a single-photon field excitation, for example in the polarization or transverse spatial mode structure. The ability to encode multiple qubits in these states is desirable for high data transmission rates and increased information processing capacity. The spectral-temporal domain offers a large Hilbert space for encoding information, well suited to integrated optical architectures owing to the low cross-talk between channels. Indeed, time-frequency encoding is an integral component of existing information technologies infrastructure. Thus, complete, coherent control of the spectral-temporal mode structure of light is essential to advancing optical quantum technologies.

Arbitrary control of single-photon states has been demonstrated in the polarization and spatial-momentum degrees of freedom however, is yet to be established in the spectral-temporal domain. Recently it was shown that spectral-temporal pulse shaping is experimentally feasible using nonlinear optical methods. However, such techniques can introduce noise photons, are challenging to implement deterministically and require specially prepared auxiliary pump pulses. Furthermore, they are typically only possible at relatively low repetition rates to avoid damage of nonlinear optical materials.

Here, we demonstrate deterministic pulse shaping of single-photon wave packets by introducing a time-varying phase. Applying linear or quadratic phase to the wave packet introduces a spectral shift or spectral broadening, respectively. Achieving significant spectral manipulation requires temporal-phase modulation on the order of π. The phase must also vary on the same time scale as the optical pulses, approximately 1 ps in duration here. This relatively rapid phase variation is achieved using a fast electro-optic phase modulator. The modulator is driven by a time-varying voltage that is synchronized with a pulse train of single-photon wave packets for accurate temporal phase control.

In this thesis, we experimentally demonstrate control of the spectral-temporal state of single-photon wave packets using this method. Heralded single-photon wave packets are generated by spontaneous parametric down conversion pumped by a frequency-doubled Titanium-Sapphire laser oscillator with 80 MHz repetition rate. To achieve significant modulation of single-photon pulses a 10 V peak-to-peak radio-frequency signal of 40 GHz drives the phase modulator, which requires approximately 3.6 V to achieve a π phase shift. The signal is synchronized with the oscillator pulse train using custom designed electronics. Details of these electronics are presented, resulting in a robust phase and amplitude controllable 40 GHz voltage source, phase locked to the single-photon pulse train.

To demonstrate the utility of this pulse-shaping method we experimentally show spectral shearing of almost 1 nm for single-photon wave packets with 830 nm central wavelength and 1 nm bandwidth. Measurement of the second-order intensity correlation before and after the wave-packet manipulation remains constant within uncertainty of the measurement, showing that the quantum nature of the single-photon source is not deteriorated by the modulator. Preservation of the wave-packet coherence is verified by two-photon interference between spectrally sheared and non-modulated single-photons.

Declaration

I confirm that the thesis I am submitting is wholly my own work. No part of my thesis has been accepted or is currently being submitted for any degree, diploma or certificate or other qualification in this University or elsewhere.

Acknowledgements

This thesis, and associated work, would not have been possible without the support and guidance provided by those around me, including my supervisor, Dr Brian Smith. I would like to thank him for giving me the opportunity to be a member of his research group and benefit from his vast knowledge and expertise.

Significant thanks go to Michał Karpiński and Christoph Söller, the two post-doctoral researchers who provided me with invaluable hands-on support and expertise throughout my DPhil. Not only did they both guide me around the laboratory but also provided friendship and fond memories. Without you both I would not have a thesis to write this acknowledgement page for! Thank you.

I would also like to thank Merlin Cooper, my fellow OQT-fledgeling for the fun and support. The Ultrafast Group have always been willing to lend a helping hand (and, more importantly, equipment!) and give advice, therefore a thank you also goes to all the members, past and present. Andrea Schiavi gets a special mention for being there throughout. You have also provided so many fantastic memories that I hope stay with me forever.

Howard Venning from Aspen Electronics Ltd also deserves a special mention for all of his expertise and extremely helpful assistance with developing the RF driving signal, one main component of the work presented in this thesis. Thank you very much for all the

useful correspondence and personal visits.

St Cross College has been a significant part of my life during my DPhil. Dedications also go out to Adam Gilbertson, Lara Vancans and Abi Tompkins for their friendship throughout and providing a lot of necessary fun and distractions along the way. Long may that continue.

To my new colleagues at Harrow School: you have been more than supportive and understanding during my transition between DPhil and teaching. A special thanks goes to CDB, first for the fantastic opportunity and secondly for all the advice on teaching and general life skills, to MTG for being a thoroughly helpful and extremely competent mentor during my first few months and to CMC for keeping me sane and sociable.

I would like to thank my parents for always being there for me throughout my educational endeavours. You have always supported me in any way you could and I have always appreciated that. My grandparents have always been exceptionally encouraging and so a special thanks goes out to them as well.

Finally, my eternal thanks goes to my partner, Tim. I could not have asked for a more supportive and inspiring presence in my life.

Author's Publications, Conference Presentations and Workshop Attendances

Journal publications

1. J. Nunn, L. J. Wright, C. Söller, B. J. Smith. "**Large-alphabet time-frequency entangled quantum key distribution by means of time-to-frequency conversion.**"*Optics Express*, 21(13):15959–15973, January 2013.
2. M. C. Cooper, L. J. Wright, C. Söller, B. J. Smith. "**Experimental generation of multi-photon Fock states .**" *Optics Express*, 21(5):5309–5317, March 2013.
3. L. J. Wright, M. Karpiński, B. J. Smith. "**Coherent Manipulation of Non-Classical Wave Packets of Light.**" *in progress*
4. L. J. Wright, N. Chen, M. Karpiński, B. J. Smith. "**Resource-Efficient Constraining of Fidelity Between Single-Photon Wave Packets.**" *in progress*

Conference Presentations

1. Oxford Quantum Information Science and Technology; Oxford, United Kingdom; September 2013; contributed talk: *Purity and fidelity of single-photons*
2. Quantum Optics VIII; Jachranka, Poland; May 2013; contributed talk: *Purity and fidelity of single-photons*
3. Photon12; Durham, United Kingdom; September 2012; contributed talk: *Purity and fidelity of single-photons*
4. QuAMP 2011: International conference on Quantum, Atomic, Molecular and Plasma Physics; Oxford, United Kingdom; September 2011; contributed talk: *Single-photon state characterization: a resource efficient diagnostic and full state tomography*

Others

1. Frontiers in Optics 2014 Conference Talk Accepted - *later withdrawn*

Workshops and Summer Schools

1. SSUSP 2011, Scottish Universities Summer School in Physics SUSSP67: Quantum Information and Coherence Summer School; University of Strathclyde, Glasgow; August 2011; part-scholarship awarded

2. ICFO Frontiers 2013 Summer School; Barcelona, Spain; July 2013; full scholarship awarded

Contents

Declaration v

Acknowledgements vii

Author's Publications, Conference Presentations and Workshop Attendances ix

List of Figures xv

List of Tables xvii

Commonly Used Abbreviations xix

1 Introduction 1
- 1.1 Our Understanding of Light . . . 1
  - 1.1.1 An Historical Perspective . . . 1
  - 1.1.2 The Quantum Revolution . . . 2
  - 1.1.3 The Particle versus Wave View Today . . . 3
  - 1.1.4 Sources and Uses of Light . . . 3
- 1.2 Quantum Optical Technologies . . . 5
  - 1.2.1 Spectral-Temporal Modes for Quantum Technologies . . . 6
  - 1.2.2 The Next Generation of Quantum Optical Technologies . . . 7
- 1.3 Spectral-Temporal Pulse Shaping of Non-Classical Light . . . 9
  - 1.3.1 Fourier Relationship Between the Spectral and Temporal Modes . . . 9
  - 1.3.2 Direct and Indirect Pulse Shaping . . . 10
  - 1.3.3 Current Methods of Spectral-Temporal Pulse Shaping . . . 10
- 1.4 Thesis Outline . . . 12

2 Wave Packets of Non-Classical Light: Theory 15
- 2.1 Introduction . . . 15
- 2.2 The Theory of Light . . . 16
  - 2.2.1 Quantization of the Electromagnetic Field . . . 16
  - 2.2.2 Modes of Light . . . 19
  - 2.2.3 The Coherence of Light . . . 21

2.3 Spectral-Temporal Wave Packets . . . 24
2.3.1 The Spectral-Temporal Modes . . . 24
2.3.2 Mode Overlap . . . 26
2.3.3 The Spectral-Temporal Electric Field . . . 26
2.3.4 The Spectral Phase . . . 27
2.3.5 Gaussian Wave Packets . . . 29
2.4 Classical Spectral-Temporal Pulse Shaping . . . 31
2.4.1 Pulse Shaping Theory . . . 32
2.5 Non-Classical Spectral-Temporal Pulse Shaping: A Review and Proposal . . 38
2.5.1 A Review of Quantum Optical Pulse Shaping . . . 38
2.5.2 Spectral Pulse Shaping via Temporal Phase Modification . . . 42
2.5.3 Linear Temporal Phase Modification . . . 42
2.5.4 Quadratic Temporal Phase Modification . . . 43
2.6 Chapter Summary . . . 44

3 A Spectrally-Pure Single-Photon Source 47
3.1 Introduction . . . 47
3.2 A Single-Photon Source . . . 48
3.2.1 Pure, Single Photon Wave Packets . . . 48
3.2.2 An Ideal Single-Photon Source . . . 50
3.2.3 Theory of Spontaneous Parametric Down-Conversion . . . 52
3.3 Building the Source . . . 55
3.3.1 Laser Preparation . . . 55
3.3.2 Second Harmonic Generation . . . 55
3.3.3 Spontaneous Parametric Down-Conversion . . . 57
3.3.4 Delay Stage and Fibre Coupling . . . 58
3.3.5 Photon Counting . . . 58
3.4 Single-Photon Source Characterization . . . 61
3.4.1 Intensity Spectra . . . 61
3.4.2 The Joint Spectral Intensity . . . 68
3.4.3 The Schmidt Decomposition . . . 74
3.4.4 Hong-Ou-Mandel Interference and Spectral Overlap . . . 79
3.5 Chapter Summary . . . 92

4 Temporal Phase Modulation Using an Electro-Optic Phase Modulator 97
4.1 Introduction . . . 97
4.2 Temporal Phase Modulation Using an Electro-Optic Modulator . . . 98
4.2.1 The Electro-Optic Modulator . . . 100
4.2.2 Electro-Optic Modulator Dispersion . . . 101
4.2.3 Electro-Optic Modulator Driving Signal . . . 102
4.2.4 Factors Dictating the Chosen Electro-Optic Modulator and Driving Signal . . . 106
4.2.5 Generating a Phase-Locked RF Driving Signal . . . 109
4.2.6 Electro-Optic Modulator Calibration . . . 116
4.2.7 Spectral Modification Predictions . . . 119
4.3 EOM Testing with Pulsed Optical Input . . . 122

4.3.1 Wave Packet Manipulation of an Attenuated Coherent State 123
4.3.2 Relative Phase Alignment Testing 126
4.4 Wave Packet Coherence Testing 129
4.4.1 Theory 130
4.4.2 Experimental Set Up 133
4.4.3 Interference Measurements 134
4.4.4 Spectral Coherence Analysis 139
4.5 Temporal Jitter 143
4.5.1 Effect of Temporal Jitter on Spectral Manipulation 145
4.5.2 Temporal Jitter Summary 154
4.6 Chapter Summary 156

5 Pulse Shaping Quantum States of Light 157
5.1 Introduction 157
5.2 Quantum Wave Packet Spectral Manipulation 157
5.2.1 Method 158
5.2.2 Spectral Manipulation Results 160
5.2.3 Summary: Quantum Wave Packet Spectral Manipulation 164
5.3 Photon-Number Testing - Second Order Correlation 164
5.3.1 The Heralded Second Order Correlation 167
5.3.2 Method 168
5.3.3 Results 170
5.3.4 Summary: Photon-Number Testing 172
5.4 Hong-Ou-Mandel Interference 173
5.4.1 Method 175
5.4.2 Results and Data Analysis 181
5.4.3 Summary of HOM Interference of Modulated Wave Packets 183
5.5 Chapter Summary 185

6 Conclusions and Future Directions 189
6.1 What Has Been Done Here? 189
6.2 Applications of this Work 191
6.2.1 Complete Quantum State Tomography of the Spectral-Temporal Domain 191
6.2.2 Quantum Key Distribution 193
6.3 The Next Generation 194
6.3.1 Tackling the Jitter 194
6.3.2 Efficient RF Signals 195
6.3.3 Arbitrary and Multiple RF Signals 196
6.3.4 Calibration of the Variable Attenuator 197
6.4 Implications of this Work 197
6.5 To End 198

A Pulse Expansion for Gaussian: Derivation 199
A.1 Derivation of Pulse Broadening 199

B Quantum State Tomography of the Spectral-Temporal Modes: A Proposal **201**
B.1 Complete Wave Packet Characterization Methods 201
B.1.1 Method: Interferometric Characterization 202
B.1.2 The Wigner Quasi-Probability Distribution 202
B.1.3 Measuring the Two-Frequency Correlation 204
B.1.4 Extracting Information from the Interference Fringes 205
B.1.5 Experimental Method 205

Bibliography **209**
*

List of Figures

1.1 The Quantum Network 8

2.1 Comparing the Spatial and Temporal Lenses 36
2.2 Schematic of a 4f Line 37

3.1 Type-II Collinear Downconversion Cones 53
3.2 Schematic of the Single-Photon Source 56
3.3 Czerny-Turner Spectrometer and Two Output Modes 62
3.4 Diode Laser Spectra to Show Instrument Response 65
3.5 Measured Intensity Spectra of Signal and Idler Photons 68
3.6 Schematic of the JSI Measurement Set Up 71
3.7 The Measured Joint Spectral Intensity 72
3.8 The Measured Joint Spectral Intensity and Marginals 73
3.9 Extracted Singles and Heralded Marginals Intensity Spectra 75
3.10 Beam Splitter Schematic 80
3.11 HOM Interference Possibilities 81
3.12 HOM Interference Spectra - Unfiltered 94
3.13 HOM Interference of Single-Photon Source 94
3.14 HOM Interference Spectra - Filtered 95
3.15 HOM Interference of Single Photon Source 95

4.1 Temporal Overlap of Optical Pulse and Electric Field 100
4.2 Schematic of The Electro-Optic Phase Modulator 102
4.3 Optical-Voltage Signal Alignment Cases 104
4.4 40 GHz Source Circuit Diagram 110
4.5 40 GHz Source Annotated Photo 111
4.6 40 GHz Source Annotated Photo 111
4.7 40 GHz Source Annotated Photo 112
4.8 PDRO Circuit Diagram 113
4.9 Phase Shifter Block Diagram 114
4.10 Variable Attenuator Block Diagram 115
4.11 Electro-Optic Modulator Calibration Experimental Set Up 120
4.12 Electro-Optic Modulator Calibration Data 121

4.13 Temporal and Linear Fits to the Driving Voltage 122
4.14 Experimental Set Up for Coherent Wave Packet Manipulation Measurement 124
4.15 Attenuated, Coherent-State Modulated Wave Packet Intensity Spectra . . . 127
4.16 Weak, Coherent Wave Packet Spectral Pulse Shaping vs. Phase Offset . . . 128
4.17 Experimental Set Up for a Coherent Wave Packet Spectral Phase Testing . 132
4.18 Schematic Showing Different Cases Tested in the MZI 134
4.19 Sample Oscilloscope Signal during MZI 137
4.20 Modulated, Attenuated, Coherent Wave Packet Interference Results 138
4.21 MZI, First Order Coherence Envelopes 140
4.22 Spectral Overlap versus MZI Visibility 142
4.23 Temporal Interference Phase Discontinuities - Smaller Time Scales 144
4.24 A Fourier Transform of Classical Interference 144
4.25 Temporal Jitter Alignment and Resulting Gradients 147
4.26 Temporal Jitter Effects Between RF and Optical Signals 148
4.27 Temporal Jitter with Linear Alignment Modelling 152
4.28 Spectral Properties vs. Temporal Jitter for Linear Alignment 153
4.29 Temporal Jitter with Linear Alignment Modelling 154
4.30 Spectral Bandwidth vs. Temporal Jitter for Quadratic Alignment 155

5.1 Experimental Set Up for Heralded, Modulated Single-Photon Spectral Measurements 159
5.2 Heralded Modulated Single-Photon Wave Packet Spectra Results 165
5.3 Spectral Properties vs. Temporal Jitter for Linear Alignment: Single-Photon Source 166
5.4 Spectral Bandwidth vs. Temporal Jitter for Quadratic Alignment: Single-Photon Source 167
5.5 $g^{(2)}(0)$ Measurement Schematic 168
5.6 Heralded Second Order Correlation Measurement Set Up 169
5.7 Heralded $g^{(2)}(0)$ Measurement Results 174
5.8 Experimental Set Up for HOM Interference 181
5.9 Measured Spectra and HOM Interference Results 186
5.10 Spectral Properties of Modulated Signal Photon versus Experiment Run Time 187

6.1 Inefficiency of 40 GHz RF Source and Proposed Alternative 196

B.1 Sagnac Interferometer for Full State Characterization 206

List of Tables

2.1 Summary of Current Quantum Pulse Shaping Methods 41

3.1 Bi-Photon Measured Spectrum Properties 75

4.1 MZI Visibility and Measured Spectra and Spectral Overlap Results 139

5.1 Spectral Non-Classical Wave Packet Shaping Results 164
5.2 Table of HOM Interference Visibility Results 183

Commonly Used Abbreviations

Abbreviation	**Description**
APD	avalanche photodiode
AR	anti-reflective
BS	beam splitter
BBO	β-barium borate
BiBO	bismuth triborate
CC	coincidence counts
CCD	charged coupled device
CW	continuous wave
DM	dichroic mirror
EM	electromagnetic
EOM	electro-optic modulator
(I)FT	(Inverse) Fourier transform
FTL	Fourier transform limited
FWHM	full width at half the intensity maximum
FWM	four wave mixing
GDD	group delay dispersion
GVD	group velocity dispersion
HOM	Hong-Ou-Mandel
IF	interference filter
IR	infra-red
(PP)KPT	(periodically poled) potassium titanyl phosphate
$LiNbO_3$	lithium niobate
MMF	multi-mode fibre
MZI	Mach-Zehnder interferometer
ND	neutral density
NLO	nonlinear optical
OSA	optical spectrum analyser
PBS	polarizing beam splitter
PDRO	phase-locked dielectric resonator oscillator
PPLN	periodically poled lithium niobate
PMF(BS)	polarization maintaining fibre (beam splitter)
QFC	quantum frequency conversion
QKD	quantum key distribution
SFG	sum frequency generation

SHG	second harmonic generation
SHM	simple harmonic motion
SLM	spatial light modulator
SMF	single-mode fiber
SNR	signal-to-noise ratio
Ti:Sapph	titanium sapphire
UV	ultra-violet
WDM	wave-division multiplexing

Chapter 1

Introduction

1.1 Our Understanding of Light

Light is an elementary component of the universe, the photon being a fundamental particle as described by the Standard Model and the mediator of the Electromagnetic (EM) Force. EM radiation is at the heart of life on earth, providing heat and driving fundamental life-sustaining processes such as photosynthesis. Through light we gather information about our world and the universe around us, from probing microscopic bodies to detecting radiation expelled by a star millions of light years away. Understanding its behaviour and employing its useful features has therefore been of high importance to us throughout human development.

1.1.1 An Historical Perspective

Some of the earliest written works on the nature of late date back to the ancient Greeks. The mathematical interpretation of light's behaviour began with the laws of reflection, first developed in 330 BC[1,2]. Over a century later, studies on refraction and dispersion were introduced[3], their founders believing in light consisting of a stream of minute particles travelling at a finite speed. It was not until the seventeenth century, however, that the first suggestion of wave-like behaviour of light was proposed with Christiaan Huygens' hy-

pothesis of light as compressible waves, producing secondary wavelets[4]. However, Isaac Newton quickly revived the atomistic view of light with his corpuscular theory in 1704[5]. His theory proposed that light was made of many particles of different colour, related to their weight and velocity. This provided an explanation as to why refraction of colours by different amounts was observed. The corpuscular theory was thus widely revered and accepted.

The opposing views, particle versus wave, endured for another century. It was not until Thomas Young's seminal two-slit experiment demonstrating interference, a result of the phase-dependent addition of waves of light, that the general view on the nature of light shifted once more[6]. The resulting revived wave theory was further endorsed once Fresnel combined Young's and Huygens' work to explain the existence of shadows as interference of secondary wavelets[7]. As such, the corpuscular theory was quietly dropped. Around the same time, Maxwell's equations of electromagnetism further propelled the wave theory of light especially so once they allowed for the successful prediction of light's finite speed to within a few percent of the exact value known today[8].

1.1.2 The Quantum Revolution

The field of optics was, however, shaken once more by Planck's work on black body radiation. For this work, he was required to make one revolutionary assumption: that heat energy was emitted and absorbed in discrete packets. A few years later, Einstein showed that these discrete packets of energy were also a feature of EM radiation and explained the photoelectric effect[9]. In doing so he introduced the term *Lichtquant*: quantum of light[10]. Following a series of experiments supporting this concept[11,12] the quantum theory of radiation was finally developed over the following few decades by Dirac, Born and Oppenheimer[13–15]. The term *photon* was coined around the same time[16], although originally in a different context, and subsequently the idea of wave-particle duality largely accepted. The understanding of the quantum nature of light was epitomized by the fol-

lowing quote from one of the leaders of the field at that time:

"All the fifty years of conscious brooding have brought me no closer to the answer to the question: What are light quanta? Of course today every rascal thinks he knows the answer, but he is deluding himself." – A. Einstein, 1954.

1.1.3 The Particle versus Wave View Today

Both classical light theory, describing the field as waves governed by Maxwell's equations, and quantum light theory, describing a corpuscular field, are regularly called upon today. In both classical and quantum theory the mode structure of the states remains the same. It is the occupation of the modes by different photon number excitation distributions which differs. The term occupation refers to how many discrete excitations, or photons, are present in a field with a well-defined mode structure. As such, classical and non-classical optics share many similarities such that their research and applications should be, and do remain, closely linked. For example, many current classical technologies can be reproduced using quantum light, but improved upon with unique advantages as described in more detail below. As such a brief description of both the development of classical and quantum technologies is included here.

1.1.4 Sources and Uses of Light

Processes involving the creation, manipulation and detection of EM radiation are central to many everyday technologies, spanning multiple fields of research and commercial applications. The early collection of man-made EM radiation sources, including the cathode-x-ray tubes and Hertz's radio transmitters and receivers, has expanded into a mature field containing multiple, tunable devices. Today, there exists an entire sub-field of laser types that are specifically tailored in terms of their frequency, intensity, duration and spatial mode. These can range from quasi-monochromatic, continuous-wave sources to single, high-intensity bursts and also pulse trains of light. There also exists a range of light sources with different occupation distributions. A classic light bulb emits thermal states,

with number distributions obeying the Bose-Einstein distribution. Whereas laser light is coherent, with all light emitted into a resonant mode obeying Poissonian statistics. Other sources of EM radiation have mastered creation of Fock states: light with a well-defined, non-varying occupation number.

Applications of EM radiation sources include medical research treatments which are aided by gamma, x-ray and microwave radiation therapies and improving diagnosis accuracies. Microscopes allow one to probe and monitor otherwise inaccessible microscopic bodies and processes operating in the near-infrared (IR), visible and ultraviolet (UV) regions. EM radiation is also used in structural analysis and machining in engineering. Both IR and UV lasers are used to read data stored in optical media and, in addition to the visible part of the EM spectrum, have also been adopted for many uses in the military. In astronomy, a large portion of the EM spectrum is collected and analysed, allowing us to make astounding discoveries about the universe. Furthermore, performing spectroscopy on EM radiation allows further indirect diagnosis of the constitution of the EM source. The success of this technique is exemplified by the discovery of the element Helium in the nineteenth century, and since, spectroscopy techniques have been an essential tool for structural analysis. IR spectroscopy has allowed for detailed extraction of the elemental and structural composition of various chemicals. Whereas ultrafast femtosecond and attosecond time-resolved spectroscopy have allowed for examination of the dynamics of charge carriers, atoms and molecules within substances, which occur on a similar time scale, too fast to be examined electronically.

The ability to control EM light has also spawned sophisticated sources for specific applications. For example, frequency combs have a spectrum consisting of discrete, equally spaced frequency components and are used to translate from one part of the EM spectrum to another for enhanced accuracy of technologies. One use of this was to bring atomic

clocks operating in the microwave region into the optical realm. Other applications include high-precision spectroscopy and optical metrology.

The ability, not only to create and detect but also, to encode and extract information contained in all modes of the EM field led to a worldwide information revolution. This began, considering EM radiation technology alone, with short range radio wave transmission in the early part of the twentieth century and has left us, today, using optical fibres thousands of kilometres long and orbiting satellites to transmit information worldwide, and even over interplanetary distances. For this communication, information is stored using phase-encoding in addition to using the profile of the spectral-temporal and amplitude degrees of freedom of the transmitted light, accelerating our communication abilities.

In this work *ultrashort* pulses of light in the optical and near IR region of the spectrum are studied for information and communication applications. These have temporal durations on the order of one picosecond and less. Ultrashort pulses have a broad range of applications including ultrafast time-resolved spectroscopy[17,18], high-precision frequency metrology[19], nonlinear microscopy[20,21], high-field laser-matter interactions and the development of atomic clocks[22] to name a few.

1.2 Quantum Optical Technologies

Over the past several decades predictions and demonstrations of our ability to harness quantum mechanical effects, to enhance the functionality and performance of classical technologies, has made significant progress. These technologies include quantum computing[23], quantum cryptography[24], truly random number generators[25,26] and quantum-enhanced metrology[27,28], amongst others. Owing to this progress, interest in, and demand for, the development of these technologies has increased significantly.

Driven partly by the large number of quantum applications with individual optimum performance settings, the types of quantum states employed in these technologies vary widely. They include atomic ensembles, molecules, superconductors and other forms of matter. Quantum states of *light*, however, are advantageous for certain applications since they do not interact well with their environment or each other. As such they are able to preserve important quantum resources, such as entanglement, for long periods of time and across large spatial distances. Quantum optical states are this ideal candidates for transmitting information between different parts of quantum systems and are often dubbed "flying qubits"[29,30]. As a result, research into creating, controlling and detecting quantum states of light is a thriving field[29].

The modes of the EM field are typically separated into the polarization, transverse spatial-mode profile and time-frequency modes. Historically, and owing to experimental ease, quantum, or non-classical pulses of light have been extensively studied and manipulated in their spatial and polarization degrees of freedom[31–33]. However, recently, the interest in working with the spectral-temporal degree of freedom has grown significantly. The spectral-temporal domain of quantum light states offers a robust information-carrying resource with high fidelity transmission over long distances in integrated optical systems when compared to the spatial degree of freedom, for example. Additionally, the broad mode structure allows for high information capacity[34,35]. It is this degree of freedom which is extensively exploited in classical communications such as in wave-division multiplexing (WDM). Thus, for efficient integration into current technological infrastructure, it is natural to develop quantum-enhanced technologies to operate with the same base components. It is this degree of freedom that is studied in this work.

1.2.1 Spectral-Temporal Modes for Quantum Technologies

Quantum light sources and quantum-enhanced optical technologies produce and employ quantum states of light with varying bandwidths. Single-photons with bandwidths on

the order of MHz, the typical linewidth of atomic transmissions, are often associated with quantum memories[36,37], furthermore long-distance, quantum information transmission[38] and temporally-resolved detection[39] are most reliable when using narrow bandwidths due to fibre dispersive effects[40]. Conversely, bandwidths many orders of magnitude broader than this have applications in quantum optical coherence tomography[41], where THz widths are commonly experienced. Larger bandwidths also allow for larger encoding spaces when resolving in the spectral domain, resulting in increased bits per photon in quantum key distribution schemes[42–47], for example, and for generating systems of entanglement[48] which can be used to perform fundamental tests of physical principles[49].

Quantum optical technologies also operate at different central wavelengths. Room temperature quantum light sources produce photons in the red spectral range, 400 to 700 nm, which is also where room temperature, solid-state detectors operate most efficiently[50]. However, the telecommunications band, with wavelengths ranging from 1.26 to 1.68 µm, is most desirable for high fidelity, low-loss transmission over large distances[51]. As such there is demand for converting the central wavelength of single photons[52–55].

Furthermore, many quantum technologies such as linear optics quantum computing (LOQC)[56,57] and quantum detection methods such as homodyne detection[58,59], rely on the interference of identical single-photon states for their operation. This interference is highly sensitive to any degree of mode mismatch, thus the ability to precisely address and modify the spectral-temporal mode structure is important to ensure excellent mode overlap between the interfering sources. Pulse shaping of the spectral-temporal modes of quantum light also has direct application in quantum metrology[28,60].

1.2.2 The Next Generation of Quantum Optical Technologies

A widely held view about the future of quantum information processing and quantum communication is that, rather than having a system based on a single quantum system such

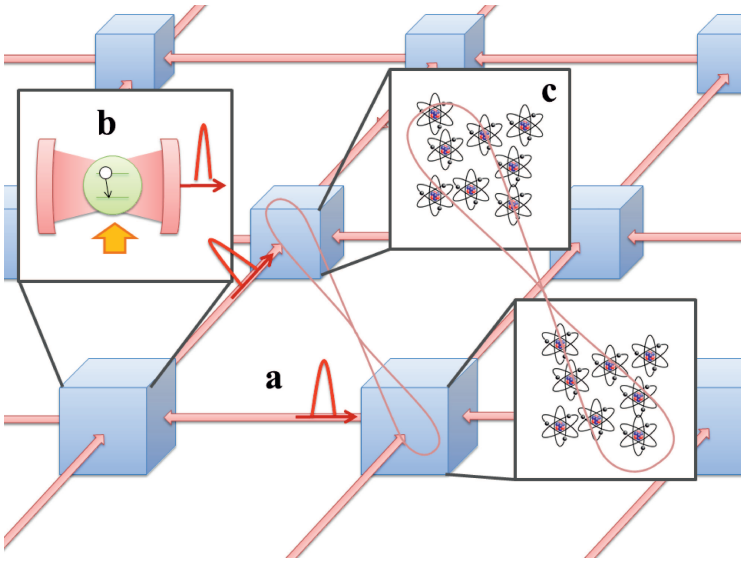

Figure 1.1: A cartoon schematic of a likely future of quantum networks. Photons are predicted to be the information carrying entities that propagate, **a**, the long distances between network nodes. At these nodes, atoms in cavities are likely to reside, **b**, ready to perform quantum electro-dynamics processes or for distribution and storage in quantum memories. These quantum memories are also likely to be comprised of large atomic ensembles, **c**.

as a single atoms, many different sources and processes will instead be brought together to create larger, integrated quantum machines or networks[61–63] as depicted in Figure 1.1. For example, quantum memories are being developed for long-term storage of quantum states of light. These are ideal for storage at quantum network nodes for states of light that have typically travelled long distances[38]. These optical states are transmitted most effectively when at telecommunication wavelengths. The nodes, however, absorb and emit photons at their own natural frequency and line shape. Thus, to match the transmitted and stored excitations, photons will require spectral-temporal mode conversion to translate information from one central frequency and/or linewidth to another. This application for quantum memories has been, very recently, experimentally demonstrated[64,65], highlighting the feasibility and drive towards integrating different quantum technology systems.

Ultimately, one can surmise that full control of creation and manipulation of the spectral-temporal mode structure of quantum light is essential for the advancement of information technologies. There are multiple incentives for developing pulse shaping methods for non-classical states of light and there is currently high interest in this area[63,66].

1.3 Spectral-Temporal Pulse Shaping of Non-Classical Light

In this work, a method of pulse shaping for quantum states of light is developed and experimentally demonstrated. For this, two important concepts must be understood,

1. the spectral and temporal modes are inherently linked,

2. it is difficult to directly manipulate both modes simultaneously.

These concepts dictate the approach used in this work to controllably manipulate the spectral-temporal modes of non-classical states of light.

1.3.1 Fourier Relationship Between the Spectral and Temporal Modes

There exists a Fourier transform (FT) relationship between frequency and time such that the variables are Fourier conjugates. This implies that a pulse with a large temporal extent will have a relatively small spectral width[1]. In the context of pulse manipulation, one can work with a pulse that has a duration long enough to be temporally modulated using a mechanical switch, a temporal gate, for example, which is typically on the order of nanoseconds. However, the spectral width would then be too narrow to access using common spectral manipulation or measurement methods such as spectral filters and monochromators, respectively. Alternatively, a spectral width on the order of a few nanometres implies a temporal width, for a FTL Gaussian, on the order of a few hundred femtoseconds. This is too fast to be addressed directly by electronically controlled temporal gates. Optical switches can be used. However, these are based on nonlinear optical (NLO) interactions requiring high temporal accuracy, resource-inefficient experimental set ups requiring reference pulses and advanced integrated optical devices[67,68]. Furthermore, they are typically dependent on the optical pulse intensity. When dealing with non-classical light with an

[1]For a Fourier-transform limited (FTL) pulse. More information on this is given in chapter 2.

average of one single-photon per femtosecond pulse, these technologies have significant challenges.

1.3.2 Direct and Indirect Pulse Shaping

Direct manipulation of the spectral-temporal modes using spectral filters and temporal gates is not compatible with quantum states of light due to the losses involved which translate to loss of information of the state. To circumvent this, *indirect* modulation of the spectral modes can be performed. This is achieved by modulating the temporal phase of the pulse, as opposed to modulating the spectral envelope directly. This is a result of the FT relationship, whereby modulation of the phase of one conjugate variable results in manipulation of the amplitude of the other variable. For example, manipulation of the spectral phase results in a change to the temporal pulse envelope, such as a shortening of the pulse which is equivalent to using a temporal gate for amplitude modification. One significant advantage of modulating the spectral phase, instead of filtering the temporal pulse, is that there is no loss of signal and it is a unitary process, hence there is no loss of information. As such, this indirect method is highly desirable when working with quantum states of light.

In this work pulses of a few hundred femtoseconds are employed. These have an associated spectral width on the order of $0.1 \rightarrow 10$ nm, just about resolvable with available spectrometers, allowing one to measure and hence evaluate the success of the pulse shaping.

1.3.3 Current Methods of Spectral-Temporal Pulse Shaping

Since the advent of lasers in 1960s [69,70], and the further development of mode-locked lasers providing a convenient source of ultrashort pulses of light, the technology to shape the spectral-temporal mode of ultrashort pulses has been in ongoing development [71–76]. Classical pulse manipulation of the spectral-temporal modes is commonly performed directly

by filtering or amplification, which is detrimental to and forbidden for quantum states of light, respectively. Classical pulse shaping also involves indirect modulation through control of the phase, is commonly implemented using a combination of phase modification of spatially dispersed optical frequencies.

In recent years an alternative set of techniques to manipulate the spectral-temporal domain of quantum pulses has been demonstrated, highlighting the steady increase in both interest and demand for this capability[77,78]. These have ranged from state preparation methods of quantum light sources[79–81] to exploiting spectral effects of quantum memories[82]. Approaches using cavity optomechanics[83] have been demonstrated, but remain technically difficult with low-temperature cooling required.

Furthermore, owing to the variety of quantum optical applications there is demand for a variety of frequency conversion techniques. There is the requirement for large shifts in frequency for example between telecom and IR to enable both high transmission rates and detection efficiencies. Other applications require more fine-tuned manipulation. For example quantum dots are, potentially, a valuable resource for quantum applications which produce single-photons that are nearly identical in their spectral properties. Therefore, techniques that can precisely tune the central frequency and bandwidth of ultrashort quantum optical pulses are also crucial[84].

In this work a technique to control the temporal phase for spectral manipulation is introduced and applied to quantum states of light in anticipation of inclusion with future quantum technologies. It requires no auxiliary pump and is implemented using “off-the-shelf” components. The range of the technique’s ability is ultimately dependent on the parameters of the chosen components, which are largely varied in their availability. Therefore this method can be applied to pulses with initially largely differing spectral properties.

This approach of modulating the temporal phase for spectral pulse manipulation has been previously applied to classical states of light [85]. However, the author believes this to be the first demonstration of the technique applied to quantum states of light.

1.4 Thesis Outline

This thesis is organised, following this introduction, into five further chapters. The second chapter, *Wave Packets of Non-Classical Light: Theory*, begins with a derivation of the quantum mechanical description of EM fields. This helps one to understand the concept of photons as single excitations of EM field modes. The difference between classical and non-classical sources of light are then discussed. The spectral-temporal modes are introduced next, since it is these which are studied in this work. The theory of spectral pulse shaping and a brief review of this field for classical and non-classical wave packets of light is then given. The method for quantum wave packet shaping by temporal phase modulation, which is the main result of this work, is finally presented and the relevant theory given.

The third chapter, *A Spectrally Pure Single-Photon Source*, first provides an overview of current methods of single-photon production widely used in the community. The choice of single-photon source used in this work is then justified before the theory behind the single-photon state production is presented. The experimental details of the source construction and characterization are then given.

The fourth chapter, *Temporal Phase Modulation Using an Electro-Optic Phase Modulator* contains all details of how controlled temporal phase modulation is achieved using an electro-optic phase modulator. The relationship between the temporal phase and the controllable parameters of the system, such as the central wavelength and pulse bandwidth is derived. The custom-built driving electronics for the modulator are then described and

their calibration presented. The spectral manipulation method by temporal phase modulation is then initially tested using classical light. Correct behaviour of the modulator is verified and the preservation of the spectral phase relationship across the wave packet is demonstrated through a classical interference measurement. The results of spectral manipulation using classical light are then analysed and it is concluded the method is suitable for application to non-classical wave packets.

The fifth chapter, *Pulse Shaping Quantum States of Light*, contains the results of applying the pulse shaping method to the specifically built single-photon source described in chapter three. The preservation of the non-classical nature of the single-photon is experimentally verified using two-photon interference and second order coherence of the non-classical wave packet before and following spectral manipulation.

Finally, the conclusion, chapter six, in addition to summarizing the presented work, includes details on two applications of this non-classical pulse shaping method which have been preliminarily explored by the author. This is done to highlight the potential and importance of this work for the advancement of quantum technologies and motivate future work to be done.

Chapter 2

Wave Packets of Non-Classical Light: Theory

2.1 Introduction

In this chapter a description of the electromagnetic (EM) field is given focusing on the spectral-temporal domain and with single excitations of the field. A discussion of methods, demonstrated to-date, to controllably modify the field without destroying, or unknowingly changing, the single excitations is then presented to highlight the need for further methods to perform state modification, specifically, in the spectral-temporal modes. Finally, a method for shaping the spectral amplitude of wave packets is given which involves temporal phase modulation of the EM field. The chapter is thus split into four sections as described below.

First, the essentials of the quantum theory of light are discussed. This introduces the nomenclature for describing the EM field in terms of its mode structure and how these modes are populated by discrete excitations. The spectral-temporal modes of light are discussed next, since these are the focus of this thesis. The unique properties of quantum, or non-classical, states of light are then quantified.

The second part then examines general ultrashort pulse properties that apply to both classical and non-classical states of light reflecting their identical, underlying mode structure. An overview of well-established, classical pulse-shaping methods is then presented. Many of these methods are able to tolerate optical losses, or make use of signal amplification, if necessary. For single quanta of the EM field, losses destroy the quantum state and state amplification is forbidden[86]. Some classical methods also rely on nonlinear optical (NLO) techniques that can be extremely challenging to implement deterministically with single-photon level fields.

In the last section a discussion of current quantum pulse shaping methods for the spectral-temporal domain is given. An alternative method of pulse shaping, which employs the technique of temporal phase modulation is then proposed. This section contains the theory necessary to understand the modulation process, and why it is highly suited for use with non-classical states of light.

2.2 The Theory of Light

In this section, some basics of the quantum theory of light are introduced alongside the conventional mathematical descriptions and nomenclature with which the EM field is described throughout the rest of this thesis. Throughout, knowledge of basic quantum mechanical axioms and notation is assumed. For a complete introduction to quantum optics, the reader can refer to many of the available introductory textbooks[87–89].

2.2.1 Quantization of the Electromagnetic Field

Light is generally described by the EM field which is composed of orthogonal electric and magnetic field vectors, $\boldsymbol{E}(\boldsymbol{r},t)$ and $\boldsymbol{B}(\boldsymbol{r},t)$. Classically, these fields obey Maxwell's four equations which prescribe the mode structure of the EM field. Maxwell's equations also

govern electromagnetism in the quantum world, however here the electric and magnetic field vectors are replaced by operators such that, $\boldsymbol{E}(\boldsymbol{r},t) \rightarrow \hat{\boldsymbol{E}}(\boldsymbol{r},t)$ and $\boldsymbol{B}(\boldsymbol{r},t) \rightarrow \hat{\boldsymbol{B}}(\boldsymbol{r},t)$.

The electric and magnetic field operators are often written in terms of conjugate, Hermitian operators: the canonical position, $\hat{p}$, and momentum, $\hat{q}$, operators respectively. These act as the in- and out-of-phase components of the EM field amplitude and are often referred to as the field quadratures. As an example of how these can be used, here, one of the most common starting points for deriving the form of the EM field as dictated by Maxwell's equations, is taken: assuming one has an enclosed cavity, free of charges or any electric or magnetic fields, with sides of length, L, and volume, $V = L^3$. Considering an EM wave propagating along the z-direction then one can show, by solving Maxwell's equations, that the the E-field, oscillating in the x-z plane, and the B-field, in the y-z plane, can be described by,

$$\hat{\boldsymbol{E}}_x(z,t) = \sqrt{\frac{2\omega^2}{V\epsilon_0}}\hat{q}(t)\sin(kz)\hat{\boldsymbol{\sigma}}_x, \tag{2.1}$$

$$\hat{\boldsymbol{B}}_y(z,t) = \frac{\mu_0\epsilon_0}{k}\sqrt{\frac{2\omega^2}{V\epsilon_0}}\hat{p}(t)\cos(kz)\hat{\boldsymbol{\sigma}}_y, \tag{2.2}$$

where ω is the frequency of the mode, $k = \omega/c = 2\pi/L$, and is the wavenumber, $\hat{\sigma}_j$, denotes the polarization direction, c is the speed of light in a vacuum and ϵ_0 and μ_0 are the vacuum permittivity and permeability respectively. This is a convenient representation since it shows the in- and out-of-phase oscillations of the E- and B-fields and their relative strengths. Fock states are a commonly used and convenient representation of the occupation of a specific EM field mode. For example, the Fock state, $|3\rangle_{\hat{\boldsymbol{\sigma}},\boldsymbol{k}}$, describes an electromagnetic field mode with polarization, $\hat{\sigma}$, and wavenumber, k, and which is occupied by two excitations. What these excitations refer to is discussed more at the end of the following subsection 2.2.2.

The field quadratures, $\hat{p}$ and $\hat{q}$, can be further written in terms of the non-Hermitian (hence non-observable) yet often more convenient, annihilation, $\hat{a}$, and creation, $\hat{a}^\dagger$, operators,

$$\hat{p} = i\sqrt{\frac{\hbar\omega}{2}}(\hat{a}^\dagger - \hat{a}) \text{ and } \hat{q} = \sqrt{\frac{\hbar}{2\omega}}(\hat{a}^\dagger + \hat{a}), \tag{2.3}$$

where $\hbar$ is Planck's constant divided by 2π. The annihilation and creation operators are named as such due to their effect when applied to a Fock state. They are defined as, $\hat{a}^\dagger|n\rangle = \sqrt{n+1}|n+1\rangle$ and $\hat{a}\,|n\rangle = \sqrt{n}\,|n-1\rangle$. These operators also obey the commutation relation such that $\left[\hat{a}, \hat{a}^\dagger\right] = 1$. This is a convenient form since the resultant electric and magnetic field operators, for the example above, then simplify to,

$$\hat{E}_x(z,t) = \mathcal{E}_0(\hat{a} + \hat{a}^\dagger)\sin(kz)\hat{\sigma_x}, \tag{2.4}$$

$$\hat{B}_y(z,t) = \frac{\mathcal{B}_0}{i}(\hat{a} - \hat{a}^\dagger)\cos(kz)\hat{\sigma_y}, \tag{2.5}$$

where $\mathcal{E}_0 = (\hbar\omega/\epsilon_0 V)^{1/2}$ and $\mathcal{B}_0 = (\mu_0/k)(\epsilon_0\hbar\omega^2/V)^{1/2}$. Note here the vector notation has been dropped for simplicity. These can then be used to determine the energy of an EM field using the definition of the Hamiltonian.

The Quantum Mechanical Hamiltonian

The quantum mechanical Hamiltonian operator describes the total energy of a system, thus can provide an insight into the quantum world of EM fields. For the quantised EM field described above, it can be shown to be given by,

$$\hat{H} = \frac{1}{2}(\hat{p}^2 + \omega^2\hat{q}^2), \tag{2.6}$$

as such, it ascribes simple harmonic motion (SHM) to the field quadratures, $\hat{p}$ and $\hat{q}$. This expression can be put into a more intuitive form by writing it as a linear combination of

the annihilation and creation operators, using the definitions in Equation 2.3,

$$\hat{H} = \hbar\omega \left(\hat{a}^\dagger \hat{a} + \frac{1}{2} \right). \tag{2.7}$$

From this expression, one can see that when the energy operator, $\hat{H}$, acts on the Fock state, $|n\rangle$, it does not alter the state:

$$\begin{aligned} \hat{H}\,|n\rangle &= \hbar\omega(\sqrt{n}\hat{a}^\dagger + \frac{1}{2})\,|n-1\rangle\,, \\ &= \hbar\omega(\sqrt{n}\sqrt{n} + \frac{1}{2})\,|n\rangle\,, \\ &= E_n\,|n\rangle\,. \end{aligned}$$

Instead it demonstrates that Fock states are eigenstates of the energy operator. Assuming the eigenstate, $|n\rangle$, has a corresponding eigenvalue, E_n, one can extract the eigenvalue equation: $E_n = (n + \frac{1}{2})\hbar\omega$. This relationship dictates the following important properties of the quantum EM field,

1. The ground state, $|0\rangle$, implies zero occupation and is known as the vacuum.
2. The vacuum's energy is non-zero, it is equal to $E_0 = \frac{1}{2}\hbar\omega$.
3. The number states of the harmonic oscillator, $|n\rangle$, have an operator $\hat{n} = \hat{a}^\dagger\hat{a}$.
4. The energy-level diagram for quantum SHM resembles a ladder with equal steps of $\hbar\omega$ starting at E_0 and reaching to infinity.

2.2.2 Modes of Light

The Fock states, discussed above, are seen to have a well-defined energy however they do not have a well-defined field. Here, the derivation of specific and complete sets of modes of the EM field is discussed. Furthermore, optical frequencies are focused on in this thesis. Most materials are not magnetic at these frequencies, nor do they couple strongly to the

magnetic field, therefore, for simplicity, the magnetic field will be neglected from now onwards.

As shown in the example above, solving the Maxwell equations for a specific set of boundary conditions allows one to extract a complete set of allowed modes. One simple example is the set of plane waves, $\left\{\boldsymbol{E}_{\boldsymbol{k},\sigma}(\boldsymbol{r},t) = \boldsymbol{A}_\sigma \mathrm{e}^{i(\boldsymbol{k}\cdot\boldsymbol{r}-\omega t)}\right\}$. This is a classical yet complex set of functions of space and time. These plane waves are denoted by the mode index, $\boldsymbol{k}$, which indicates the transverse spatial mode and, σ, the polarization mode. Their conjugate, $\left\{\boldsymbol{E}^*_{\boldsymbol{k},\sigma}(\boldsymbol{r},t)\right\}$, is also part of the complete set.

Typically, the creation and annihilation operators also have the subscript $\boldsymbol{k}, j, \sigma$, such that the operation of $\hat{a}^\dagger_{\boldsymbol{k},j,\sigma}$ on the vacuum creates a number state in the mode with propagation direction given by $\boldsymbol{k}$, transverse spatial mode denoted by j and polarization mode by σ. These operators obey the canonical commutation relations such that, $\left[\hat{a}_{\boldsymbol{k},j,\sigma}, \hat{a}^\dagger_{\boldsymbol{k'},i,\sigma'}\right] = \delta_{\boldsymbol{k}\boldsymbol{k}'}\delta_{ij}\delta_{\sigma\sigma'}$.

In the quantum-mechanical treatment of the EM field, the same boundary conditions and equivalent Maxwell equations are obeyed as with the classical field, however the field instead becomes an Hermitian operator. As such, one can express the quantum field operator in terms of these complex functions,

$$\begin{aligned}\hat{\boldsymbol{E}} &= \sum_i \left[\boldsymbol{E}_i(\boldsymbol{r},t)\hat{a}_i + \boldsymbol{E}^*_i(\boldsymbol{r},t)\hat{a}^\dagger_i\right], \\ &= \sum_i \left[\hat{\boldsymbol{E}}^{(-)}_i + \hat{\boldsymbol{E}}^{(+)}_i\right].\end{aligned} \tag{2.8}$$

This is a sum over all possible modes labelled, i. The operator $\hat{a}^\dagger_i$ ($\hat{a}_i$) describes the creation (annihilation) of an excitation in the field mode labelled i. The modes themselves are described by the functions, $\boldsymbol{E}_i(\boldsymbol{r},t)$, that are applicable to both quantum and classical

fields. It is the detail of the occupation of the modes that differs between classical and quantum fields. The quantum field operator is commonly written as a sum of the negative, $\boldsymbol{E}_i^{(-)}$, and positive, $\boldsymbol{E}_i^{(+)}$, frequency components of the operators, as has been shown in the second line above.

The Photon

Following this introductory section, the term *photon* is now defined. It is interpreted as one quanta of energy, of magnitude $\hbar\omega$ where ω is the frequency of the field mode, occupying one specific mode of the EM field with mode indices, $\boldsymbol{k}$, j and σ assigning the mode a certain polarization, angular frequency and so on. This is the definition of a photon that will be used in this work when referring to this quantum particle.

2.2.3 The Coherence of Light

In general, light can be comprised of multiple excitations of many different modes with superpositions between different numbers of excitations within a single mode and also even across the modes. As such the quantum description of light fields involves extremely large dimensional Hilbert spaces. In this work, the distribution of only one excitation across a well-defined set of spectral-temporal modes is considered. However, being able to distinguish this true single-photon from a highly attenuated, incoherent superposition of the same modes (such that the average photon number measurement across the same well-defined set of spectral-temporal modes is equal to one) is crucial to identifying a single-photon source.

A key parameter that enables one to distinguish between quantum and classical light sources is the *second order correlation function*, $g^{(2)}(\tau)$. This is a statistical measure of the fluctuation of intensity of two fields. In this section, the coherence of optical states is discussed in terms of $g^{(2)}(\tau)$. Analysing the statistical properties of classical and quantum light allows one to extract two distinct regimes of second order coherence values which

differentiate between classical and quantum sources of light.

Quantum states of light can be verified by measuring the number of single photons detected in very short time periods, and ensuring that one, and only one photon is detected at any time. However, owing to optical losses, detector inefficiencies and the finite counting times of photon detectors, direct measurement is difficult. The solution to identifying quantum light sources lies in analysing the photon number statistics of the source. The second order correlation function allows one to relate the intensity emitted over periods of time to the uncertainty in the occupation number of the state. Thus one can experimentally classify light as classical, coherent or quantum.

The Second Order Correlation Function

The second order correlation function of a classical light field with a temporal mode described by, $E(t)$, and with intensity, $I(t) = E^*(t)E(t)$, is defined as,

$$g^{(2)}(\tau) = \frac{\langle E(t)E(t+\tau)E^*(t)E^*(t+\tau)\rangle}{\langle E(t)E^*(t)\rangle \langle E(t+\tau)E^*(t+\tau)\rangle}, \tag{2.9}$$

$$= \frac{\langle I(t)I(t+\tau)\rangle}{\langle I(t)\rangle \langle I(t+\tau)\rangle}. \tag{2.10}$$

Here the angled brackets indicate an ensemble average, such as achieved with many repeat measurements of the same source. The variable, τ, represents the temporal delay between two copies of the field, $E(t)$.

How this measure allows one to distinguish between different types of light is best explained using an example. Consider a field with a constant average intensity such that, $\langle I(t)\rangle = \langle I(t+\tau)\rangle$. Writing the intensity as the average plus a fluctuation from the mean, $\langle I(t)\rangle = \langle I\rangle + \Delta I(t)$, and using the fact that the average intensity fluctuation is zero over

a long time period: $\Delta I(t) = 0$, one can show

$$g^{(2)}(\tau) = \frac{\langle I(t)I(t+\tau)\rangle}{\langle I(t)\rangle^2} = \frac{\langle [\langle I\rangle + \Delta I(t)]\,[\langle I\rangle + \Delta I(t+\tau)]\rangle}{\langle I(t)\rangle^2} = \frac{\langle I\rangle^2}{\langle I(t)\rangle^2} = 1. \tag{2.11}$$

This holds when the delay, τ, is much larger than the light source's coherence time, τ_c, such that $\tau >> \tau_c$, where $\tau_c = 1/\Delta\lambda$ and $\Delta\lambda$ is the spectral bandwidth of the EM field mode. Thus one does not expect to observe any temporal correlations between $I(t)$ and $I(t+\tau)$ such that $g^{(2)}(\tau) = 1$

When looking at time scales where the coherence time of the source is important, such that $\tau << \tau_c$, then one *does* expect to see correlations between $I(t)$ and $I(t+\tau)$. For the limiting case when $\tau = 0$, then,

$$g^{(2)}(0) = \frac{\langle I(t)^2\rangle}{\langle I(t)\rangle^2}. \tag{2.12}$$

For classical light, when considering real intensities where $I(t) = E^*(t)E(t)$, one can apply the Cauchy-Schwarz inequality, $\langle I^2\rangle \geq \langle I\rangle^2$, to the above and show[90],

$$1 \leq g^{(2)}(0) < \infty. \tag{2.13}$$

When analysing these cases for quantum fields, one must use the positive and negative frequency components of the quantum mechanical field operators. Ordering of the field terms, which are operators, is now important, thus the second order quantum correlation function becomes,

$$g^{(2)}(\tau) = \frac{\left\langle \hat{E}^{(-)}(t)\hat{E}^{(-)}(t+\tau)\hat{E}^{(+)}(t+\tau)\hat{E}^{(+)}(t)\right\rangle}{\left\langle \hat{E}^{(-)}(t)\hat{E}^{(+)}(t)\right\rangle \left\langle \hat{E}^{(-)}(t)\hat{E}^{(+)}(t)\right\rangle}. \tag{2.14}$$

For a single-mode field of the form given in Equation 2.8, this reduces to,

$$g^{(2)}(\tau) = \frac{\left\langle \hat{a}^\dagger(t)\hat{a}^\dagger(t+\tau)\hat{a}(t)\hat{a}(t+\tau)\right\rangle}{\langle \hat{a}^\dagger(t)\hat{a}(t)\rangle \langle \hat{a}^\dagger(t+\tau)\hat{a}(t+\tau)\rangle}. \tag{2.15}$$

For a Fock number state of the form, $|n\rangle$, one can show that this becomes $g^{(2)}(0) = (n-1)/n$. Therefore the second order correlation is always less than one. This is outside of the range allowed classically. As such, this is interpreted as a quantum mechanical behaviour of the light source since it takes on classically forbidden values. For a single-photon state where $n = 1$ then $g^{(2)}(0) = 0$. For a Fock state with $n \to \infty$, then, $g^{(2)}(0) \to 1$. Thus, a common measure of non-classicality for optical quantum states is that the source's measured $g^{(2)}(0)$ falls in the range $[0, 1)$,

$$0 \leq g^{(2)}(0) < 1. \tag{2.16}$$

Following from these two bounding equations, one can see that any measurement of $g^{(2)}(0)$ between zero and one implies the light source is non-classical.

2.3 Spectral-Temporal Wave Packets

In this section, the spectral-temporal modes of light are introduced. A general description of the spectral-temporal wave packet is then presented and certain important aspects discussed. This will include a minor deviation discussing the spectral phase. The use of Gaussian wave packets is then motivated and properties of its functional form discussed.

2.3.1 The Spectral-Temporal Modes

In this thesis the conjugate pair, frequency and time, will be studied. Furthermore, the quantum states of light used are assumed to be single-photons propagating in a well-defined direction, with well-defined transverse spatial and polarization modes. Therefore, the labelling of the mode will be omitted such that the simplified notation of the creation operator, $\hat{a}^\dagger_{\boldsymbol{k},j,\sigma} \to \hat{a}^\dagger(\omega)$, will be used to indicate that the spectral properties of the state are being studied. Once more, the creation and annihilation operators obey the commutation relationship such that, $\left[\hat{a}(\omega), \hat{a}^\dagger(\omega')\right] = \delta(\omega - \omega')$. There also exist the equivalent

temporal creation and annihilation operators such that $\left[\hat{a}(t), \hat{a}^\dagger(t')\right] = \delta(t - t')$.

When considering single-photon states composed of more than one frequency component, the state is defined by the general expression,

$$|\psi\rangle = \int_0^\infty \tilde{\psi}(\omega)\hat{a}^\dagger(\omega)\,|0\rangle\,d\omega. \tag{2.17}$$

This describes a single excitation in a mode comprised of frequencies weighted by the function $\tilde{\psi}(\omega)$ that describes a single spectral-temporal mode. (The ˜ symbol is used here, and throughout, to distinguish the spectral amplitude from the temporal.) This function is the spectral probability amplitude, describing the occupation of each angular frequency mode. The functions are thus normalized such that $\int_0^\infty |\tilde{\psi}(\omega)|^2 d\omega = 1$. Note, also, that the limits of integration are from zero to infinity. This is because the negative part of the frequency spectrum contains no additional information[91].

The equivalent representation of the state in the temporal domain can be determined by applying a Fourier transform (FT) to $\tilde{\psi}(\omega)$. Depending on the application and context of the work, the definition of the FT and inverse Fourier transform (IFT) have slight variations. Throughout this work, the following definitions will be used to determine a function in the temporal degree of freedom, $f(t)$, given the function in the spectral degree of freedom, $\tilde{f}(\omega)$,

$$\begin{aligned} f(t) = \mathcal{F}[\tilde{f}(\omega)] &= \frac{1}{\sqrt{2\pi}} \int_{-\infty}^{\infty} \tilde{f}(\omega) \mathrm{e}^{-i\omega t} d\omega, \\ \tilde{f}(\omega) = \mathcal{F}^{-1}[f(t)] &= \frac{1}{\sqrt{2\pi}} \int_{-\infty}^{\infty} f(t) \mathrm{e}^{i\omega t} dt. \end{aligned}$$

Here, $\mathcal{F}$ indicates a Fourier transform and $\mathcal{F}^{-1}$, the inverse. Throughout this work, the factor of $(2\pi)^{-1/2}$ will be assumed as contained within the normalization of the state and omitted from all following FT usages.

There is high interest for working with broadband non-classical states of light with bandwidths on the order of a few nanometres, as motivated in chapter 1. As dictated by the FT relation, these broadband states of light, typically, have short temporal durations. The temporal widths of the non-classical states of light studied in this work are classified as ultrashort pulses with temporal durations on the order of a few picoseconds to a few hundred femtoseconds. These ultrashort pulses of light will be referred to, throughout this these, as temporal-spectral *wave packets*: states of light with a probability distribution of finding the photon within a certain, well-defined region of the spectral-temporal interval.

2.3.2 Mode Overlap

A useful calculation to determine the similarity of two pulse modes is the spectral-temporal mode overlap. This is given by the scalar product between the two modes,

$$\langle\psi|\phi\rangle = \int_0^\infty \psi^*(\omega)\phi(\omega)d\omega. \tag{2.18}$$

As discussed previously, having extremely well-matched quantum states is crucial for applications such as LOQC and testing the fidelity of quantum operations. Therefore, the mode overlap is an important definition when manipulating and comparing quantum states.

2.3.3 The Spectral-Temporal Electric Field

The temporal description of the electric field of light is typically written in the following form [92],

$$E(t) = |E(t)|e^{-i\omega_0 t}e^{i\theta(t)} + \text{c.c.}, \tag{2.19}$$

where $|E(t)|$ is the slowly-varying, time-dependent wave packet amplitude, referred to as the envelope, and $\theta(t)$ is the time-dependent phase. The carrier frequency, ω_0, is the an-

gular frequency around which the spectral amplitude is centred. The second term in this definition, c.c., indicates the complex conjugate of the first and is included to ensure that the electric field is real-valued. It is given in the definition here for completeness but will be left out from now onwards for simplicity.

The spectral representation, $\tilde{E}(\omega)$, is given by applying a FT to Equation 2.19. This is also often written in the following form,

$$\tilde{E}(\omega) = |\tilde{E}(\omega)|e^{i\phi(\omega)} + \text{c.c.}, \tag{2.20}$$

where $|\tilde{E}(\omega)|$ is the spectral envelope and $\phi(\omega)$ is the spectral phase. However, note that there is no simple relationship between $|\tilde{E}(\omega)|$ and $|E(t)|$.

2.3.4 The Spectral Phase

As discussed in the introduction, the spectral phase is a central property of the electric field wave packet and which can be modulated in order to controllably change the temporal envelope. Thus, a clear understanding of the properties and effects of the phase on the spectral wave packet is crucial for this work.

For a given spectral amplitude, $|\tilde{E}(\omega)|$, the spectral phase determines the wave packet duration and shape. The shortest duration is achieved when $\phi(\omega)$ contains a combination of constant and/or linear terms only. In this case the wave packet is said to be *Fourier transform limited* (FTL). In general, the spectral phase plays an important role in governing the properties of the electric field of light. There are a few well-defined and widely used quantities related to the spectral phase, described below.

Performing a Taylor expansion of the spectral phase around the central frequency of the

wave packet, ω_0, one can rewrite the phase as,

$$\phi(\omega) = \phi\Big|_{\omega_0} + \phi^{'}\Big|_{\omega_0}(\omega-\omega_0) + \frac{\phi^{''}}{2}\Big|_{\omega_0}(\omega-\omega_0)^2 + ... + \frac{\phi^n}{n!}\Big|_{\omega_0}(\omega-\omega_0)^n, \tag{2.21}$$

where $\phi^{'}$ is the first derivative of the phase, given by $\phi^{'} = d\phi(\omega)/d\omega$, $\phi^{''}$ is the second derivative, $\phi^{''} = d^2\phi(\omega)/d\omega^2$, and so on. The first three terms of the expansion are the most prevalent in work on ultrashort pulses. Higher order contributions often have negligible effect. Therefore a minor detour to provide an insight into the meaning of the first few terms will be taken here.

$\phi(\omega_0)$ - Global Phase

The first term is the *global phase*. It is the constant found by evaluating the spectral phase at the carrier frequency. Applying an IFT leaves this unchanged. As such this constant term remains unchanged in both the spectral and temporal wave packet representations. Furthermore, this is non-measurable and often neglected in analysis where there are multiple oscillations of the EM field per wave packet.

$\phi^{'}$ - Group Delay

The first derivative, $\phi^{'}$, is given by the derivative of the phase with respect to frequency, $d\phi(\omega)/d\omega$. It is known as the first-order dispersion or *group delay*. For constant phase, the delay is zero. For linear phase, the delay is a constant thus can be used to describe the position of the pulse maximum, for example.

$\phi^{''}$ - Group Delay Dispersion

The third term contains the second derivative of the phase with respect to the frequency, $\phi^{''} = d^2\phi(\omega)/d\omega^2$. It is known as the second-order dispersion or as the *group delay dispersion* (GDD). This is the quadratic component of the phase centred around ω_0. When there is a quadratic phase on a wave packet, then increasing frequency components have

a linearly increasing temporal delay. This is commonly referred to as *chirp*: a spectrally varying temporal delay. The ultimate effect is an increase in pulse duration.

Group Velocity Dispersion

Another commonly defined property of dispersive media is the *group velocity dispersion* (GVD). This is defined as the group delay dispersion per unit length of material. Many optical component manufacturers provide a Dispersion parameter, D_λ, which is in fact the GDD, and is related to the GVD by,

$$D_\lambda = -\frac{2\pi c}{L\lambda_0^2}\text{GVD}. \tag{2.22}$$

The dispersion parameter has units of ps/(nm km) since it is often dependent on the central wavelength, λ_0, and is typically quoted for optical fibres which involve propagation over long distances, indicated by L.

2.3.5 Gaussian Wave Packets

This work focuses on shaping wave packets which have Gaussian envelopes. Gaussian wave packets are a useful set to work with; they remain Gaussian under Fourier transform and when dispersed, up to second-order. The functional form of a Gaussian wave packet mode with central angular frequency, ω_0, and zero phase, such that it is FTL, is given by,

$$\tilde{\psi}(\omega) = \tilde{N}\mathrm{e}^{-\frac{(\omega-\omega_0)^2}{2\sigma^2}}, \tag{2.23}$$

where $\tilde{N} = 1/\sqrt{2\pi\sigma^2}$ and ensures normalisation, and σ is a constant related to the spectral bandwidth. A single-photon state occupying this spectral mode is thus given by substituting Equation 2.23 into Equation 2.17.

Returning to the properties of the functional form of the Gaussian wave packet mode,

the constant, σ, can be related to the full width at half maximum (FWHM) of the intensity spectrum, $\Delta\omega$, also referred to as the spectral bandwidth, by,

$$\begin{aligned}\Delta\omega &= 2(\omega_{\frac{I}{2}} - \omega_0),\\ &= 2\sigma\sqrt{\ln(2)},\end{aligned} \tag{2.24}$$

where $\omega_{\frac{I}{2}}$ is the angular frequency where the Gaussian falls to half of its maximum intensity amplitude, $\frac{I}{2}$. Furthermore, the bandwidth in terms of wavelength, the variable that is physically measured in this work, can be determined by differentiating the relationship between wavelength and angular frequency, $\omega = \frac{2\pi c}{\lambda}$,

$$\Delta\omega = \frac{2\pi c}{\lambda^2}\Delta\lambda. \tag{2.25}$$

The Temporal Gaussian Wave Packet

The equivalent temporal description of the same Gaussian wave packet is determined by applying an IFT to Equation 2.23,

$$\psi(t) = N\mathrm{e}^{-\frac{t^2}{T^2}}\mathrm{e}^{-i\omega_0 t}, \tag{2.26}$$

where $N = 1/\sqrt{\pi T^2}$ and $T^2 = 2/\sigma^2$. The equivalent temporal FWHM for $\psi(t)$ is given by $\tau_p = T\sqrt{2\ln(2)}$.

The Time-Bandwidth Product

The product of the spectral bandwidth and temporal FWHM for the FTL wave packet is,

$$\Delta\omega_p\tau_p = 4\ln(2) = 2\pi c_B, \tag{2.27}$$

where c_B is a constant, equal to 0.441 for the Gaussian pulses discussed here. This relation is useful when estimating the temporal duration using the measured spectral width, since

the extremely short temporal durations are challenging to access experimentally.

2.4 Classical Spectral-Temporal Pulse Shaping

Since the invention of the continuous wave (CW) laser, just over fifty years ago, significant progress led to the development of ultrashort light sources in the 1980s[93,94]. The development was partly driven by the many uses and applications of these ultrashort pulses, including studies of ultrashort processes in both biological[95] and solid-state materials[96], for characterization of high-speed electronic and optoelectronic devices and systems[97], optical communications[98] and medical imaging[99] to name a few. As such there is high demand for techniques to control and modify these wave packets to tailor their properties for the desired application of the user[71].

These ultrashort pulse shaping techniques include linear filtering, dispersive effects and, most effectively, a combination of these two. There are many subdivisions of these three main areas, including techniques such as using deformable mirrors[100] and interference methods[101]. In this section, a brief overview of those techniques relevant to the work here is given. These include linear filtering, the time lens and the 4f line and are discussed here because they either share similar characteristics to the pulse shaping method presented in this work, or provide an insight into the need for a method that is compatible with non-classical states of light. This review presented here is not extensive, for more information on classical pulse shaping the reader should refer to the literature[71,72,102,103].

A parallel is first drawn between wave-front shaping of the spatial-momentum modes. This field of pulse shaping has historically been easier to implement experimentally. Additionally, the direct visual effects of pulse shaping these modes enables easier access to understanding the methods involved. The underlying equations governing the spatial-momentum and the spectral-temporal modes are the same. Thus, by first discussing

wave-front shaping of the spatial-momentum modes, the understanding of pulse shaping in the spectral-temporal modes should be more clear.

Complete control of the spatial-momentum domain has been demonstrated using a unitary programmable mode converter (UPMC) which is capable of performing any spatial unitary transform of the light field[104]. Once again, calling upon the analogy with the spectral-temporal modes, there is a current drive towards developing an analogous method for complete control over the spectral-temporal modes.

2.4.1 Pulse Shaping Theory

When modifying spectral-temporal wave packets, typically, one envisions cutting out parts of the pulse, for example using a spectral filter or a time gate. This linear amplitude filtering is the most basic form of pulse shaping but introduces losses. When considering conjugate bases it is possible, instead, to exploit the Fourier relationship between the two. For example, modifying the spectral phase can result in a temporal amplitude manipulation and vice versa. It is this useful relationship that is often exploited in pulse shaping techniques to provide advantageous results, or to circumvent impractical experimental implementations.

The idea of manipulating the spectral (temporal) phase to modify the temporal (spectral) amplitude may seem, at first, abstract. However, this is operationally identical to effects seen in the spatial-momentum domain such as when focusing with lenses. The direct analogy commonly taken when comparing the spectral-temporal ($\omega - t$) and spatial-momentum ($x - k$) domains, is to map the spatial variable to the temporal, $x \mapsto t$ and the momentum variable to the spectral, $k \mapsto \omega$[105]. Following this mapping, the spectral-temporal analogy for the iris is a temporal aperture, more commonly referred to as a *time gate*. The equivalence of a lens in the spectral-temporal domain is the application of a quadratically varying temporal phase. Both these analogies are expanded on below.

Linear Filtering

The first analogy considered is a collimated, free-space propagating, Gaussian spatial mode. This has an intensity profile which is rotationally symmetric about the propagation axis. If one wishes to reduce the radius of the spatial distribution, the most straight forward solution would be to insert an iris, for example. This blocks the unwanted outer regions of a circular spatial mode and is known as linear filtering. In the plane exactly after the iris (i.e. with no additional free-space propagation) the spatial mode has been modified as desired. Since energy, and hence information, of the original beam has been removed, this is a non-unitary processes.

The linear filtering process can be described in either the temporal or spectral domain. Time-invariant linear filtering occurs when one uses a spectral filter and its action is defined in the spectral degree of freedom by the frequency response function, $\tilde{h}(\omega)$. This describes the amplitude of which discrete spectral components are to be transmitted. The application to a wave packet, $\tilde{\psi}(\omega)$, is given by, $\tilde{\psi}_{\text{out}}(\omega) = \tilde{h}(\omega)\tilde{\psi}_{\text{in}}(\omega)$. As dictated by the Fourier relationship between the two degrees of freedom, this spectral filtering results in temporal broadening. For filters that remove original amplitudes then the output remains un-normalized such that $\int |\tilde{\psi}_{\text{out}}(\omega)|^2 d\omega \leq 1$. Temporal gating is similar to spectral filtering and is described as a frequency-invariant linear filter. The application of a temporal gate, allowing only certain temporal portions of the ultrashort pulse to pass, results in spectral broadening and reshaping.

Linear filtering is detrimental to quantum wave packets since removing frequency (temporal) components results in loss of amplitude and thus of the photon's state information.

Phase Modulation

The second analogy between the spatial-momentum and spectral-temporal domains is drawn by comparing the amplitude profile outcome of a linear filter method and a phase modulation method. In the spatial-momentum domain, one is able to achieve the same spatial modulation as an iris by using a telescope apparatus comprised of two lenses. The first lens applies a spatially-dependent phase to a collimated beam to alter the beam's transverse momentum profile such that, after passing through the lens and propagating in free space, it becomes focused at the focal point. A second lens, with a different focal length, and hence different effect on the momentum distribution, is inserted one focal length away to re-collimate the lens resulting in an enlarged or reduced spatial distribution, depending on the relative length of the two focal lengths.

This method directly addresses the phase in one variable to modify the amplitude of the conjugate variable. This method can be shown to be unitary, preserving all of the original state. Furthermore, there is an equivalent phase-modulation method in the spectral-temporal domain in order to achieve the same amplitude profile of a spectral filter or temporal gate, for example. This approach allows one to access, for example, extremely short time scales, usually very difficult to control with time gates which operate on time scales orders of magnitude greater than hundreds of femtoseconds. One successful development of this method is the *time lens* and is described in more detail below.

Time Lens

A time lens, where the spectral-temporal analogy of the optical lens is employed, is commonly used to control the temporal shape of ultrashort wave packets through stretching and compression, for example in chirped pulse amplification[106]. This technique is analogous to propagating a diffracted beam through a thin optical lens as described in more detail below.

In a traditional thin, spatially-varying, optical lens the beam is first propagated in free space towards the lens. Whilst passing through the lens, a phase is introduced which varies quadratically in the spatial mode, $\phi(x) = ax^2$, and, following further propagation in free space, results in either a compression or stretching of the spatial mode, seen by the focusing or expansion of the spatial mode.

The temporal analogue, following the domain mapping discussed above, consists of applying a phase that varies quadratically in the temporal domain, $\phi(t) = \alpha t^2$, to an initially spectrally dispersed wave packet. Following the temporal phase modulation the wave packet then undergoes further propagation to induce further spectral dispersion. The result is the wave packet is either compressed or stretched in time.

The schematic in Figure 2.1 presents a side-by-side comparison of the lensing techniques applied in both the spatial-momentum (above) and spectral-temporal (below) domains. The phase induced on the wave packet as a result of propagation through each part of the three-step process is labelled alongside the process in both diagrams. The temporal lens theory is well established[72,105,107] and the technique has been utilised in many optical pulse shaping applications, ranging from simple magnification to modifying one member of an entangled state.

The 4f Line

Many of the early developments of pulse shaping techniques for sub-nanosecond pulses involved filtering of optical frequency components which had been first spatially dispersed by a pair of diffraction gratings. As a result of this spatial dispersion, the pulses were often distorted. In 1983, the 4f-line, also known as the “zero dispersion pulse compressor”, was introduced to the field of linear pulse shaping[108] and is now the most widely adopted method[109]. It relied on the spectrally-dependent angular dispersion of the light pulse,

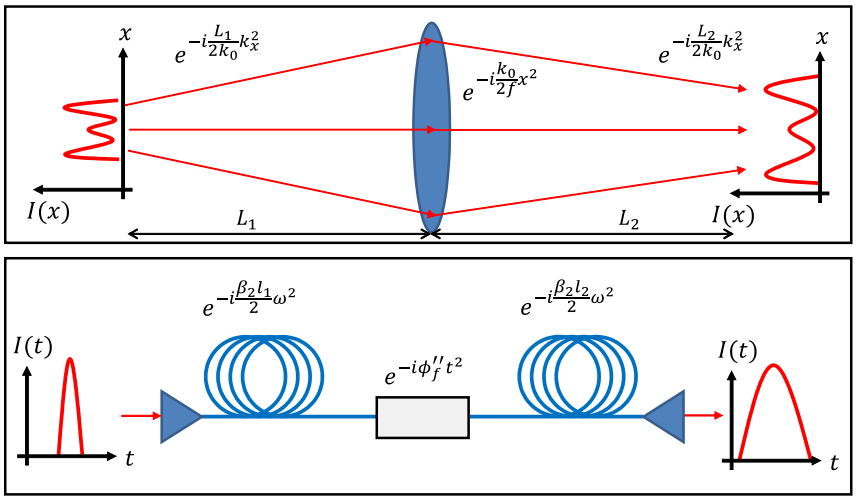

Figure 2.1: The comparison of manipulating the spatial-momentum and the spectral-temporal modes is depicted schematically. Propagation through a traditional, thin, optical lens, **(a)**, is compared to fibre propagation and an electro-optic modulator (EOM), **(b)**. Free space propagation, over a length, L_1, results in a quadratic phase of the form $(L_1/2k_0)k^2$ where k_0 is constant depending on the wave vector of the original pulse. A similar effect is seen in the spectral-temporal domain, where a phase of $(\beta_2 l_1/2)\omega^2$ is experienced from propagating through a fibre of length l_1 with GVD, β_2. The traditional lens applies a spatially varying phase of the form $(k_0/2f)x^2$, where f is the focal length of the lens, whereas the NLO process induced a phase of $\phi'' t^2$, where ϕ'' is the dispersion of the EOM. A final propagation in free space, of length L_2, for the spatial-momentum manipulation, and through a second fibre of length l_2, for the spectral-temporal domain, results in a reshaped pulse.

using a grating, followed by a lens to produce a collimated beam of light varying spectrally in the transverse direction. A filter, or mask was then applied in the Fourier plane of the dispersed, collimated beam to perform the desired pulse shaping. The inverse focusing and angular dispersion was then applied to retrieve the original spectral profile.

A schematic of this is shown in Figure 2.2. The "4f" refers to the use of two optical elements with identical focal lengths such that the gratings and filtering mask are located at the focal points. In principle the 4f line allows for arbitrary spectral phase to be applied to the optical pulse and is the most widely adopted pulse shaping method since the inserted mask can be specifically designed for the desired outcome. A spatial light modulator (SLM) is frequently used for arbitrary programming and control of the mask applied in the Fourier plane and has since been combined with other degrees of freedom to

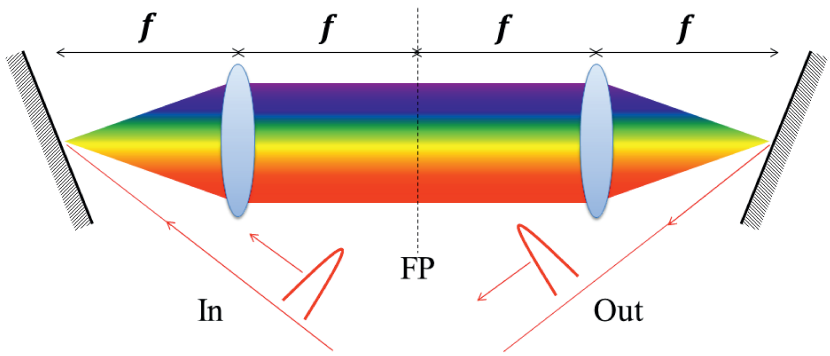

Figure 2.2: The 4f line is a dispersion-free pulse-shaping apparatus for ultrashort pulses. An incident pulse is dispersed by the first diffraction grating and the spatially separated spectral components collimated by the first thin lens. One focal length away from this lens, lies the Fourier plane (FP). In this plane, spatial and phase masks can be placed to target different spectral components of the initial incident pulse. The second lens, placed another focal length away performs a second Fourier transform from the Fourier "mask" plane to the plane of the second grating. The second lens and grating recombine all the frequencies back into a collimated beam.

successfully demonstrate control of the transverse spatial profile[110], the polarization[111] and the phase of the ultrashort pulse[109]. The 4f-line pulse shaping technique has also been successfully demonstrated for entangled photon pairs[112] and for the observation of entanglement between spatial modes[113]. In practice, however, the 4f line does have some difficulties including a limited size of the SLM and inter-SLM-pixel losses. Despite the simple concept, there can be a trade-off between the optical set-up parameters and the achievable spectral resolution for manipulation[114].

2.5 Non-Classical Spectral-Temporal Pulse Shaping: A Review and Proposal

In this section, a brief review of the field of quantum pulse shaping methods for the spectral-temporal modes is given. An approach to quantum pulse shaping, that is tunable and quantum-state preserving, and which is the main result of this thesis, is then introduced as a viable alternative to the recently demonstrated methods. The theory describing this method: spectral amplitude modulation through temporal phase modification, is finally presented.

2.5.1 A Review of Quantum Optical Pulse Shaping

In recent years, a range of pulse shaping methods for non-classical states of light has been developed. These began with the easier-to-access polarization modes for applications in QKD[115,116] to general phase manipulation[117]. Now methods for the spectral-temporal modes are being proposed and tested, highlighting the growing interest in the area[118]. In this section a selection of some of the more successful of these demonstrations are discussed.

Quantum Frequency Conversion

Single-photon frequency conversion, also known as quantum frequency conversion (QFC), has been studied since 1990 when it was predicted that the quantum nature of single-photons can be preserved when undergoing frequency conversion by the NLO process of four-wave mixing (FWM)[119]. This was then first experimentally demonstrated two years later by the same author, with the non-classical nature of the frequency converted light shown to be preserved[120]. QFC has been verified to preserve quantum correlations[121–124] and even quantum non-Gaussianity[125]. However, many of these methods rely on NLO processes, such as sum frequency generation (SFG), which are often a victim of noise and inefficiencies. Understanding and reducing these noise contributions remains an active

area of research[126].

Quantum Wave Packet Shaping

Wave packet temporal expansion of a non-classical two photon, or *bi-photon*, state was first experimentally studied in 2002, in an attempt to understand the process and effect upon the quantum statistics of the system for real-life applications[127]. Pulse shaping of both the temporal and spectral modes of a single-photon by spectrally or temporally filtering the other photon in an entangled photon pair, was the next significant development[128,129]. Temporal shaping of a heralded single-photon wave packet was later experimentally demonstrated using a similar method: applying chirp broadening and interference effects to one photon with direct time detection of the other[130].

Quantum Memories as Pulse Shapers

Precision spectral manipulation has also been demonstrated in a photon echo quantum memory[131]. It was found that a frequency shift of the retrieved light was achieved by adding or subtracting energy to the light whilst stored in the quantum memory. However, the pulses involved in this process are of narrow bandwidth.

Nonlinear Optical Processes

Recently, spectral pulse shaping methods have been developed using NLO interactions such as spectral shifting using FWM in fibres[132,133]. However, NLO processes are intrinsically probabilistic. Furthermore, these processes create noise photons such as from stimulated Raman scattering[132]. The challenges associated with nonlinear processes include suppressing this noise, in addition to scatter of light from the original pump and limited repetition rates to reduce optical damage to the nonlinear material.

Another recent demonstration required interference with a specially prepared optical wave packets for sum-frequency generation[134], but this limits the tunability of the method.

Pulse shaping in the form of up-conversion[1] of quantum dots has also been demonstrated but, again, with its own associated challenges mainly owing to the specific properties and preparation of the system in hand[135,136].

A Brief Summary

Table 2.1 contains a summary of major experimental developments in spectral pulse shaping for single-photons and non-classical light. This does not include some recently proposed methods, that have yet to be experimentally verified, such as QFC using a Sagnac interferometer[137], SFG in a whispering-gallery-mode resonator[138], real-time, arbitrary waveform manipulation using NLO processes[139] and even wavelength conversion via cavity optomechanics[83]. There have also been other advancements and proposals where QFC methods are used as part of larger applications such as quantum pulse gates[140], mode-resolved photon counting[141] and subtracting mode-dependent single-photons from non-classical beams[142,143], which are also omitted from the table. Nonetheless, they highlight the growing interest in and demand for arbitrary quantum pulse shaping.

Despite these many developments, a general spectral-temporal pulse shaping method has yet to be developed. Ideally one wishes to use a black box into which any arbitrary single-photon can be admitted, and arbitrary spectral-temporal reshaping performed whilst preserving all information contained within the quantum state. Nonetheless, work towards this goal is ongoing throughout the community[63].

The Ideal Quantum Pulse Shaper

Following the above discussion, it is possible to define the ideal single-photon pulse shaper operation: an ideal single-photon pulse shaper would admit a single-photon wave packet with arbitrary frequency and bandwidth and would deterministically apply a pre-defined spectral-temporal modification. The pulse shaper would achieve this without removing

[1] A process where light is emitted with photon energies higher than those of the incident light.

Result, *Process Details*	Spectral Change	Year	Quan. Pres.	Tunable
First QFC demonstration, *NLO, SFG in type-II KTP*[120]	1065 → 532 nm, $\Delta\lambda = 533$ nm	1992	✓	✗
Complete Bell state measurement of QFC photons, *NLO, SFG in type-I and type-II crystals*[144]	885 → 420 nm, $\Delta\lambda = 465$ nm	2001	✓	✗
Large, tunable QFC as an application for efficient detection, *SFM with strong pump at 1064 nm in PPLN*[52]	1548 → 631 nm, $\Delta\lambda = 917$ nm	2004	✗	✓
QFC in fibre, *QFC using FWM in PCF*[133]	683 → 659 nm, $\Delta\lambda = 24$ nm	2010	✓	✓, 660 → 760 nm
QFC of single-photons from a Quantum Dot, *SFG in PPLN waveguide and amplitude modulation in an EOM*[135]	1300 → 710 nm, $\Delta\lambda = 590$ nm	2011	✓	✗
Quantum preserving, QFC from visible-to-telecommunication, *NLO, PPLN waveguide*[145]	780 → 1522 nm, $\Delta\lambda = 742$ nm	2011	✓	✗
QFC with polarization entanglement conserved, *NLO: in PPKTP crystal*[146]	810 → 532 nm, $\Delta\lambda = 278$ nm	2012	✓	✓
Bandwidth and Frequency Manipulation, *Gradient echo memory*[147]	1.4MHz, $\frac{1}{2}$FWHM→ 2×FWHM	2012	✓	✓
Linear adiabatic wavelength conversion, *optical microcavity*[148]	$\Delta\lambda = 0.5$ nm	2012	✗	✓
Bandwidth compression, *NLO, SFG with strong laser pulse of opposite chirp, in BiBO*[134]	$\frac{1}{40}$ FWHM	2013	✗	✓, $70 \times \Delta\lambda$

Table 2.1: Summary of major experimentally demonstrated non-classical spectral pulse shaping methods. See abbreviations list in chapter for acronyms. "Quan. Pres." indicates if the method demonstrates preservation all photon-number statistics. "Tunable" indicates if the method can be applied to different spectral frequencies and bandwidths. Note, this is not a complete list, it includes the major experimental demonstrations, for example when a new method was demonstrated or significant advancement of technique.

any of the incident signal, or stored information and preserve the photon statistics of the state. Furthermore, the method must also preserve any existing entanglement in the state. Mathematically, this operator, denoted as $\hat{U}$ would be be unitary and would operate on a state such that $\sum_j \hat{U}_{ij}\hat{a}_j^\dagger = \hat{b}_i^\dagger$ where the j and i label the input and output modes. This would also preserve the commutation relation such that $\left[\hat{a}_i, \hat{a}_i^\dagger\right] = 1$.

In this thesis, a step towards developing this black box is taken. A robust and adaptable technique of temporal phase modulation is presented. The process is deterministic and intensity independent, favourable for single-photon states of light. How this is done, is described in more detail below.

2.5.2 Spectral Pulse Shaping via Temporal Phase Modification

To modify the spectral amplitude, $\tilde{\psi}(\omega)$, the temporal phase of the optical wave packet is manipulated. Controlling the temporal phase of ultrashort wave packets is challenging, largely owing to the extremely short time scales involved. Nonetheless, a deterministic, ultrashort phase shaping method is presented below, compatible with single-photon quantum states at high laser repetition rates. The mathematical details of this method are presented below.

2.5.3 Linear Temporal Phase Modification

Consider a wave packet in its temporal representation, $\psi(t)$. Applying a linear temporal phase of the form, $\phi(t) = \alpha t$, results in a modified wave packet, $\psi_{\text{mod}}(t)$, of the form,

$$\psi_{\text{mod}}(t) = \psi(t)\mathrm{e}^{i\alpha t}. \tag{2.28}$$

The effect of this on the wave packet's spectral representation is found by applying a FT to give,

$$\begin{aligned}\tilde{\psi}_{\text{mod}}(\omega) &= \int \psi_{\text{mod}}(t)\mathrm{e}^{i\omega t}dt, \\ &= \int \psi(t)\mathrm{e}^{i(\omega+\alpha)t}dt, \\ &= \tilde{\psi}(\omega+\alpha). \end{aligned} \tag{2.29}$$

The result is a spectral shift of the wave packet from ω to $(\omega + \alpha)$, a consequence of the Fourier transform shift theorem. This is referred to as a *spectral shear*. In the same way, a spectral shift in the opposite direction can be achieved by applying a negative temporal phase, $\phi(t) = -\alpha t$.

Further manipulation of the wave packet's spectral amplitude can be achieved by applying different forms of the temporal phase.

2.5.4 Quadratic Temporal Phase Modification

The result of applying a quadratic temporal phase of the form $\phi(t) = \beta t^2$ depends on the form of the input field. The case of a Gaussian wave packet of the form give in Equation 2.26, is considered here. It is this form of amplitude that is well-suited for optical quantum communications[40] and used for experimental demonstration later in this thesis.

The wave packet has carrier frequency, ω_0 and initial spectral bandwidth, $\Delta\omega_0 = 2\sigma\sqrt{\ln(2)}$, such that the temporal width is given by $\tau_p = 2\ln(2)/\sigma$. Applying the quadratic temporal phase to the state results in,

$$\psi_{\text{mod}}(t) = \psi(t)\mathrm{e}^{i\beta t^2}. \tag{2.30}$$

The resultant spectral form, found by applying the FT, is,

$$\begin{aligned}\tilde{\psi}_{\mathrm{mod}}(\omega) &= \int \psi(t) \mathrm{e}^{i(\omega t+\beta t^2)} dt, \\ &= \tilde{N} \mathrm{e}^{-\frac{(\omega-\omega_0)^2}{2\sigma^2_{\mathrm{mod}}}} \mathrm{e}^{\theta_{\mathrm{mod}}(\omega)},\end{aligned} \tag{2.31}$$

where $\sigma^2_{\mathrm{mod}} = \sigma^2(1 + 4\beta^2/\sigma^4)$ and the final term describes the resultant spectral phase, $\theta_{\mathrm{mod}}(\omega) = -i\beta T^2(\omega - \omega_0)^2/2\sigma^2_{\mathrm{mod}}$. The constant, $\tilde{N}$ ensures normalization. The full derivation for this expression is found in Appendix A.

Thus the spectral bandwidth has increased by a factor of $\sqrt{1 + 4\beta^2/\sigma^4}$ (see section A.1). Hence, applying a quadratic temporal phase to a FTL pulse results in spectral expansion. Note, since the constant β is squared in the final spectral form of the wave packet, application of both positive ($+\beta$) and negative ($-\beta$) quadratic temporal phase results in spectral expansion for the Gaussian wave packet.

This process is exactly analogous to the spectral expansion experienced by a pulse propagating through a material with second-order dispersion, ϕ'', as discussed in chapter 2. The result in that case is an increase in the temporal bandwidth, originally given by τ_p, to

$$\tau_{p,\mathrm{mod}} = \tau_p \sqrt{1 + \left(\frac{4\ln(2)\phi'' z}{\tau_p^2}\right)^2}, \tag{2.32}$$

where z is the distance travelled in the material[92].

2.6 Chapter Summary

At the beginning of this chapter, the theory necessary to understand photons as excitations of quantum field modes was presented. A discussion on how to distinguish non-classical and classical light sources was then included. The spectral-temporal modes were intro-

duced along with a general introduction to the theory of pulse shaping, and the most common classical wave packet approaches.

In the final section, a review of current non-classical pulse shaping methods was given. This motivated the description of pulse shaping by direct temporal phase modification as an alternative. This method of spectral pulse shaping by temporal phase modification is a unitary process and will be implemented using quantum wave packets of light in the following chapters of this thesis.

Chapter 3

A Spectrally-Pure Single-Photon Source

3.1 Introduction

Demonstrating the quantum pulse-shaping technique, introduced in this thesis, necessitated construction of a pulse-mode quantum light source. There are a range of non-classical light sources currently employed in the quantum optics community with a diversity of characteristics. Here, the choice of source and its specifications is driven by the requirement to demonstrate the pulse-shaping method, which needs a train of short optical pulses. The constructed single-photon state must also be characterized to provide a baseline upon which to compare the pulse-shaping effects and to quantity the technique's performance.

This chapter is split into three sections. First, the ideal properties of a non-classical wave packet, for demonstration of the spectral quantum pulse shaping technique presented here, are discussed. One useful prerequisite is a pure-state single-photon source, the definition and implications of which are given. This discussion then motivates the choice of the single-photon source which was built specifically for this work.

The next section provides the theoretical background and experimental construction details of the chosen single-photon source.

Finally, the quality of the constructed single-photon source is evaluated. This includes measuring the spectral intensities, performing a joint spectral intensity measurement and quantum interference measurements.

3.2 A Single-Photon Source

In this section, a short discussion of the desirable properties of a single-photon source for demonstration of spectral quantum wave packet pulse shaping is given. This is followed by a quick overview of the available sources that have been developed over the past few decades, and continue to be employed for different applications.

3.2.1 Pure, Single Photon Wave Packets

The single-photon state of light presented in Equation 2.17, and given again here, is a *pure state*,

$$|\psi\rangle = \int_0^\infty \tilde{\psi}(\omega)\hat{a}^\dagger(\omega)d\omega\,|0\rangle\,, \tag{3.1}$$

since it is described by a coherent superposition of single mode states and can be represented as a single vector in the state space of the optical field. The function $\tilde{\psi}(\omega) = \langle\omega|\psi\rangle$, describes the probability amplitude of the state in the frequency basis and is normalized such that $\int_0^\infty |\tilde{\psi}(\omega)|^2 d\omega = 1$.

A state is pure when it can be represented in this manner, i.e. by a single state vector, $|\psi\rangle$. This is in contrast to a *mixed state*. For a mixed state it is only possible to identify a set of possible state vectors, $\{|\psi_j\rangle\}$, with associated probabilities, $\{p_j\}$. In this case, the state must be represented by a *density operator*, $\hat{\rho}$. The general form for a density operator is given by,

$$\hat{\rho} = \sum_i p_i\,|\psi_i\rangle\,\langle\psi_i|, \tag{3.2}$$

where p_i is the probability that the system may be found in the pure state $|\psi_i\rangle$. For the pure case $p_i = 1$, for some i in an appropriate basis, and all other contributions are zero. The density operator thus expresses the mixed state as an incoherent sum of pure state density operators, $|\psi_i\rangle \langle\psi_i|$.

When working in the continuous mode basis, the definition of the density matrix becomes,

$$\hat{\rho} = \int\int \rho(\omega, \omega')\hat{a}^\dagger(\omega) |0\rangle \langle 0| \hat{a}(\omega')d\omega d\omega'. \tag{3.3}$$

Here $\hat{a}^\dagger(\omega) |0\rangle$ is a pure single-photon frequency state, the set of which forms a complete basis. The function, $\rho(\omega, \omega')$, is the density matrix element that describes the probability distribution and provides information about any relative phase between different elements. The value of $d\omega\rho(\omega, \omega)$ provides the probability of detecting a photon with frequency between ω and $\omega + d\omega$.

Purity

For a pure state, the density operator can be written as,

$$\hat{\rho}_{\text{pure}} = |\psi\rangle \langle\psi| . \tag{3.4}$$

In this case the total number of pure states required to describe the state, N, also referred to as the *rank* of the corresponding density matrix, is equal to one. Mixed states can have a value of $N = 2 \rightarrow \infty$. The *purity*, denoted as $\mathcal{P}$, is a useful property to quantify the quantum state,

$$\mathcal{P} = \text{Tr}\left[\hat{\rho}^2\right], \tag{3.5}$$

where Tr denotes the trace of the operator. The trace of an operator is equal to the sum of the diagonal elements of a matrix representation of the operator. For a diagonalised density matrix, as in Equation 3.2, this leads to the following expression for the purity,

$\mathcal{P} = \sum_i^N p_i^2$. One can therefore see that a pure state has $\mathcal{P} = 1$ and a mixed state can take any value in the range $[0, 1)$.

The pure state is the most desirable to work with for quantum information applications. If one can fully describe the effect of an operation on an appropriately chosen set of pure states, then one will be able to determine the effect on a mixed state comprised of these pure states. This is because the action of an operation on a mixed state can be viewed as a weighted sum of the operation on the set of pure states. Furthermore, any mixedness is equivalent to incoherence in the system and reduces the visibility of interference phenomena and fidelity of quantum operators. In this work, a single-photon source created in a pure state is highly desired. Additionally, the state's mode must also be a well-defined wave packet, more specifically a Gaussian in the spectral-temporal domain.

In the next section, a brief overview of the most commonly used single-photon sources is given. The many sources are varied in their methods of experimental implementation and resultant optical properties reflecting the variety of uses to which they are applied. Following this, the single-photon source chosen for this work is introduced.

3.2.2 An Ideal Single-Photon Source

There exist many approaches for generating quantum states of light that are produced with widely varying properties. Here, single-photon sources are considered, which are an essential part of a broad range of applications. It is generally agreed[149,150] that there exist some inherent properties that an ideal single-photon source should possess: An ideal single-photon source should emit one, and only one, photon "on-demand" as required by the user: for example, at the push of a button and at an arbitrary time and with each subsequently emitted photon indistinguishable. Each photon would be emitted in a single, well-defined, spatio-temporal mode, selected, or pre-determined, in advance of its emission.

In practice there exist two main approaches to experimentally realize single-photon sources: *deterministic* and *probabilistic*. The former includes quantum dots (QDs)[151], single atoms coupled to optical cavities[152], atomic ensembles[153] and nitrogen-vacancy (NV) centres in diamond[154] to name a few. Single-photon emission from such sources is typically in response to a trigger event.

Probabilistic sources employ processes where the decay of one photon and creation of a pair of single-photons is stimulated by random vacuum fluctuations in nonlinear optical (NLO) materials. For such probabilistic sources optically pumped by quasi-monochromatic or continuous-wave (CW) light, the photon pairs are created at random times. However, when optically pumped with pulsed light, the creation time is restricted to within the pump's transit time through the nonlinear medium. The probabilistic processes often employed are parametric down-conversion (PDC) which is performed in NLO materials such as bulk crystals and waveguides[155–158], and FWM performed in optical fibres[159,160]. Despite being probabilistic, these photon pair sources can be operated in herald mode where the detection of one photon is used to herald the existence of the other, this is referred to as heralded detection. However, these processes also have non-zero probabilities of creating higher-order photon states, such as multiple-photon pairs. These events can add noise to the single-photon source, however these probabilities are, typically, much less than the probability of creating the single-photon pairs.

Finally, there also exist other sources which do not fall in either category, such as in semiconductors and exciting cyrogenically-chilled molecules[150], the details of which are beyond the scope of and relevance to this work.

The most pure single-photon states produced have been realized via spontaneous parametric down-conversion (SPDC) in a bulk crystal[161]. A pulsed source is employed here

to demonstrate the quantum pulse-shaping technique. The basic theory detailing the production of this source is presented below, followed by technical details of the set up.

3.2.3 Theory of Spontaneous Parametric Down-Conversion

Parametric down-conversion (PDC) is a three-wave mixing process. In the case considered here one photon in the "pump" field, labelled p, propagating through a crystal with a second-order nonlinear response, denoted by $\chi^{(2)}$, spontaneously decays into a pair of photons, historically labelled s and i for the "signal" and "idler" fields respectively. This processes obeys energy and momentum conservation such that the angular frequencies are related by, $\omega_p = \omega_i + \omega_s$, and the wavevectors by, $\boldsymbol{k}_p = \boldsymbol{k}_i + \boldsymbol{k}_s$. Due to the momentum and energy constraints, PDC can create photons which are entangled in the equivalent degrees of freedom, namely their momentum and spectrum. Furthermore, momentum conservation allows for two different geometries of the emitted pair to be satisfied, *collinear*: when they emerge in the same direction or *non-collinear*: when they have wave vectors in opposite directions around the axis of propagation, creating "cones" of down-conversion, as shown in Figure 3.1. PDC is further, commonly, divided into *Type I* and *Type II* if the daughter pair are emitted with the same or perpendicular polarizations, respectively. PDC occurs in two regimes: *spontaneous* and *stimulated*. In the spontaneous regime, photons are created only due to the vacuum electromagnetic field fluctuations. In stimulated PDC, the emission process is amplified by stimulation from an intense, external auxiliary pump. By aligning the auxiliary pump with a down-conversion mode of the same wavelength this stimulates the emission in the down-conversion mode and its conjugate indirectly.

To adhere to the properties of an ideal single-photon for this thesis, the source was tailored to operate in the **spontaneous** regime with low conversion efficiency such that, largely, only heralded single-photon states were produced and the abbreviation SPDC can be used. Furthermore, the source is **collinear** and **Type II** with a specific choice of crystal to ensure correct phasematching for pure states. A full theoretical derivation of the optical

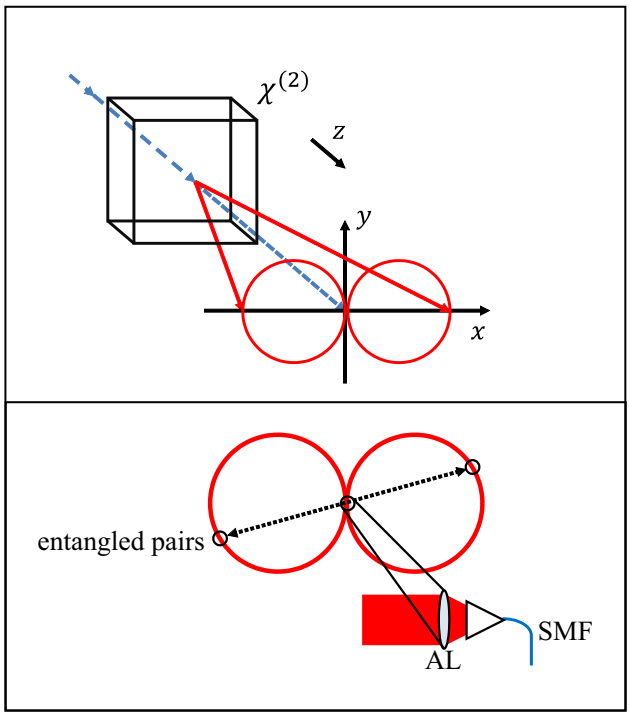

Figure 3.1: The top diagram shows the geometry of the cones created in downconversion. The pump laser (blue, dashed line) is propagated through the NLO material, $\chi^{(2)}$, in the z-direction. The downconverted photons are emitted into cones on the output (red, solid lines). In the lower part, the black, dotted line indicates existing entanglement between two opposing locations on the cones. The ideal location for fibre coupling of the cones to ensure that a separable state is collected, is indicated. The beam path must be centred on the aspheric lens (AL) for coupling into the single mode fibre (SMF).

state produced by SPDC can be found in the literature[162,163]. For finer details on the design of the source used in the work, the reader can refer to[161].

The Pure Bi-Photon State

The bi-photon state, $\left|\Psi^{(2)}\right\rangle$, produced by the SPDC source, is typically written in the following form[161],

$$\left|\Psi^{(2)}\right\rangle = |0\rangle + \eta \int_0^\infty \int_0^\infty f(\omega_\mathrm{s}, \omega_\mathrm{i}) \hat{a}_\mathrm{s}^\dagger(\omega_\mathrm{s}) \hat{a}_\mathrm{i}^\dagger(\omega_\mathrm{i}) \, |0\rangle_\mathrm{i} \, |0\rangle_\mathrm{s} \, d\omega_\mathrm{s} d\omega_\mathrm{i}, \tag{3.6}$$

where η is an efficiency constant primarily related to the nonlinear coupling coefficient and pump pulse amplitude. The spectral mode distribution of the bi-photon state is given by $f(\omega_\mathrm{s}, \omega_\mathrm{i})$ which is referred to as the joint spectral amplitude (JSA) whose modulus squared gives the probability distribution of the photon pairs. It is a function of both the idler and signal frequencies and contains phase information describing any correlations between the down-converted photon pair.

A Pure Single-Photon State?

In line with the definition of pure states given at the start of this section one can see that the bi-photon state in Equation 3.6 is pure. However, the JSA may describe correlations in frequency between the signal and idler photons. In this case, when detecting one photon to herald the other, that photon may be projected into a mixed state if the heralding measurement is not able to distinguish between different heralding modes. This is detrimental for producing the ideal, pure, single-photon state.

In this work, the idler state will be used as the herald. The form of the signal state after heralded detection can be found by taking the partial trace of the density operator of the bi-photon state in Equation 3.6 given by, $\hat{\rho}^{(2)} = \left|\Psi^{(2)}\right\rangle \left\langle\Psi^{(2)}\right|$, over the idler. This allows one to extract the density operator of the final, signal state,

$$\begin{aligned}\hat{\rho}_{\mathrm{s}} &= \mathrm{Tr}_{\mathrm{i}}\left[\hat{\rho}^{(2)}\right], \\ &= \int \langle\omega|\, \hat{\rho}^{(2)}\, |\omega\rangle_i \, d\omega, \\ &= \int\int \rho_{\mathrm{s}}(\omega_{\mathrm{s}}, \omega'_{\mathrm{s}}) \hat{a}^{\dagger}_{\mathrm{s}}(\omega_{\mathrm{s}}) \,|0\rangle\, \langle 0|\, \hat{a}_{\mathrm{s}}(\omega'_{\mathrm{s}}) d\omega_{\mathrm{s}} d\omega'_{\mathrm{s}},\end{aligned}$$

where, $\rho_{\mathrm{s}}(\omega_{\mathrm{s}}, \omega'_{\mathrm{s}}) = \int f(\omega_{\mathrm{s}}, \omega) f^{*}(\omega'_{\mathrm{s}}, \omega) d\omega$.

One solution to ensure a heralded, pure, single-photon is to engineer the JSA such that it is a factorable product of functions of signal and idler frequencies such that, $f(\omega_{\mathrm{s}}, \omega_{\mathrm{i}}) = g(\omega_{\mathrm{s}})h(\omega_{\mathrm{i}})$. In this case the detection of one photon has no effect on the other as seen by substituting this form into the integral above.

The SPDC source used here was carefully designed so that frequency correlations in the JSA were eliminated[161]. This is accomplished through engineered phase matching of the pump, signal and idler fields using a combination of a spatially chirped pump pulse and

appropriately chosen focusing into the specifically chosen nonlinear crystal. The result of this combination is a heralded, spectrally-pure, single-photon state[161].

3.3 Building the Source

The heralded, single-photon SPDC source was built as shown in Figure 3.2. The basic set up involved frequency doubling a Titanium Sapphire (Ti:Sapph) laser oscillator of 80 MHz repetition rate, with central wavelength of 830 nm to produce a 415 nm pulsed pump for the down-conversion source. By focusing this blue pump into a specifically cut bulk crystal for SPDC, photon pairs with central wavelength 830 nm were created and coupled into optical fibres. The specific details of each part of the source are given below and clearly boxed-off in the figure.

3.3.1 Laser Preparation

A Ti:Sapph oscillator (Spectra Physics, Tsunami) with repetition rate of 80 MHz was pumped by a 9 W continuous-wave diode laser (Spectra Physics, Millennia Pro s-Series) and emitted approximately 1.6 W of pulsed laser light with central wavelength $\lambda_0 = 830$ nm and a FWHM of approximately $\Delta\lambda = 10$ nm, in the fundamental transverse spatial mode. The laser was initially passed through a prism pair as part of a folded dispersion compensation line[164] (DCL), comprising two dispersive prisms (N-SF11 flint glass, 25 mm), separated by approximately 200 mm with one mounted on a linear translation stage, to prepare a FTL pulse.

3.3.2 Second Harmonic Generation

The pulsed laser, with a Gaussian spatial mode, was found to be slightly elliptical. A spatial bandwidth, or FWHM, of (2.0 ± 0.1) mm was measured parallel to the optical table and a FWHM of (1.5 ± 0.1) mm perpendicular to the optical table. This was measured approximately 0.5 m before being focused into a nonlinear β-barium-borate (BBO) crystal

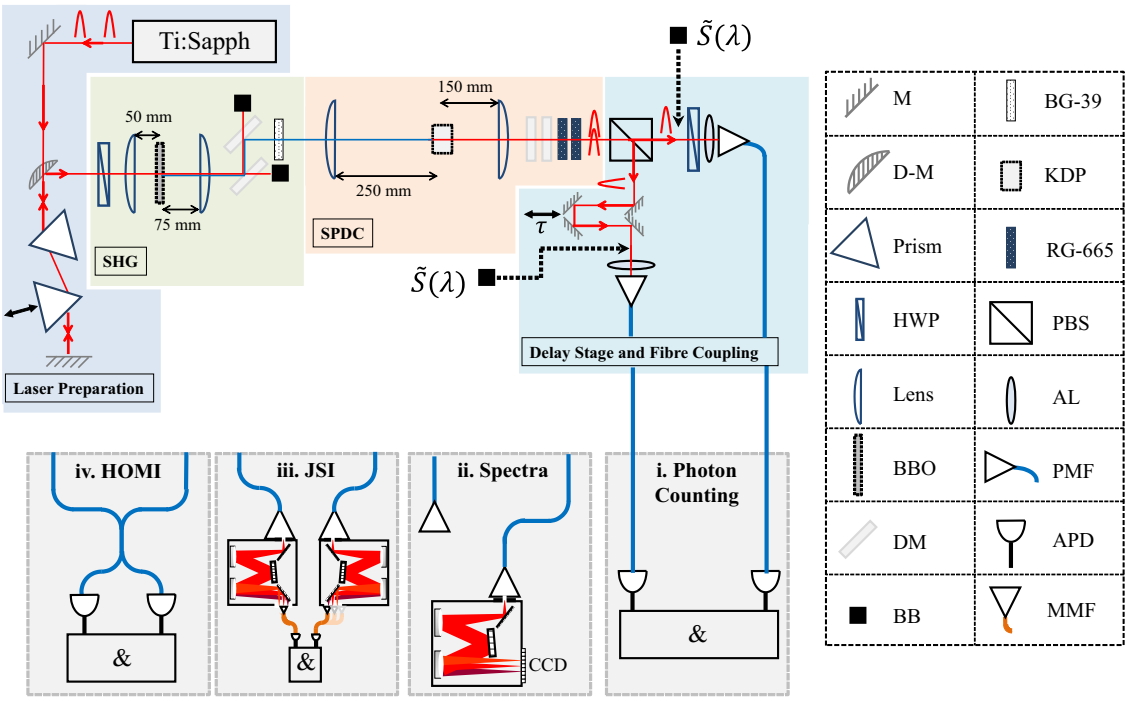

Figure 3.2: Laser Preparation: The single-photon source is derived from an 80 MHz pulsed Ti:Sapph oscillator with central wavelength 830 nm. Dispersion is adjusted for using a folded DCL comprised of two prisms and a tilted mirror. **SHG**: The resultant pulse is then picked-off the original beam path using a "D"-mirror and focused into a BBO crystal for SHG to produce the 415 nm pump. This is then filtered using two dichroic mirrors (DM) and a blue glass filter (BG-39). **SPDC**: The resultant SHG is then focused into a KDP crystal for SPDC. The resultant beam is filtered by two DMs, at approximately $\pi/2$ incident angle, and two colour glass filters (RG-665). **Delay Stage and Fibre-Coupling**: The remaining SPDC photon pair are spatially separated using a PBS. Each of the photon pair are coupled into polarization-maintaining fibre (PMF). One of the photon pair can be temporally delayed, τ, using a translation stage and four-mirror combination. Beam dumps labelled with $\tilde{S}(\lambda)$ indicate the location of the beam blocks (BB) for spectral-intensity background measurements, $\tilde{S}(\lambda)$. The output of the PMF collection fibres are used for four, interchangeable measurements: **i. Photon Counting**, **ii. Spectra**, **iii. JSI** and **iv. HOMI**. A legend of the components is provided on the right.

(Foktek, Type I, width, $w = 5$ mm, height, $h = 5$ mm, length, $\ell = 0.7$ mm, crystal optical axis at $\theta_{\text{BBO}} = 28.2^{\text{o}}$ and anti-reflection (AR) coatings for 830 nm and 415 nm) using a lens with focal length $f = 50$ mm. The Type I BBO crystal was cut to produce a second harmonic generation (SHG) pump signal with central wavelength, $\lambda_{0,\text{p}} = 415$ nm. A half wave plate (HWP) was included before the first lens for correct alignment between the pump polarization and crystal axis to optimize the SHG power. The power was further optimized by adjusting the DCL. Maximum SHG conversion occurs in this thin crystal for

zero phase mismatch between the incident signal and crystal[92]. FTL pulses are also used since the conversion efficiency is related to the interaction strength, which scales with the pulse intensity. By adjusting the DCL to achieve maximum pump power, it was assumed FTL pulses were produced. A second lens with $f = 75$ mm was inserted one focal length after the BBO crystal to collimate the frequency-doubled light.

Two dichroic mirrors (DMs) (CVI Melles Griot, highly reflecting for 415 nm and highly transmitting for 830 nm) were inserted after the BBO to filter out the original laser light. To eradicate further any original oscillator leak-through, a blue Schott glass filter (CVI Melles Griot, BG-39, 3 mm) was placed after the dichroic mirrors. The remaining SHG pump was measured to have a power of approximately 350 mW and a central wavelength length of $\lambda_0 = 415$ nm, a spectral bandwidth of approximately 4 nm and a spatial chirp of (0.48 ± 0.07) nm/mm and (0.33 ± 0.05) nm/mm was measured in the vertical and horizontal directions, respectively.

3.3.3 Spontaneous Parametric Down-Conversion

The pulsed, 415 nm pump beam was then loosely focused into a potassium dihydrogen phosphate (KDP) crystal (Foktek, Type II, $w = 10$ mm, $h = 10$ mm, $\ell = 8$ mm, with crystal angle $\theta_{\mathrm{KDP}} = 67.8^{\mathrm{o}}$, AR coated for 830 nm and 415 nm) for SPDC, using a lens with $f = 250$ mm. The angle of this crystal had been specifically cut for phase and group velocity matching to produce a pair of spectrally pure photons at 830 nm. A second collimating lens, $f = 150$ mm, was then positioned one focal length away following the KDP to collimate the 830 nm single-photons. The two lenses and the KDP were mounted on translation stages with x-y-z control to allow for slight adjustments to optimize the count rates of the source. Following the down-conversion crystal, two further dichroic mirrors (DMs) were inserted at near-normal incidence angle to remove the 415 nm pump beam. These allowed 830 nm to pass and reflected 415 nm. In addition, two long-wave-pass, colour, glass filters (Schott, RG-665, 3 mm thick) also removed residual transmission

of the SHG pump laser such that only photons generated from SPDC remained in the beam path.

3.3.4 Delay Stage and Fibre Coupling

A polarizing beam splitter (PBS) was used to spatially separate the paths of the orthogonally polarized signal and idler fields. This resulted in there being two separate arms for manipulation and detection of the photons. In each arm, the fields were directed towards fibre coupling stages using broadband, dielectric mirrors (M) (Thorlabs, BB1-E03), highly reflective at 830 nm, to minimize loss. Aspheric lenses (ALs) (Newport, 5725-H-B, focal length, $f = 11$ mm) were used to fibre-couple the field into polarization maintaining fibre (PMF) (Thorlabs, P1-780PM-FC) with a single spatial propagation mode for 830 nm. The fibres were mounted on three-axis nanometre-precision stages (Thorlabs, MAX313D). A half-wave plate (HWP) was also included in one arm to rotate the polarization by $\pi/2$ and match the polarization of the down-converted fields. Throughout this work the signal and idler are, thus, assumed to occupy identical spatial and polarization modes for all purposes.

3.3.5 Photon Counting

During alignment of the SPDC source, the output of the PMFs containing the photon pair modes were connected to two single-photon-counting avalanche photodiode (APD) modules (PerkinElmer, SPCM-AQ4C, quantum efficiency $\approx 40\%$ for $\lambda = 830$ nm). This is shown in the box labelled "i. Photon Counting" in Figure 3.2. The output signal from the APDs was monitored using a field programmable gate array (FPGA) (Xilinx SP 605) labelled "&" in Figure 3.2. This allowed for monitoring of individual detector count rates, which are also referred to as singles, as well as coincidence count rates.

Coincidence count rates indicate the rate of detection of downconverted photon pairs by comparing the time of arrival of the detection of one photon, in one arm, in comparison to

a detection in the other arm. The SPDC source here operates in the spontaneous regime with low pump powers, such that one expects to create an average of one photon pair per pump pulse. Photons individually detected by detectors 1 and 2, at time values, t_1 and t_2 are, thus, defined as coincident if $(t_2 - t_1) \leq T_{\mathrm{w}}$, where T_{w} is the coincidence window length. The 80 MHz pump produces pulses every 12.5 ns, thus the coincidence window was set at 8 ns throughout to avoid associating two photons created from subsequent pulses as an SPDC pair.

Heralding Efficiency

The detected coincidence event rates, R_{CC}, and singles rates for the signal, R_{s}, and idler, R_{i}, single-photon wave packets are not equal to the photon-pair production rate, R_{SPDC}, in the KDP crystal. The detected count rates are reduced due to optical losses in each photon's path. This path extends from the source of the photon production in the KDP to the aspheric lenses inclusive. The count rates are further reduced due to coupling losses into the fibres. The reductions due to these losses are η_{s} and η_{i} for the signal and idler, respectively. The efficiencies of the detectors, η_1 and η_2, also contribute to the reduction in count rates such that, $R_{\mathrm{s}} = \eta_{\mathrm{s}}\eta_1 R_{\mathrm{SPDC}}$, $R_{\mathrm{i}} = \eta_{\mathrm{i}}\eta_2 R_{\mathrm{SPDC}}$ and $R_{\mathrm{CC}} = \eta_{\mathrm{s}}\eta_{\mathrm{i}}\eta_1\eta_2 R_{\mathrm{SPDC}}$ (assuming no dark counts nor any independent background contributions to the single detector count rates).

As such, from the singles and coincidence counts rates, one can determine the *heralding efficiency* of one photon, η_μ, for $\mu =$ s,i. This is the ratio of the probability of detecting both photons of a pair to the probability of detecting just one photon. It is interpreted as the probability to find a signal (idler) photon in the signal (idler) fibre when a detection event has occurred in the idler (signal) mode. These provide a measure of source efficiency. The heralding efficiency for the signal photon, η_{s}, assuming the idler is detected by APD

number two, is thus given by[165],

$$\eta_{\mathrm{s}} = \frac{R_{\mathrm{CC}}}{R_{\mathrm{i}}} = \eta_{\mathrm{s}}\eta_{1}, \tag{3.7}$$

with an equivalent definition for the idler photon.

The spatial mode structure of SPDC-emitted bi-photons consists of non-concentric cones. One must ensure that the part of each cone corresponding to the pure-state heralded single-photon is coupled into each fibre. This part is at the point of intersection of the cones, as indicated in Figure 3.1[166]. Alignment of the coupling optics with the SPDC cones, such that the point of intersection of the cones was collected by the single-mode fibres, was established by optimizing the detector singles rates and then the coincidence events. However, high coincidence counts can also be achieved when coupling parts of the two cones which are mirrored in both the x- and y-axis, also indicated in Figure 3.1. Thus a protocol was established to ensure the intended part of the cones are being coupled: recall that the signal and idler are spatially separated from their common optical path after SPDC by a polarizing beam splitter and directed to different coupling optics. Consider the highly undesirable case where the two independent sets of coupling optics are aligned such that opposite parts of the cones were coupled and both singles and coincidence rates were relatively large. If one switches the propagation of the signal and idler modes at the beam splitter to each other's coupling optics, they would no longer be aligned to correlated locations on the cones and coincidence counts would disappear. Therefore, a half-wave plate (HWP) was inserted before the polarizing beam splitter, as seen in Figure 3.2. By rotating the half-wave plate one would expect to see the coincidence and singles counts preserved (within a factor of the detector and propagation efficiencies in each arm). Furthermore, the detected spectra of the spatial mode would also remain unchanged.

Typical heralding efficiencies between 20% and 25% for both the signal and idler were

obtained with singles count rates on the order of $R_1 = 100$ ks^{-1}, $R_2 = 75$ ks^{-1} for the signal and idler arms respectively and coincidence counts on the order of 15 ks^{-1}. These are in rough agreement with the original demonstration of the source[161], and other, similar source-builds[166,167].

3.4 Single-Photon Source Characterization

Once the source was built, diagnostics were performed to confirm the source was behaving as expected and required. In this section, four methods to characterize the single-photon state are presented and their results analysed. In order, these are: measuring the intensity spectra, measuring the Joint Spectral Intensity, calculating the bi-photon state purity using The Schmidt Decomposition and, finally, performing a two-photon interference measurement.

3.4.1 Intensity Spectra

Once coincidences and heralding efficiencies were maximised, the intensity spectra of the individual wave packets were measured using a spectrometer with a single-photon-sensitive charge coupled device (CCD) detector on the output as indicated in the box "ii. Spectra" in Figure 3.2.

The CCD is a square-law detector, with the measured signal, $\tilde{S}$, proportional to the modulus squared of the electric field, $\tilde{S} \propto |\tilde{E}|^2$. All phase information is therefore lost during the measurement process. Nonetheless, the intensity spectra is a key tool in analysing the wave packets in this work and the measurement process must be well-understood for correct processing and interpretation of data. The intensity spectral measurement details using this spectrometer are given below.

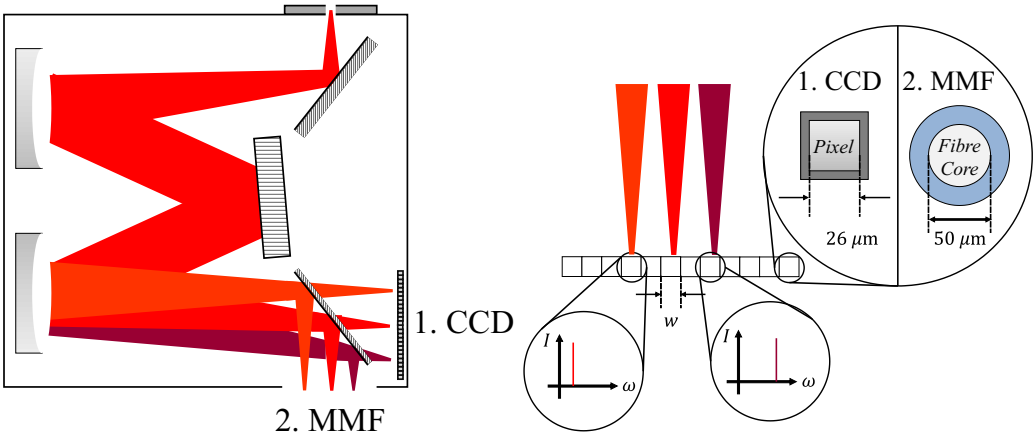

(a) Czerny-Turner Spectrometer **(b)** Spectral Bins at Spectrometer Output

Figure 3.3: (Left) A schematic of the C-T spectrometer with two concave mirrors used to direct the light onto the line grating and then to the flipper mirror to select either the 1. CCD array or 2. a scanning MMF. (Right) A magnified view at the output detection methods including dimensions of the pixel and fibre core apertures.

Spectral Intensity Measurement Details

A Czerny-Turner spectrometer (Andor, Shamrock 303i-B) with alignment similar to that shown in Figure 3.3(a), was used to measure the spectra. A diffraction grating of 1200 lines/mm was used, blazed at 800 nm and with mirror focal length 303 mm. The output of the spectrometer was sent to one of two possible detectors, indicated in Figure 3.3(a):

1. a single-photon sensitive CCD camera (Andor, iDus 401, DU420A-OE) with a (1024× 127) pixel line-array with pixel size 26×26 µm and 26.6 × 3.3 mm image size[168],

2. a multi-mode fibre (MMF) (Thorlabs, M42L05) with core diameter, d =50 µm, mounted on a translation stage with motion parallel to, and in the plane of, the exit aperture.

The spectral resolution, $\delta\lambda$, of the measurement device restricts the bandwidth of light that can be reliably resolved. The measured spectrum of a quasi-CW source, with vanishingly narrow spectral width, $\Delta\lambda$, such that $\Delta\lambda << \delta\lambda$ is known as the instrument response. For the case when $\Delta\lambda$ is on the order of, or less than, $\delta\lambda$ this will distort the measured spectra. The instrument response function is dependent on a number of parameters of

the system including the entrance slit width, the size of the detection aperture on the output, diffraction phenomena and optical aberrations arising from imperfect mirror and diffraction grating manufacturing. It is important to accurately measure and extract the instrument response function, especially when working with sources that have bandwidths on the order of the instrument resolution.

The instrument response function for the spectrometer used in this work was investigated by sending a narrow emission line laser (Power Technology Inc., PPM-830-20, LD1859, $\lambda_0 = 830$ nm, 50 mW maximum output) into the spectrometer using the CCD for measurement. The measured spectrum is shown in the top plot in Figure 3.4. Each data point corresponds to a pixel reading on the CCD. Vertical error bars are given by the error on the detected counts for the pixel: a count of N photons has error given by the Poissonian error, $\sqrt{N}$, assuming each count is independent. The bottom plot in Figure 3.4 shows the same laser diode measured using an optical spectrum analyser (OSA), (Ando, AQ6317B).

Comparing the two, one sees that the spectrum measured using the CCD is distorted from the ideal single line emission, to a Lorentzian-type response. This is likely due to a focussing issue in the spectrometer alignment. The spectrum measured using the OSA is narrower and symmetric with a Gaussian-type functional form. As such, here it is assumed that the instrument response of the spectrometer and CCD limits the resolution of the spectral measurements, rather than the detection method on the output.

To obtain an approximate idea of the spectral bandwidth of the instrument response seen in Figure 3.4, a skewed Lorentzian of the following form was fit to the data[169],

$$L(\lambda) = \frac{2a/\pi\gamma(\lambda)}{1 + 4\left[(\lambda - \lambda_0)/\gamma(\lambda)\right]^2}. \tag{3.8}$$

The fit was performed using a least square estimate fit in Matlab[170]. Here, a is a constant, λ_0 relates to the location of the maxima and the function $\gamma(\lambda)$ gives the width of the profile and is equal to,

$$\gamma(\lambda) = \frac{2\gamma_0}{1 + \mathrm{e}^{a(\lambda-\lambda_0)}}, \tag{3.9}$$

with γ_0 an additional constant. This fitted function is plotted in Figure 3.4. The spectral bandwidth, or FWHM, was found by using the fit to determine the two wavelength values, $\lambda_{\pm I/2}$, where the measured intensity, $\tilde{I}(\lambda)$, was half of the maximum signal, $\tilde{I}_{\max}/2$. The difference of these values gave the FWHM,

$$\Delta\lambda = |\lambda_{+I/2} - \lambda_{-I/2}|. \tag{3.10}$$

This was calculated to be $\Delta\lambda = (0.2\pm0.07)$ nm. The uncertainty, $\alpha_{\Delta\lambda} = 0.07$ nm, (where α is used here and throughout to denote an uncertainty) arises from the wavelength accuracy of $\lambda_{\pm I/2}$ due to the CCD pixel array, given by $\alpha_{\lambda_{\pm I/2}} = 0.05$ nm. When summing values, as is done in equation Equation 3.10 the square of the uncertainty on the result is given by the sum of the squares of the individual contributing errors. In this case the error is equal to,

$$\alpha_{\Delta\lambda} = \sqrt{\alpha^2_{\lambda_{+I/2}} + \alpha^2_{\lambda_{-I/2}}}, \tag{3.11}$$

and gives $\alpha_{\Delta\lambda} = \sqrt{2 \times 0.05^2} = 0.07$ nm.

The CW laser spectrum measured using the OSA was fitted with a Gaussian of the form,

$$G(\lambda) = A\mathrm{e}^{-\frac{(\lambda-\lambda_0)^2}{2\sigma^2_\lambda}}, \tag{3.12}$$

using a least-squares estimate fit. Here, A, is the amplitude of the function and is related to the original signal intensity, transmission of the equipment and the detection efficiency. The constant, λ_0, is the central location of the Gaussian peak and the constant, σ_λ is

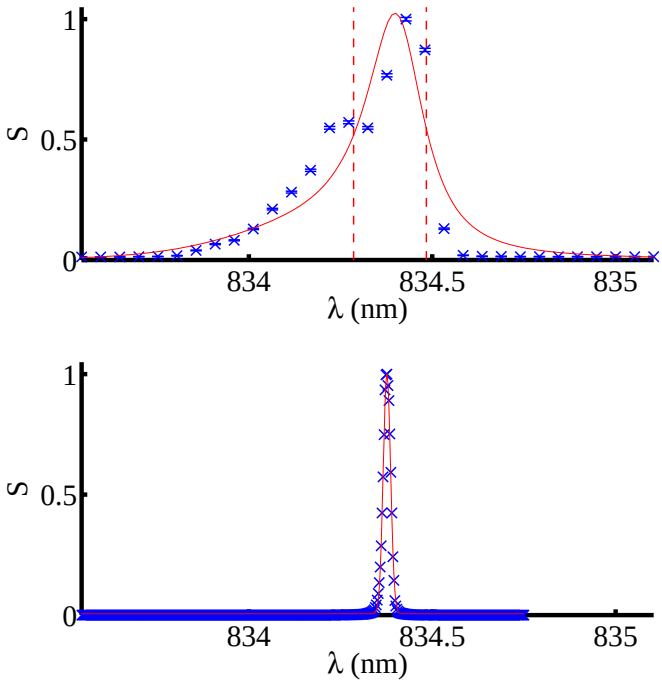

Figure 3.4: CW laser intensity spectral intensity, S, measured using the spectrometer and CCD (top) and the OSA (bottom) (blue crosses). The rescaled intensity measurement has been plotted: $S = I/I_{\max}$ where $I_{\max}$ is the maximum intensity of the data. Error bars have been omitted from the OSA data for clarity. A Lorentzian curve has been fit to the top set of data (red, solid line) and a Gaussian function fitted to the bottom set (red, solid line). The FWHM of the spectra are (0.20 ± 0.07) nm and (0.023 ± 0.006) nm for the top and bottom spectra, respectively and is indicated in the top spectra (red, dotted line).

related to the intensity bandwidth, $\Delta\lambda$, as in Equation 2.24. The fit was weighted, taking into account the error on each count. The bandwidth and its uncertainty was determined as described in Equation 3.10 and Equation 3.11 above, which gave $\Delta\lambda = (0.02 \pm 0.01)$ nm. Once again, the error was propagated through from the wavelength accuracy of the detector at the output of the OSA, 0.004 nm.

For sources with a spectral bandwidth significantly larger than the spectral response function the instrument response need not be deconvolved from the measured spectra. In this work, all bandwidth are wider than the FWHM of the response function. Nonetheless, it can be seen that the limiting factor to the spectral measurement taken with the Andor spectrometer is the FWHM of the instrument response. A value of ± 0.2 nm will now be assigned to the uncertainty on any spectral measurement made with this spectrometer and, following a similar argument, a value of 0.02 nm associated with measurements taken on the OSA.

Calibration

When operating the spectrometer with the CCD on the output, the internal factory calibration of the wavelength to the pixel number was used. However, when using the spectrometer with the scanning multi-mode fibre on the output, calibration of the fibre position, x, to wavelength, λ was required. This was done as follows: the original Ti:Sapph oscillator intensity spectrum was first measured using the spectrometer and CCD. The same signal was then measured using the spectrometer and scanning the multi-mode fibre on the output, detecting using a PD. Thus two sets of signal were obtained: one from the CCD as a function of wavelength, $\tilde{S}_{\mathrm{CCD}}(\lambda)$, and the signal taken using the multi-mode fibre as a function of actuator position, $S_{\mathrm{MMF}}(x)$.

Gaussian functions, of the same form as Equation 3.12, were fitted to both sets of intensity spectra using a least-squares estimate fit. Both fits were weighted, taking into account the error on each count. Values for the central location of each Gaussian, λ_0 and x_0, and their spectral width, σ_λ and σ_x, were extracted from the fits.

It was assumed that the wavelength, λ, and multi-mode fibre position, x, were linearly related such that, $x = m\lambda + c$, since angles were relatively small in the alignment of the spectrometer. The two unknowns, m and c, were determined by formulating two simultaneous equations 1. $x_0 = m\lambda_0 + c$ and 2. $(x_0 + \sigma_x) = m(\lambda_0 + \sigma_\lambda) + c$ and solving for m and c to relate λ and x.

Background Correction

For all spectral measurements taken using the CCD, $\tilde{S}(\lambda)$, a background measurement, $\tilde{S}_{\mathrm{BG}}(\lambda)$, was first taken to correct for any stray light and dark noise on the CCD. The background measurement was taken by blocking the optical beam path with a beam block (BB) before the collection lens of the fibre that was connected to the spectrometer, as

indicated in Figure 3.2, labelled $\tilde{S}(\lambda)$. Each background measurement was taken for a length of time equal to the corresponding spectral measurement. The corrected signal, $\tilde{S}_{\text{cor}}$, was then determined by subtracting the background signal,

$$\tilde{S}_{\text{cor}} = \tilde{S}(\lambda) - \tilde{S}_{\text{BG}}(\lambda). \tag{3.13}$$

For intensity spectra of attenuated coherent-state measurements, the duration of measurement was such that signal-to-noise ratio (SNR) was on the order of $\approx 10\%$.

Measured Spectra Results

The measured spectra of the signal and idler photons from the single-photon source are plotted in Figure 3.5. Gaussian functions were fitted to both of these spectra, weighted by the error on each count, with a functional form the same as that in Equation 3.12, once again, using a least squares estimate fit. This allowed extraction of the central wavelength. The spectral bandwidth, or FWHM, was calculated in two ways: 1. from the fit of the Gaussian function to the data and 2. directly from the data, by identifying the location of half the intensity maximum, $\lambda_{\pm I/2}$, as described above calculated using Equation 3.10. These wavelength locations, $\lambda_{\pm I/2}$, are indicated in Figure 3.5. Both methods returned spectral bandwidths that agreed with each other.

The signal photon has a central wavelength, $\lambda_{0,\text{s}} = (828.6 \pm 0.2)$ nm and was found to have a bandwidth of $\Delta\lambda_{\text{s}} = (3.7 \pm 0.3)$ nm. The broader, idler photon was measured with $\lambda_{0,\text{i}} = (828.3v \pm 0.2)$ nm and bandwidth of $\Delta\lambda_{\text{i}} = (15.4 \pm 0.3)$ nm. The error on the central wavelength is given by the resolution of the spectrometer due to the instrument response and the error on the bandwidth calculated using Equation 3.11. The difference in spectral bandwidths is expected and is due to the group velocity matching in the birefringent crystal during SPDC[166]. The labels signal and idler are purely historical and have been assigned here since the broadband photon is used as the herald. Note, in the

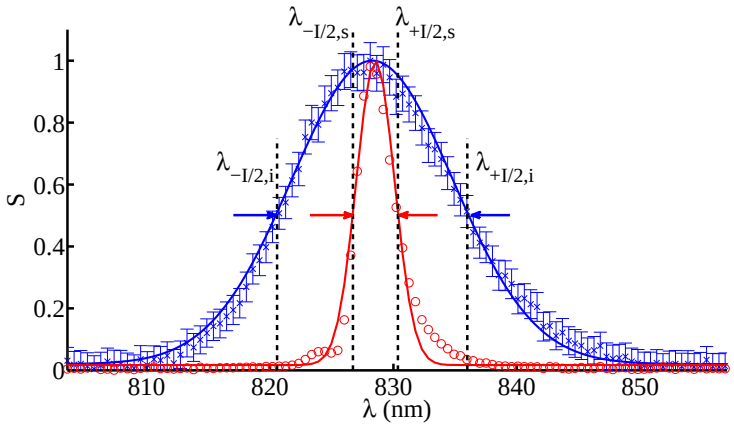

Figure 3.5: Measured intensity spectra data for the signal (red circles) and idler (blue crosses) spectral wave packets.f The rescaled intensity measurement has been plotted: $S = I/I_{\max}$ where $I_{\max}$ is the maximum intensity of the data, for easy comparison. Gaussian functions were fitted to each set of data and are also plotted (solid lines). The signal intensity wave packet was found to have $\lambda_{0,\mathrm{s}} = (828.6 \pm 0.2)$ nm and $\Delta\lambda_{\mathrm{s}} = (3.7 \pm 0.3)$ nm. The idler intensity wave packet was found to have $\lambda_{0,\mathrm{i}} = (828.3 \pm 0.2)$ nm and $\Delta\lambda_{\mathrm{i}} = (15.4 \pm 0.3)$ nm. The bandwidth is indicated (black, dashed lines) by the width between the wavelengths at half the intensity maximum, $\lambda_{-\frac{I}{2}}$ and $\lambda_{+\frac{I}{2}}$.

figure, not all measured data points are plotted for clarity.

3.4.2 The Joint Spectral Intensity

Measuring the individual spectrum of the signal and idler photons using the spectrometer and the CCD array does not distinguish between photons originating from the SPDC bi-photon state, as desired, or from photons that are simply noise, for example from reflected light from the original Ti:Sapph oscillator. Furthermore, they also provide no information of any spectral correlation in the bi-photon state. By measuring the joint spectral intensity (JSI) of the idler and signal modes, additional information can be gained about the bi-photon state. The JSI is related to the joint spectral amplitude, as introduced in Equation 3.6, through $\mathrm{JSI} = |\mathrm{JSA}|^2$, as such it provides no information about the phase of the bi-photon state. Nonetheless, it does provide access to other useful information as discussed below.

JSI Measurement Details

Two spectrometers were required to address each photon from the down-converted pair individually and both photons simultaneously. The output from both spectrometers was detected using multi-mode collection fibres mounted on an x-y-z translation stage. To perform this measurement the outputs of the fibre-coupled signal and idler fields are connected to the fibre inputs of each spectrometer as shown in box "iii. JSI" in Figure 3.2. A more detailed schematic of the two-spectrometer set up is presented in Figure 3.6. One of the spectrometers (Andor, Shamrock 303i-B) had a diffraction grating with 1200 lines/mm blazed for 800 nm. This is labelled A in Figure 3.6. The second spectrometer (Instruments SA, Inc., S/N 10229-4-89, HR32013938) had a grating with 1800 lines/mm, and focal length of 300 mm. This is labelled B in Figure 3.6. This second spectrometer was calibrated similarly to the first, as described above, to relate the multi-mode fibre position to the detected wavelength.

A multi-mode fibre (Thorlabs, M42L05, core diameter 50 µm) was mounted in the optical plane on the output of each spectrometer. The output signal from the spectrometers was collected directly into the multi-mode fibre without any coupling optics. Both of the multi-mode fibres on the output of spectrometer A and B were mounted on a linear translation stage with motorized movement parallel to the optical plane, in the x direction, and manual adjustment in the y-z directions. The two manual adjustment axes allowed for accurate positioning of the mounted fibres at the correct position in the focal planes of the spectrometers. The output of each multi-mode collection fibre was connected to an APD with count rates monitored using the FPGA.

By scanning the two collection fibres across the entire output of both spectrometers, and recording coincidence events, R_{CC}, between the two spectrometers, one can identify any spectral intensity correlation between the signal and idler photons, within the instrument

resolution. For the Andor spectrometer this was ±0.2 nm and for the Instruments SA spectrometer this was ±1 nm. The JSI was thus measured by performing a raster scan through the joint frequency space. The collection fibre on the output of the idler photon's spectrometer was set at one position. The position of the signal photon's collection fibre was then scanned over the output of the signal spectrometer. The idler photon's collection fibre is then shifted along to the next location and the signal fibre, once again, scanned across the output of the signal's spectrometer. This process is repeated until all locations for the idler photon collection fibre have been visited.

The idler photon fibre input was connected to spectrometer A. During the JSI measurement, a total of 71 locations of the multi-mode fibre were scanned on the output. These locations were spatially separated by a distance equal to the fibre-core diameter. This was to ensure independent modes were measured at the output. The signal photon input fibre was connected to the second spectrometer, B. Due to the smaller bandwidth of this wave packet, a total of 23 positions were scanned on the output, once again with the positions separated by the fibre-core diameter. The scanning of the stages and the photon counting data measurement was controlled by a custom-built LabView virtual instrument (VI).

Before transmission through the spectrometer, the observed coincidence count rate was approximately $R_{\mathrm{CC}} = 24\ \mathrm{ks}^{-1}$. After transmission through the JSI set up, coincidence count rates were reduced to approximately $7\ \mathrm{s}^{-1}$ at the maximum of the JSI. A total of $23 \times 71 = 1633$ measurements were taken across the JSI with counts measured for 8 s at each location, with a total experimental run time of approximately four hours.

JSI Results

The measured JSI for the SPDC source is shown in Figure 3.7. Upon visual inspection, the JSI appears spectrally separable to within the resolution of the spectrometer and spectral range, being symmetric around the central wavelengths of signal and idler fields.

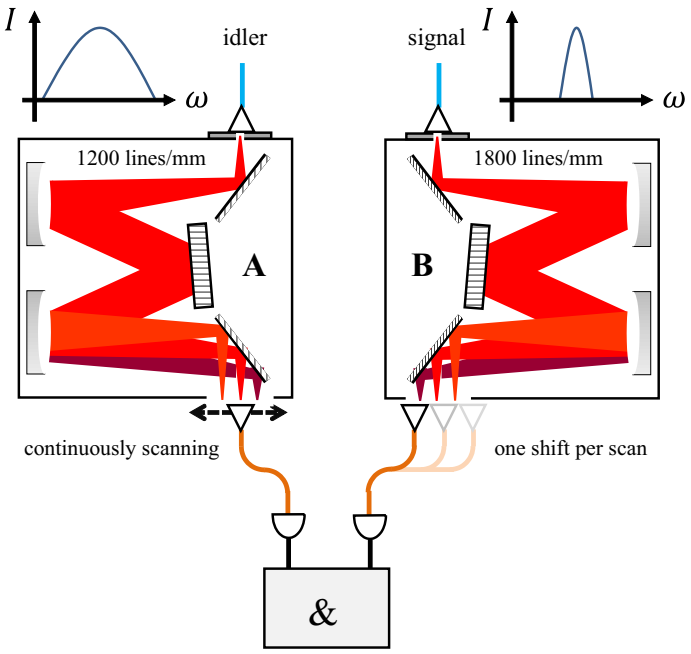

Figure 3.6: The JSI measurement used two Czerny-Turner type spectrometers, labelled A and B. The idler photon wave packet was transmitted through A with a grating of 1200 lines/mm. At the output, a mounted multi-mode fibre (MMF) was scanned across the optical plane between 71 bins to measure the spectral intensity. The MMF was connected to an APD for detection. The signal photon wave packet was transmitted through B with a grating of 1800 lines/mm. A second MMF was located in the optical plane on the output. The MMF measured the spectrum at 23 bins and was also connected to an APD for detection. Both APDs were connected to an FPGA, & to record singles and coincidence events. For the JSI measurement, the MMF in spectrometer A was scanned continuously with the MMF on the output of B moving one location per full scan of the MMF on the output of A.

This implies it may act as a reliable, heralded pure single-photon source. This intensity measurement provides no phase information about the state yet spectral phase correlations between the two photons are not expected[161]. The JSI also allows one to place limits on the bi-photon state as detailed below in subsection 3.4.3.

JSI Spectral Probability Densities

The spectral probability density, $|\tilde{\psi}(\omega)|^2$, of one of the bi-photon pair can be extracted by summing the heralded JSI over the other photon. For example, the signal probability

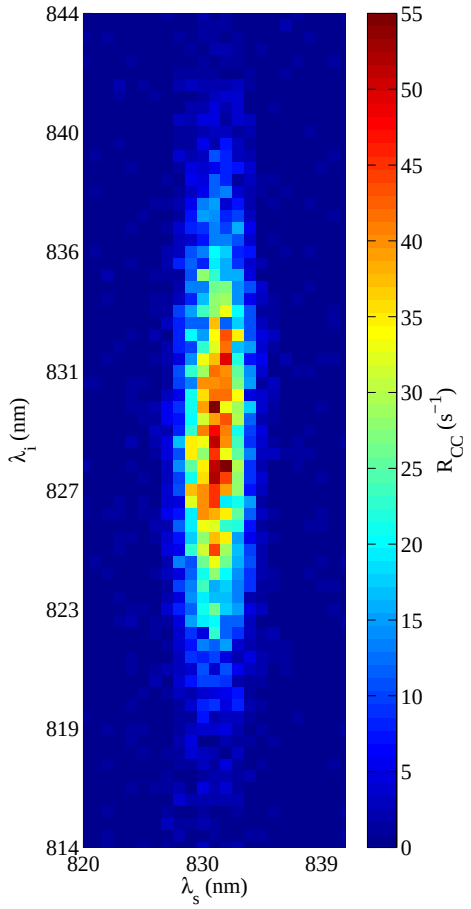

Figure 3.7: Density plot showing the measured JSI from the coincidence event detection rates, R_{CC}. The idler wavelength, λ_i, is plotted along the vertical axis and the signal photon, λ_s, on the horizontal. The JSI appears symmetric, within instrument resolution, in a plane parallel with both the y-axis and the x-axis. This indicates that the intensity spectra are separable: the detection of one single-photon state at a certain wavelength provides no information about the wavelength of the other photon.

density is determined using,

$$|\tilde{\psi}(\omega_{\mathrm{s}})|^2 = \int |\Psi^{(2)}(\omega_{\mathrm{s}}, \omega)|^2 d\omega, \tag{3.14}$$

with a similar definition for the idler photon. From this summed results, one is able to retrieve the spectral amplitude, $\tilde{\psi}(\omega_\mu)$, for $\mu = \mathrm{s}$, i, if a flat phase is assumed across the wave packet. This summation was performed on the measured JSI and the results are plotted in Figure 3.8. The probability densities are plotted with the JSI and aligned along their respective JSI axes to indicate the performed summation. Gaussian functions, of the same form as Equation 3.12, were fitted to these data and are also plotted in the

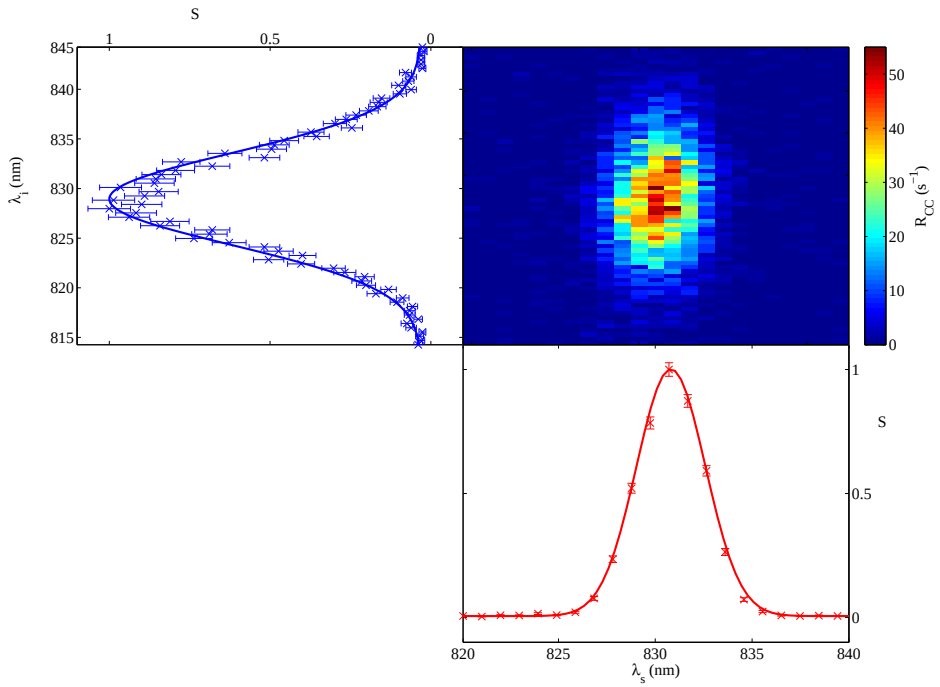

Figure 3.8: The measured JSI is plotted with both marginals of the idler (top left) and signal (bottom right) wave packets. The marginals were determined by summing over the spectral degree of freedom describing the other photon. The marginals have been orientated to represent this summing operation. The rescaled intensity measurement has been plotted: $S = I/I_{\max}$ where $I_{\max}$ is the maximum intensity of the data. Gaussian fits were performed on both marginals and are also plotted (solid lines). The signal intensity wave packet was found to have $\lambda_{0,\mathrm{s}} = (830.8 \pm 0.2)$ nm and $\Delta\lambda_{\mathrm{s}} = (4.1 \pm 0.3)$ nm. The idler photon was found to have $\lambda_{0,\mathrm{i}} = (828.9 \pm 0.2)$ nm and $\Delta\lambda_{\mathrm{i}} = (10.9 \pm 0.3)$ nm.

figure. The fit was weighted by the error on each count. From the Gaussian fit, central wavelengths of $\lambda_{0,\mathrm{s}} = (830.6 \pm 0.2)$ nm and $\lambda_{0,\mathrm{i}} = (828.9 \pm 0.2)$ nm were extracted. The spectral bandwidths were determined by identifying the wavelengths at half the maximum, $\lambda_{\pm I/2}$, and using Equation 3.10. Spectral bandwidths of $\Delta\lambda_{\mathrm{s}} = (4.1 \pm 0.3)$ nm and $\Delta\lambda_{\mathrm{i}} = (10.9 \pm 0.3)$ nm were determined for the idler and signal photons respectively. The errors for the central wavelength and bandwidth are given by resolution of the spectrometer and CCD, as described in section 3.4.1, and by propagating through these same errors using Equation 3.11, respectively.

Single Count Rates Spectral Measurement

During the JSI measurement raster scan, the individual detector count rates, R_s and R_i, were also recorded. These non-heralded measured spectra for the signal and idler photons, as given by the singles count rates, R_s and R_i respectively, are plotted in Figure 3.9(a) and Figure 3.9(b) respectively. Gaussian functions, of the same form as Equation 3.12, were fitted to the data, weighted by the error on each count. The fit returned central wavelengths of $\lambda_{0,\mathrm{s}} = (831.0 \pm 0.2)$ nm and $\lambda_{0,\mathrm{i}} = (828.3 \pm 0.2)$ nm for the signal and idler respectively. Spectral bandwidths of $\Delta\lambda_\mathrm{s} = (5.1 \pm 0.3)$ nm and $\Delta\lambda_\mathrm{i} = (11.1 \pm 0.3)$ nm were also determined by finding the wavelengths at half of the intensity maximum, $\lambda_{\pm I/2}$ and using Equation 3.10.

Spectral Comparison

Plotted in Figure 3.9 are the heralded and non-heralded spectral intensities for both the signal and idler photons. Their extracted central wavelength and spectral bandwidth are listed in Table 3.1 along with the spectra taken using the CCD. One can see the bandwidth varies relatively largely for the signal and idler for the three different measurements. This indicates that the non-heralded CCD measurement and JSI singles data are measuring spectral components that do not originate from the bi-photon state, resulting in wider bandwidths, and affect the central wavelength. As such, this comparison highlights the importance to measure heralded spectra when working with single-photon sources.

3.4.3 The Schmidt Decomposition

The JSI in Figure 3.7 does not show any spectral intensity correlations. However this does not provide a quantitative measure of the separability of the source. To estimate the purity of the heralded single-photon state using Equation 3.5 one would need to perform full state tomography [59] on the state to extract the density matrix. This is a challenging and time-consuming process. Instead, one is able to make reasonable assumptions and

Measurement Method	$\lambda_{0,s}$ (nm)	$\Delta\lambda_s$ (nm)	$\lambda_{0,i}$ (nm)	$\Delta\lambda_i$ (nm)
CCD	828.5	3.7	828.3	15.6
R_{CC}	830.8	4.1	828.9	11.1
R_μ, μ =s,i	828.3	4.9	83.0	11.1

Table 3.1: Bi-photon Measured Spectrum Properties. Errors on the central wavelength are given by ±0.2 nm and on the bandwidth are ±0.3 nm

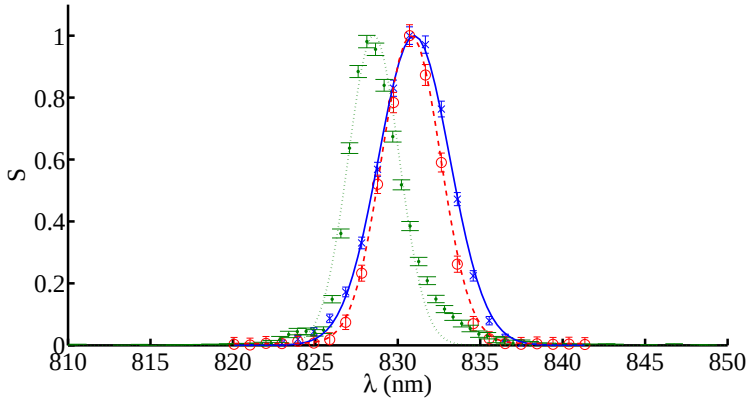

(a) Signal Photon

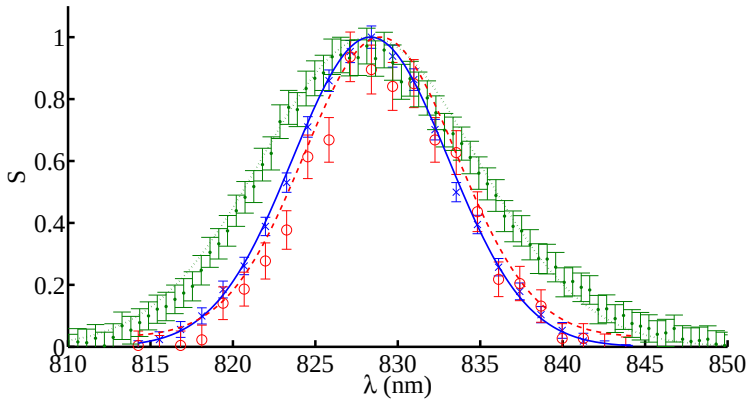

(b) Idler Photon

Figure 3.9: Plotted are the (a) signal and (b) idler intensity spectra measured in three different ways: using the spectrometer and CCD (green dots), using the singles measured during the JSI (blue crosses) and heralded, using the coincidence count rates measured during the JSI (red circles). Gaussian fits for these data are also plotted (dotted, solid and dashed lines, respectively). The rescaled intensity measurement has been plotted: $S = I/I_{max}$ where I_{max} is the maximum intensity of the data, for easier comparison.

approximations to determine the purity via other methods, such as based upon the Schmidt Decomposition. This is done here and described below.

Theory of Schmidt Decomposition

One tool used to quantify entanglement in the continuous frequency degree of freedom of a bi-photon state, is the Schmidt decomposition[171]. This decomposition expresses the bi-photon state in terms of a complete set of paired basis states, $|\chi_j\rangle_{\mathrm{s}} |\xi_j\rangle_{\mathrm{i}}$, with one of the pair being dependent on only the signal, $|\chi_j\rangle_{\mathrm{s}}$, and one on the idler state, $|\xi_j\rangle_{\mathrm{i}}$. Here the j denotes the index of the pair of states and s(i) labels the signal (idler) mode. These basis states are orthonormal, such that $\langle\chi_j|\chi_k\rangle_{\mathrm{s}} = 0$.

The Schmidt decomposition of a state, $|\psi\rangle$, is then written as a linear superposition of these product pair states leading to the following expression,

$$|\Psi\rangle = \sum_{j=1}^{\infty} \sqrt{\lambda_j}\, |\chi_j\rangle_{\mathrm{s}} |\xi_j\rangle_{\mathrm{i}}. \tag{3.15}$$

The states $|\chi_j\rangle_{\mathrm{s}}$ and $|\xi_j\rangle_{\mathrm{i}}$ are known as the Schmidt modes and represent the j^{th} pair of orthonormal paired basis states. The constant, λ_j, is known as the Schmidt coefficient and is the weighting of the j^{th} pair. These coefficients are normalized such that $\sum_j \lambda_j = 1$.

A completely factorable, hence unentangled, state would have $\lambda_1 = 1$ and $\lambda_{j>1} = 0$. The number of pairs of basis states with non-zero weightings indicates the separability of the bi-photon state. This is more commonly quantified using the Schmidt number, K, defined as[172,173],

$$K = \frac{1}{\sum_j \lambda_j^2}. \tag{3.16}$$

The ideal bi-photon state used for heralding would, therefore, have $K = 1$. Whereas, a maximally entangled state would require an infinite number of Schmidt modes to describe

it. The weighting for each would be vanishingly small and, thus, $K \to \infty$.

One can extend this idea by defining the density matrix of the state in terms of the Schmidt decomposition:

$$\begin{aligned}\hat{\rho} &= |\Psi\rangle \langle\Psi| \,, \\ &= \sum_{j,k}^{\infty} \sqrt{\lambda_j \lambda_k}\, |\chi_j\rangle_{\mathrm{s}}\, |\xi_j\rangle_{\mathrm{i\,s}} \langle\chi_k|_{\,\mathrm{i}} \langle\xi_k|.\end{aligned}$$

From this expression the reduced density matrix of the signal photon state can be extracted by performing a partial trace on $\hat{\rho}$ over the idler photon state to yield the signal photon,

$$\begin{aligned}\hat{\rho}_{\mathrm{s}} &= \mathrm{Tr}_{\mathrm{i}}(\hat{\rho}), \\ &= \sum_{l}^{\infty} \sum_{j,k}^{\infty} \sqrt{\lambda_j \lambda_k}\, |\chi_j\rangle_{\mathrm{s\,s}} \langle\chi_k|\, \langle\xi_l|\xi_j\rangle_{\mathrm{i}}\, \langle\xi_k|\xi_l\rangle_{\mathrm{i}} \,, \\ &= \sum_{l}^{\infty} \lambda_l\, |\chi_l\rangle_{\mathrm{s\,s}} \langle\chi_l|,\end{aligned}$$

where $\langle\xi_l|\xi_j\rangle_{\mathrm{i}} = \delta_{l,j}$ and $\langle\xi_k|\xi_l\rangle_{\mathrm{i}} = \delta_{k,l}$. A similar operation can be done to extract the idler photon state,

$$\hat{\rho}_{\mathrm{i}} = \mathrm{Tr}_{\mathrm{s}}(\hat{\rho}) = \sum_{m}^{\infty} \lambda_m\, |\xi_m\rangle_{\mathrm{i\,i}} \langle\xi_m|. \tag{3.17}$$

Recall, the definition of the purity of an individual single-photon state, as given in Equation 3.5. Substituting the above into this equation results in a new expression for purity,

$$\begin{aligned}\mathcal{P} =& \mathrm{Tr}\left[\hat{\rho}_{\mathrm{s}}^2\right], \\ =& \sum_{n}^{\infty} \sum_{l}^{\infty} \lambda_l \lambda_n \mathrm{Tr}\left[|\chi_l\rangle_{\mathrm{s}} \langle\chi_l|\chi_n\rangle_{\mathrm{s}} \langle\chi_n|_{\mathrm{s}}\right], \\ =& \sum_{n}^{\infty} \lambda_n^2, \\ =& \mathrm{Tr}\left[\hat{\rho}_{\mathrm{i}}^2\right],\end{aligned}$$

where $\langle \chi_l | \chi_n \rangle_{\mathrm{s}} = \delta_{l,n}$ and $\mathrm{Tr}\left[|\chi_n\rangle_{\mathrm{s}} \langle \chi_n |_{\mathrm{s}} \right] = 1$. The final line shows how the purity of both sub-systems are equal. Recalling the definition of the Schmidt number, K, in Equation 3.16 allows one to relate this to the purity of the state through,

$$\mathcal{P} = \frac{1}{K}. \tag{3.18}$$

Estimating the Schmidt Number from the Measured JSI

The Schmidt decomposition requires knowledge of the specific set of bi-photon states which describe the SPDC source, here. Unfortunately, this information requires full state tomography[174] to be performed. However, one can circumvent this deficit by using the singular value decomposition (SVD). This is a matrix factorization technique that is the analogue of the Schmidt decomposition. The SVD can be computed numerically from the JSI[175], assuming that the measured JSI, $\tilde{S}(\omega_{\mathrm{s}}, \omega_{\mathrm{s}})$, contains no spectral phase correlations between the two states. This implies that,

$$\tilde{S}(\omega_{\mathrm{s}}, \omega_{\mathrm{i}}) = |\langle \Psi | \Psi \rangle|^2 = |f(\omega_{\mathrm{s}}, \omega_{\mathrm{i}})|^2,$$

with the function $f(\omega_{\mathrm{s}}, \omega_{\mathrm{i}})$ describing the spectral mode distribution of the bi-photon state, originally defined in Equation 3.6. One can determine the bi-photon distribution from the square root of the measured joint spectral intensity $\sqrt{\tilde{S}(\omega_{\mathrm{s}}, \omega_{\mathrm{i}})}$. This state is then described as in a matrix form, $\hat{F}$, where F_{mn} is the matrix element representing $f(\omega_{\mathrm{s}}, \omega_{\mathrm{i}})$ with $\omega_{\mathrm{s(i)}}$ being the discrete frequency components as sampled for the signal (idler) spectral intensity during the JSI measurement. Here, m is the index of the signal photon frequency and n is the index of the idler photon frequency.

The SVD expresses the matrix form of the bi-photon state, $\hat{F}$, as a product of three matrices, $\hat{F} = \hat{U}\hat{D}\hat{V}^{\dagger}$. The first and last of these are unitary matrices representing the modes into which the initial state has been decomposed. In this case $\hat{U}$ is an $[M \times J]$

matrix where M is the number of signal frequency components of the signal state and the j^{th} column, of the total number of J Schmidt pairs, represents the signal Schmidt mode $|\chi_j\rangle_{\text{s}}$. Similarly, $\hat{V}$ is an $[N \times J]$ matrix for the idler state with N frequency components and where the j^{th} row represents the idler Schmidt mode ${}_{\text{i}}\langle\xi_j|$.

The matrix, $\hat{D}$, is diagonal with elements indicating how much of each of the signal and idler modes, in $\hat{U}$ and $\hat{V}^{\dagger}$ respectively, are mixed at each frequency pair, $\omega_{\text{s},m}$ and $\omega_{\text{i},n}$, to form $\hat{F}$. Following normalization of $\hat{D}$, the sum of the square of these elements gives the Schmidt number, K [161].

The SVD was performed on the measured bi-photon state JSI, plotted in Figure 3.7. The sum of the square of the elements in the corresponding $\hat{D}$ matrix was found to be 1.056. Thus, for the case where there are no spectral phase correlations in the bi-photon state, the state can be assumed, at best, to have a purity, $\mathcal{P}_{\max} = 0.947$, assuming no spectral phase correlations.

3.4.4 Hong-Ou-Mandel Interference and Spectral Overlap

Hong-Ou-Mandel (HOM) interference is a common tool in the field of quantum optics used to probe quantum states of light [176]. It is the observed phenomena of photons coalescing when interfered at a beam splitter. This relatively simple measurement provides invaluable information, allowing one to probe the state's purity [177] and the distinguishability or presence of correlations between two states [178,179]. In this section, a HOM interference measurement is performed between the SPDC bi-photon pair to probe the purity of the source.

The theory behind HOM interference is well known, as is the experimental signature: the HOM "dip". However, a brief overview will be given here to frame the results of the HOM interference measurement performed between the signal and idler photon states of

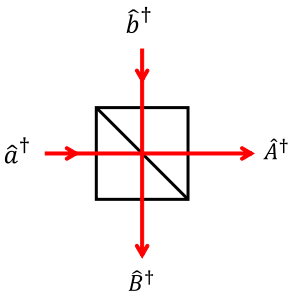

Figure 3.10: A beam splitter with input ports modes with creation operators labelled as $\hat{a}^\dagger$ and $\hat{b}^\dagger$ and output port mode creation operators labelled as $\hat{A}^\dagger$ and $\hat{B}^\dagger$.

the bi-photon source. This will allow one to understand what the results of the interference performed here tell you about the bi-photon state.

The 50:50 Beam Splitter

Consider two independent photons incident at the input ports of a 50:50 beam splitter (BS), similar to that shown in Figure 3.10. One photon occupies the spectral-temporal wave function described by $\tilde{\psi}(\omega) = \langle\omega|\psi\rangle$ and the second photon occupies $\tilde{\phi}(\omega) = \langle\omega|\phi\rangle$ where the state has been expressed in the spectral basis. The input state to the beam splitter, $|\Psi_{\text{in}}\rangle$, written in terms of the creation operators at the input ports, $\hat{a}^\dagger(\omega)$ and $\hat{b}^\dagger(\omega)$, is given by,

$$|\Psi_{\text{in}}\rangle = \int\int \psi(\omega)\hat{a}^\dagger(\omega)\phi(\omega')\hat{b}^\dagger(\omega')\,|0\rangle\,d\omega d\omega'. \tag{3.19}$$

The output port creation operators of the beam splitter are denoted by $\hat{A}^\dagger$ and $\hat{B}^\dagger$, as indicated in Figure 3.10 and are related to the input port creation operators as follows, using the beam splitter transformations[89],

$$\hat{a}^\dagger(\omega) = \frac{1}{\sqrt{2}}\Big(i\hat{A}^\dagger(\omega) + \hat{B}^\dagger(\omega)\Big), \tag{3.20}$$

$$\hat{b}^\dagger(\omega') = \frac{1}{\sqrt{2}}\Big(\hat{A}^\dagger(\omega') + i\hat{B}^\dagger(\omega')\Big). \tag{3.21}$$

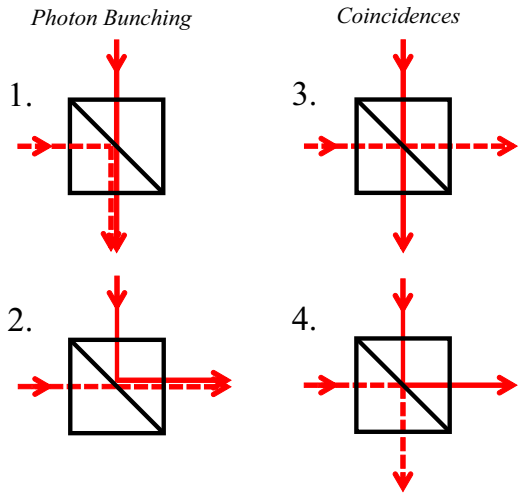

Figure 3.11: With two single-photon modes incident on the input ports of a 50:50 beam splitter, the four possible outcomes are shown. 1. and 2. Both photons exit via the same output port. This is known as photon bunching. 3. and 4. Photons exit out of distinct output ports. In this case, one would measure coincidence events if photon detectors were placed on the output ports.

The Output State

The output state can then be written in terms of the output port creation operators by substituting $\hat{a}^\dagger(\omega)$ and $\hat{b}^\dagger(\omega)$ in Equation 3.19 for $\hat{A}^\dagger(\omega)$ and $\hat{B}^\dagger(\omega)$,

$$\begin{aligned}|\Psi_{\text{out}}\rangle &= \frac{1}{2}\int\int \psi(\omega)\Big(i\hat{A}^\dagger(\omega)+\hat{B}^\dagger(\omega)\Big)\phi(\omega')\Big(\hat{A}^\dagger(\omega')+i\hat{B}^\dagger(\omega')\Big)d\omega d\omega'\,|0\rangle\,,\\ &= \frac{1}{2}\int\int \psi(\omega)\phi(\omega')\Big(i\hat{A}^\dagger(\omega)\hat{A}^\dagger(\omega')+\hat{A}^\dagger(\omega')\hat{B}^\dagger(\omega)\\ &\qquad -\hat{A}^\dagger(\omega)\hat{B}^\dagger(\omega')+i\hat{B}^\dagger(\omega)\hat{B}^\dagger(\omega')\Big)d\omega d\omega'\,|0\rangle\,. \end{aligned} \tag{3.22}$$

The four terms in this output state represent the four possible outcomes of the two photons incident on the beam splitter. These four cases are shown in the schematic in Figure 3.11. Two of these cases, labelled 1 and 2 in the figure, are when the two photons exit the beam splitter from the **same** output port (the $\hat{A}^\dagger(\omega)\hat{A}^\dagger(\omega')$ and $\hat{B}^\dagger(\omega)\hat{B}^\dagger(\omega')$ terms). The other two cases are when the photons exit from **distinct** output ports (the $\hat{A}^\dagger(\omega')\hat{B}^\dagger(\omega)$ and $\hat{A}^\dagger(\omega)\hat{B}^\dagger(\omega')$ terms). These events are measured as coincidence counts when photon-counting detectors are placed at the two output modes.

Measuring Coincidence Counts

Consider now placing photon-counting detectors at the two output ports which are broadband, have a flat frequency response and are slow compared to the coherence time of the single-photon source. One can define the operator that describes measuring the state $\chi(\omega)$, for $\chi = \psi, \phi$, at the C output port of the BS as,

$$\hat{\Pi}_C = \eta_C \int \hat{C}^\dagger(\omega) \left|0\right\rangle \left\langle 0\right| \hat{C}(\omega) d\omega, \tag{3.23}$$

where $C = A, B$ and η_C is the detection efficiency of the photon-counting detector at output port, C. The operator for coincidence detection is therefore given by

$$\hat{\Pi}_{\mathrm{CC}} = \eta_A \eta_B \int\int \hat{A}^\dagger(\omega) \hat{B}^\dagger(\omega') \left|0\right\rangle \left\langle 0\right| \hat{A}(\omega) \hat{B}(\omega') d\omega d\omega', \tag{3.24}$$

The probability of measuring coincidence events, $P_{\mathrm{CC}} = \left\langle \Psi_{\mathrm{in}}\right| \hat{\mathrm{CC}} \left|\Psi_{\mathrm{in}}\right\rangle$, can, thus, be shown to equal,

$$\begin{aligned} P_{\mathrm{CC}} &= \frac{1}{2}\eta_A \eta_B \left[1 - \left| \int \psi^*(\omega)\phi(\omega) \right|^2 d\omega \right], \\ &= \frac{1}{2}\eta_A \eta_B \left[1 - \left| \left\langle \psi | \phi \right\rangle \right|^2 \right]. \end{aligned} \tag{3.25}$$

This expression includes the spectral mode function overlap, $\mathcal{O}_{\psi,\phi} = \langle\psi|\phi\rangle$, as discussed in subsection 2.3.2. This implies that for identical states, where the mode overlap is unity, one will never measure coincidence events. Hence, for independent and identical states the photons will always leave at the same exit port of the beam splitter.

Introducing a Temporal Delay

For HOM interference measurements, a temporal delay is commonly introduced to one of the two input states to controllably introduce distinguishing information between the input modes to the interference beam splitter. This delay can then be scanned to map

out the signature HOM dip. The HOM interference dip allows the visibility, V_{HOM}, and temporal coherence, τ_{HOM}, of the interference to be extracted which both provide valuable information about the two states.

Adding a temporal delay, τ, to one of the input states, the input port labelled b, has the following effect on the creation operator: $\hat{b}^{\dagger}(\omega') \rightarrow \hat{b}^{\dagger}(\omega')\mathrm{e}^{i\omega'\tau}$. Propagating this through the derivation above, one can determine the following final expression for the coincidence count measurement,

$$P_{\mathrm{CC}}(\tau) = \frac{1}{2}\eta_A\eta_B\left[1 - \left|\int \psi^*(\omega)\phi(\omega)\mathrm{e}^{i\omega\tau}d\omega\right|^2\right]. \tag{3.26}$$

The visibility of HOM interference is then given by the difference of coincidence counts from when $\tau \rightarrow \infty$ (where $P_{\mathrm{CC}}(\tau \rightarrow \infty) = \frac{1}{2}\eta_A\eta_B$) and $\tau = 0$ (where, $P_{\mathrm{CC}}(0) = \frac{1}{2}\eta_A\eta_B\left[1 - |\mathcal{O}_{\psi,\phi}|^2\right]$) divided by $P_{\mathrm{CC}}(\tau \rightarrow \infty)$. This gives,

$$\begin{aligned} V_{\mathrm{HOM}} &= \frac{P_{\mathrm{CC}}(\tau \rightarrow \infty) - P_{\mathrm{CC}}(0)}{P_{\mathrm{CC}}(\tau \rightarrow \infty)}, \\ &= \frac{1 - \left[1 - |\mathcal{O}_{\psi,\phi}|^2\right]}{1}, \\ &= |\mathcal{O}_{\psi,\phi}|^2. \end{aligned} \tag{3.27}$$

The visibility of the HOM interference is, thus, equal to the spectral overlap squared of the two states.

In general, the visibility of the HOM interference between two states, described by, $\hat{\rho}_1$ and $\hat{\rho}_2$, is given by[87],

$$V_{\mathrm{HOM}} = \mathrm{Tr}(\hat{\rho}_1\hat{\rho}_2). \tag{3.28}$$

For the case of two pure states, the visibility is equal to the mode overlap. However, for a mixed state the visibility is reduced. Therefore, the HOM measurement can also provide

information about the purity of two identical states, for example.

In the following section, HOM interference is performed between the signal and idler photons from the single-photon source and the results presented. The photon wave packets are spectrally filtered such that their spectral intensity profiles are nearly identical. Thus, by assuming they are independent, i.e. that the source is not entangled, and measuring near 94% interference visibility (as dictated by the result of the Schmidt Decomposition in subsection 3.4.3) one can deduce that the heralded single-photon state is spectrally pure. The experimental details and results for this measurement are given below.

HOM Interference Experimental Details

The HOM interference measurement was set up with the source as in Figure 3.2. The outputs of the signal and idler photon fibres were connected to the inputs of a polarization-maintaining fibre beam splitter (PMFBS) as shown by the box labelled "iv. HOM". This beam splitter is referred to as the *interfering* beam splitter taking place of the bulk cube beam splitter depicted in Figure 3.10. The two outputs ports of the fibre beam splitter were connected to two APDs with the electronic signal monitored by the FPGA. The temporal delay, included in the idler arm, labelled τ in the figure, was scanned relative to the signal photon, over the complete temporal support of the signal wave packet whilst measuring coincidences for a variable count time, T. Assuming each count is independent, if a total number of N coincidences were measured during this time period then the associated error is given by $\sqrt{N}$. Thus the error on the coincidence count rates is given by,

$$\alpha_{R_{\mathrm{CC}}} = \frac{\sqrt{N}}{T}. \tag{3.29}$$

Definitions for the count rates and count rate errors can be calculated similarly for the singles, R_1 and R_2.

Spectral Filtering

HOM interference was performed between the signal and idler photons as produced by the SPDC. To create identical spectral mode functions, a pair of interference filters (IF) with bandpass of 3.2 nm (typical) FWHM (Semrock MaxLine® filter, LL01-830-12.5) centred at $\lambda_{0,\mathrm{s}}$ was included in the SPDC source following the KDP. HOM interference was then repeated with the identically spectrally filtered photons.

Background Coincidences Correction

If there are higher-order photon states, for example second-, $|2\rangle_{\mathrm{s}}|2\rangle_{\mathrm{i}}$, or third-, $|3\rangle_{\mathrm{s}}|3\rangle_{\mathrm{i}}$, order as written in the Fock state basis, being created during SPDC these will contribute as false coincidences in the HOM measurement. This will happen when the higher-order state propagates to the beam splitter and the state occupation probabilistically splits at the output. Nonetheless, these background contributions can be easily measured and the coincidence rates corrected. This is done by blocking the optical path of one of the input ports to the interfering beam splitter. In this case, coincidences will only be registered if there are higher-order states being created in the source and splitting probabilistically as described above. These background coincidence contributions can be measured and the background coincidence rates calculated for both arms, R_{BG1} and R_{BG2}. The average coincidence count rates are then subtracted off the measured HOM coincidence count rate as follows,

$$R_{\mathrm{CC,BG}} = R_{\mathrm{CC}} + (R_{\mathrm{BG1}} + R_{\mathrm{BG2}})\,. \tag{3.30}$$

The uncertainty on the background count rates, determined similarly to Equation 3.29, were also propagated through to determine the corrected error for $R_{\mathrm{CC,BG}}$ using the following relation,

$$\alpha_{R_{\mathrm{CC,BG}}} = \sqrt{\alpha^2_{R_{\mathrm{CC}}} - \alpha^2_{R_{\mathrm{BG1}}} + \alpha^2_{R_{\mathrm{BG2}}}}. \tag{3.31}$$

Interference Visibility Extraction

The form of the HOM interference dip is typically Gaussian for interfering Gaussian spectra[177]. To determine an accurate value for the visibility, V_{HOM}, an inverted Gaussian function can be fit to data using a weighted nonlinear least squares estimate. The following functional form will, therefore, be used to fit the data,

$$f(\tau) = A\left(1 - B\mathrm{e}^{-\frac{(\tau-\tau_0)^2}{2\sigma_\tau^2}}\right) + m(\tau - \tau_1), \tag{3.32}$$

where τ is the temporal delay added in one arm during the interference scan. Here, the parameter A represents the non-temporally interfering coincidence count rate, i.e. the value of $R_{\mathrm{CC}}(\tau \to \infty)$. B Is the ratio of maximum coincidence counts to minimum i.e. the value of $R_{\mathrm{CC}}(\tau = 0)/R_{\mathrm{CC}}(\tau \to \infty)$. The value of τ_0 corresponds to the location of perfect temporal overlap, at the centre of the HOM dip, and σ_τ is related to the full width at half maximum of the interference by Equation 2.24. Finally, the second term, $m(\tau - \tau_1)$, where $\tau_1 = \tau(1)$ is the minimum value of the delay, takes into account if the underlying coincidence count rate is increasing or decreasing due to drifting alignment, for example. Thus m is essentially a gradient with units of coincidence count rate per unit time. The fit to the measured data, $R_{\mathrm{CC,BG}}$, was weighted by the error on the measurement, $\alpha_{R_{\mathrm{CC,BG}}}$.

The visibility of the HOMI dip is then given by,

$$V_{\mathrm{HOM}} = \frac{R_{\mathrm{CC}}(\tau \to \infty) - R_{\mathrm{CC}}(\tau = 0)}{R_{\mathrm{CC}}(\tau \to \infty)}. \tag{3.33}$$

These values required for the calculation, as defined in subsection 3.4.4, and their associated errors, can be determined using the inverted Gaussian fit to the interference data.

Finally, the extracted visibility of the HOM interference was also corrected for by the beam splitter transmission and extinction ratios and the input mode polarizations. For

an ideal beam splitter with a 50:50 splitting ratio one can achieve perfect interference, $V = 1$. However, if the reflection and transmission is not equal, this will reduce the maximum interference possible, with unequal signal in each arm. The splitting ratio of the fibre beam splitter output arms was determined by measuring the output power, using the same photodetector, at the two ends of the fibre beam splitter. The transmission, T, indicating the proportion of power sent to one output arm, and the reflection, R, indicating the proportion of power sent to the other output were calculated. The HOM visibility was then corrected using:

$$V_{\text{cor}} = \frac{(T^2 + R^2)}{2TR} V. \tag{3.34}$$

The polarizations of the two wave packets were matched by including a half-wave plate in the signal wave packet arm, before the aspheric lens, as shown in Figure 3.2. However, due to non-perfect beam splitters used in the source set up, there is a small amount of non-matched polarization in each arm. This can reduce the interference visibility since non-identical polarization modes will not interfere. The amount of "noise" polarization in each arm was determined by measuring the polarization extinction, PE, on each of the output arms of the fibre beam splitter. The polarization extinction is defined as the ratio of minimum intensity of transmitted light through a beam splitter, whilst rotating the polarization of the incident light, to the minimum transmitted intensity. Once the polarization extinction of each arm, PE_1 and PE_2, is determined, the visibility can be corrected by,

$$V_{\text{cor}} = \left(1 - \frac{1}{2}(\text{PE}_1 + \text{PE}_2)\right) V. \tag{3.35}$$

HOM Interference Measurement Results

A HOM interference measurement was taken three times for both the non-spectrally filtered and spectrally filtered measurements and the corrected data are shown in Figure 3.13 and Figure 3.15, respectively.

Un-Filtered

For the non-spectrally filtered case, the three measured, and corrected, HOM interference data are plotted in Figure 3.13. A weighted-average visibility of $V_{\mathrm{HOM}} = (20.9 \pm 0.5)\%$ was extracted. The width of the dip, given by the FWHM of the inverted Gaussian was determined as $\tau_p = (294 \pm 9)$ fs.

Filtered

For the spectrally filtered case, the three measured, and corrected, HOM interference data are plotted in Figure 3.15. A weighted average visibility of $V_{\mathrm{HOM}} = (86.7 \pm 0.5)\%$ was extracted. The width of the dip, given by the FWHM of the inverted Gaussian was determined as $\tau_p = (373 \pm 7)$ fs.

Spectral Intensity Measurement

The filtered idler and signal spectral intensities, $\tilde{S}_{\mathrm{s,filt}}(\omega)$ and $\tilde{S}_{\mathrm{i,filt}}(\omega)$, were measured using the spectrometer and CCD and were background-corrected, as described previously. Note, in these plots, the spectra have been scaled such that the maxima for both are one for comparison. A Gaussian function, of the same form as in Equation 3.12, was fitted to each of the signal intensity profiles. This fit, as before, was weighted by the error on the measured intensity data where a photon count of N was assigned an error of $\sqrt{N}$.

Un-Filtered

The measured, and background corrected intensity spectra for the signal and idler photon states are shown in Figure 3.12. A central wavelength of $\lambda_{0,\mathrm{s}} = (826.9 \pm 0.2)$ nm and bandwidth of $\Delta\lambda_{\mathrm{s}} = (2.6 \pm 0.3)$ nm were extracted. The central wavelength of the idler spectral intensity was found to be approximately $\lambda_{0,\mathrm{i}} = (826.8 \pm 0.2)$ with bandwidth $\Delta\lambda_{\mathrm{i}} = (14.6 \pm 0.3)$ nm.

Filtered

The measured, and background corrected spectra, for the filtered signal and idler intensity spectra are shown in Figure 3.14. One can see that the filtered idler spectra now displays a top-hat profile. This is a result of the spectral filtering by the interference filter which, typically, has a top-hat profile. The transmitted spectral mode function, $\tilde{\psi}_{\text{out}}(\omega)$, is related to the product of the incident spectral mode function, $\tilde{\psi}_{\text{in}}(\omega)$, with the filter transmission profile, $\tilde{t}(\omega)$, through,

$$\tilde{\psi}_{\text{out}}(\omega) = |\tilde{t}(\omega)\tilde{\psi}_{\text{in}}(\omega)|^2. \tag{3.36}$$

The filter bandwidth is on the same order as the signal photon's bandwidth. However, the idler spectral amplitude is over twice as broadband than the signal, thus the filter has a noticeable effect on the spectral profile.

A central wavelength, for the signal spectral amplitude, of $\lambda_{0,\text{s}} = (826.8 \pm 0.2)$ nm and bandwidth of $\Delta\lambda_{\text{s}} = (1.9 \pm 0.3)$ nm were extracted from the Gaussian fit. The central wavelength of the idler, top-hat, function was found to be approximately $\lambda_{0,\text{i}} = (826.8 \pm 0.2)$ using the Gaussian fit. A FWHM of (2.8 ± 0.3) nm was determined by finding the width at half of the intensity maximum.

Spectral Overlap Calculation

The spectral overlap, which is expected to agree with the HOM interference visibility, was calculated using Equation 2.18 via two methods:

1. Initially it was calculated directly from the measured spectral intensity data, $\tilde{S}_{\mu}(\omega)$, for $\mu =$(s,i), denoting the signal and idler data respectively. The intensity data used in this calculation was selected from a region of the complete wavelength space of the measurement defined by, $(\lambda_0 \pm 3\Delta\lambda)$ The associated spectral wave packet amplitude

function, $\tilde{\psi}_\mu(\omega)$, was extracted from the selected measured data as follows,

$$\tilde{\psi}_\mu(\omega) = N_\mu \sqrt{\tilde{S}_\mu(\omega)}, \tag{3.37}$$

where N_μ is the normalization constant given by,

$$N_\mu = \frac{1}{\sqrt{\int \tilde{S}_\mu(\omega) d\omega}}. \tag{3.38}$$

The resultant overlap was then numerically calculated using Equation 2.18. One difficulty with this direct method was that it did not allow one to easily extract an error on the calculation.

2. To extract a spectral overlap value with an associated error, the calculation was also performed using a Monte Carlo-type algorithm. This method employed the Gaussian fits to each set of data. Two Gaussian spectral intensity were simulated with the following form,

$$I_\mu(\lambda) = \mathrm{e}^{-\frac{(\lambda-\lambda_0)^2}{2\sigma^2}}, \tag{3.39}$$

for μ = (s,i). The variable parameters for the simulated intensity, λ_0 and σ, were chosen randomly from a normal distribution. This normal distribution had a mean given by the corresponding parameter's extracted value from the Gaussian fit. The standard deviation of the normal distribution was given by the error on that parameter returned from the Gaussian fit. After defining the two simulated intensity spectra, I_s and I_i, the corresponding spectral amplitudes were determined as above, using Equation 3.37, and the spectral overlap calculated using Equation 2.18.
This process was repeated for a total of 10^4 iterations, with different values assigned for the parameters in the simulated intensity spectra each time. An average of all 10^4 calculated spectral overlaps and the standard deviation of these values could

then be extracted to assign as the error.

The resultant spectral overlaps were calculated for both sets of spectra using both of these methods and are given below.

Un-Filtered

The unfiltered spectra measured intensities resulted in a spectral overlap of 59%. However, the numerically simulated value, using the Gaussian fits gave a value of $(35 \pm 1)\%$.

Filtered

When calculating the filtered spectra spectral overlap using the data, a value of 89% was determined. When using the second method, the numerical calculation using the Gaussian fit results, an overlap of $(96 \pm 1)\%$ was calculated.

Summary: HOM Interference and Spectral Overlap

Hong-Ou-Mandel interference was performed between the signal and idler wave packets, produced by the SPDC single-photon source. The two wave packets were then spectrally filtered to achieve nearly indistinguishable spectral amplitudes and the interference measurement was repeated. By also measuring their spectral intensities, to extract an estimate of their spectral amplitudes, one can calculate an upper limit of the expected interference visibility.

For the original, non-filtered case an average HOM visibility of $\langle V_{\mathrm{HOM}} \rangle = (20.9 \pm 0.5)\%$ was extracted from three repeat interference measurements. The square of the spectral overlaps was calculated as $(35 \pm 1)\%$ and 59% using the two methods discussed above, respectively. These are all significantly different. It is expected that the spectral overlap calculated using the measured data (method 1 as described above), with data shown in Figure 3.12, is grossly overestimated. This is due to the non-zero contributions seen in

the outer arms of the narrow signal spectra. These non-zero contributions are a remnant of background noise and dark counts on the CCD and cannot be completely corrected for. These contribute a significant amount to the overlap calculation due to their superposition with regions of large relative intensity of the more spectrally broadband idler spectrum. Nonetheless, the spectral overlap calculated using the Gaussian fits and Monte Carlo type simulation also does not agree with the measured HOM interference visibility. Furthermore, recall that, assuming there is a flat phase between the bi-photon pair, the upper limit on their purity is 94.71%, as calculated using the measured JSI and a Schmidt decomposition in subsection 3.4.3. Therefore, it is already expected that the HOM interference visibility may be reduced from the pure, ideal case.

For the filtered case, there should be less noise added to the spectral overlap from these intensity background contributions. For this data, an average HOM interference visibility of $\langle V_{\mathrm{HOM}} \rangle = (87 \pm 1)\%$ was extracted from three repeat measurements. The two methods of overlap calculation resulted in values of 89% and $(96 \pm 1)\%$, respectively. Once again, the overlap value calculated using the intensity data was overestimated. Upon inspection of this data in Figure 3.14 one can see that there are non-zero contributions in the outer-arms of the spectra which increase the final spectral overlap value. Nonetheless, the spectral overlap calculated using the raw data lies only two errors away from the HOMI visibility value. Since the idler wave packet has a flat distribution maximum, it is not expected that the MC method would produce an accurate result.

3.5 Chapter Summary

This chapter has presented the background of the single-photon source to be used for implementation of the quantum pulse shaping method presented in this thesis. This began with a brief overview of single-photon sources and the theory behind the production of a separable bi-photon pair used in this work for heralded single-photon generation. Details

of the experimental implementation and its characterization was provided. This included measuring the intensity spectra, the JSI and performing HOM interference between the bi-photon pair. Using the measured JSI and performing a Schmidt decomposition allowed one to place an upper limit of a purity of 94.71% on the bi-photon source. Thus, it is expected there may be a reduction in HOM interference visibilities, as seen in this chapter, and in future two-photon interference measurements, from that predicted from the spectral overlap, if the wave packets remain unfiltered.

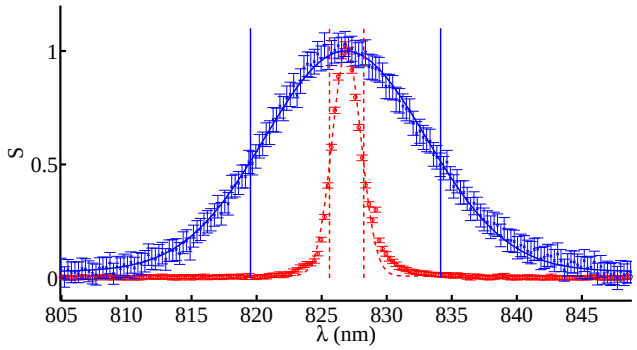

Figure 3.12: Measured intensity spectra for the signal (red circles) and idler (blue crosses) wave packets, corresponding to the interfered wave packets for the HOM measurement, are plotted. The rescaled intensity measurement has been plotted: $S = I/I_{\max}$ where $I_{\max}$ is the maximum intensity of the data. Gaussian fits were performed on both sets of data and are plotted. Vertical lines indicate the location of half the intensity maximum, $\lambda_{\pm\frac{I}{2}}$, for both sets of data. Central wavelengths of $\lambda_{0,\mathrm{s}} = (826.9 \pm 0.2)$ nm and $\lambda_{0,\mathrm{i}} = (826.8 \pm 0.2)$ nm for the signal and idler wave packets were extracted with spectral bandwidths of $\Delta\lambda_{\mathrm{s}} = (2.6 \pm 0.3)$ nm and $\Delta\lambda_{\mathrm{i}} = (14.6 \pm 0.3)$ nm.

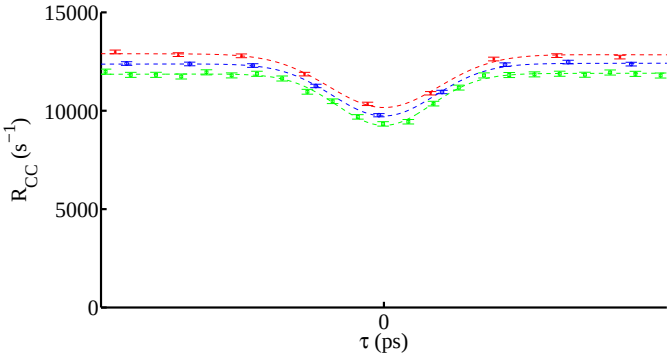

Figure 3.13: Three repeat measurements of the HOM interference between the signal and idler photons produced by the SPDC are shown. The coincidence count rate, R_{CC}, is plotted versus the temporal delay, τ, between the idler and signal photon wave packets. This data has been corrected for background coincidence counts and polarization mismatch and splitting ratios of the beam splitter. An average visibility of $\langle V_{\mathrm{HOM}} \rangle = (20.9 \pm 0.5)\%$ was extracted by fitting an inverse Gaussian function to the data, also plotted here.

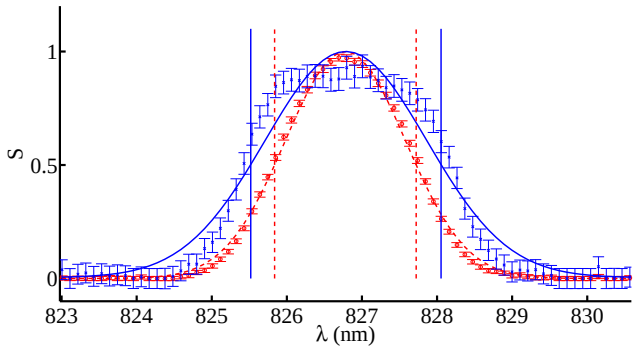

Figure 3.14: Measured intensity spectra for the signal (red circles) and idler (blue crosses) spectrally filtered wave packets, corresponding to the interfered wave packets for the HOM measurement, are plotted. The rescaled intensity measurement has been plotted: $S = I/I_{\max}$ where $I_{\max}$ is the maximum intensity of the data. Gaussian fits were performed on both sets of data and are plotted. Vertical lines indicate the location of half the intensity maximum, $\lambda_{\pm\frac{I}{2}}$, for both sets of data. Central wavelengths of $\lambda_{0,\mathrm{s}} = (826.8 \pm 0.2)$ nm and $\lambda_{0,\mathrm{i}} = (826.8 \pm 0.2)$ nm for the signal and idler wave packets were extracted using the fit along with $\Delta\lambda_{\mathrm{s}} = (1.9 \pm 0.3)$ nm. Vertical lines indicate the location of half the intensity maximum, $\lambda_{\pm\frac{I}{2}}$, for both sets of data. The FWHM was determined using this width for the idler wave packet and gave $\Delta\lambda_{\mathrm{i}} = (2.8 \pm 0.3)$ nm

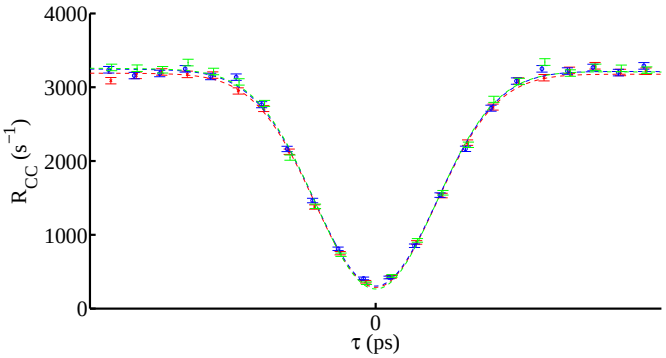

Figure 3.15: Three repeat measurements of the HOM interference between the spectrally filtered signal and idler photons produced by the SPDC are shown. The coincidence count rate, R_{CC}, is plotted versus the temporal delay, τ, between the two wave packets. This data has been corrected for background coincidence counts and polarization mismatch and splitting ratios of the beam splitter. An average visibility of $\langle V_{\mathrm{HOM}} \rangle = (86.7 \pm 0.5)\%$ was extracted by fitting an inverse Gaussian function to the data, also plotted here.

Chapter 4

Temporal Phase Modulation Using an Electro-Optic Phase Modulator

4.1 Introduction

Manipulating the spectral phase, for spectrally broadband pulses, is relatively easy, for example using a 4f line. However, owing to the Fourier relation between the two, the temporal phase is difficult to access. Conversely, narrow band light temporal phase is relatively easy to access but the spectral phase is more challenging. There is a relatively small bandwidth regime in which both the spectral and temporal modes can be accessed simultaneously. This is typically true for pulses of a few picoseconds in duration, as focused on in this thesis.

Previous approaches of controlling the temporal phase focused primarily on nonlinear phase modulations[180,181]. Here, an alternative approach is proposed and tested which sees the optical pulse propagated through a relatively slowly-varying electro-optic material. By applying a controlled electric field across the material, one can control the phase applied to the optical pulse. More specifically, well-defined linear and quadratic temporal phases are applied to the pulse train using an electro-optic phase modulator (EOM).

In this chapter, experimental implementation of temporally-varying phase-modulation using an EOM is discussed. The method is first described qualitatively before details on the design for generating a radio frequency (RF) voltage source that drives the electro-optic material is given. This RF source is engineered to be phase-locked to the incident pulsed optical light and capable of a variable driving voltage for precise control of the applied temporal phase. The design details of the RF source are then followed by calibration of the RF source. This calibration allows one to predict the range of spectral manipulation that can be achieved with this experimental set up. In the final part of the chapter, the pulse-shaping method is tested using a coherent, laser pulse train. This classical light source has optical properties, such as central wavelength, bandwidth and pulse repetition rate, similar to the single-photon source that will, ultimately, be used to test this pulse-shaping method in the quantum domain in this thesis. This allows one to verify correct operation of the driving signal source and the results act as a base line for applying the pulse-shaping method to the single-photon source as described in chapter 3.

4.2 Temporal Phase Modulation Using an Electro-Optic Modulator

Temporal phase modulation is achieved in this work using an electro-optic phase modulator (EOM). Coherent manipulation of the wave packet is performed by applying the phase modulation in a regime where the optical pulse duration is shorter than variations in the phase modulation signal. This work follows a method which was first implemented with a weak coherent pulse[85].

Previous work has shown electro-optical modulation of single-photons created by a quasi-monochromatic downconversion source[48]. This source produced frequency-entangled photons which were spatially separated and sent to two end users. Temporal phase mod-

ulation is then applied to each photon by the end user, using an EOM. The temporal phase modulation on the quasi-monochromatic mode distribution is sinusoidal and results in a spectral amplitude featuring sidebands. These sidebands are then spectrally filtered by the communicating end users and single photons detected. Coincidence measurements between the two detectors are then analysed. This method allows one to determine the degree of frequency entanglement in the downconversion source[182].

Electro-optic modulation has also been used in a quasi-monochromatic downconversion single-photon source, with varying electric field applied to the downconversion crystal itself to control the frequency spectrum of the emitted photons[183]. Work has also demonstrated electro-optic modulation of entangled photons to achieve phase and amplitude modulation[184]. However these photons had temporal widths on the order of a hundred nanoseconds. This renders them spectrally-irresolvable when detected using standard spectral detection methods.

The author of this work believes this is the first time an electro-optic modulator has been used to deterministically transform the spectral amplitude distribution of an ultrashort, single-photon wave packet of light. A brief overview into how this is achieved is now described before the details of the EOM operation are given.

The EOM is driven by a temporally, sinusoidally varying electric field. The period of oscillation of this driving signal is chosen such that it is much longer than the optical pulse duration. When the optical pulse propagates through the EOM, it therefore experiences a phase given by the instantaneous form of the temporally varying electric field.

Consider the case when the optical pulse propagates through the EOM when the sinusoidally varying electric field is at its peak. This is shown more clearly in Figure 4.1

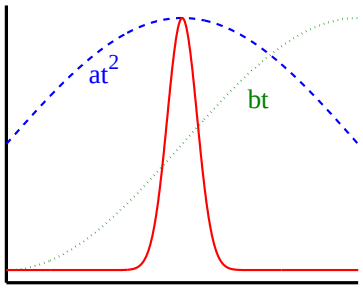

Figure 4.1: This schematic demonstrates the relative temporal alignment of a Gaussian optical temporal wave packet (red, solid line) with a linear (green, dotted line) and quadratic (blue, dashed line) electric field to achieve a linear and quadratic temporal phase, respectively.

where the optical pulse and electric field are plotted. The optical pulse is temporally aligned with the peak of the sinusoidal curve. In this case, the electric field is of the form $E(t) \propto at^2$. This results in a temporal phase modulation of the form $\phi(t) \propto \alpha t^2$. As shown in subsection 2.5.4, when a quadratic phase is applied to an optical pulse, the result is spectral broadening. Also shown in this plot is the case when the optical pulse propagates through the EOM and aligns with the positive linear region of sinusoidal curve, such that $E(t) \propto bt$, resulting in a temporal phase modulation of the form $\phi(t) \propto bt$. In this case, as described in subsection 2.5.3, the result is a linear shift in spectrum.

Thus by synchronizing the EOM driving field with an optical pulse train, one can achieve both spectral shearing and expansion. The experimental challenges associated with this method include generating a high-frequency driving signal capable of providing substantial phase shift and synchronizing this modulation field with the optical pulse train. The details on how this is done are now given.

4.2.1 The Electro-Optic Modulator

The modulator used in this work is a channel waveguide fabricated from lithium niobate ($LiNbO_3$), as shown in the basic schematic in Figure 4.2. Lithium niobate is an electro-optic material that exhibits the transverse Pockels effect[185]. The resultant refractive index experienced by any transmitted light is highly dependent on its polarization, propagation direction and applied voltage.

The modulator used here is fabricated such that any transmitted light whose polarization is in the direction of the optic axis, as indicated in Figure 4.2 and referred to as the fast axis, experiences the maximum birefringence change when an electric field is applied. This is achieved in the modulator by attaching electrodes perpendicular to the propagation direction of transmitted light, also seen in the figure.

The change in refractive index in the x-direction of the optical material is given by, $\Delta n_3 = -\frac{1}{2} n_3 r_{33} E_3$, where r_{33} is the relevant electro-optic coefficient of the coupling between the electric field and refractive index, n_3 is the refractive index with no electric field applied and the electric field, given by $E_3 = V/w$, where w is the channel width, as labelled in Figure 4.2, and V, the applied voltage. Thus, the phase induced on an incident wave packet due to modulation of the refractive index is linear in voltage and over a path length, L, is given by,

$$\Delta\phi_{\text{EOM}} = \Delta n \frac{2\pi}{\lambda} L = -\frac{L n_3^3 r_{33} \Gamma}{\lambda w} \pi V = \frac{\pi V}{V_\pi}. \tag{4.1}$$

There is a reduction indicated by Γ to account for the inhomogeneity of the EOM. The constants in Equation 4.1 are often grouped together and denoted by $V_\pi = -\frac{\lambda w}{L n_3^3 r_{33} \Gamma}$. This constant is known as the π, or half-wave, voltage, and is the voltage required to achieve a π phase shift. This value is thus specific to each individually manufactured modulator. Note, that if the wave packet is travelling along the slow axis, it will not experience this phase change.

4.2.2 Electro-Optic Modulator Dispersion

The polarization-maintaining fibre used throughout the optical set up (Nufern, 780PM Panda) had a dispersion rating of 34 fs^2/km [186]. Lithium niobate has a GVD of 406.24 fs^2/mm at $\lambda = 830$ nm [187] which is an order of magnitude larger. Thus, with a waveguide

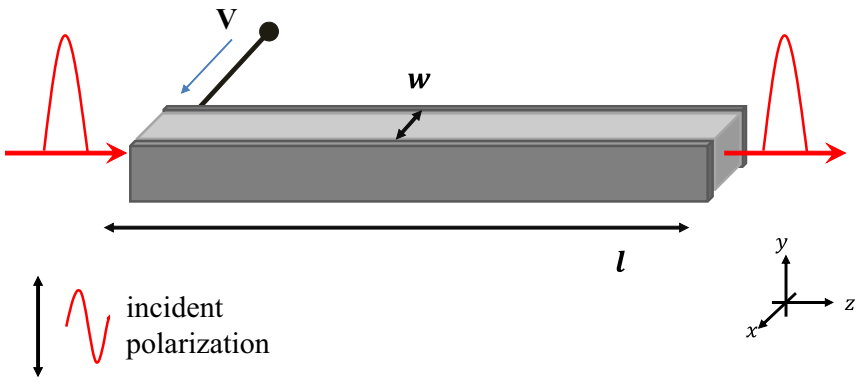

Figure 4.2: A basic schematic of the channel waveguide electro-optic modulator (EOM). The waveguiding region is made of $LiNbO_3$ with electrodes attached perpendicular to the propagation of light, z. An e-ray, with polarization in the plane defined by y and the optical axis as shown above, will experience a phase change when a voltage, V is induced across the waveguide. The magnitude of phase change is dependent on the width, w, and the length, l, of the waveguide, amongst other things.

length of approximately 100 mm, the EOM is expected to introduce some dispersion to the phase modulated wave packet. The expanded pulse width, due to this second-order dispersion term, can be calculated by,

$$\tau = \tau_0 \sqrt{1 + \frac{4\ln(2)\mathrm{GDD}}{\tau_0^2}}, \tag{4.2}$$

where τ_0 is the initial pulse duration. Assuming a pulse with initial temporal duration, τ_0 of 500 fs, this will be temporally expanded to 550 fs, an effect on the order of 10%. However, a pulse with initial temporal duration of 1 ps will only be temporally expanded to 1.006 ps. Since this is the order of temporal duration studied in this thesis, it is not expected that the modulator will have a significant effect on the spectral phase.

4.2.3 Electro-Optic Modulator Driving Signal

Applying a temporally varying voltage, $V = V(t)$, to the modulator results in a temporally dependent phase change,

$$\phi_{\mathrm{EOM}}(t) = \frac{\pi}{V_\pi} V(t). \tag{4.3}$$

In this case, it is assumed that the response of the medium to the applied voltage is instantaneous. The switching speed of the modulator is limited by electrical capacitive effects, which are on the order of femtoseconds[188], thus negligible here.

The modulator design is based on a broadband, travelling-wave transmission-line electrode[189]. Therefore, applying a sinusoidal voltage to drive the modulator results in the following form of

$$V(z,t) = V_{\mathrm{D}} \sin(k_D z - \omega_{\mathrm{D}} t + \phi_{\mathrm{D}}), \tag{4.4}$$

where V_{D} is the peak driving voltage, ω_{D} is the angular driving frequency, k_{D} is the electrode wave vector and ϕ_{D} the global phase offset. The oscillation period is $T_{\mathrm{D}} = 2\pi/\omega_{\mathrm{D}}$. Typically the phase velocity of the driving voltage is matched to the optical pulse such that the signal remains constant during propagation through the modulator.

If the optical pulse has a temporal duration, τ_p, which is much smaller than the time period of the driving signal, $\tau_p << T_{\mathrm{D}}$, then the voltage signal varies slowly in the moving frame of the wave-packet envelope. As the ultrashort pulse propagates through the modulator, it experiences phase modulation over a short time period compared to the oscillation driving period. By controlling the temporal alignment of the relatively slow driving voltage and the ultrashort optical wave packet, using the phase, ϕ_{D} introduced in Equation 4.4 above, one can select the desired region of time-varying voltage to induce a time-varying phase.

This is shown more clearly in Figure 4.3. Note that in these plots the signals are plotted in the moving frame of the optical pulse. In Figure 4.3a. the wave packet is temporally aligned to the driving signal such that the voltage varies linearly across the pulse, $V \propto -t$. As dictated by Equation 2.29, the negative linear temporal phase results in a positive, or blue-shift such that $\tilde{\psi}(\omega) \rightarrow \tilde{\psi}(\omega + \alpha)$. In Figure 4.3b. the wave packet is aligned with

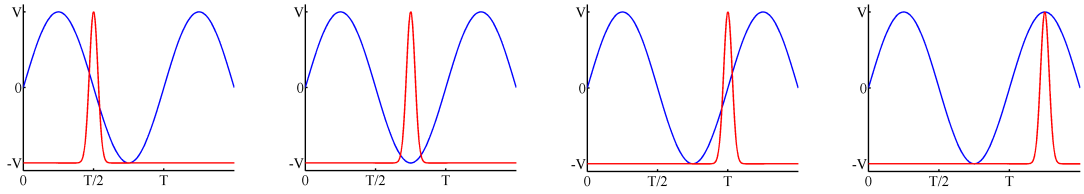

(a) Negative, linear **(b)** Positive, quadratic **(c)** Positive, linear **(d)** Negative, quadratic

Figure 4.3: Four cases of optical wave packet alignment with the voltage signal are shown above. The relative phase between the voltage signal (blue sinusoid) and the optical wave packet (red Gaussian pulse) is controlled to achieve each alignment. The optical wave packet thus only "sees" a narrow region of the voltage signal which dictates the induced phase across the wave packet. These plots are in the moving frame of the optical pulse.

the quadratic region of the driving voltage such that $V \propto -t^2$. In this case the wave packet undergoes quadratic temporal phase modulation, resulting in spectral expansion, as seen by Equation 2.31. A positive increasing voltage is experienced by the wave packet in Figure 4.3c and hence undergoes a spectral red-shift such that $\tilde{\psi}(\omega) \rightarrow \tilde{\psi}(\omega - \alpha)$. Finally, in Figure 4.3d, the optical wave packet experiences the positive quadratic temporal phase and, once again, becomes spectrally expanded.

In the following sections, the theoretical description of the alignment with a linear and quadratically varying driving signal is presented to relate the spectral manipulation to the physical properties of the experimental set up.

Linear Alignment

Recall from Equation 2.29 the magnitude of the spectral shift achieved, α, is equal to the gradient of the linear temporal phase. For the modulator driven by a sinusoidal signal, $V(t)$, the spectral shear is proportional to gradient of the linear region of the driving signal. To achieve maximum spectral shift, the wave packet must be temporally aligned with the sinusoidally varying voltage where the gradient is the steepest. For the sinusoidal signal, this occurs when $(\omega_{\mathrm{D}} t + \phi_{\mathrm{D}}) = n\pi$, for $n \in \mathbb{Z}$. For $n = 0$ and all even values of n, a positive linear gradient is seen, for odd values of n, the gradient is negative. The magnitude of the

gradient for both the positive and negative slopes can be determined by expanding the phase around $t = 0$.

$$\begin{aligned}\Delta\phi(t) &= \phi_0(\sin(\omega_{\mathrm{D}}t)),\\ &\approx \Omega t,\end{aligned} \tag{4.5}$$

where,

$$\Omega = \phi_0\omega_{\mathrm{D}} = \frac{\pi V_{\mathrm{D}}\omega_{\mathrm{D}}}{V_\pi}. \tag{4.6}$$

Applying this phase to a wave packet, $\psi(t)$, results the following modification,

$$\begin{aligned}\tilde{\psi}_{\mathrm{mod}}(\omega) &= \int \psi(t)\mathrm{e}^{i\omega t}\mathrm{e}^{i\phi_0\sin(\omega_{\mathrm{D}}t)}dt,\\ &\approx \int \psi(t)\mathrm{e}^{i(\omega+\Omega)t}dt,\\ &= \tilde{\psi}(\omega+\Omega).\end{aligned} \tag{4.7}$$

The spectral shift induced by the modulator is therefore directly proportional to the driving voltage frequency, ω_D, and strength, V_D, and inversely proportional to the modulator half-wave voltage, V_π.

Quadratic Alignment

As shown in Equation 2.31, for the case of a Fourier transform limited (FTL) Gaussian pulse, of the same form as Equation 2.23, the effect of applying a quadratic temporal phase of the form $\phi(t) = \beta t^2$, increases the bandwidth by a factor of $(1 + 4\beta^2\sigma^{-4})^{1/2}$. The wave packet will experience a quadratic temporal phase when passing through the modulator when temporally overlapped with the peak or trough of the driving voltage signal as shown in Figure 4.3(c) and Figure 4.3(d). This occurs when $\omega_{\mathrm{D}}t = m\pi/2$, where $m \in \mathbb{Z}$. The phase shift induced around these points can be well-approximated by a Taylor expansion

as,

$$\begin{aligned}\Delta\phi(t) &= \phi_0(\cos(\omega_{\mathrm{D}}t)),\\ &\approx \phi_0(1-\frac{1}{2}\omega_{\mathrm{D}}^2t^2),\end{aligned} \tag{4.8}$$

The first, constant term can be disregarded since it becomes incorporated into the constant, global phase, ϕ_0, of the wave packet. The parameter β originally used in Equation 2.31 and which parametrizes the spectral expansion becomes,

$$\beta = \frac{\phi_0\omega_{\mathrm{D}}^2}{2} = \frac{\pi V_{\mathrm{D}}\omega_{\mathrm{D}}^2}{2V_\pi}, \tag{4.9}$$

such that,

$$\begin{aligned}\tilde{\psi}_{\mathrm{mod}}(\omega) &= \int \psi(t)\mathrm{e}^{i\omega t}\mathrm{e}^{i\phi_0\sin(\omega_{\mathrm{D}}t+\pi/2)}dt,\\ &\approx \int \psi(t)\mathrm{e}^{i(\omega t+\beta t^2)}dt,\end{aligned}$$

where a phase factor has been omitted here for simplicity. For a Gaussian pulse experiencing this quadratic temporal phase with initial FWHM, $\Delta\omega_0$, this results in an expanded spectral bandwidth, $\Delta\omega$, given by,

$$\Delta\omega = \Delta\omega_0\sqrt{1+\left(\frac{8\ln(2)\beta}{\Delta\omega^2}\right)^2}, \tag{4.10}$$

using the result found in Equation 2.31. The effect is thus more prominent for pulses with an initially narrower bandwidth.

4.2.4 Factors Dictating the Chosen Electro-Optic Modulator and Driving Signal

Until now it has not been necessary to distinguish between quantum or classical wave packets of light when discussing the modulation technique. This is because the spectral

shaping technique presented here is applicable to both, being a linear operation of the field amplitude. This is highly advantageous for testing and calibration. Furthermore, specific values for the modulator driving voltage and frequency have been omitted. This is because the spectral shaping technique is generally applicable to wave packets with a range of temporal widths. One only needs to ensure that the modulator signal can be approximated as quadratic or linear during the temporal support of the optical wave packet to be manipulated. This is achieved by careful matching of the driving voltage time period of oscillation to the temporal width of the optical wave packet.

The key result presented in this thesis is demonstration of the pulse shaping technique using quantum states of light. The shaping was performed on the single-photon source discussed in the previous chapter. The temporal properties of the wave packet therefore influences the modulator and driving electronic specifications. Thus, the main properties of the modulator-driving electronics that were chosen are described below.

There are a variety of commercially available EOMs, engineered for specific applications and with the market highly dominated by the telecommunications industry. These include EOMs engineered for a low V_π, to transmit specific optical frequencies and for different driving signal frequencies to name a few. When choosing the modulator to employ for phase modulation, the temporal width of the wave packet must be considered. For example, assuming a FTL pulse, and using the minimum time-bandwidth product for Gaussian pulses, subsection 2.3.5, a spectral bandwidth in the range of $\Delta\lambda = 1 \rightarrow 3.5$ nm as produced by the heralded single-photon source is equivalent, at a central wavelength of 830 nm, to a temporal width on the order of $\tau_{G,\mathrm{min}} \approx 0.3 \rightarrow 1$ ps. The modulator must therefore be driven at a frequency such that the time period of one oscillation, $T_\mathrm{D} = 2\pi/\omega_\mathrm{D} >> 1$ ps. However, one must bear in mind that as the temporal duration decreases the spectral bandwidth increases, thus the achievable spectral expansion is reduced, as dictated by

Equation 4.10. Furthermore, since the magnitude of spectral shift depends linearly on ω_D, as indicated in Equation 4.6. The driving signal should, therefore, be made as large as possible.

The fastest commercially available modulators currently run at 40 GHz[190–192]. A 40 GHz signal has a time period, $T_D = 25$ ps, compatible with the temporal duration of the single-photon wave packet created by the single-photon source described in chapter 3. Therefore, a 40 GHz travelling waveguide electro-optic phase modulator was provided by EOSpace (Model: PM-AV5-40-PFU-PFU-830-S, S/N 241518) with 5 dB optical insertion loss. The modulator was fabricated for operation at 830 nm with two polarization maintaining fibres pigtailed at either end to allow for all-fibre implementation. To drive the modulator, a 40 GHz RF driving source was required.

Alongside considerations for the EOM, the driving electronics must also be carefully chosen to meet the needs of the temporal phase shift operation. These parameters include the driving signal frequency (already selected as 40 GHz), the signal strength and phase offset, as dictated by Equation 4.6 and Equation 4.9. The magnitude of spectral shift is proportional to the driving signal strength, V_D, thus a high voltage signal is desirable. For tunable control of the spectral manipulation, a variable voltage source is also desirable. The relative temporal alignment of the RF signal and optical wave packet is critical, thus a variable phase shifter was also included in the design. Furthermore, when the EOM is synchronized with an 80 MHz optical pulse train as used for the single-photon source in chapter 3, the 40 GHz signal undergoes $T_\ell/T_D = 500$ sinusoidal oscillations for each optical wave packet that passes through the modulator, where $T_\ell = 12.5$ ns and is the temporal period between subsequent optical pulses from the Ti:Sapph oscillator. To ensure accurate, repeatable implementation of the wave packet manipulation over an experimental time period, which can be up to on the order of an hour, the 40 GHz signal must also be

phase locked to the pulse train over this time.

The details on the design and build of the RF driving signal source are now given. Another important experimental parameter is the half-wave voltage, V_π, of the modulator which is device-dependent. This required accurate calibration for operation at 40 GHz, with 830 nm optical wave packets, thus is also described later in this section.

4.2.5 Generating a Phase-Locked RF Driving Signal

The circuit design, construction and testing was done in collaboration with Aspen Electronics[193]. This design is similar to that implemented by Kang and Dorrer[194], which operated at 10 GHz. A schematic of the basic circuit to realise the voltage and phase-tunable 40 GHz driving signal for the phase modulator is shown in Figure 4.4. Initially, to realize the radio frequency driving signal, a phase-dielectric resonator oscillator (PDRO), with 40 GHz nominal resonance frequency, is locked to a 40 GHz signal derived from the 80 MHz optical pulse train. This signal is then passed through a phase shifter with manual control. The signal is then fed into a motor-driven variable attenuator for electronic control. Finally, the signal is amplified before input to the EOM. In between all components, high frequency cable (AT38A-3436-89, loss rating 3.3 dB/m at 40 GHz) with 2.92 mm inner conductor diameter connectors (standard for 40 GHz) was used to minimize loss. Finally, the circuit was mounted in a 19-inch rack unit, a radio and electronics industry standard frame[195], for easy combination with other electrical components. The operation details of each individual component of the RF source are included below.

Phase-Locked Dielectric Resonator Oscillator

A basic block diagram of the PDRO is shown in Figure 4.8. The 40 GHz driving signal was generated using a dielectric resonator oscillator (DRO) in a phase-locked loop circuit. A DRO is typically a small, cylindrical piece of dielectric material with a large dielectric constant and low dissipation factor at resonant frequency. The DRO produces a standing

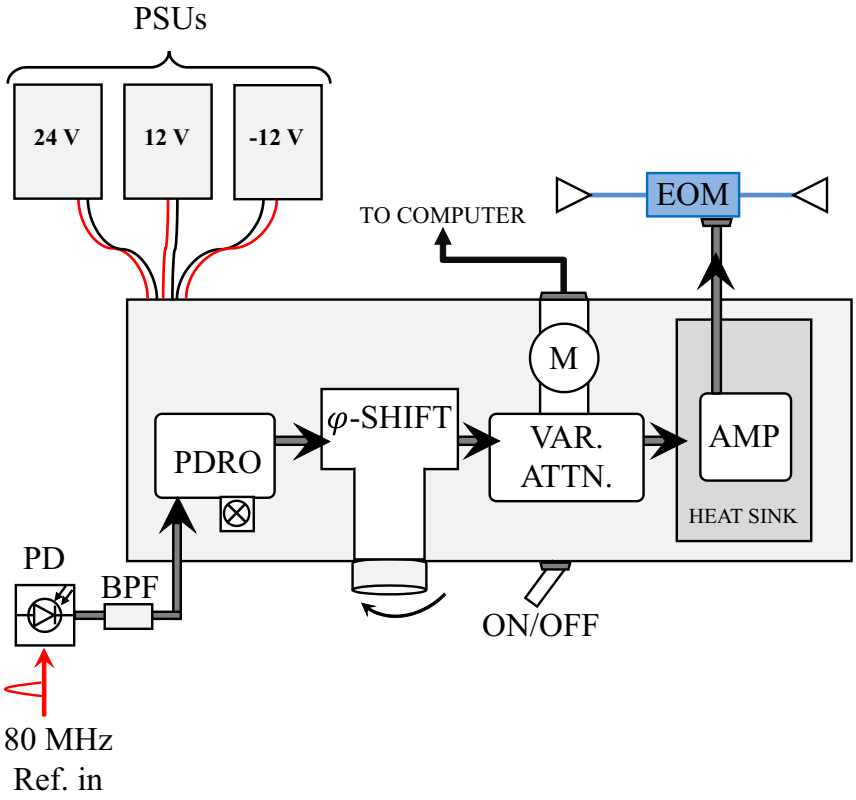

Figure 4.4: Circuit diagram showing the order of components required to produce the RF phase-locked driving signal to power the electro-optic modulator (EOM). An 80 MHz reference signal is derived from the oscillator's 80 MHz optical pulse train using a photodiode (PD). This signal is then filtered using a band-pass filter (BPF) to reduce any electronic noise. The 80 MHz reference is then fed into the PDRO which outputs 40 GHz. The signal is then passed to a manual phase-shifter (ϕ SHIFT) to control the relative temporal alignment between the RF and optical signals. The signal is then passed into a variable attenuator (VAR. ATTN.) which is driven by a motor (M), and controlled by a computer interface. The signal finally passes through an amplifier (AMP). The circuit contains an output RF connector to connect to the EOM. The components require a 24 V and two 12 V power supply units (PSU) to power the driving signal circuit.

wave in response to an applied voltage at the resonant frequency. Each DRO is therefore fabricated to a specific geometry such that standing waves of the desired frequency form inside. Phase locking with the pulse train of the single-photon source, in this case, is achieved by deriving the input signal to the PDRO from the original laser pulse train used to pump the single-photon source. During operation the PDRO requires a 12 V DC power supply unit.

A photodiode (Thorlabs, DET10A) was used to detect a small ($\approx$ 1%) pick-off from

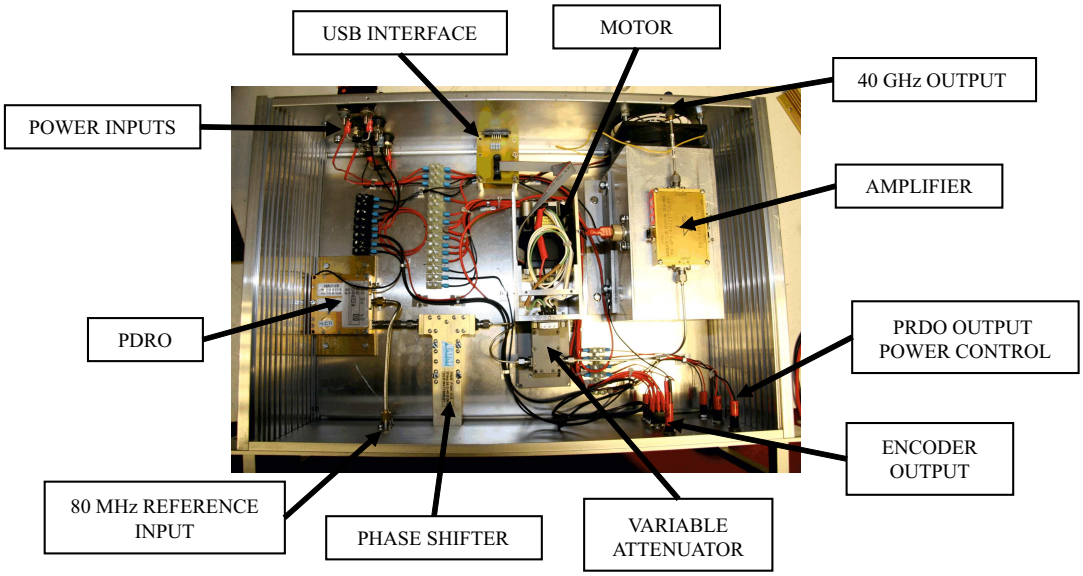

Figure 4.5: Image of the rack-mounted 40 GHz driving signal source with main components labelled. The width of the unit is approximately 0.40 m.

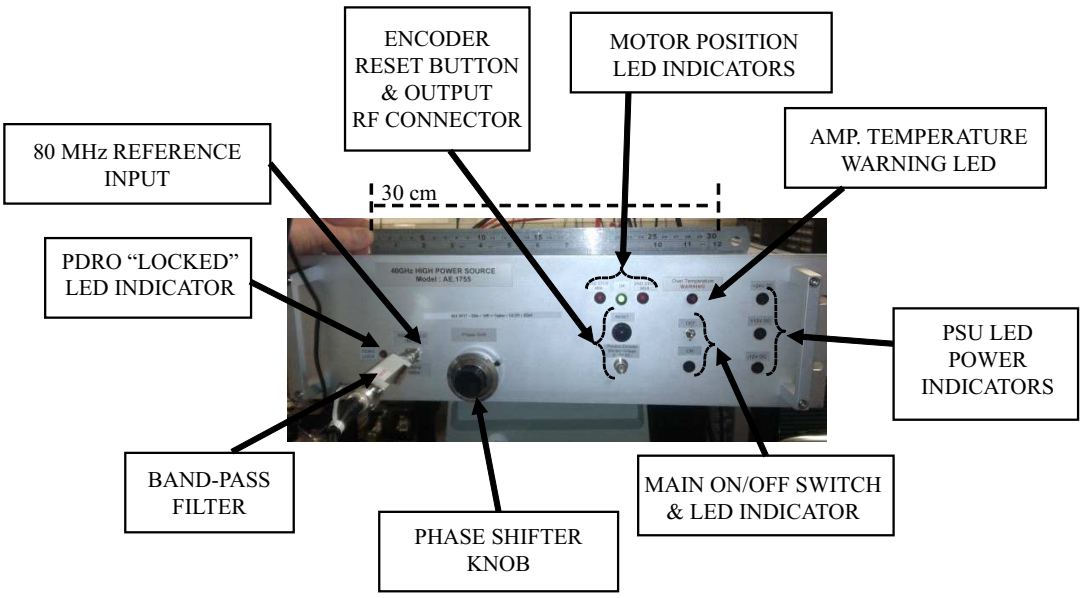

Figure 4.6: Front Panel Image of the rack-mounted 40 GHz driving signal source.

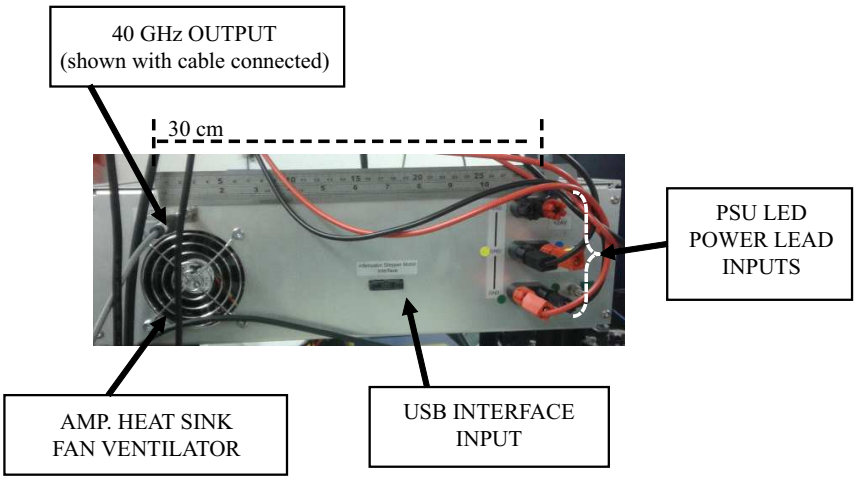

Figure 4.7: Back Panel Image of the rack-mounted 40 GHz driving signal source.

the 80 MHz Ti:Sapph oscillator pulse train. The photodiode signal was routed through a band pass filter (BPF) (ASPA, B80-3/T-6C) centred at 80 MHz ± 40 kHz to provide a reference signal with a well-defined frequency to drive the PDRO. This filtered signal was then used as an input to the phase-locked DRO (PDRO) (Herley-CTI, PRDO-4000). To achieve phase-locking between the reference and RF signal, the phase of the 80 MHz input is initially sampled by the phase detector, labelled ϕ in Figure 4.8. The feedback signal from the 40 GHz output of the circuit is also sampled. The phase detector then generates a voltage which represents the phase difference between two signals. The voltage output was used to power an LED indicator on the side of the module to alert the user to when the reference and output RF signal are phase locked. The reference signal is then passed on to the loop filter which controls the input to the DRO and ensure the phase between the two remains constant. A low pass filter is finally included to ensure only desired frequencies pass through and to eradicate reference phase noise. The PDRO thus emits a 40 GHz signal which is the 500^{th} harmonic of, and phase locked to, the 80 MHz input reference. The signal of the PDRO was output with peak voltage of 316 mV (Power = 20 mW).

The phase detector's output voltage was monitored whilst shortening and lengthening the Ti:Sapph oscillator cavity to increase and decrease the repetition rate, respectively.

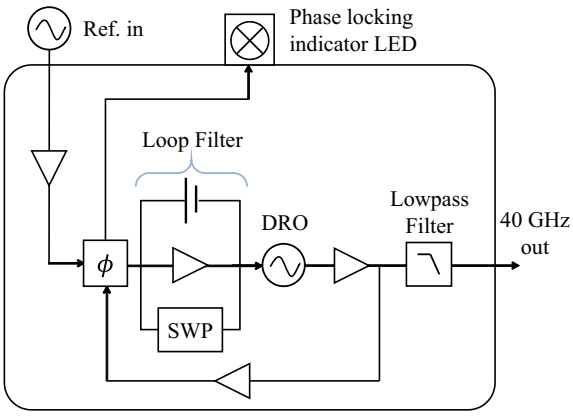

Figure 4.8: A basic circuit diagram for the PDRO is shown. A reference signal is fed into the sampling phase detector, ϕ. This also takes in a sample of the PDRO output. The phase between the two is calculated and a voltage, proportional to the phase difference of the two, emitted. This voltage powers an LED to indicate when phase-locking is achieved. Following the phase sampler, the reference signal is sent into a loop filter. This contains a sweep circuit (SWP) used to control the phase of the reference signal input to the dielectric resonator oscillator (DRO). The output of the DRO is passed through a low pass filter to remove any of the original reference signal. The circuit's resistors have been omitted for simplicity.

When the PDRO is locked with the reference signal, a voltage of 2.5 V is emitted and the LED indicator on the front panel, as labelled in Figure 4.6, is illuminated. When it is not locked, the value decreases to a few millivolts. The locking of the input reference signal, derived from the optical pulse train, and DRO output was found to remain stable, with the phase detector emitting 2.5 V, between 79.94500 and 80.00284 MHz, as read off from the Ti:Sapph laser electronics (Spectra Physics, Model 3955 and Model 3930 Lok-to-Clock®). Laboratory temperature fluctuations on the order of one degree Celsius over a period of twenty minutes were observed. Thus, it was expected that the laser cavity length may drift slightly, therefore the cavity length was set at the centre of this range, $R_\ell = 79.99700$ MHz, to ensure stable operation of the PDRO.

Phase Shifter

Exiting PDRO, the 40 GHz signal is then passed through a co-axial, low-loss, precision manual phase shifter (ATM, P28K-413), labelled ϕ-SHIFT in Figure 4.4. The unit provides a minimum of 2π of phase change with resolution of less than a $2\pi/360$ when operated at 40 GHz. This type of phase shifter is called a "line-stretcher": the length of the waveguide region is either increased or decreased, resulting in a change of the physical length of the RF transmission line[196]. The design used here a "trombone-type" line

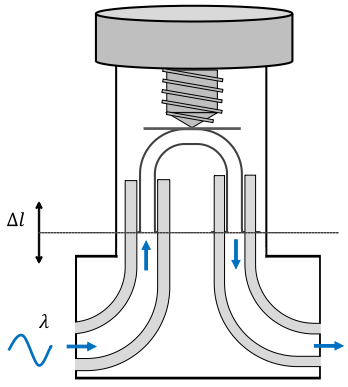

Figure 4.9: Block diagram for the trombone-type, line-stretcher, manual phase shifter. The path length of the waveguide region is increased and decreased, indicated by Δl to alter the phase of the transmitted signal.

stretcher and a basic schematic of its operation is shown in Figure 4.9. The phase offset is given by, $\Delta\phi = 2k\Delta\ell$, where k is the propagation wave-vector in the transmission line and $\Delta\ell$ is the additional length of the transmission line. The phase is controlled manually by a rotator knob that is accessed on the outside of the unit as shown in Figure 4.6.

Variable Attenuator

A variable attenuator was included in the RF source design to allow for precise control of the output driving voltage, V_{D}. This enables tunable control of the spectral manipulation. The chosen attenuator required a high-precision adjustment and, ideally, electronic control for automation. Additionally, the attenuator should maintain the phase of the signal. A "lossy wall" variable attenuator was, therefore, chosen (ATM, AT40A-3637-C40AV-06). This type of variable attenuator introduces an attenuating element into the outer walls of a coaxial waveguide. This architecture ensures constant phase length over the attenuation range. The attenuating element is moved into position by means of a screw thread, as shown in Figure 4.10. The upper diagram shows a transverse cross section of the co-axial waveguide with the attenuator only slightly introduced causing minor attenuation. The lower diagram shows maximum attenuation with the lossy wall fully inserted.

The screw controlling the variable attenuator was adapted and attached to a stepper motor (Schneider Electric Motion, MDrive17Plus: MDI1FRD17B4-N) which required a

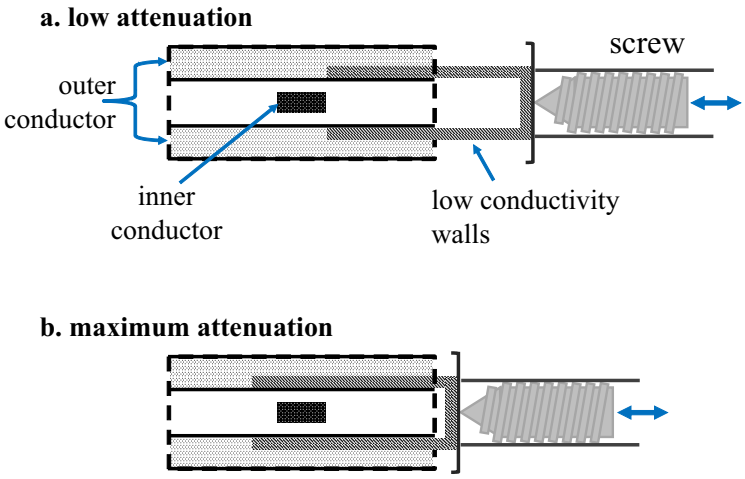

Figure 4.10: A transverse cross section of the lossy-wall type variable attenuator is shown. The top plot shows the configuration for low attenuation, with the low-conductivity walls removed from outside of the waveguiding region by means of a manual screw. In the waveguiding region are the inner and outer conductors through which the electric signal passes. In the bottom plot, the configuration for maximum attenuation is shown with the lossy-wall fully inserted.

24 V DC power supply. This motor was chosen such that small increments could be applied for precise control of the attenuation. A USB Programming cable (Schneider Electronic MD-CC400-001 USB to RS-422/485) was attached to the motor control for computer interface. An encoder was also included in the adapted variable attenuator and motor system to monitor the number of turns made. The voltage output of the encoder could be monitored concurrently with the motor control.

Throughout this work, the variable attenuator was set at a minimum attenuation to allow the highest power RF signal to be generated. The calibration and implementation of the variable-voltage facility requires further work to be fully automated and tested. For this seminal, proof-of-principle of quantum pulse shaping, this function was not required.

Amplifier

Finally, the signal was amplified using a 1 W amplifier (Quinstar, QPN-40003330-A0) with a power gain of 30 dB. This required a 12 V DC power supply. This high frequency amplifier required a large heat sink (also supplied by Quinstar) with an internal fan and

was the main source of heat and required a couple of minutes of operation to stabilize before experiments could be conducted. To minimize transmission loss, which can be detrimental at 40 GHz, the amplifier's, 40 GHz 2.92 mm RF output connector was not transmitted by cable. Instead a 2.92 mm to 2.4 mm connector (AARN, AT36A-3436) was attached to allow for direct connection to the input RF terminal of the EOM.

Driving Signal Output Power

A total output power of (9.5 ± 0.1) dBm was measured at the output of the amplifier using two 10 dB attenuators and 0.5 m of 40 GHz coaxial cable (ATM, AT38A-3436-89-01.0) with a loss rating of 3.3 dB/m. Taking this into account, it was assumed that the modulator would receive (31.15 ± 0.1) dBm, or (1.000 ± 0.001) W, of average power. The root mean square (RMS) of the sinusoidal voltage applied to the modulator, with a termination resistance of 50 Ω, was thus calculated to be $V_{\mathrm{RMS}} = \sqrt{P_{\mathrm{avg}} R} = (7.07 \pm 0.04)$ V. Finally, the driving voltage, V_{D}, is equal to the maximum sinusoidal voltage and given by $V_{\mathrm{max}} = \sqrt{2} V_{\mathrm{RMS}} = (10.000 \pm 0.005)$ V.

4.2.6 Electro-Optic Modulator Calibration

Determining the temporal phase introduced by the individual EOM requires knowledge of its half-wave voltage, V_π, at the driving frequency. The V_π is specific to each EOM, the value for the EOM used in this work was obtained by calibrating the modulator with continuous-wave (CW) laser light with central wavelength $\lambda_0 = 830$ nm. Electro-optic modulators acting on CW laser light can generate additional spectral components that are not present in the initial laser spectrum, referred to as *sidebands*. The size and distribution of these sidebands are related to the V_π, V_{D} and ω_{D} of the modulator, as detailed below.

Electro-Optic Modulation of Quasi-Monochromatic Light

A monochromatic light source has an electric field amplitude typically described by,

$$E_{\mathrm{CW}}(t) = E_0 \mathrm{e}^{i\omega_0 t}, \tag{4.11}$$

where ω_0 is the optical frequency and E_0 the complex amplitude. The inverse Fourier transform of this field yields a spectral amplitude that is a Dirac delta function centred at ω_0,

$$\tilde{E}_{\mathrm{CW}}(\omega) = \mathcal{F}^{-1}[E_{\mathrm{CW}}(t)] = \delta(\omega - \omega_0)E_0. \tag{4.12}$$

The coherence time of the CW source can thus be considered infinite. When passing through the modulator the CW light experiences the complete sinusoidal phase modulation. The effect on the CW light electric field amplitude is,

$$E_{\mathrm{mod}}(t) = E_0 \mathrm{e}^{i[\omega_0 t + \phi_0 \sin(\omega_{\mathrm{D}} t)]}. \tag{4.13}$$

The electric field can be expanded using the Jacobi-Anger identity[197],

$$\mathrm{e}^{i\alpha \sin(\theta)} = \sum_{n=-\infty}^{\infty} J_n(\alpha)\mathrm{e}^{in\theta}, \tag{4.14}$$

where $J_n(\alpha)$ is the n^{th}-order Bessel function evaluated at α. The modified CW electric field in Equation 4.13 then becomes,

$$\begin{aligned} E_{\mathrm{mod}}(t) &= E_0 \sum_{n=-\infty}^{\infty} J_n(\phi_0)\mathrm{e}^{i(\omega_0 + n\omega_{\mathrm{D}})t}, \\ &= E_0 \left(J_0(\phi_0)\mathrm{e}^{i\omega_0 t} + J_1(\phi_0)\mathrm{e}^{i(\omega_0 \pm \omega_{\mathrm{D}})t} + J_2(\phi_0)\mathrm{e}^{i(\omega_0 \pm 2\omega_{\mathrm{D}})t} + \ldots \right). \end{aligned} \tag{4.15}$$

One can see that each term contributes a different frequency component with the n^{th} term centred at $(\omega_0 \pm n\omega_{\mathrm{D}})$. These are known as the spectral sidebands. The amplitude of the n^{th} sideband is given by the n^{th}-order Bessel function, J_n, evaluated at $\phi_0 = \pi V_{\mathrm{D}}/V\pi$,

$J_n(\phi_0)$,

Thus by measuring the spectral intensity of modulated CW light one is able to deduce the value for ϕ_0, the expected phase modulation depth, and hence V_π as described in detail below.

Calibration of V_π

The experimental set up used to calibrate the modulator V_π is shown in Figure 4.11. A fibre-coupled CW laser diode module (Power Technology Inc., PPM LD1859) with central wavelength, $\lambda_0 = 830$ nm, and bandwidth, $\Delta\lambda < 0.05$ nm, was connected to the input fibre of the modulator. The 40 GHz signal was also connected to the modulator. Note that for this measurement phase locking of the RF signal with the optical field was not required. The variable attenuator was set such that the maximum driving signal was sent through the modulator. The output PMF of the modulator was then connected to the optical spectrum analyser (OSA) (as described in subsection 3.4.1) and the output spectrum measured with a resolution of $\delta\lambda = 0.003$ nm, as specified by the manufacturer.

Initially the CW spectrum was measured with the RF signal turned off to obtain the unmodulated spectrum, plotted in Figure 4.12 (blue, crosses). The RF signal was then turned on and, after stabilization of the modulator due to heating effects taking approximately two minutes, the modulated spectrum was measured, also plotted in Figure 4.12 (red circles). The central peak, labelled $n = 0$, has $N = 9$ pairs of sidebands equally spaced by 40 GHz (0.146 nm). The sideband pairs should be of equal amplitude. The amplitude, a_n, of each of the n, peaks, where $n = \{1, N\}$, located at frequency, ω_n, was extracted. The relative amplitude of these peaks was then calculated by normalizing to the central peak amplitude to give $a_{n,\mathrm{N}} = a_n/a_0$.

The EOM manufacturer provided an expected range for the half-wave voltage, 4 V $> V_\pi$,

and the driving signal voltage was previously measured as $V_{\mathrm{D}} = (10.000 \pm 0.005)$ V. Using this information, the value for V_π was then determined using the following algorithmic method:

1. An estimate of the value of ϕ_0, was made by selecting a value for the half-wave voltage, $V_{\pi,\mathrm{est}}$, within the manufacturer's given range to then calculate $\phi_{0,\mathrm{est}} = \pi V_{\mathrm{D}}/V_{\pi,\mathrm{est}}$

2. The associated predicted amplitude, α_n, for this value of $V_{\pi,\mathrm{est}}$ could then be determined by evaluating the N Bessel functions at $\phi_{0,\mathrm{est}}$.

3. The estimated amplitudes, α_n, of each of the Bessel functions can then be extracted. These were then normalized to the central peak to give $\alpha_{n,\mathrm{N}} = \alpha_n/\alpha_0$.

4. The sum of the squares of the differences between the normalized measured, $a_{n,\mathrm{N}}$ and estimated, calculated amplitudes, $\alpha_{n,\mathrm{N}}$ was determined by,

$$\Delta = \sum_n |a_n - \alpha_n|^2, \tag{4.16}$$

5. Steps 1. to 4. were then repeated until the full range provided by the manufacturer, $0 < V_\pi < 4$ V, was tested with intervals of 0.1 V.

The value of Δ will be a minimum for the estimated value of V_π that best represents the measured data's experimental set up.

The difference, Δ, was found to be a minimum for $\phi_0 = (8.8 \pm 0.1)$ radians. With a known driving voltage of $V_{\mathrm{D}} = (10.000 \pm 0.005)$ V, this implies an effective V_π of (3.57 ± 0.04) V.

4.2.7 Spectral Modification Predictions

The implication of the calibration result is that, with this equipment, and using the result from Equation 4.6, a maximum phase modulation of $\Omega \approx 2.8\pi$ is possible, equivalent to a

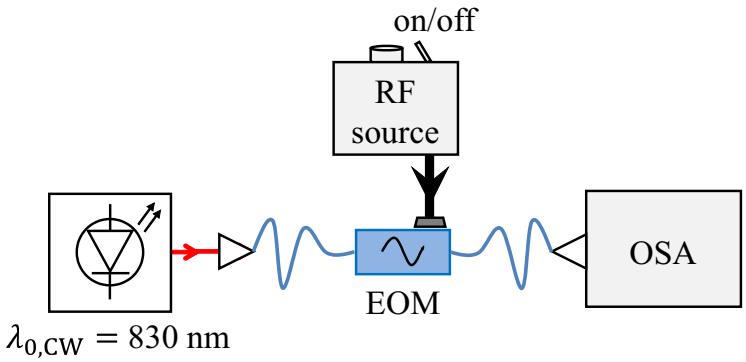

Figure 4.11: Experimental set up for calibration of the modulator (EOM) using CW light. A CW diode at 830 nm was fibre coupled into the PMF on the input of the modulator. The 40 GHz RF source was also attached to the modulator. The output fibre from the modulator was inserted into an optical spectrum analyser (OSA). Spectra were measured for the 40 GHz RF signal turned off to get the original CW laser spectrum, and then turned on, to see the sidebands generated by the modulator. The phase was not adjusted since it would have no effect in this CW case.

wavelength shift of (0.81 ± 0.01) nm at 830 nm. Furthermore, using the variable attenuator, any value from zero up to this maximum should be possible. The longest temporal durations that can be tolerated for this system are on the order of a few picoseconds. At 830 nm a temporal duration of 1 ps equates to a spectral bandwidth of 1 nm. For larger durations, the spectral bandwidth is even less. Therefore, using this method, it is possible to achieve a spectral shift on the order of the spectral bandwidth. The significance of this is the ability to shift a pulse to an orthogonal spectral mode.

For a wave packet with initial bandwidth $\Delta\lambda = 1$ nm it is expected, using the relationship derived in Equation 4.10, that the bandwidth can be expanded by approximately 1%,

$$\sqrt{1 + \left[2\frac{8.8(\omega_{\mathrm{D}}^2/2)}{\sigma^2}\right]^2} = 1.01\%. \tag{4.17}$$

The change is minor since it is extremely sensitive to the initial bandwidth. If an initial bandwidth of 0.1 nm was used, for example, there would be a 13% increase to 0.113 nm.

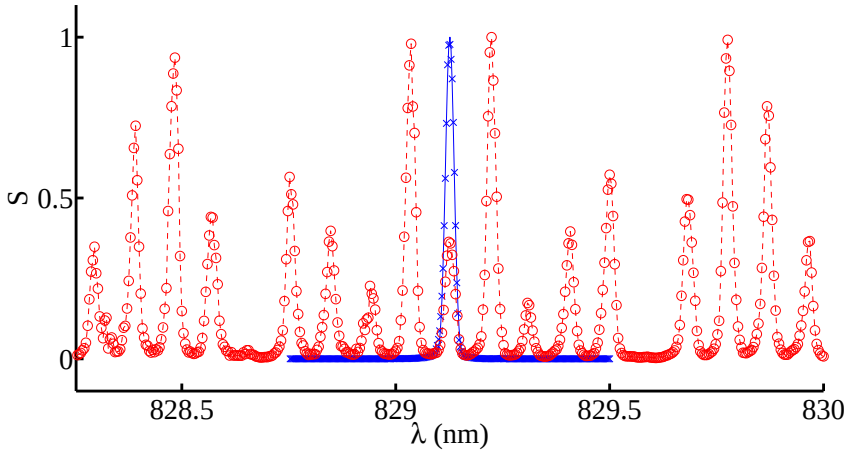

Figure 4.12: The unmodulated, CW laser spectrum (blue, crosses) and the modulated CW spectrum with sidebands (red circles) are shown. The original CW spectrum is also shown for comparison. The sidebands are equally spaced at 40 GHz (0.146 nm) frequency (spectral) intervals. The rescaled intensity measurement has been plotted: $S = I/I_{\max}$ where $I_{\max}$ is the maximum intensity of the data.

A Comment on the Linear and Quadratic Approximations

The 40 GHz RF driving signal described by Equation 4.4 is plotted in Figure 4.13 for $V_{\mathrm{D}} = 10$ V and from $t = 0$ to $3T_D/2$. A quadratic function, given by the first-order Taylor expansion of the signal centred at $\omega_{\mathrm{D}}t = \pi/4$, see Equation 4.8, is also plotted. The sinusoidal driving signal remains quadratic to within 5% of the Taylor expansion for a time window of approximately 7.3 ps. This region is indicated by the dashed purple lines around the maximum in the sine curve in Figure 4.13.

One can also approximate the temporal width of the linear region for the sinusoidal driving signal in the same way. The Taylor expansion around $t = 2\pi$, given by Equation 4.5, is also plotted in Figure 4.13. The RF driving signal is calculated to be within 5% of the linear approximation for an even smaller time window of approximately 4.2 ps, with boundaries also plotted in the figure.

From the result of these approximations, and taking into account the minimum resolution

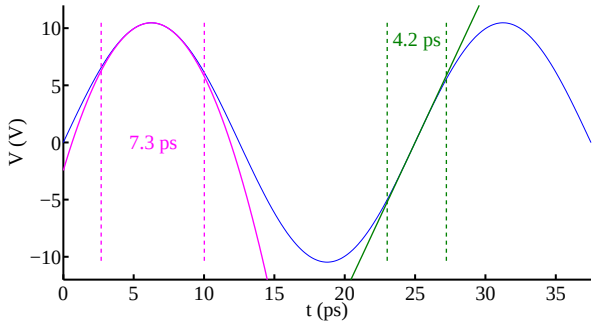

Figure 4.13: The sinusoidal driving voltage with frequency, 40 GHz, and $V_D = 10$ V is plotted in solid blue. The quadratic approximation (purple) is plotted around the first sinusoidal peak. By calculating the difference between the driving voltage and the fitted quadratic function, the temporal width during which the driving voltage was within 5% of the quadratic function was determined. This temporal width is indicated through the dashed vertical lines and is 7.3 ps. The same method was repeated but expanding the sinusoid around $\omega_D t = \pi$ to determine the a linear region (green line) in the figure. The driving voltage was found to remain within 5% of the linear approximation for a temporal width of 4.2 ps, also indicated by vertical dashed lines.

of $\delta\lambda = 0.2$ nm for the single-photon level spectral measurements using the spectrometer (CCD), the bandwidth was filtered down to approximately 1 nm. Assuming a FTL Gaussian pulse, this gives a pulse duration of 2.8 ps, suitably narrow such that the main support of the wave packet overlaps within the linear, and quadratic, regions of the driving signal.

The maximum temporal duration of wave packet that can be used with this specific modulator and driving signal, such that the assumptions that it is linear to 5% as described above hold, is 4.2 ps. For a FTL pulse, this is equivalent to a spectral width of approximately 0.47 nm. This will undergo a maximum spectral expansion of approximately twice the original bandwidth to 0.99 nm.

4.3 EOM Testing with Pulsed Optical Input

In this section, the operation of the EOM and RF driving signal system is tested with a classical pulsed optical input. This is done with attenuated laser pulses with spectral properties similar to the quantum light source described in the previous chapter. Since the technique is linear to the spectral amplitude it should act on the modes of both classical

and quantum light in the same manner. If the modulator behaves as predicted when used with the classical light, which enables faster characterization of the mode manipulation than can be achieved using quantum light, then one can apply it to the quantum source with confidence.

Initially, spectral shifting and expansion is achieved by applying linear and quadratic temporal phase to the pulsed, classical light. The spectral intensities are measured using the spectrometer and CCD system. Following this, the preservation of the coherence of the temporal wave packet is examined. This is achieved by interfering two copies of the same initial pulsed coherent laser in a Mach-Zehnder interferometer. One pulse is subject to a linear temporal phase such that it is spectrally shifted while the other mode is unmodified.

4.3.1 Wave Packet Manipulation of an Attenuated Coherent State

The experimental set up for applying the spectral manipulation technique to a classical pulsed laser is shown in Figure 4.14. The pulsed Ti:Sapph laser, used as a pump for the SHG in the single-photon source, is used as the source of classical pulsed light for testing the EOM. Thus the pulse repetition rate is equal to the quantum light source. The oscillator has a central wavelength of approximately $\lambda_0 = 830$ nm, and bandwidth on the order of $\Delta\lambda = 10$ nm. To create a similar spectral profile as the single-photon source, the laser pulse train was spectrally filtered using two bandpass interference filters (IF) (Semrock MaxLine® filter, LL01-830-12.5). The filters were orientated $\approx 3^o$ from the normal of the incident laser light, as shown in the experimental schematic in Figure 4.14. This allowed for a narrower spectral bandwidth to be achieved.

The oscillator emitted an average power of 1.5 W. The classical spectral shaping testing was to be analysed using the same methods as to be used with the single-photon source. Thus, neutral density (ND) filters were inserted into the beam path to achieve an average optical power of $P_{\text{avg}} \approx 1$ μW so as not to saturate the single-photon CCD

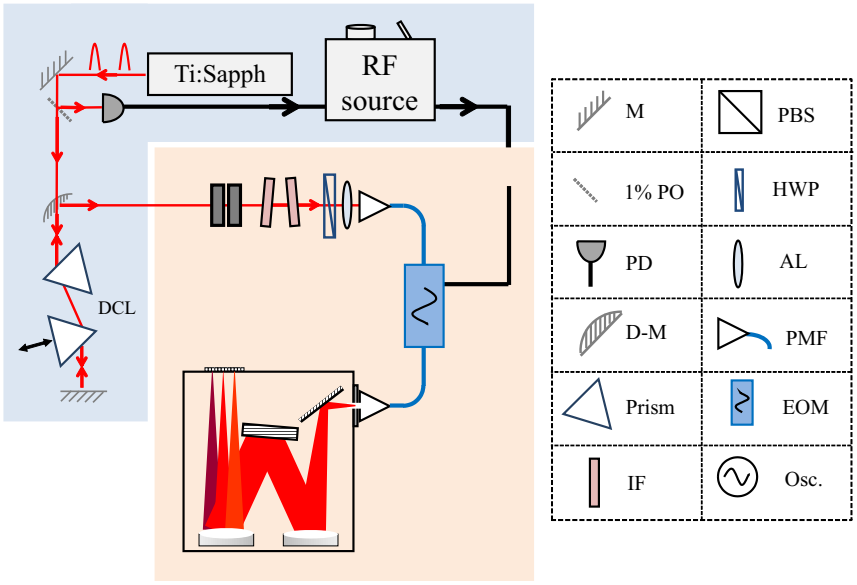

Figure 4.14: Experimental set up for the spectral measurements of the weak, coherent wave packet temporal phase manipulation. The optical wave packet is derived from the 80 MHz Ti:Sapph oscillator. The laser is then filtered both in power and spectrum using neutral density (ND) and interference filters (IF) respectively. The filtered light is then coupled into the polarization-maintaining fibre (PMF) attached to the input of the modulator (EOM) using an aspheric lens (AL). The modulator is driven using the RF source, fed by ($\approx 1\%$) optical pick-off from the original pulsed laser, detected by a photodiode (PD), to establish phase locking between the two. The fibre output of the modulator is connected to a spectrometer with a single-photon CCD at the output. The user views the spectrum on the output via the computer interface and adjusts the phase shifter on the RF GHz source accordingly to realise the linear temporal phase and quadratic temporal phase to produce spectral shift and expansion, respectively.

array or cause nonlinear effects in the PMF. Following spectral and intensity filtering, the pulsed laser light was coupled into the input, polarization maintaining fibre of the modulator. The modulator was driven by the RF source and phase locked to the coherent light. The output fibre of the modulator was attached to the spectrometer with the CCD on the output. The relative temporal alignment of the optical wave packet and the 40 GHz signal was established by manually adjusting the phase shifter incorporated in the RF source and monitoring the spectrum on the CCD.

Original Spectrum

Initially, the RF source was turned off such that no voltage was applied across the modulator and the original spectrum could be established as a base line. This measured data

is shown in Figure 4.15 (blue crosses). This data was measured for 1 ms. A central wavelength of $\lambda_0 = (829.8 \pm 0.2)$ nm and a bandwidth $\Delta\lambda = (1.2 \pm 0.3)$ nm were determined by fitting a Gaussian function to the data (blue, solid line), weighted by the error on the count. Errors are given by resolution of the spectrometer and CCD, as described in section 3.4.1. Assuming a FTL pulse this corresponds to an electric field wave packet with spectral bandwidth of $\Delta\lambda_E = (1.7 \pm 0.4)$, hence a wave packet temporal width of $\tau_E = (0.6 \pm 0.2)$ ps. Therefore, the wave packet is short enough to remain within the linear and quadratic regions of the sinusoidally varying driving voltage.

Spectral Shearing

The RF driving signal was then turned on. A positive and negative temporal linear phase was applied to the coherent state pulse train such that a blue and red shift was produced, respectively. This was achieved by manually adjusting the phase-shifter. The measured spectral intensities for this are shown in Figure 4.15(a) (red circles) plotted with the original unmodulated spectrum for comparison. Gaussian fits, weighted by the error on the count, performed on the data yielded central wavelengths for the blue and red shifted spectra of $\lambda_{0,-\Omega} = (829.3 \pm 0.2)$ nm and $\lambda_{0,+\Omega} = (830.4 \pm 0.2)$ nm, respectively. Errors are given by resolution of the spectrometer and CCD, as described in section 3.4.1. This indicates a total shift of $2\Omega_\lambda = (1.1 \pm 0.3)$ nm. However, the modulated spectral also yielded bandwidths of $\Delta\lambda_{-\Omega} = (1.3 \pm 0.3)$ nm, and $\Delta\lambda_{+\Omega} = (1.3 \pm 0.3)$ nm, approximately 10% larger than the original spectrum.

Spectral Expansion

The RF phase-shifter was adjusted once more to apply a quadratic temporal phase to the wave packet to achieve spectral bandwidth expansion. The measured intensity spectra for the wave packet under this condition is shown in Figure 4.15(b), (red circles) with the original spectrum (blue crosses), for comparison. The spectral bandwidth of the spectrally expanded wave packet was extracted as $\Delta\lambda_{\Omega^2} = (1.8 \pm 0.3)$ nm, an increase of

52% from the original bandwidth. The central wavelength was also slightly increased with $\lambda_{0,\Omega^2} = (829.9 \pm 0.2)$ nm. Errors are given by resolution of the spectrometer and CCD, as described in section 3.4.1.

4.3.2 Relative Phase Alignment Testing

When tuning the phase offset of the RF driving signal, ϕ_D in Equation 4.4, one expects to observe oscillatory shifts in the spectral profile of the modulated optical pulse. The phase-shifter was thus manually scanned such that ϕ_{D} was adjusted over a 4π range. Gaussian functions were fitted to the measured spectra, weighted by the error on the count, and the central wavelength, λ_0, and spectral bandwidth, $\Delta\lambda$, extracted. Plots of the central wavelength and the bandwidth as a function of relative phase are shown in Figure 4.16(a) and Figure 4.16(b), respectively (blue crosses). Here, the phase offset, ϕ_D, is zeroed at the beginning of the scan, thus the relative phase value is plotted.

A maximum spectral shift is expected when the optical wave packet is aligned with a linear region of the RF signal. This alignment induces the maximum linear temporal phase due to the maximum gradient. Hence, over the scan, one would expect to see two maximum spectral shifts corresponding to the negative and positive linear regions. This is indeed seen in Figure 4.16(a): as ϕ_{D} initially increases, the central wavelength shifts from the original, unmodulated value (indicated by the central, blue, dotted line) to a maximum when it is red-shifted, then back to the original value. As ϕ_{D} increases further, the central wavelength continues to decrease reaching the minimum, blue-shifted value before returning to the original central wavelength.

At the locations where the wave packet's central wavelength returns to its original value the wave packet is temporally aligned with the quadratic regions of the RF signal. In these regions one expects the wave packet to undergo spectral expansion. Furthermore, recall from Equation 2.31, applying both negative and positive quadratic temporal phase

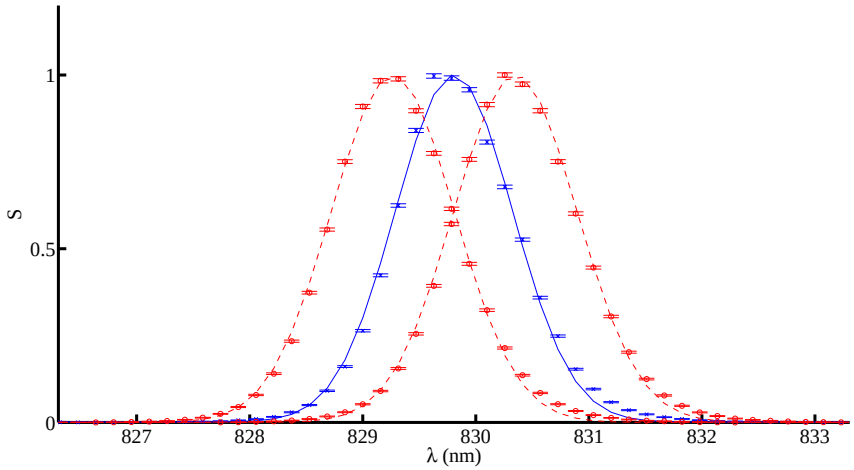

(a) Unmodulated (blue crosses) and Spectrally Shifted (red circles) Intensity Spectra.

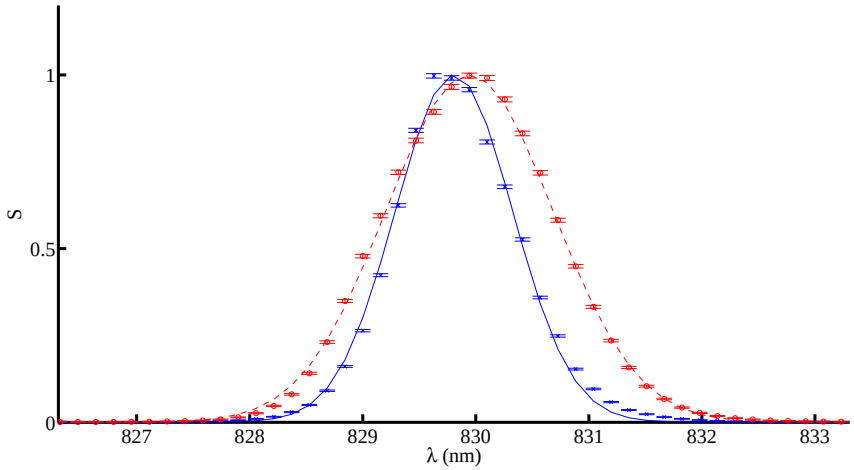

(b) Unmodulated (blue crosses) and Spectrally Expanded (red circles) Intensity Spectra.

Figure 4.15: (a) The original pulsed wave packet data (blue crosses) and its Gaussian fit (blue, solid line) are plotted. A central wavelength of $\lambda_0 = (829.8 \pm 0.2)$ nm and bandwidth $\Delta\lambda = (1.2 \pm 0.3)$ nm were extracted. The measured spectra for the wave packet with negative and positive linear temporal phase applied are also plotted (red circles). Gaussian fits were also performed on this data giving, $\lambda_{0,-\Omega} = (829.3 \pm 0.2)$ nm, $\Delta\lambda_{-\Omega} = (1.3 \pm 0.3)$ nm and $\lambda_{0,+\Omega} = (830.4 \pm 0.2)$ nm, $\Delta\lambda_{+\Omega} = (1.3 \pm 0.3)$ nm, respectively. **(b)** The original wave packet (blue, solid line) is plotted again alongside the spectrally expanded wave packet with $\lambda_{0,\Omega^2} = (829.9 \pm 0.2)$ nm and $\Delta\lambda_{\Omega^2} = (1.8 \pm 0.3)$ nm extracted from the Gaussian fit. Note in both plots, the rescaled intensity measurement has been plotted: $S = I/I_{\max}$ where $I_{\max}$ is the maximum intensity of the data, for easy comparison.

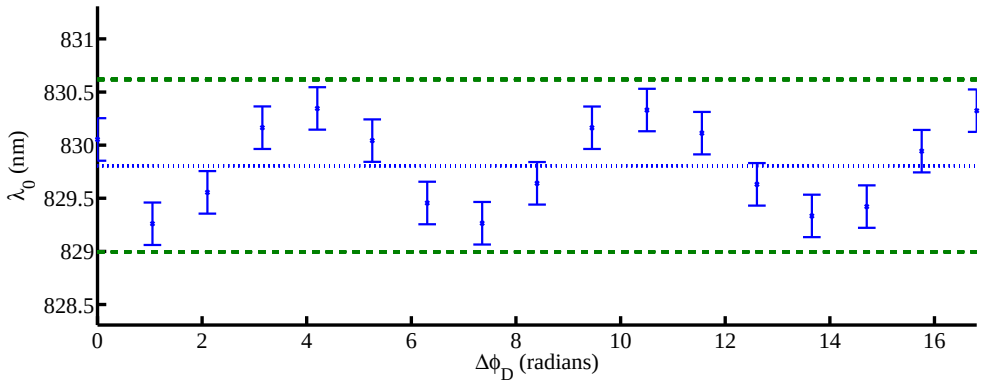

(a) Central Wavelength vs. Phase Offset

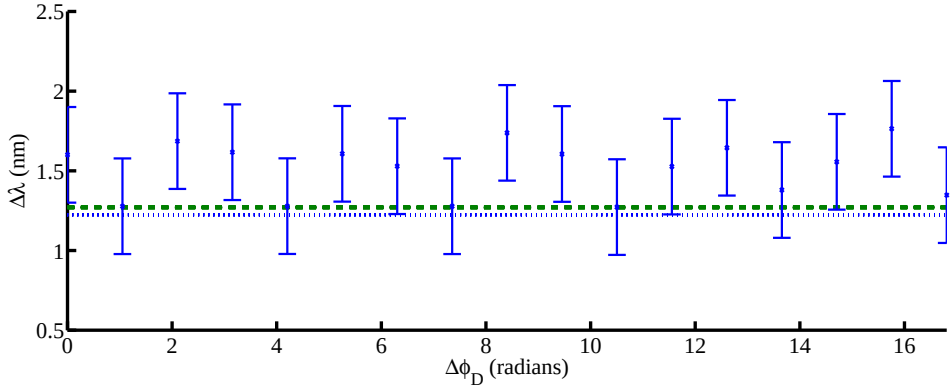

(b) Spectral Bandwidth vs. Phase Offset

Figure 4.16: The relationship between the central wavelength, λ_0 and relative phase $\Delta\phi$ of the optical and driving voltage signals is plotted in **(a)** and shows oscillatory spectral shifting, as expected. The bandwidth, $\Delta\lambda$ versus $\Delta\phi$, shown in **(b)**, also displays an oscillating relationship but with twice the frequency, as expected since both negative and positive quadratic temporal phase results in expansion. The predicted spectral shifts and expansion is also indicated in each plot by a dashed green line. This prediction is calculated using the known and experimentally calculated parameters of the system. Note, the vertical error bars for the central wavelength are given by ± 0.2 nm and ± 0.3 nm for the central wavelength and spectral bandwidths, respectively.

result in identical spectral expansion. Therefore, plotting the spectrally manipulated wave packet spectral bandwidth versus $\Delta\phi_{\mathrm{D}}$, one expects to see an oscillation which is $\pi/2$ out of phase with the variation of λ_0 versus $\Delta\phi_{\mathrm{D}}$ and with twice the oscillation frequency. This is indeed what is seen in Figure 4.16(b).

The unmodulated spectrum's central wavelength and spectral bandwidth are indicated on their respective plots by dotted, blue horizontal lines. The predicted FWHM and

spectral shifts, calculated using Equation 4.6 and Equation 4.9 respectively, are indicated by horizontal, green, dashed lines in Figure 4.16. The propagated error boundaries are also plotted (fainter green dashed lines). These errors arise from the uncertainty of the half-wave voltage and peak driving signal.

The maximum spectral shift of the central wavelength and the spectral bandwidth modulation observed differ from those values predicted at the end of subsection 4.2.7. The maximum spectral shifts, (0.6 ± 0.2) and (0.5 ± 0.2) nm, are only two thirds of what was predicted, (0.81 ± 0.05) nm. Furthermore, the spectral expansion was 42%, far exceeding the predicted 4%. The spectrally shifted spectra also demonstrated expansion.

It is understood that the primary reason for the difference between the observed and predicted behaviour comes from the imperfect locking of the RF signal to the optical pulse train. This will be explored in more detail in section 4.5 after examining the optical wave packet temporal coherence following temporal modulation, below.

4.4 Wave Packet Coherence Testing

A key requirement of the pulse shaping technique is that it induces temporal phase as expected. In the context of the temporal phase modulation technique implemented here this means it must induce either a linear or quadratic form to controllably change the wave packet's spectral amplitude. It must not alter the spectral phase profile of the state in any unknown manner. If other forms of phase are added this can change the wave packet shape. From the results above, it is clear that the phase modulation technique produces the desired spectral shift and bandwidth expansion. However, one cannot tell from this data whether there is additional temporal or spectral phase change, since the intensity measurement does not allow access to the phase. The spectral phase must be probed indirectly.

In this section, the spectral phase preservation of the wave packet is demonstrated through interference of spectrally identical copies of the classical wave packet in a Mach-Zehnder interferometer (MZI). One copy is then subject to spectral manipulation using the temporally-varying phase modulation technique. The interference visibility in a MZI, V_{MZI}, is dependent on the fidelity of the interfering pulses, as described in more detail below. If the reduction in measured visibility is equal to the expected reduction due to spectral distinguishability alone, one can be confident that no unknown phase has been added to the modulated pulse.

4.4.1 Theory

Consider an electric field wave packet of the form: $E(t) = E_0(t)\mathrm{e}^{i\omega_0 t}$, transmitted into an interferometer, where $E_0(t)$ describes the wave packet temporal envelope. If one labels the two paths as A and B, and includes a temporal delay, τ, in path B, then, up until the point they reach the second beam splitter for interference, the two electric fields will be of the form, $E_{\mathrm{A}}(t) = E_0(t)\mathrm{e}^{i\omega_0 t}$, and $E_{\mathrm{B}}(t) = E_0(t+\tau)\mathrm{e}^{i\omega_0(t+\tau)}$, respectively. This assumes the path lengths are identical and have no other phase difference. The temporal intensity, $I(t)$, measured on one output of the fibre beam splitter will be proportional to the square of the sum of the fields such that,

$$\begin{aligned} I(t) \propto & |E_{\mathrm{A}}(t) + E_{\mathrm{B}}(t)|^2, \\ \propto & \Big(I_{\mathrm{A}}(t) + I_{\mathrm{B}}(t) + 2\,\mathrm{Re}\left[E^*_{\mathrm{A}}(t)E_{\mathrm{B}}(t)\right]\cos\left(\omega_0\tau\right)\Big), \end{aligned} \tag{4.18}$$

where $I_\mu(t) = E^*_\mu(t)E_\mu(t)$ for μ = A,B. Thus, on the output one expects to measure interference fringes with oscillation period $2\pi/\omega_0$. The visibility of these interference fringes can be determined by finding the maximum intensity, $I_{\max}(t)$, and the minimum intensity, $I_{\min}(t)$, of the fringes and using these to calculate,

$$V_{\mathrm{MZI}}(t) = \frac{I_{\max}(t) - I_{\min}(t)}{I_{\max}(t) + I_{\min}(t)}. \tag{4.19}$$

Using the definition of the measured fringe intensity above is possible to show that the visibility of these fringes, V_{MZI}, is equal to the real part of the spectral overlap. First by determining the expected maximum and minimum intensities,

$$I_{\max}(t) \propto \Big(I_{\mathrm{A}}(t) + I_{\mathrm{B}}(t) + 2\,\mathrm{Re}\left[E^*_{\mathrm{A}}(t) E_{\mathrm{B}}(t)\right] \Big),$$
$$I_{\min}(t) \propto \Big(I_{\mathrm{A}}(t) + I_{\mathrm{B}}(t) - 2\,\mathrm{Re}\left[E^*_{\mathrm{A}}(t) E_{\mathrm{B}}(t)\right] \Big),$$

and substituting them into the Equation 4.19 above,

$$V_{\mathrm{MZI}}(t) = \frac{2\,\mathrm{Re}\left[E^*_{\mathrm{A}}(t) E_{\mathrm{B}}(t)\right]}{I_{\mathrm{A}}(t) + I_{\mathrm{B}}(t)}, \tag{4.20}$$
$$= \mathrm{Re}\left[\int \tilde{E}^*_A(\omega) \tilde{E}_B(\omega) d\omega \right]. \tag{4.21}$$

Here, it has been assumed that the measurement in time implies a sum over all frequencies, $\int_{-\infty}^{\infty} d\omega$. In the second line an integration over spectrum has been included where $\int_{-\infty}^{\infty} I_A(t) d\omega = 1$ and similarly for I_B.

Therefore, by determining the spectral overlap and measuring the interference visibility for a modulated wave packet, and showing that these agree, one is able to show that the pulse-shaping method presented in this work preserves the single-mode nature of the input wave packet.

The MZI measurement is commonly used to investigate the first order correlation of a wave packet. In subsection 2.2.3 the second-order coherence was discussed since it provided information about the photon-number statistics of a source of light. Conversely, the first order coherence allows one to determine the coherence time, τ_{c}, of two wave packets. This is the time over which the phase relation between the two wave packets is well-defined.

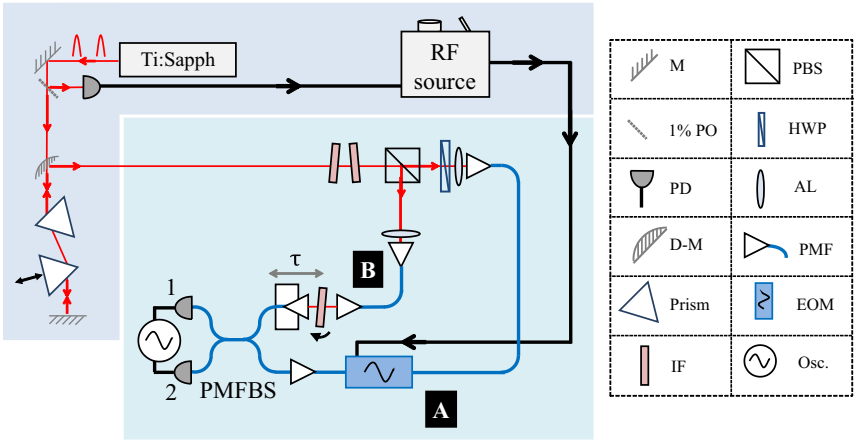

Figure 4.17: Experimental set up for the spectral phase preservation testing of wave packets is shown. The Ti:Sapph oscillator is spectrally filtered using two interference filters (IFs) and split to two arms, A and B, using a polarizing beam splitter (PBS). The optical paths are fibre-coupled into polarization maintaining fibres (PMFs) using aspheric lenses (ALs). One of the two PMFs, arm A, is connected to the PMF input of the modulator (EOM). The EOM is driven by the RF source which is, itself, fed by a small ($\approx 1\%$) optical pick-off from the original Ti:Sapph, measured using a photodiode (PD). The output of the EOM is incident on one of two inputs of a polarization-maintaining fibre beam splitter (PMFBS). The second arm, arm B, contains the reference wave packet. This wave packet is transmitted through another IF and re-coupled into the fibre on the other input of the fibre beam splitter. This fibre is, additionally, mounted on a linear translation stage to lengthen that arm and introduce a temporal delay, τ. The two output arms of the beam splitter are connected to photodiodes (PD1 and PD2) for detection and their signal measured using a fast oscilloscope (Osc.).

The first order correlation function is defined as,

$$g^{(1)}(\tau) = \frac{\langle E^*(t)E(t+\tau)\rangle}{[\langle E^2(t)\rangle \langle E^2(t+\tau)\rangle]^{\frac{1}{2}}}, \tag{4.22}$$

assuming identical spatial modes. For the Gaussian wave packet here with temporal electric field wave function as defined in Equation 2.26, this becomes,

$$g^{(1)}(\tau) = \mathrm{e}^{-\frac{\tau}{\tau_c}}\mathrm{e}^{\omega_0\tau}. \tag{4.23}$$

One can see this equation contains an oscillatory term, describing the fringes, and an amplitude term, describing the envelope with a width related to the temporal coherence of the two. This is the final term in the equation above, Equation 4.18 describing the measured intensity at the output of the interferometer.

4.4.2 Experimental Set Up

The experimental set up for the measurement of the wave packet coherence is shown in Figure 4.17. The wave packets are generated from the Ti:Sapph oscillator which is passed through a dispersion compensation line (DCL) to create a FTL pulse, before being spectrally filtered using two interference filters (IFs) (Semrock MaxLine® filter, LL01-830-12.5). A 50:50 polarizing beam splitter (PBS) is used to divide the light intensity equally into two arms, labelled A and B. A half wave plate (HWP) is included at the input of arm A to allow polarization matching of the wave packets for high visibility interference. The output of the beam splitter into arm A is fibre-coupled to the polarization-maintaining fibre on the input of the EOM. The other wave packet is fibre-coupled into a second collection polarization-maintaining fibre.

The wave packet, in arm A, is transmitted through the EOM with the output fibre connected via an FC/PC to FC/PC connector (OzOptics PMPC-03) to one of two inputs of a polarization-maintaining fibre beam splitter (PMFBS) (OzOptics, Fused-22-830-5/125-50/50-3S3S3S3S-1-0.5-PM). The second wave packet, in arm B, is collimated using a variable collimation package (Thorlabs, CFC-11X-B, focal length, $f = 11.0$ mm, AR for 650-1050 nm) as it exits the original collection fibre and passes through a third interference filter (same as above) before being coupled into the second input of the polarization-maintaining fibre beam splitter using an aspheric lens and fibre-coupling stage. This second input to the beam splitter is mounted on an electronically controlled linear translation stage to extend the length of arm B and introduce a temporal delay, labelled τ in Figure 4.17.

With path lengths matched for both arms, the two wave packets then interfere in the fibre beam splitter. The output arms of the fibre beam splitter are connected to two photodiodes (PD1 and PD2) (Thorlabs, DET10A, 200-1100 nm) and the resultant electronic signals sent to a fast oscilloscope (Tektronix, MSO5104) for data acquisition.

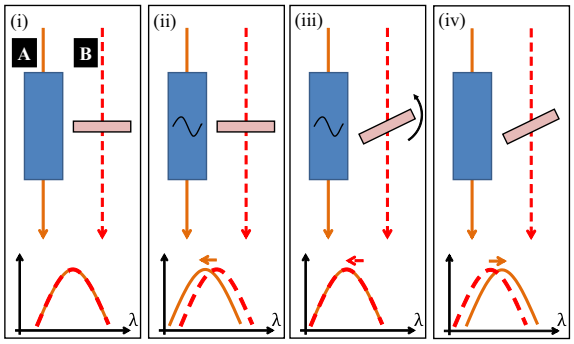

Figure 4.18: This basic schematic summarizes the four wave packet cases that were tested using the MZI. In (i), the RF source is switched off and arms A and B are spectrally matched to achieve very high visibility interference. In (ii), the RF source is turned on so that the wave packet in A undergoes a negative linear temporal phase modulation. The wave packet therefore is blue-shifted. In (iii) the IF in arm B is rotated in order to prepare the wave packet with the same spectral profile as arm B. This is possible since a spectrally broad wave packet is typically sent into arm B such that the rotating IF only "picks out" a certain spectral profile. The spectra are therefore matched one again. Finally, in (iv), the RF source is turned off to retrieve the original wave packet in A. This is an analogue of (ii) where it is demonstrated that the reduction in visibility is due to the spectral difference alone, to verify that rotating the IF adds no additional phase.

4.4.3 Interference Measurements

The interference visibility was extracted for four spectral combinations of the two interfering wave packets. These are listed here and summarised in the schematic in 4.18,

(i) Well-matched wave packets. No phase modulation (RF source turned off).

(ii) Distinguishable wave packets. Wave packet A phase-modulated with a negative spectral shear.

(iii) Well-matched wave packets. Wave packet A phase-modulated with a negative spectral shear. Wave packet B interference filter rotated.

(iv) Distinguishable wave packets. No phase modulation (RF source turned off). Wave packet B interference filter remains rotated.

Method

For each of the four cases above, the method described here was followed. The photodiode signal was recorded whilst scanning the temporal delay between the two wave packets, τ,

in arm B at a constant rate using a scanning actuator. The photodiode signal consisted of pulses separated by 12.5 ns from the 80 MHz optical pulse train, with peak voltage of the pulse proportional to the intensity of light at the output of the fibre-beam splitter which the photodiode is monitoring. An example of this output is shown in Figure 4.19 where a measured *frame* of length 100 ns is plotted. The signal measured simultaneously by both PD1 and PD2 is shown. Note, the signals were corrected for varying detector efficiencies and splitting ratio of the beam splitter.

To determine the visibility of interference, one needed to extract the temporal interference fringes. The time period of the fringes is related to the speed of the stage divided by the optical wavelength and here is roughly 27 ms. Frames of length 200 ns, were measured every $40-100$ μs. Owing to memory capabilities of the oscilloscope, a total of 6125 frames were recorded at one time. Measurement times of between 250 and 600 ms were achieved.

A value for the voltage, proportional to the optical signal in each arm, was determined for each frame of duration 200 ns. During this time the optical signal is assumed not to vary. In each frame, the individual pulses were integrated, as indicated in Figure 4.19, and a value for the integrated voltage, V, determined. The average of all integrated pulses in each frame was then used as the voltage detected by the photodiode for that duration of time (200 ns), $V_{\rm av}$. This method was repeated for all 6125 frames. A plot of the average of the integrated voltages for each frame, $V_{\rm av}$, versus the temporal delay between the wave packets, τ, thus reveals the measured temporal interference fringes. For the first measurement with well-matched wave packets, the fringes are shown in Figure 4.20(a) for a duration of one millisecond. Note, for clarity, a portion of the 6125 integrated frames have been omitted.

The interference visibility, $V_{\rm MZI}$, was determined by first fitting a sinusoidal function,

of the form,

$$f = a\sin(b\phi_D + c) + d, \tag{4.24}$$

using a least squares estimate method, to both sets of fringes with the condition that they have the same period of oscillation. Using the maximum and minimum of the fitted function the visibility was calculated using Equation 4.19. The error on the visibility is propagated through from the uncertainties on the fit. These were given by the two sigma confidence interval of the fit to the data.

The intensity spectra of the wave packet in each arm, $\tilde{I}_{\mathrm{A(B)}}(\omega) \propto |\tilde{\psi}_{\mathrm{A(B)}}(\omega)|^2$, were also measured using the spectrometer and CCD array with measurement details as given in section 3.4.1. The output from one arm of the fibre beam splitter was connected to the fibre input of the spectrometer and the intensity spectrum of each arm measured whilst the other input arm was blocked. Gaussian functions, of the same form as in Equation 3.12, were fitted to each of the spectra and the central wavelength and spectral bandwidths were extracted. The fits were weighted by the error on the data, given by Poissonian statistics where a CCD detection of N photons has an error given by $\sqrt{N}$.

For each of the four measurements listed above, the extracted interference fringes are measured spectral intensities are plotted in Figure 4.20. The extracted visibility and spectral properties are summarised in Table 4.1.

Spectral Overlap

To test the assumption that the temporal phase modulation introduces no additional spectral phase, the spectral overlap of the two interfering spectra was calculated. In the case that the wave packets have a flat spectral phase, as expected here, one can mathematically demonstrate that the spectral overlap is equal to the interference visibility, Equation 4.21. This is a maximum since it acts as an upper bound on the expected

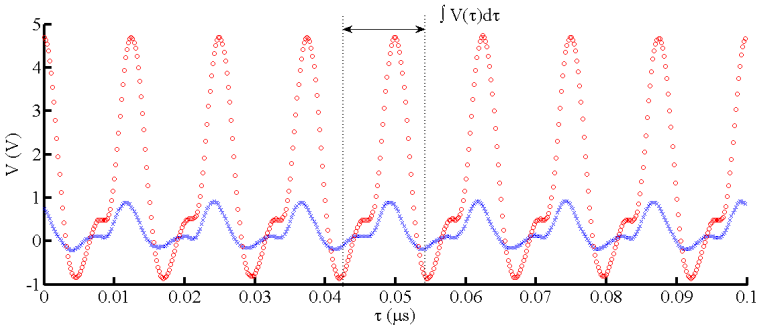

Figure 4.19: A sample interference signal measured on the oscilloscope from the two photodiodes, V_1 (red circles), and V_2 (blue crosses), during the MZI interference measurement are shown. The voltage measured is plotted versus the temporal delay, τ, scanned during the MZI interference measurement. The typical photodiode impulse response from a fast signal is seen, characterized by a pre-pulse region, a sharp increase to maximum and ringing. The voltage for each 12.5 ns pulse is calculated by integrating the signal in the region indicated by the vertical lines. The MZI arms are seen to be π out of phase.

interference visibility. The normalized spectral wave function amplitude, $\tilde{\psi}_{\mathrm{A(B)}}(\omega)$, was approximated using,

$$\tilde{\psi}_{\mu}(\omega) = \sqrt{\frac{\tilde{I}_{\mu}(\omega)}{\sum \tilde{I}_{\mu}(\omega)}}, \tag{4.25}$$

where μ = A,B. Thus, by extracting the interference visibility and showing it is equal to the estimated spectral overlap, one can demonstrate there is no additional spectral phase introduced by the temporal phase modulation technique.

The estimated visibility was numerically calculated using the spectral overlap, Equation 4.21, by replacing the $\tilde{\psi}_{\mathrm{A}}(\omega)$ and $\tilde{\psi}_{\mathrm{B}}(\omega)$ in Equation 4.21 with two Gaussian functions with spectral parameters of the interfering wave packets. The numerical calculation was then performed using a Monte Carlo simulation to randomly assign a value for the central wavelength and bandwidth using the error given on the fit of the spectral parameters. A total of 10^4 calculations were performed and the average determined. This estimated visibility is also included in the summary in Table 4.1.

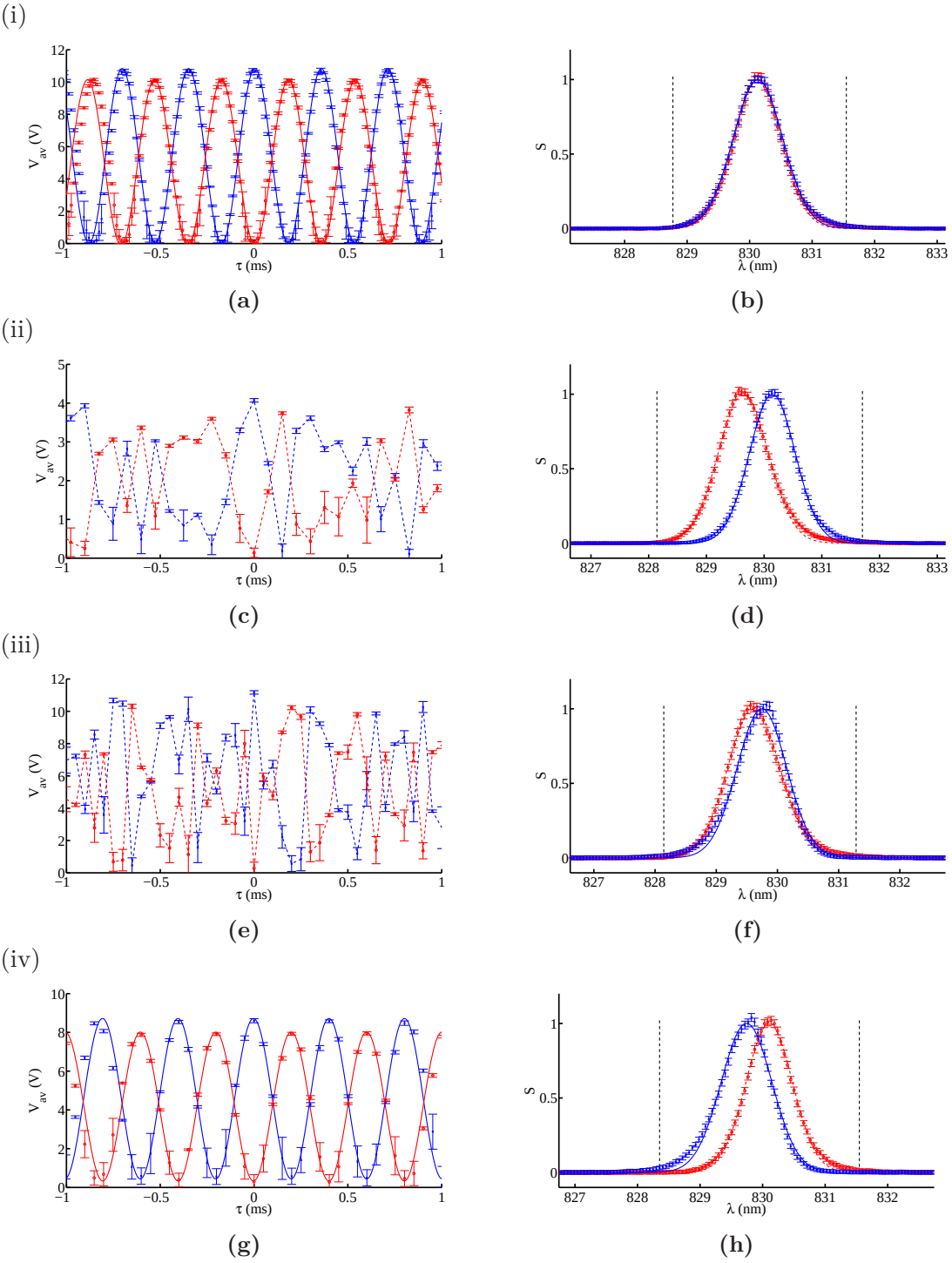

Figure 4.20: Four sets of temporal interference fringes (left) and the associated interfering wave packet intensity spectra (right) are shown. For the temporal interference fringes, blue crosses and red circles indicate the two output signals and τ is the relative temporal delay of the two arms. The rescaled intensity measurement has been plotted: $S = I/I_{\max}$ where $I_{\max}$ is the maximum intensity of the data, for comparison. Refer to the main text for extracted visibility and spectral properties.

	Signal		Idler		$\langle\psi_s\|\psi_i\rangle$		V_{MZI}		
	λ_0 (nm)	$\Delta\lambda$ (nm)	λ_0 (nm)	$\Delta\lambda$ (nm)	Data (%)	M-C (%)	Env. (%)	Sin (%)	τ_c (ps)
(i)	830.1	0.9	830.1	0.9	99.9(1)	99.9(1)	105	101(5)	1.95
(ii)	829.6	1.0	830.1	0.9	74.7(3)	83.2(1)	97	-	2.32
(iii)	829.6	1.0	829.7	0.9	98.1(1)	98.7(1)	95	-	2.18
(iv)	830.1	0.9	829.7	0.9	78.2(3)	89.5(1)	89.7	91(6)	2.05

Table 4.1: A summary of the measured spectra parameters: the central wavelength, λ_0, and the bandwidth, $\Delta\lambda_0$, and the predicted spectral overlap, $\langle\psi_A|\psi_B\rangle$, are given with the extracted interference visibility. The visibility, V_{MZI} was determined using two methods: 1. a fit to the first order coherence enveloped (labelled Env.) and 2. using a sinusoidal fit to the interference fringes (labelled Sine). Finally, the temporal width of the coherence envelope is given, τc. The error on all central wavelength values, λ_0, is ± 0.2 nm and the error on all bandwidth values, $\Delta\lambda$, is ± 0.3 nm, given by resolution of the spectrometer and CCD, as described in section 3.4.1.

4.4.4 Spectral Coherence Analysis

Immediately one sees a striking difference in the interference fringes when the EOM is turned on from when it is off, plotted in Figure 4.20(c) and Figure 4.20(e). The fringes appear to have been lost, however, on closer inspection, one can still observe small regions of interference on the order of tens of microseconds but with discontinuous phase jumps. Since a sinusoidal function could no longer be fitted to the interference fringes for measurements (ii) and (iii) the visibility was instead extracted using the full interference envelope instead.

The interference envelope for the MZI measurements (ii) and (iii) are shown in Figure 4.21. These are the same data as plotted in the fringes in Figure 4.20 but on a longer time scale.

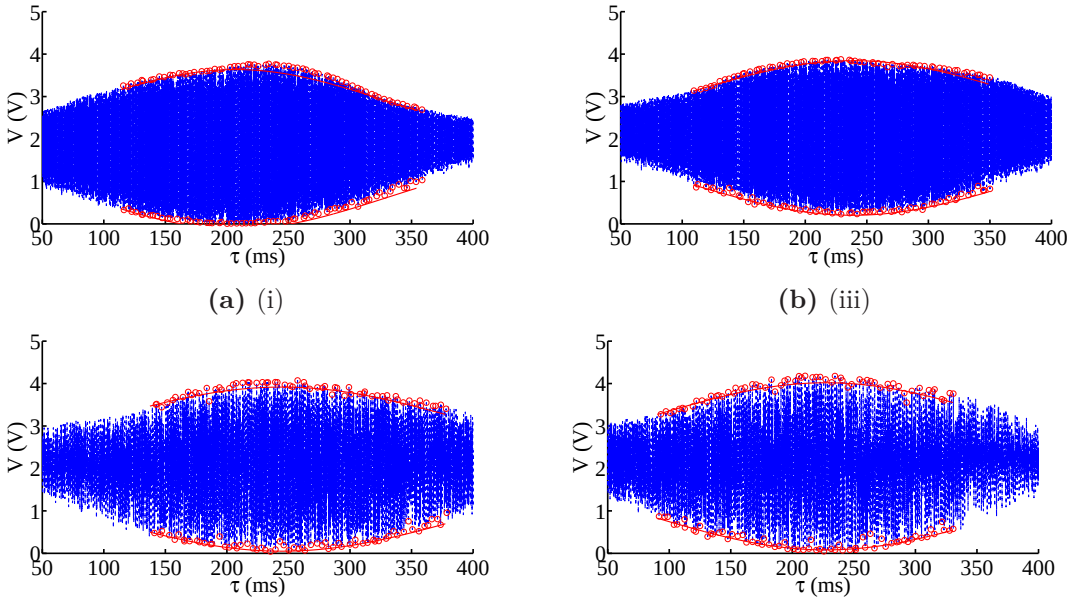

Figure 4.21: MZI fringes for the cases (ii) and (iii) for which one of the interfering wave packets was temporally phase modulated by the EOM. The full temporal envelope of the interference is measured. Gaussian fits were performed on the envelope to extract the interference visibility.

The interference fringes mapped out the interference envelope at the peaks and troughs of the fringes. An algorithm was thus established to extract the envelope data points of these fringes, as follows. The total data set was 6125 points long. This was split into smaller windows containing 50 data points. Within this window, the maximum and minima of the data set were identified. These selected maxima were grouped together, and the same done for the minima. As such, one extracted two sets of data representing the upper and lower bounds of the interference envelope. The selected data is indicated by small red rings in Figure 4.21. A Gaussian function of the form,

$$G_{\pm}(\tau) = \pm A \mathrm{e}^{-\frac{(\tau-\tau_0)^2}{2\sigma_\tau^2}} + B + C\tau, \tag{4.26}$$

was fitted to the two data sets concurrently, where $\pm$ refers to relative sign of the fit applied to the maximum and minimum data sets, respectively. Here A, corresponds to the height of the Gaussian, B to the constant offset and C the gradient due to account for any optical

drifting as the linear stage was scanned. During the fit, the parameters were constrained to be equal for both sets of data. This was repeated for the fringes measured on both photodiodes, PD1 and PD2. Furthermore, the fit was only performed over $V_{\max} \pm 120ms$ where $V_{\max}$ was found to be the maximum of the data, outside of this region the Gaussian form was degraded due to optical alignment instabilities.

The maximum and minimum voltages at the centre of the interference envelope were extracted from the Gaussian fit to calculate the visibility. This was done for both sets of data from both photodiodes. An average visibility of $\langle V_{\mathrm{MZI}} \rangle = 97\%$ for data set (ii) and $\langle V_{\mathrm{MZI}} \rangle = 95\%$ for data set (iii) was found. This was also done for the first and last fringes for comparison. All four values are given in Table 4.1.

The width of the envelope was also extracted from the Gaussian fit and calculated by converting this into width of pulse using the stage velocity. These are listed in Table 4.1 and are on the order of 2 ps. One can see that there is a slight increase in coherence time for the modulated wave packets. Once the temporal modulation has been removed, the coherence time decreases.

The results can be summarized by plotting the interference visibility versus the spectral overlap as is done in Figure 4.22. One can see there is a positive trend between the spectral overlap and visibility as expected. Added to the plot is the expected trend, $V_{\mathrm{MZI}} = \langle \psi_A | \psi_B \rangle$. Since the two wave packets travel down different arms, one might suspect their to be a spectral phase difference between the two. Moreover, it is likely that the MZI interference visibility was systematically overestimated, as indicated by the extraction of visibilities of over 100%. This may be a result of noise voltage in the system. Nonetheless, the general trend is as expected.

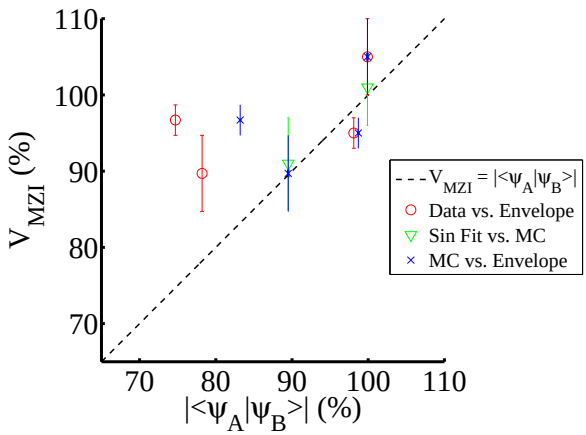

Figure 4.22: The spectral overlap, $\langle\psi_A|\psi_B\rangle$, is plotted against the MZI visibility. The black dashed line indicates the expected directly proportional relationship, with gradient of one.

Fringe Instability: Possible Explanation

To investigate the observed unstable fringes further, a constant temporal delay between the two wave packets was chosen, within the region of temporal overlap of the wave packets, and the output signal on the two photodiodes measured. A sample of these, for a duration of 100 μs, are shown in Figure 4.23. The variation of signal strength from the maximum to the minimum voltage on one photodiode, hence a π phase shift, occurs over a period of a few microseconds. This is much faster than can be accounted for by mechanical vibrations in the MZI. Nonetheless, there appear to be small regions of stability in between the phase switching. One can make out modes of oscillation: recurring voltages where the voltage appears constant (as expected for this time period during the temporal interference), if only for short time periods. These modes have been indicated by dashed, black horizontal lines in Figure 4.23.

A Fourier transform was performed on the phase-discontinuous interference signal to analyse its temporal structure. This is plotted in Figure 4.24. One can see the main peak just under 80 MHz corresponding to the repetition rate of the laser which was set at $R_L = 79.997$ MHz, as detailed in subsection 4.2.5. Subsidiary peaks appear at regular

intervals around the central peak, separated by approximately 29 kHz.

The reference frequency of the PDRO, intrinsic to the dielectric resonator oscillator, is 80 MHz. The reference signal driving the EOM, R_L, was set ≈ 30 kHz below this factory setting. The author, therefore, proposes that there may be a resonance effect present within the PDRO causing this instability. This laser repetition rate was set as such since, monitoring the voltage output of the phase sampler in the PDRO as described in subsection 4.2.5, its operation was found to be the most stable reference frequency for phase-locking the PDRO. Nonetheless, there may be more subtle effects occurring due to this detuning which are revealed in the instability of the quick measurements made in the MZI.

The effect of the random phase discontinuities observed is akin to a very fast vibrating mirror in the interferometer. It merely washes the fringes out, however, within the time frame of measurement, the interference can still be measured and it can be confidently assumed that the spectral pulse shaping technique preserves the spectral phase relationship across the wave packet (within minor optical discrepancies due to the non-identical optical paths in the two arms).

4.5 Temporal Jitter

The results in this chapter indicate that it is possible to coherently control the wave packet structure of light using this approach of temporal phase modulation with an EOM. However, the experimental results show deviation from the ideal operation. When attempting to implement a linear temporal phase for spectral shifting, the shifts achieved were only 66% of the predicted. Furthermore the measured bandwidth was also expanded from (1.2 ± 0.3) nm to (1.3 ± 0.3). The bandwidth expansion achieved when applying a quadratic phase was also an order of magnitude larger than predictions. The Mach-Zehnder

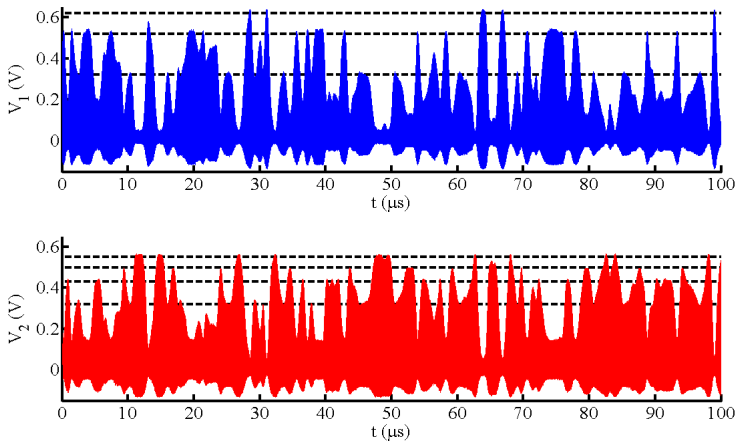

Figure 4.23: The raw photodiode signal from both outputs of the MZI are shown as a function of measurement time. The MZI's temporal delay has been set at a specific position to monitor the stability of the interference. One can see there appear to be phase jumps with the relative phase of the two arms changing on the order of tens of microseconds. What appear to be "preferred" modes of oscillation have been highlighted by the black, dashed horizontal lines. These levels indicate voltage ratios, which are repeatedly returned to and stable for a few microseconds. These can be interpreted as relative phase settings of arms A and B in the MZI.

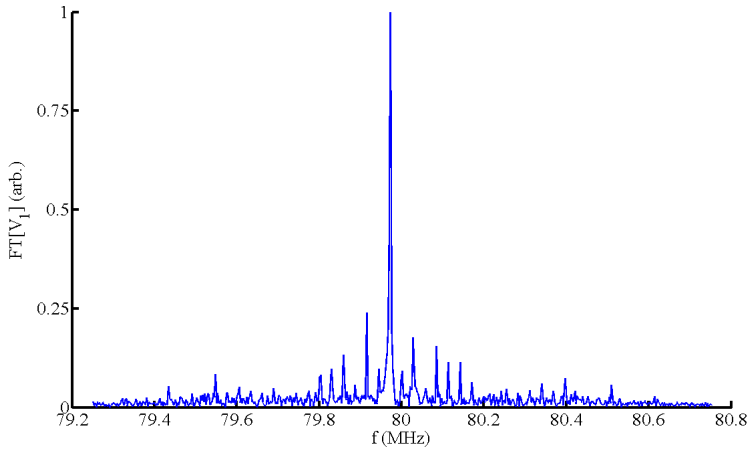

Figure 4.24: The Fourier transform of a 400 μs duration measurement of the temporal interference to analyse the temporal structure of these oscillations. The Ti:Sapph oscillators frequency, just below 80 MHz is observed. This is surrounded by regular frequency amplitudes separated by ≈ 29 kHz.

interference results demonstrated some temporal instability during operation of the EOM. Phase discontinuities were observed in the interference fringes. It was assumed that this was a result of a small temporal mismatch between the optical pulse train and the 40 GHz driving signal for the EOM. Here, the indirect effects of the temporal mismatch on the optical pulse train are simulated and the predictions of the existence of this instability shown to be consistent with the spectral observations.

4.5.1 Effect of Temporal Jitter on Spectral Manipulation

The spectral shear, $\Omega = \pi V_{\mathrm{D}} \omega_{\mathrm{D}} / V_{\pi}$, defined in Equation 4.6 and bandwidth expansion given by Equation 4.10 are not consistent with the measured values in the results above. This can be explained if one assumes the system is experiencing a *temporal jitter*: a temporal delay between the driving signal and the optical pulse which randomly takes on a value within a certain range. This jitter is assumed between the optical wave packet pulse train and the sinusoidally varying driving voltage for the EOM, it is also assumed to occur on a time-scale much smaller than the spectral measurement such that many temporal jitters may be experienced in one spectral reading.

In the ideal case, for linear temporal phase modulation, the optical wave packet, with Gaussian spectral amplitude, and RF driving signal temporally overlap at the positive linear region. This case is shown in Figure 4.25 where the optical pulse (red, solid line) is located at $t = t_0$. The optical wave packet is aligned with the RF driving signal (blue, sinusoidal solid line in Figure 4.25 at the point of maximum gradient, with gradient equal to Ω. The effect on the spectral amplitude, $\tilde{\psi}(\omega)$, is a frequency shift of magnitude Ω. When working with wavelengths, the variable in which the spectra are measured in this work, the shift in wavelength can be determined by converting using Equation 2.25. Here, the spectral shift in wavelength will be denoted by Ω_λ such that the amplitude is shifted as, $\tilde{\psi}(\lambda) \rightarrow \tilde{\psi}(\lambda - \Omega_\lambda)$.

Now, consider a situation in which there is a temporal jitter present in the system. In one instant, this causes the relative temporal alignment between the RF driving signal and the optical wave packet to be shifted by a small amount, τ_{jit}. The wave packet is now temporally aligned with a different region of the driving signal. This is also shown in Figure 4.25 (red, dashed line). In this case, the region of the driving signal in the temporal overlap with the optical pulse is still approximately linear, but with a smaller gradient. Here this gradient will be denoted by Ω', where $\Omega > \Omega'$. Due to symmetry, this will be the same for the wave packet with a jitter of both $\pm\tau_{\text{jit}}$. Both positive and negative cases are plotted on Figure 4.25. An optical wave packet aligned at $t = (t_0 \pm \tau_{\text{jit}})$, therefore, undergoes a spectral shift such that $\tilde{\psi}(\lambda) \rightarrow \tilde{\psi}(\lambda - \Omega'_\lambda)$, which is of smaller magnitude than the case where $t = t_0$ since $\Omega_\lambda > \Omega'_\lambda$.

The resultant, modulated spectrum of the two wave packets are plotted in Figure 4.26(a). The original wave packet is shown (solid, red line) which has no temporal phase applied and is located at central wavelength, $\lambda_0 = 830$ nm. For the modulated wave packet located at $t = t_0$, the wave packet undergoes the largest spectral shift to: $\lambda_\Omega = (\lambda_0 - \Omega_\lambda)$ (purple, solid line). However, for the wave packet with a temporal offset located at $t = (t_0 \pm t_{\text{jit}})$, the wave packet is spectrally shifted by a smaller amount and moves to $\lambda_{\Omega'} = (\lambda_0 - \Omega'_\lambda)$ (blue, dashed line).

In this section, an assumption is taken about the nature of the jitter. This assumption is that the temporal alignment of the wave packet experiencing jitter would be randomly distributed around t_0, with a characteristic width of distribution. This characteristic width will be referred to as the *jitter width*. Multiple, subsequent wave packet transmissions through the EOM will, thus, be offset by different delays and acquire different temporal phases. The resultant spectral envelope would be a statistical mixture of shifted spectra ranging from the maximum shift of Ω_λ, when exactly aligned at t_0, to a minimum that is

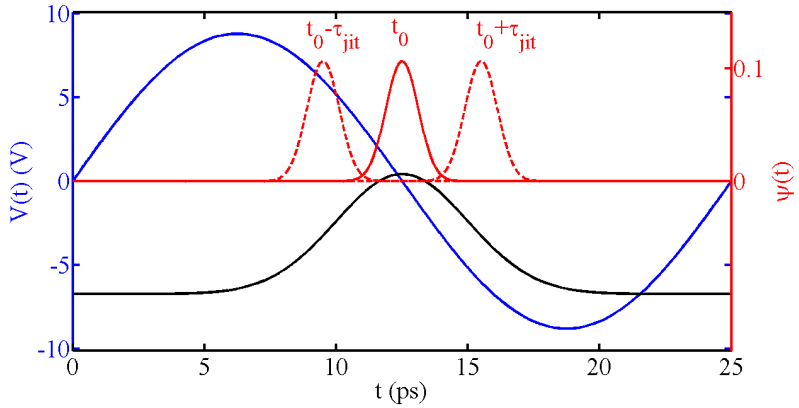

Figure 4.25: Temporal Alignment of the driving signal, V_{D}, (blue solid sinusoid), and the optical pulse, $\psi(t)$, (red solid Gaussia). Both positive and negative relative temporal alignment due to temporal jitter is shown with the optical pulse aligned at $(t_0 \pm \tau_{\mathrm{jit}})$ where t_0 is the desired alignment for maximum spectral shift. The black solid Gaussian indicates a normal probability distribution of the temporal jitter with temporal width $T = 1$ ps.

dictated by the jitter width. This is shown pictorially in Figure 4.26(b) where the spread of jitter is on the order of half of the driving signal's time period, $T_{\mathrm{D}}/2 = 12.5$ ps. Multiple shifted spectra are plotted (blue, dashed lines) alongside the original wave packet (red, solid line) and the maximally shifted wave packet (purple, solid line labelled λ_{Ω}).

The relatively long acquisition time of the spectral measurement, compared to the temporal interval between subsequent pulses, results in an ensemble average measurement. The resultant spectrum would then be an intensity averaged mixture of all possible spectrally shifted wave packets. This is shown by the Gaussian spectrum in Figure 4.26(b), labelled λ_m (solid, green line). This is the measured spectrum from subsection 4.3.1. The overall effect is a broadened spectrum with a smaller spectral shift.

This model is now explored in further detail below, assigning a function to the distribution of the jitter and comparing the measured data to the analytic model.

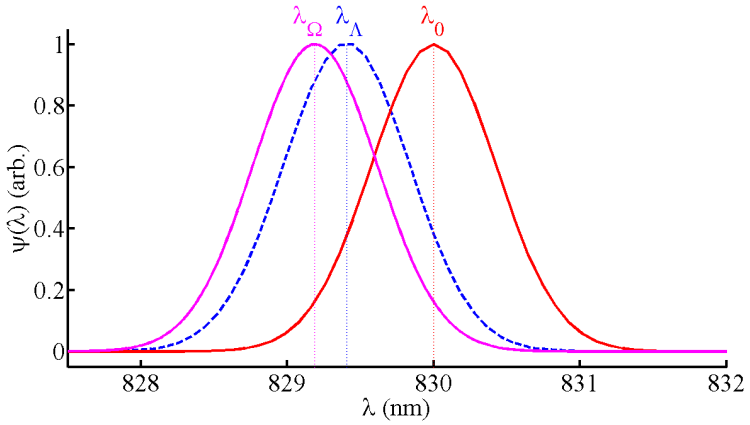

(a) The effect of the temporal jitter on the spectrum is shown. The original, unmodulated pulse is shown (red, solid Gaussian), centred at $\lambda_0 = 830$ nm. For the case of exact temporal alignment at t_0, a shift to $\lambda_\Omega = 829.19$ nm is expected, indicated by the labelled solid magenta line. However, if the optical pulse experiences a temporal jitter then it will be modulated with a temporal phase of a smaller gradient, Ω'. Hence the spectral shift is less as indicated by the blue dashed Gaussian labelled λ_Λ.

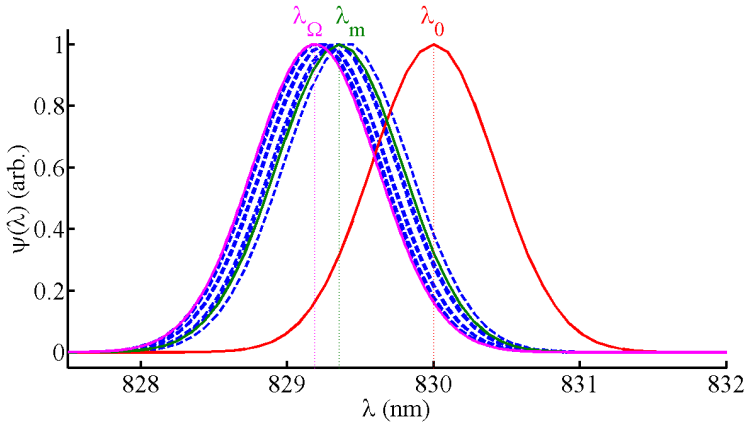

(b) The final measured spectrum is integrated over a time period which is long compared to the temporal separation of subsequent optical pulses. Thus, the spectrum becomes a statistical mixture of multiply modulated wave packets. These wave packets may all experience a different jitter. As such the spectrum will appear to have been shifted less than the maximum, furthermore it will be slightly broadened.

Figure 4.26: For these figures, the central wavelength of the original wave packet is $\lambda_0 = 830$ nm and the FWHM is 0.87 nm. A temporal jitter is modelled with a normal probability distribution with width $T = 1$ ps.

Numerical Modelling

Numerical modelling of the expected temporal jitter is now performed and compared with the measured results from previous sections. The temporal jitter is parametrized in the theoretical description of the temporal phase modulation. The parametrized temporal phase is then applied to a Gaussian wave packet pulse and the effect propagated through to the final spectral intensity measurement. A probability distribution of the temporal jitter parameter, described by a Normal distribution, centred around t_0 and with a characteristic probability distribution width, T_{jit}, is assumed.

To begin, a definition for the temporal wave packet that has undergone modulation is given,

$$\psi_{\text{mod}}(t, \tau_j) = \psi(t) \mathrm{e}^{i\phi_{\text{jit}}(t,\tau_j)}, \tag{4.27}$$

where ϕ_{jit} is the temporally varying phase that has been applied and which causes the spectral shift. This now becomes a function of both time and the variable representing jitter, τ_j,

$$\phi_{\text{jit}}(t, \tau_j) = \phi_0 \sin(\omega_{\text{D}}(t - \tau_j)). \tag{4.28}$$

Note here, that the Taylor expansion is not used as in the original derivation (Equation 4.5 and Equation 4.8). This is because if the jitter, parametrized by τ_j, is on the sane order as the driving signal time period, T_D, the optical pulse may experience both linear and quadratic temporal phase simultaneously. Thus the full expression of the phase function must be used.

I. Temporal Jitter Simulated with Linear Alignment

Initially, it is assumed that the wave packet, $\psi(t)$, is assumed located at $t = t_0 = T_{\text{D}}/2$ to achieve the ideal temporal overlap for frequency shearing as shown in Figure 4.25. The variable, τ_j, introduced above, then allows one to model the temporal jitter that each

individual pulse experiences as it passes though the EOM. This is included as a temporal shift of the driving signal to $(t - \tau_j)$. If one assumes that the origin of the jitter is due to random fluctuations then it is reasonable to assume that τ_j is continuous and located around t_0. The probability distribution of experiencing a temporal delay, τ_j, is given by a normal probability distribution with width T_{jit},

$$P(\tau_j) = N \exp^{-\frac{\tau_j^2}{2T_{\text{jit}}^2}}, \tag{4.29}$$

where $N = 1/\sqrt{2\pi T_{\text{jit}}^2}$. This probability distribution is plotted for $T_{\text{jit}} = 1$ ps indicated by the black solid line in Figure 4.25.

The measured signal is thus given by weighting the resultant modulated wave function, $\psi(t - \tau_j)$ by the probability distribution in terms of τ_j.

$$I_{\text{mod,jit}}(t) = \int_{-\infty}^{\infty} P(\tau_j)\psi^*_{\text{mod}}(t, \tau_j)\psi_{\text{mod}}(t, \tau_j)d\tau_j. \tag{4.30}$$

To determine the wave packet's spectral envelope, as is experimentally accessed in this work, a FT is applied to this to give,

$$\tilde{I}_{\text{mod,jit}}(\omega) = \mathcal{F}^{-1}\left[I_{\text{mod,jit}}(t)\right] = \int_{-\infty}^{\infty} P(\tau_j)\mathcal{F}\left[\int_{-\infty}^{\infty} \psi^*_{\text{mod}}(t - \tau_j)\psi_{\text{mod}}(t - \tau_j)\mathrm{e}^{i\omega t}dt\right] d\tau_j. \tag{4.31}$$

The effect of the jitter on the modulated spectra was then numerically simulated since an exact form could not be easily derived.

The model was tested with a simulated wave packet with original central wavelength $\lambda_0 = 830$ nm and intensity bandwidth of $\Delta\lambda = 0.87$ nm. The effect of the jitter was tested with T_{jit} in the range 0.25 to 12.5 ps in 0.25 ps intervals, such that 50 values were sampled in total. The resultant spectra, determined numerically using Equation 4.31, were then

fitted with a Gaussian function to extract the central wavelength, λ_0, and bandwidth, $\Delta\lambda$, of the modulated spectra with jitter. In Figure 4.27 a selection of the jitter-affected modulated spectra are plotted (blue, dashed Gaussian).

Reducing the Spectral Shift

In Figure 4.28(a) the resultant central wavelength, $\lambda_{0,\mathrm{mod,jit}}$, is shown as a function of the jitter width, T_{jit}. The original central wavelength is indicated (dashed red horizontal line).

The predicted spectral shift is (0.81 ± 0.01) nm as determined following the calibration of the EOM in subsection 4.2.6. Looking at the results of the spectral shifting in the previous section, a shift of only (0.5 ± 0.3) nm was measured for the coherent wave packet and similarly for the non-heralded single-photon wave packet data. This shift is included as a horizontal green dashed line at $\lambda = 829.3$ nm in Figure 4.28(a). If the reduced spectral shift was attributed solely to jitter in the system then, reading off the horizontal axis of Figure 4.28(a), this corresponds to a temporal jitter width of approximately 10 ps.

However, not only is the spectral shift reduced, but the spectral bandwidth has also increased from 1.2 nm to 1.3 nm. This should not be changed at all if only a linear phase was applied. The effect of jitter on the bandwidth is also shown in Figure 4.28(b) with the extracted intensity FWHM, $\Delta\lambda$, plotted as a function of T_{jit}. For a temporal jitter of 10 ps, the bandwidth would be expected to increase to 1.4 nm. However, this was not measured. Instead, a jitter width of approximately 7 ps results in the measured increased bandwidth to 1.3 nm.

The reduced spectral shift corresponds to a temporal jitter width of 10 ps. However, the spectral expansion also observed on the shifted spectra corresponds to a temporal jitter width of 7 ps. Throughout the above, it is assumed that the EOM is lossless and all of the generated driving signal is applied across the EOM. The value of $V_{\mathrm{D}} = (10.000 \pm 0.005)$

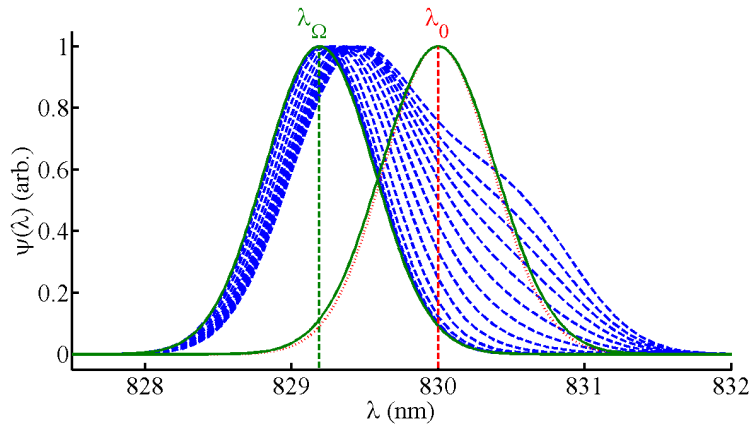

Figure 4.27: A sample of cases for spectral shifting due to temporal modulation are plotted (blue, dashed line). These are suffering from temporal jitter, with an increasing width of the jitter distribution from left to right. The original, (red, dotted line) spectra and the maximally shifted spectra for the ideal case of no jitter, (green, solid line) are also shown.

V was used in the model. However it could be the case that the maximum peak voltage is less than this maximum value generated due to losses in the RF connectors. Therefore the spectral shift would be less than currently predicted. The spectral expansion is purely a result of the jitter so is not affected by the magnitude of the driving signal's voltage.

II. Temporal Jitter Simulated with Quadratic Alignment

The numerical analysis was repeated with the optical wave packet ideally aligned to the quadratic region of the driving signal at $t = T_D/4$. The effect of the jitter causes the wave packet to now also experience a small amount of linear phase modulation and hence a small spectral shift. This jitter moves the relative location of the optical wave packet and driving signal towards both the negative and positive linear gradient region. Multiple transmissions through the EOM with different amounts of temporal jitter being experienced, would therefore result in both red and blue-shifting of the spectra as well as spectral expansion, as indicated in Figure 4.30. The overall effect on the measured spectra would also be spectral broadening but no change to the central wavelength.

A plot of the spectral bandwidth versus the characteristic width of the temporal jitter

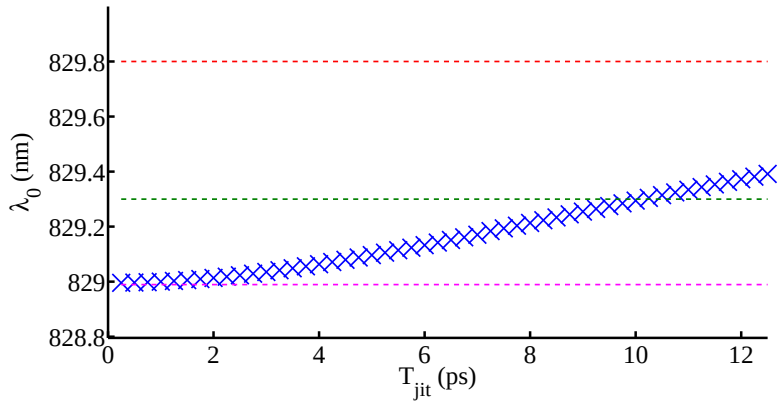

(a) Central Wavelength vs. Temporal Jitter Width for Linear Temporal Phase

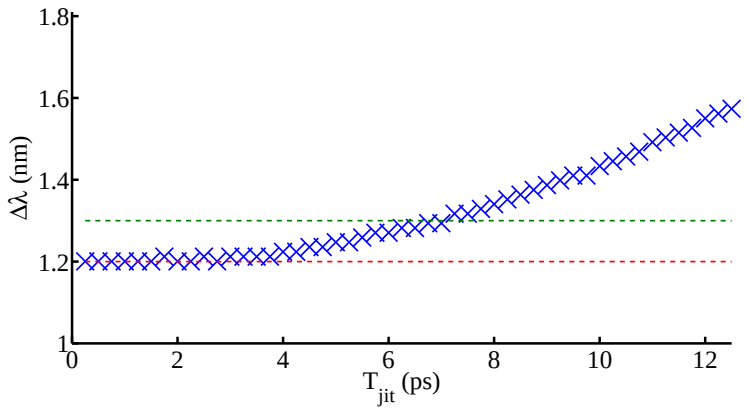

(b) Spectral Bandwidth vs. Temporal Jitter Width for Linear Temporal Phase

Figure 4.28: Plotted is the extracted central wavelength of the wave packet with linear phase modulation and with temporal jitter (blue crosses). This is plotted against the temporal jitter's characteristic width, T_{jit}. For these figures, the central wavelength of the original wave packet is $\lambda_0 = 829.8$ nm and the spectral width is $\Delta\lambda = 1.2$ nm. In (a) the dashed horizontal red lines indicate the original wavelength 829.8 nm. The magenta horizontal line is the predicted shift to 829.0 nm. The green line is the measured shift to 829.3 nm. In (b) the dashed horizontal red lines indicate the original spectral bandwidth 1.2 nm. The green line is the measured spectral bandwidth of 1.3 nm. Where the modelled data intersects with the measured data, here at approximately 10 ps in (a) and 7 ps in (b), indicates the level of temporal jitter extracted in this measurement.

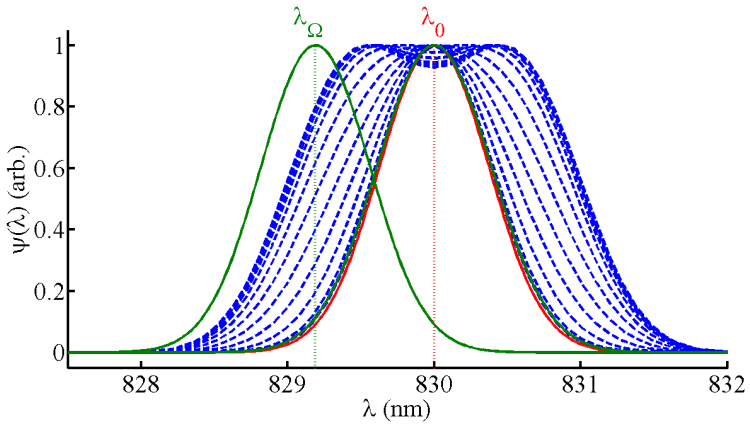

Figure 4.29: A sample of cases for spectral shifting due to temporal modulation are plotted. For varying temporal jitter, the resultant detected spectra is shown (blue, dashed line). The original, (red, dotted line) spectra and the expected shifted spectra for the case of no jitter with linear temporal alignment (green, solid line) is also shown.

T_{jit}, is shown in Figure 4.29. The red line indicates the original bandwidth, $\Delta\lambda = 1.2$ nm. This is the bandwidth of the original optical pulse, modelled here, for comparison with the experimental data in subsection 4.3.1. The expected spectral expansion is to 1.25 nm, this is also plotted in the figure (magneta, dashed line).

Also plotted in Figure 4.29 is the line, $\Delta\lambda = (1.3 \pm 0.3)$ nm, corresponding to the experimentally measured spectral width in subsection 4.3.1. This intercepts with the numerical model at approximately 5 ps. This is similar to a very recent measurement of the using a fast oscilloscope (Tektronix MSO5104). This detected jitter was on the order of 5 ps.

4.5.2 Temporal Jitter Summary

In this section, the effect of the presence of some temporal jitter in the system has been indirectly tested. The unpredicted effects seen on the modulated spectra (such as smaller shifting than expected and a spectral expansion) and the modulated spectrum temporal interference measurements (including phase discontinuities in the interference data) were assumed a result of this jitter. As such they were independently analysed.

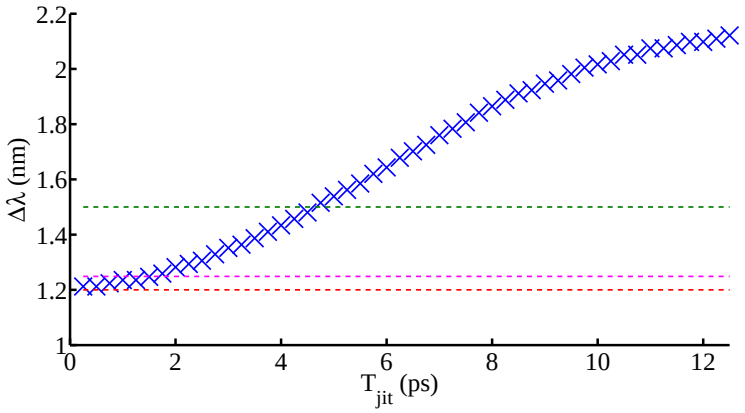

Figure 4.30: Spectral Bandwidth vs. Temporal Jitter Width for Quadratic Temporal Phase Modulation. Plotted is the extracted spectral bandwidth of the modulated wave packet with quadratic temporal phase and temporal jitter (blue crosses) . This is plotted against the temporal jitter's characteristic width, T_{jit}. For these figures, the central wavelength of the original wave packet is $\lambda_0 = 829.8$ nm and the spectral width is $\Delta\lambda = 1.2$ nm. The dashed horizontal red lines indicate the original spectral bandwidth of 1.2 nm. The magenta line is the predicted spectral expansion to 1.25 nm. The green line is the measured spectral bandwidth of 1.5 nm. Where the modelled data intersects with the measured data, here at approximately 5 ps, indicates the level of temporal jitter extracted in this measurement.

A numerical simulation of the presence of temporal jitter was performed first. By propagating through a temporal jitter term in the temporal phase, applied to the wave packet, the effect upon the wave packet's spectral amplitude was investigated. This was done by assuming the jitter was random, but with distribution described by a normal distribution function with a characteristic width. By simulating different widths and looking at the resultant spectrum, one could correlate the measured spectrum with the simulated spectrum corresponding to a characteristic temporal width of the temporal jitter. This resulted in a temporal jitter distribution on the order of 5 ps to be predicted. This is in agreement with the jitter measured using the fast oscilloscope, as mentioned above. Any discrepancies may arise due to incorrect assumptions of a Gaussian probability distribution during the modelling.

Performing a Fourier transform on the modulated spectrum interference fringes allowed one to probe any underlying temporal structure. Frequencies separated by 30 kHz were

observed. This was the same detuning of the laser repetition rate frequency from 80 MHz. Since the driving signal for the EOM originated from a resonator oscillator which required driving at 80 MHz, it was predicted this may be the source of the temporal jitter.

4.6 Chapter Summary

In this chapter, a detailed description of the RF source, that was custom-designed and built to drive the EOM, was described. Technical details on each of the components have been given such that the experimental set up could be built by a third party. Following this, the calibration of the EOM using a quasi-monochromatic laser was then presented and used to determine a value for the specific V_π of the EOM.

Coherent light interference of a phase modulated wave packet and an identical reference resulted in very high visibility interference. However, phase discontinuities were observed. It is expected that the duration of these oscillations can be tested directly against the reference laser's detuning from 80 MHz. Despite the fringes being washed out on a long scale, the first-order coherence envelope was still observed and a value for the visibility extracted from this.

Finally, the origin of these phase discontinuities was investigated. It was proposed that there was some temporal jitter present in the system between the 40 GHz driving signal and the optical pulse train. This jitter was investigated indirectly by simulating the effects of different amounts of jitter on the temporally-phase modulated spectral intensity measurements. From this investigation, an approximate estimate of the extent of this jitter, on the order of a few picoseconds, was made. Despite this drawback, it is expected that the pulse-shaping method can still be applied to a non-classical source of light.

Chapter 5

Pulse Shaping Quantum States of Light

5.1 Introduction

To demonstrate the potential of the EOM temporal-phase modulation approach to pulse-shaping in the quantum domain, spectral shearing and bandwidth expansion of single-photon states is presented in this chapter. Spectral shearing of (0.9 ± 0.1) nm and bandwidth expansion of 73% is demonstrated with heralded single-photon states of initial central wavelength $\lambda_0 = (831.6 \pm 0.2)$ nm and initial spectral bandwidth $\Delta\lambda = (1.0 \pm 0.3)$ nm. The pulse-shaping technique does not add photon noise to the quantum states, shown by preservation of the second order intensity correlation, $g^{(2)}(0)$. Furthermore, high visibility quantum interference of a modulated single-photon state is demonstrated.

5.2 Quantum Wave Packet Spectral Manipulation

In this section, heralded single photons, generated from the SPDC source introduced and calibrated in chapter 3, are utilized to demonstrate the pulse shaping technique, presented in chapter 4, in the quantum domain. The heralded spectral intensity measurements are presented and the achieved spectral manipulation compared with the theoretical predictions, given in subsection 4.2.7.

5.2.1 Method

The experimental set up for applying the pulse shaping method to single photons, and measuring the resultant spectral intensity, is shown in Figure 5.1. The set up of the source is the same as described in section 3.3 up until the polarizing beam splitter (PBS) used to spatially separate the signal and idler downconverted photons. In the measurement here, the idler photon is used to herald the existence of the signal photon. It is coupled into a polarization-maintaining fibre (PMF) using an aspheric lens (AL) and the output connected to an APD for detection, labelled H in the figure. The signal photon is first spectrally filtered using two interference filters (IF), with bandpass of a FWHM of 3.2 nm (typical) (Semrock MaxLine® filter, LL01-830-12.5) centred at 830 nm. The filtered signal photon is then fibre-coupled into the input fibre of the EOM using an aspheric lens. The RF driving signal applied to the EOM is triggered by a small ($\approx 1\%$) optical pick-off from the original Ti:Sapph laser pulse train, detected using a photodiode (PD), to achieve phase-locking between the optical pulse train and driving signal.

Following transmission through the EOM, the signal photon was directed to a spectrometer (Andor, Shamrock 303i-B) with a multi-mode fibre on the output for heralded spectral intensity measurements. The heralded spectral measurement was performed similarly as described in subsection 3.4.1: a multi-mode fibre (MMF) (Thorlabs, M42L05) with core diameter, d =50 µm was mounted on a linear translation stage at the spectrometer output. The translation stage had motorized movement in, and parallel to, the optical output plane of the spectrometer and manual adjustment for the y-z directions. The multi-mode fibre collected the transmitted modulated signal photon with no further coupling optics. The output of the multi-mode fibre was then connected to an APD, labelled S in the figure, for detection. The APD output was connected to the field-programmable gate array (FPGA) (Xilinx SP 605) (labelled "&" in the figure). The output of the APD detecting the herald photon was also connected to the FPGA which was then used to extract the coincidence

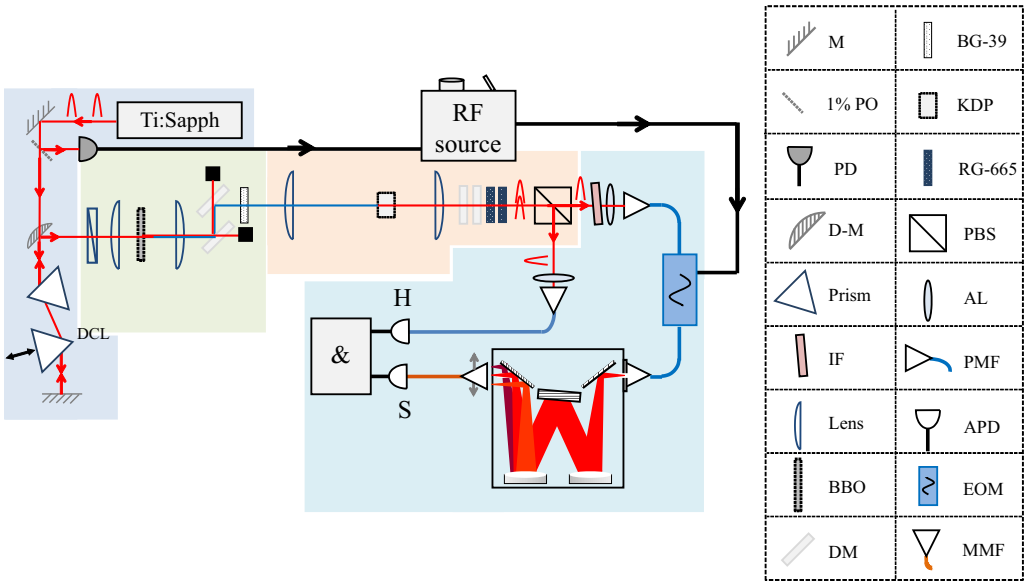

Figure 5.1: Experimental set up for heralded single-photon wave packet spectral measurements. The Ti:Sapph oscillator pumps the single-photon source, described in detail in section 3.3. An optical pick-off of $\approx 1\%$ is taken from the original pulse train, detected using a photodiode (PD), as a reference input for the RF source to drive the EOM. The single-photon source consists of a BBO crystal for SHG and a KDP for SPDC. The photon pair is separated by a polarizing beam splitter (PBS). The signal photon is spectrally filtered using an interference filter (IF) and then fibre-coupled to the input fibre of the EOM using an aspheric lens (AL). The optical output sent into a spectrometer. A motorized-stage-mounted multi-mode fibre (MMF) is located at the output of the spectrometer. The MMF output is connected to an APD for detection, labelled S. The MMF is scanned across the spectrometer output. The herald photon from the single-photon source is also fibre-coupled into a SMF connected to a second APD, labelled H. Coincidences between S and H are recorded using an FPGA (&).

count rates, R_{CC}, between the two detectors. Finally, by scanning the multi-mode fibre across the output of the spectrometer one could measure the heralded, phase-modulated, single-photon intensity spectrum.

First, the heralded spectral intensity of the unmodulated single-photon wave packet was measured to act as a baseline. Then, the RF driving signal was turned on and both positive and negative linear and quadratic temporal phases applied to the wave packet by manually scanning the phase shifter on the RF source. Heralded spectral intensities were taken for all settings. The results of these measurements are presented below.

5.2.2 Spectral Manipulation Results

The SPS was set up with single counts rates of approximately $R_s = 210$ ks^{-1} and $R_i = 190$ ks^{-1} for the signal and idler photons, respectively and coincidence count rates of $R_{CC} = 50$ ks^{-1} resulting in heralding efficiencies of approximately 26% and 24%, respectively. Following spectral filtering, transmission through the EOM and the spectrometer, single counts of 11 ks^{-1} were measured for the signal photon. The coincidence count rates were reduced to 2.4 ks^{-11}. After transmission through the spectrometer, coincidences of $R_{CC} = 60$ s^{-1} were detected at the spectral wave packet maximum on the output.

Whilst scanning the multi-mode fibre on the output of the spectrometer, counts were measured for 20 s at each location of the fibre (see section 3.4.1 for more details on this scanning-spectrometer measurement). This was done to obtain errors on the order of 15 to 20% at the intensity minima and conduct all measurements in a reasonable time frame. To accurately retrieve the spectral profile, 70 equally spaced points were selected over the spectral range of the spectrometer output. The scanning multi-mode fibre would then detect at each of these points for the 20 s designated above. These locations were separated by the fibre core diameter, such that each measured location was independent and the range chosen to adequately span the frequency space of the wave packet. Each spectral measurement took approximately 25 minutes to collect.

The heralded spectral intensity measured for the unmodulated, spectrally shifted and expanded signal photon wave packet are presented below.

Original Spectrum

The unmodulated, heralded spectrum of the single-photon wave packet is shown in Figure 5.2(a). Coincidence count rates of approximately $R_{CC} \approx 60$ s^{-1} were detected at the spectrum maximum. However, note that in the figure, the data has been normalized such that

$S = R_{\mathrm{CC}}/R_{\mathrm{CC,\,max}}$ is plotted where $R_{\mathrm{CC,\,max}}$ is the maximum of the data. The Gaussian fit to the spectra is also plotted. This fit was weighted by uncertainties given by assuming Poissonian count statistics where a count of N photons has an associated error $\sqrt{N}$. This fit allowed a central wavelength of $\lambda_0 = (831.6 \pm 0.2)$ nm to be extracted. The spectral intensity bandwidth was calculated by finding the two wavelengths where half of the maximum signal was detected, $\pm\lambda_{I/2}$, and using Equation 3.10. This gave a value of $\Delta\lambda = (1.0 \pm 0.3)$ nm. Errors on the central wavelength and bandwidth are given by resolution of the spectrograph and multi-mode fibre measurement, as described in section 3.4.1 and by propagation of uncertainties, using Equation 3.11, respectively.

This spectral intensity measurement corresponds to a Gaussian wave packet amplitude with spectral bandwidth of $\Delta\lambda_\psi = (1.3 \pm 0.3)$. Assuming a FTL pulse, this is equivalent to an electric field temporal width of $\tau_\psi = (2.1 \pm 0.2)$ ps. The wave packet is thus short enough to remain within the linear and quadratic regions of the sinusoidally varying driving voltage, assuming zero spectral phase.

Spectral Shearing

The measured heralded intensity spectra of the positive, $+\Omega$, and negative, $-\Omega$, linearly shifted single-photon wave packets are also plotted in Figure 5.2(a). Their weighted Gaussian fits are also shown and gave central wavelengths of $\lambda_{0,+\Omega} = (832.1 \pm 0.3)$ nm and $\lambda_{0,-\Omega} = (831.2 \pm 0.2)$ nm, giving a total measured spectral shift of $2\Omega_\lambda = (0.9 \pm 0.3)$ nm. This is less than the expected shift of $2\Omega_\lambda = (1.62 \pm 0.01)$ nm, as predicted by Equation 4.6. The shifted spectra had bandwidths of $\Delta\lambda_{+\Omega} = (1.1 \pm 0.3)$ nm and $\Delta\lambda_{-\Omega} = (1.1 \pm 0.3)$ nm, determined by finding the two wavelengths where half of the maximum signal was detected, $\pm\lambda_{I/2}$, and using Equation 3.10. This is an increase of 10% from the original bandwidth. Coincidence count rates of approximately 40 s^{-1} and 30 s^{-1} were detected at the spectrum maximum. These were reduced from the original spectrum measurement due to long-term drifting of the coupling alignment of the source. In the figure, these data

have also been scaled such that such that $S = R_{\mathrm{CC}}/R_{\mathrm{CC,\ max}}$ is plotted where $R_{\mathrm{CC,\ max}}$ is the maximum of the data. This allows for clear comparison with the original spectrum.

Once again, the spectrally sheared wave packets have been subject to spectral expansion. It is believed this is due to a presence of temporal jitter in the system as discussed in the final section of chapter 4. In the previous discussion on temporal jitter, a model of the temporal jitter was proposed and the effect of this jitter on the temporally-phase modulated spectra was simulated numerically. The results of this simulation were compared with the measured and extracted spectra properties for the classical pulse undergoing temporal phase modulation. This allowed one to extract an estimate on the amount of jitter in the system. Here, this numerical simulation of temporal jitter is now repeated assuming original spectral characteristics measured for the single-photon source, as described above. The results will then be compared with the actual measured shifted and expanded spectra for the single photon source, also as described above.

The reader can refer back to section 4.5 for complete details on the model and numerical simulation. For the numerical analysis performed here, the model assumed a pulse undergoing phase modulation with initial central wavelength of $\lambda_0 = (831.6 \pm 0.2)$ nm and bandwidth of $\Delta\lambda = (1.0 \pm 0.3)$ nm. These are the values measured above, corresponding to the original signal photon. The temporal jitter probability distribution was assumed Gaussian, described by Equation 4.29, and with a characteristic width, T_{jit}. The simulation was then performed with varying characteristic jitter widths ranging from 0.25 ps to 12.5 ps, in 0.25 ps intervals.

This was first done assuming a linear temporal phase modulation. The dependency of the resultant central wavelength and bandwidth of the modulated wave packet for different values of T_{jit} are shown in Figure 5.3. Once again the expected and measured central

wavelength and bandwidth are indicated by horizontal, dashed lines. Where these intercept with the simulated data returned from the model provides an estimate of the temporal jitter expected in the system. In this case the central wavelength shift corresponds to a temporal jitter of 12 ps and the expanded bandwidth corresponds to a jitter of 8 ps.

Spectral Expansion

The measured heralded single-photon spectral intensity that resulted from applying a quadratic temporal phase to the original wave packet is plotted in Figure 5.2(b). The modulated wave packet bandwidth was calculated as $\Delta\lambda_{\Omega^2} = (1.60 \pm 0.01)$ nm, determined by finding the two wavelengths where half of the maximum signal was detected, $\pm\lambda_{I/2}$, and using Equation 3.10. This indicates an expansion of approximately 73% from the original spectrum. The central wavelength was unchanged, with the Gaussian fit giving $\lambda_{0,\Omega^2} = (831.6 \pm 0.3)$ nm. Coincidence count rates of approximately 35 s^{-1} were detected at the spectrum maximum. Once again these data have been scaled in Figure 5.2(b) such that $S = R_{CC}/R_{CC,\,max}$ is plotted where $R_{CC,\,max}$ is the maximum of the data.

This spectral expansion is 25% larger than the predicted expansion of $\Delta\lambda = (1.2 \pm 0.03)$ nm as given by Equation 4.10 and using the system parameters summarized in subsection 4.2.7. Once again, this large expansion is likely due to temporal jitter in the system. The temporal jitter numerical simulation described above was repeated but now assuming a quadratic phase modulation to see what effect the jitter would have on the original single photon wave packet. The expected dependency of the measured bandwidth on the temporal jitter width is plotted in Figure 5.4. Once again, the measured and expected bandwidth expansions are indicated as horizontal dashed lines. Where the numerically simulated data intercepts the measured data, this indicates the level of temporal jitter estimated in the system. In this case it is just under 7 ps.

Wave Packet	λ_0 (nm)	$\Delta\lambda$ (nm)	$\Delta\tau_p$ (ps)	Spectral Change Observed	Spectral Change Predicted
original	831.6	1.0	1.0	-	-
blue-shifted	831.2	1.1	0.9	$\lambda_0 - 0.43$ nm, $\Delta\lambda = +10\%$	$\lambda_0 - 0.811$ nm
red-shifted	832.1	1.1	1.0	$\lambda_0 + 0.47$ nm, $\Delta\lambda = +10\%$	$\lambda_0 + 0.811$ nm
expanded	831.6	1.6	0.7	$\Delta\lambda = +45\%$	$\Delta\lambda = +20\%$

Table 5.1: A summary of the spectral pulse shaping by temporal phase modulation for the heralded single -photon source is given. The central wavelength, λ_0, spectral bandwidth, $\Delta\lambda$ and pulse width $\Delta\tau_p$ assuming a FTL pulse are given for the original single photon source, the spectrall blue and red-shifted and the spectrally expanded heralded spectral measurements. Errors on the central wavelength, λ_0, are ± 0.2 nm. Errors on the spectral bandwidth, $\Delta\lambda$, are ± 0.3 nm. The Observed and Predicted spectral shifts and expansions are also summarized.

5.2.3 Summary: Quantum Wave Packet Spectral Manipulation

Table 5.1, summarises the main spectral parameters, the central wavelength, λ_0 and the bandwidth, $\Delta\lambda$, for the heralded quantum wave packet undergoing spectral pulse shaping by temporal phase modulation. The wave packet pulse widths, τ_p, assuming FTL pulses are also given such that one can see the pulse should temporally overlap with the liner and quadratic regions of the sinusoidal temporal phase as desired. Once again, the system appears to be affected by temporal jitter. The magnitude of jitter appears to have increased from the classical pulse-shaping data. Nonetheless, clear deterministic spectral manipulation of quantum wave packets of light has been experimentally demonstrated in this section.

5.3 Photon-Number Testing - Second Order Correlation

Modification of the pulse-mode structure of a single-photon state using a temporal-phase modulation was demonstrated in the previous section. However, the single-photon nature of the heralded source was not verified after the modulation. This is important because the modulation technique must preserve the non-classical nature of the light. In this section,

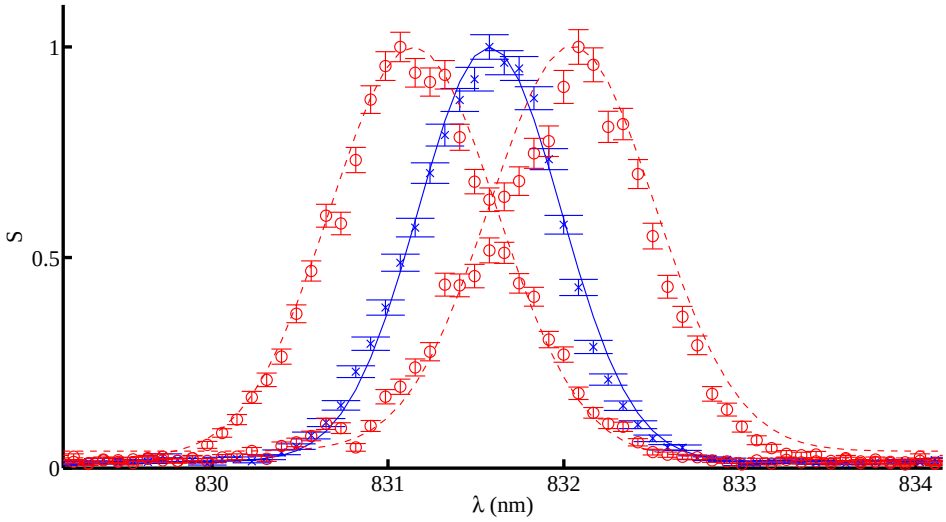

(a) Heralded Quantum Wave Packet Spectral Shifting

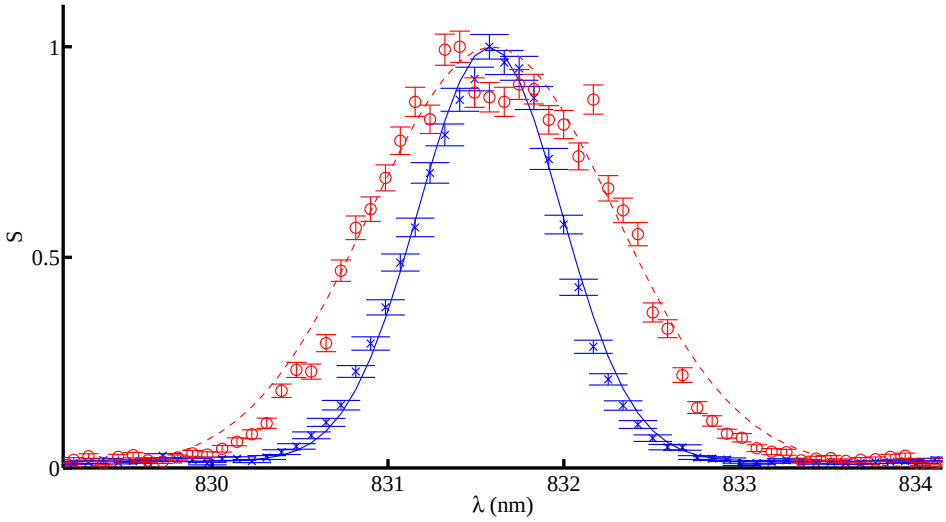

(b) Heralded Quantum Wave Packet Spectral Expansion

Figure 5.2: The heralded, modulated single-photon wave packet spectra are shown. **(a)** The original pulsed wave packet data (blue crosses) and its Gaussian fit (blue, solid line) are plotted. A central wavelength of $\lambda_0 = (831.6 \pm 0.2)$ nm and bandwidth $\Delta\lambda = (1.0 \pm 0.3)$ nm were extracted. The measured spectra for the wave packet with negative and positive linear temporal phase applied are also plotted (red circles). Gaussian fits were also performed on this data giving, $\lambda_{0,-\Omega} = (831.2 \pm 0.2)$ nm, $\Delta\lambda_{-\Omega} = (1.1 \pm 0.3)$ nm and $\lambda_{0,+\Omega} = (832.1 \pm 0.2)$ nm, $\Delta\lambda_{-\Omega} = (1.1 \pm 0.3)$ nm, respectively. **(b)** The original wave packet (blue, solid line) is plotted again alongside the spectrally expanded wave packet with $\lambda_{0,\Omega^2} = (831.6 \pm 0.2)$ nm and $\Delta\lambda_{\Omega^2} = (1.6 \pm 0.3)$ nm extracted from the Gaussian fit. Note in both plots, In both plots, the rescaled intensity measurement has been plotted: $S = R_{\mathrm{CC}}/R_{\mathrm{CC,\ max}}$ where $R_{\mathrm{CC,\ max}}$ is the maximum of the data, for easy comparison.

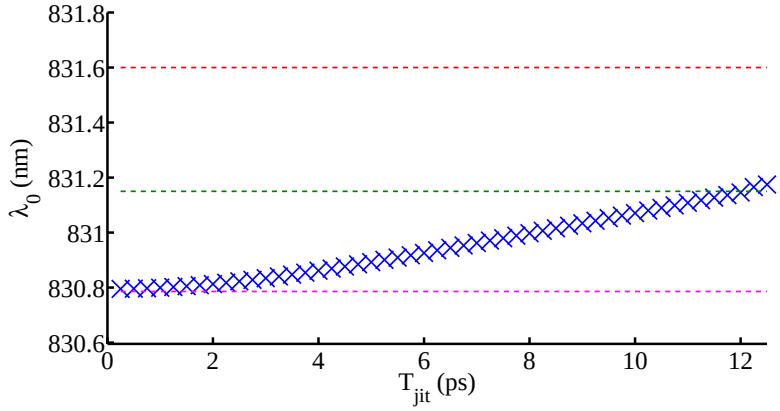

(a) Central Wavelength vs. Temporal Jitter Width for Linear Temporal Phase

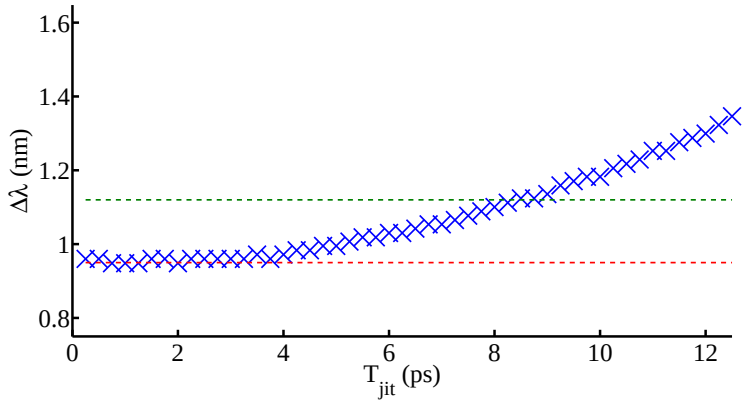

(b) Spectral Bandwidth vs. Temporal Jitter Width for Linear Temporal Phase

Figure 5.3: Plotted is the extracted central wavelength, λ_0, and spectral bandwidth, $\Delta\lambda$, of the single-photon wave packet with linear phase modulation and with temporal jitter (blue crosses). This is plotted against the temporal jitter's characteristic width, T_{jit}. For these figures, the central wavelength of the original wave packet is $\lambda_0 = (831.6 \pm 0.2)$ nm and the bandwidth is $\Delta\lambda = (1.0 \pm 0.3)$ nm. In (a) the dashed horizontal red lines indicates the original wavelength. The magenta horizontal line is the predicted shift to 830.8 nm. The green line is the measured shift to (831.2 ± 0.2) nm. In (b) the dashed horizontal red lines indicate the original spectral bandwidth. The green line is the measured spectral bandwidth of (1.1 ± 0.3) nm. Where the modelled data intersects with the measured data, here at approximately 12 ps for (a) and 8.5 ps for (b), indicates the level of temporal jitter expected in this measurement.

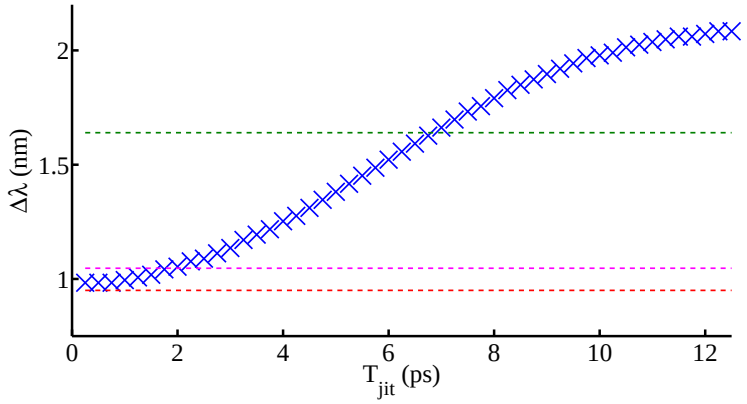

Figure 5.4: Spectral Bandwidth vs. Temporal Jitter Width for Quadratic Temporal Phase Modulation. Plotted is the extracted spectral bandwidth of the modulated single-photon wave packet with quadratic temporal phase and temporal jitter (blue crosses) . This is plotted against the temporal jitter's characteristic width, T_{jit}. For these figures, the central wavelength of the original wave packet is $\lambda_0 = (831.6 \pm 0.2)$ nm and the FWHM is $\Delta\lambda = (1.0 \pm 0.3)$ nm. The dashed horizontal red lines indicate the original spectral bandwidth. The magenta line is the predicted spectral expansion to 1.2 nm. The green line is the measured spectral bandwidth of (1.6 ± 0.3) nm. Where the modelled data intersects with the measured data, here at approximately 7 ps, indicates the level of temporal jitter expected in this measurement.

the single-photon nature of the light transformed by the EOM is measured. As discussed in subsection 2.2.3, a measurement of the second order correlation at zero time delay, $g^{(2)}(0)$, of a source of light allows one to determine the photon-number statistics of the light source. A value of less than one indicates sub-Poissonian photon-number statistics, consistent with a non-classical light source. In this section the second order correlation is measured for the single-photon source before and after it undergoes temporal phase modulation for control of the spectral amplitude. By showing that the value of $g^{(2)}(0)$ remains constant, this demonstrates that this quantum pulse shaping methods approach does not introduce additional photon number noise.

5.3.1 The Heralded Second Order Correlation

The second order correlation at zero time delay, $g^{(2)}(0)$, of a light source can be measured by directing the source onto a beam splitter and monitoring coincidence detection events between the two outputs. A schematic of this is shown in Figure 5.5(a). For the heralded

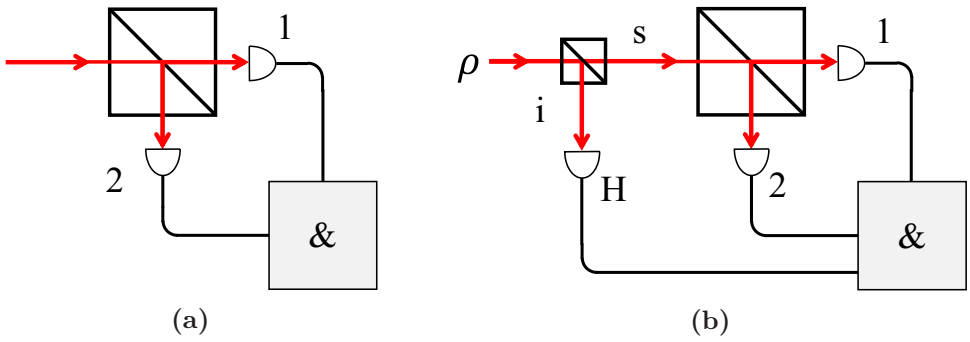

Figure 5.5: Second order correlation measurement basic set up. (a) The light source is incident on a beam splitter and detectors, 1 and 2, are placed on the beam splitter outputs to measure the signal. Coincidence measurements are monitored on the output, indicated by &. (b) For the heralded measurement, a third detector is used to monitor the herald signal. The two photons in the light source, ρ, are split by an initial beam splitter to two paths, s and i. The signal photon is then incidence on a second beam splitter with detectors, 1 and 2, on the output. The herald photon is detected by a third detector, H. All three signals are monitored and coincidences measured by &.

single-photon source used in this work, the measurement of a coincidence detection event on the output of the beam splitter must be triggered by the detection of the second photon created in the bi-photon pair. Thus a third detector must also be used and three-fold coincidence events between all three detectors monitored. This is shown in Figure 5.5(b). This leads to the following definition of the heralded second order correlation, $g_{\mathrm{H}}^{(2)}(0)$ [198],

$$g_{\mathrm{H}}^{(2)}(0) = \frac{R_{\mathrm{H12}} R_{\mathrm{H}}}{R_{\mathrm{H1}} R_{\mathrm{H2}}}. \tag{5.1}$$

Here R_{H12} is the three-fold coincidence detection event count rate between the two detectors, labelled 1 and 2 in the figure, and the herald photon detector, labelled H. R_{H} is the single herald detector count rate and $R_{\mathrm{H1(2)}}$ the coincidence event count rate between the herald photon detector and the detector labelled 1(2).

5.3.2 Method

The heralded second order correlation was measured using the experimental set up shown in Figure 5.6. The single-photon source set up is the same as described in section 3.3 up until the polarizing beam splitter (PBS) used to spatially separate the signal and idler

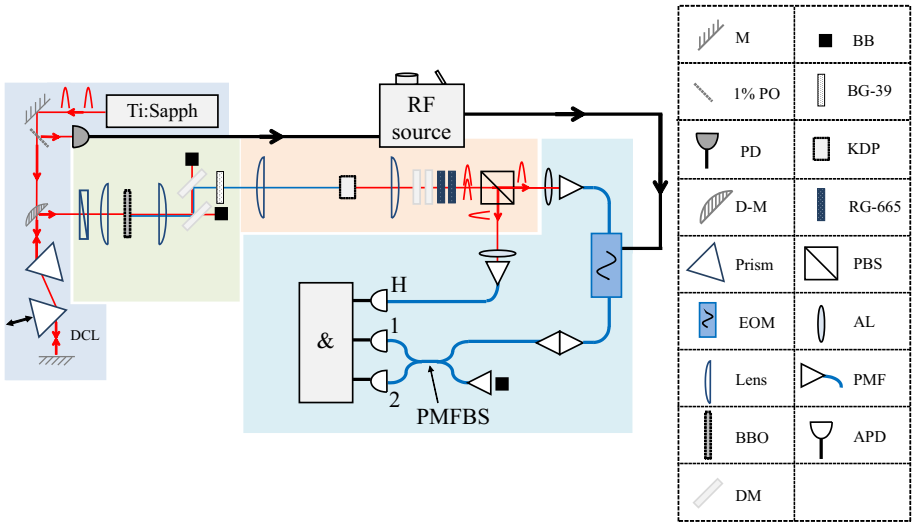

Figure 5.6: Experimental set up for the heralded $g^{(2)}(0)$ measurement is shown. The single-photon source set up is used as described in detail in section 3.3. The signal photon is transmitted through the EOM, driven by the RF source, and then into a polarization-maintaining fibre beam splitter (PMFBS). The two output arms are connected directly to two APDs, labelled 1 and 2. The other input arm is blocked by a beam block (BB). The second photon from the down converted pair, the idler, is coupled into a polarization maintaining fibre (PMF) using an aspheric lens (AL). The output of the PMF is connected to a third APD, labelled H. The measured counts by all three APDs are analysed by the FPGA (&) to extract singles, two-fold and three-fold coincidence events.

photons. The idler photon is used to herald the existence of the signal photon, as such is coupled into a polarization-maintaining fibre (PMF) and the output connected to an APD for detection. The signal field is fibre-coupled into the input of the EOM. The RF driving signal applied to the EOM is triggered by a small ($\approx 1\%$) optical pick-off from the original Ti:Sapph laser pulse train. In this case the temporal jitter present in the system is not expected to have any affect on the measurement.

The signal photon, after passing through the EOM, was input to one arm of a polarization-maintaining fibre beam splitter (PMFBS). The second input of the beam splitter was blocked. The fibre beam splitters two output ports were connected to APDs, labelled 1 and 2. Along with the herald APD, labelled H, the output signal from the detectors was monitored by a field-programmable gate array (FPGA) (with details in subsection 3.3.5).

5.3.3 Results

The second order correlation was measured for two cases: 1. with the driving signal for the EOM turned off and 2. with it on. The results of these measurements are given below.

1. Original, Unmodulated

To determine the second order correlation, singles and two- and three-fold coincidence event count rates were recorded for a measurement time of $T = 9$ s. The count rates errors were determined as described in subsection 3.4.4 using Equation 3.29. A total of 6000 measurements were made giving a total experimental run-time of 15 hours. This also resulted in 6000 sets of singles and coincidence event count rates, $\{R_{\mathrm{H}}, R_{\mathrm{H1}}, R_{\mathrm{H2}}, R_{\mathrm{H12}}\}$ as required for the $g^{(2)}_{\mathrm{H}}(0)$ measurement, Equation 5.1. Thus, 6000 sets of errors were also extracted $\{\alpha_{R_{\mathrm{H}}}, \alpha_{R_{\mathrm{H1}}}, \alpha_{R_{\mathrm{H2}}}, \alpha_{R_{\mathrm{H12}}}\}$.

During the measurement the singles count rates were seen to oscillate, due to the fluctuating laboratory environment. The single count rates, R_1 and R_2, are plotted as a function of the experimental run-time in Figure 5.7(b). The count rates are seen to vary by nearly 50%, taking approximately fifteen minutes for this variation. Therefore, the second order correlation for the complete set of data was calculated in two ways:

1. For each of the 6000 sets of data, the second order correlation was calculated using Equation 5.1. The error for each of the 6000 values was given by propagating through the count rate errors,

$$\alpha_{gi} = g^{(2)}_{\mathrm{H}}(0)\sqrt{\left(\frac{\alpha_{R_{\mathrm{H12}}}}{R_{\mathrm{H12}}}\right)^2 + \left(\frac{\alpha_{R_{\mathrm{H1}}}}{R_{\mathrm{H1}}}\right)^2 + \left(\frac{\alpha_{R_{\mathrm{H2}}}}{R_{\mathrm{H2}}}\right)^2 + \left(\frac{\alpha_{R_{\mathrm{H}}}}{R_{\mathrm{H}}}\right)^2}. \tag{5.2}$$

   An average of the $N = 6000$ values was then calculated.

   When calculating an average, A, of a set of N numbers, $\{a_i\}$, with associated errors,

$\{\alpha_{a_i}\}$, the error on the average is given by,

$$\alpha_A = \frac{1}{N}\sqrt{\sum_{i=1}^{N}(\alpha_{a_i})^2}. \tag{5.3}$$

The error on these averages were calculated using this method and the error for each count rate as defined in Equation 3.29. This resulted in an average second order correlation from the whole data set of $g_{\mathrm{H}}^{(2)}(0) = (0.038 \pm 0.001)$.

2. A running average of the second order correlation was also calculated. This was done to ensure that the observed drifting of the count rates had no effect on the calculated second order correlation. The running average was determined by splitting the data into sixty lots of fifteen minute blocks. This is the same time period as the variation seen in the count rates above. Each fifteen minute block contained $(15 \times 60)/9 = 100$ sets of singles and coincidence event count rates

   The heralded second order correlation, $g_{\mathrm{H}}^{(2)}(0)$, was calculated for each of the individual data sets in the fifteen minute block. The average of these 100 values was then calculated. The error on this average was calculated in a similar way as defined in Equation 5.3.

   This was repeated for all sixty blocks of data to extract an average $g_{\mathrm{H}}^{(2)}(0)$ value every fifteen minutes. This running average is plotted in Figure 5.7. The scatter of the $g_{\mathrm{H}}^{(2)}(0)$ values seen in the figure demonstrates that, despite fluctuation of the coincidence count rates, the second order correlation value was randomly distributed around an average, and not drifting over the long-term. The average of these sixty averages was determined to be $g_{\mathrm{H}}^{(2)}(0) = (0.037 \pm 0.005)$, with error on this average calculated similarly as in Equation 5.3.

2. Modulated

The EOM was then turned on to apply a temporal-phase to the single-photon wave packet. Count rates were measured, once again, with a count time of $T = 9$ s. A total number of 6500 sets of count rate data, $\{R_{\mathrm{H}}, R_{\mathrm{H1}}, R_{\mathrm{H2}}, R_{\mathrm{H12}}\}$, were recorded resulting in an experimental run time of 16 hours and 15 minutes. Note that between measurements of the unmodulated and modulated heralded second order correlation, the alignment of the coupling optics was optimized due to the falling count rates experienced in the measurement set above. As such, larger count rates were measured for this data set.

Variations in the single count rates were observed once again, as shown by the count rates, R_1 and R_2, plotted in Figure 5.7(b). Thus, both an overall average and a running average were calculated as described above.

1. The total average of all the 6500 values was calculated and gave, $g_{\mathrm{H}}^{(2)}(0) = (0.040 \pm 0.001)$.

2. A running average was calculated every fifteen minutes and is shown in Figure 5.7(b). This also appears to be randomly distributed around the average. The total average of these averages was determined to be $g_{\mathrm{H}}^{(2)}(0) = (0.039 \pm 0.002)$.

5.3.4 Summary: Photon-Number Testing

The second order correlation function was calculated for the signal photon produced by the single-photon source, prepared as described in section 3.3. A total of 6000 measurements of two- and three-fold coincidence count rates were taken over a period of 15 hours, allowing one to extract a value of $g_{\mathrm{H}}^{(2)}(0) = (0.038 \pm 0.001)$. This indicates that the SPDC single-photon source demonstrates sub-Poissonian photon-number statistics, hence it is a non-classical light source.

The second order correlation was measured again, this time with the signal photon under-

going temporal-phase modulation. This was done to show that the pulse-shaping method presented in this thesis does not alter the photon-number statistics. A total of 6500 measurements of the coincidences were taken over a time period of 16 hours and 15 minutes. This resulted in an average second order correlation of $g_{\mathrm{H}}^{(2)}(0) = (0.040 \pm 0.001)$.

Long-term drifting of the count rates, indicating a steady misalignment of the coupling optics, was seen in the first set of data. Therefore, in the time between the two heralded $g^{(2)}(0)$ measurements, the coupling optics were re-aligned to optimize the count rates. This resulted in a larger three-fold coincidence rate. The running average errors bars were also smaller, and the scatter around the mean less.

Nonetheless, the value for the second order correlation before and following temporal-phase modulation agree, within error. This demonstrates that the method does not add any significant photon number noise to the modes. However, it can add loss which affects number statistics but not the $g^{(2)}(0)$ value.

5.4 Hong-Ou-Mandel Interference

To show that the wave packet coherence is preserved, following the temporal phase modulation for spectral amplitude modification, interference in a Mach-Zehnder interferometer (MZI) was performed in section 4.4. An alternative approach is to use a Hong-Ou-Mandel-type interference between the modulated wave packet and a reference pulse.

Hong-Ou-Mandel (HOM) interference is a two-photon quantum interference effect due to the bosonic nature of light. The theory describing this effect is presented in subsection 3.4.4. Very high visibility can be measured between two independent single-photon wave packets when they are pure and indistinguishable. Consider applying a linear temporal phase modulation to one of these two wave packets such that it undergoes a spectral shear. If

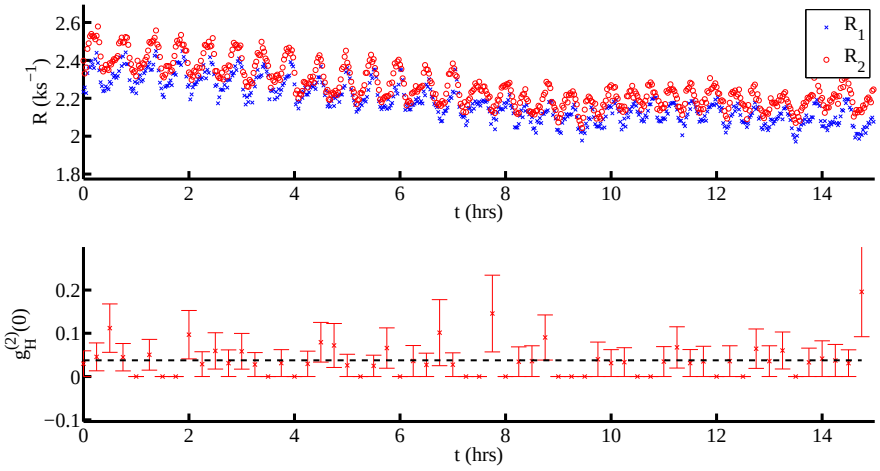

(a) Original, Unmodulated

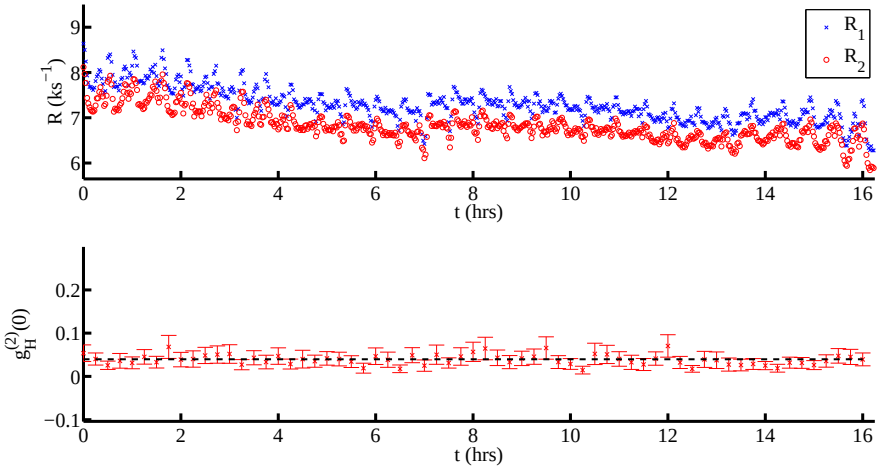

(b) Modulated

Figure 5.7: Second order correlation results for (a) Unmodulated and (b) Modulated single-photon wave packet. In the top plot in both (a) and (b), the singles count rates for the herald wave packet, R_{H}, are plotted as a function of experimental time. Note, error bars have been omitted on this data since they are on the same order as the size of the data point. A clear oscillating drift is seen with a time period of approximately 30 minutes. However, as seen in the plot, this drifting does not affect the heralded $g^{(2)}(0)$, which is plotted. A running average has been calculated every fifteen minutes and is seen randomly scattered around the average of all the data measurements. This average is indicated by the black-dashed line. An average heralded $g^{(2)}(0)$ of (0.038 ± 0.001) for the data in (a) and (0.040 ± 0.001) for the data in (b) was determined from a running average calculated every fifteen minutes.

the temporal-phase modulation method *only* changes the central wavelength of the phase-modulated pulse, then one should be able to achieve HOM interference with the reduction in visibility, from the indistinguishable case, only due to the applied wavelength shift. The expected reduction can be determined from the spectral overlap of the two wave packets, recall Equation 3.25. Thus, by measuring the HOM interference visibility and the intensity spectra and calculating the square of the spectral overlap and showing these agree, one can be confident the temporal-phase modulation technique does not alter the wave packet in any other, undesirable, way.

One advantage to this method compared to the MZI measurement, is that the temporal jitter should not affect the result. In quantum interference, the result is global-phase independent. If one assumes that the temporal jitter is only a phase offset then it should have no effect.

In this section, the method for a Hong-Ou-Mandel (HOM) interference measurement between the spectrally modified signal and idler photon wave packets is described. The SPDC source is prepared and the resultant down-converted signal and idler wave packets are spectrally filtered to prepare identical states. The signal photon wave packet is passed through the EOM to undergo a linear temporal phase modulation. The idler photon acts as the reference wave packet. The modulated-signal and reference-idler wave packets are then interfered in a beam splitter with coincidence counts measured on the beam splitter outputs. The reference-idler wave packet is then temporally scanned relative to the modulated-signal wave packet in order to trace out the signature HOM interference "dip". The results are then analysed and presented.

5.4.1 Method

The HOM interference measurement, experimental set up is shown in Figure 5.8. The single-photon source is the same as described in section 3.3 up until the polarizing beam

splitter (PBS) used to spatially separate the signal and idler photons. The signal photon wave packet has a half-wave plate (HWP) following the beam splitter to match the polarization of the signal and idler wave packets. The signal and idler fields are fibre-coupled into polarization-maintaining fibres (PMF) which act as the input arms to the HOM interferometer. These are labelled A and B in Figure 5.8.

The signal photon, in arm A, was spectrally modified by temporal phase modulation using the EOM. The RF driving signal applied to the EOM is triggered by a small ($\approx 1\%$) optical pick-off from the original Ti:Sapph laser pulse train. This was adjusted by manually scanning the phase shifter to achieve a linear temporal phase. The fibre output of the EOM was connected to one of two fibre inputs of a polarization-maintaining fibre beam splitter (PMFBS-1). The second fibre-input of the beam splitter is blocked. The outputs are used for two different measurements. One output arm is connected to the spectrometer with the CCD on the output for a spectral intensity measurement. The second output arm is connected to a second polarization-maintaining fibre beam splitter (PMFBS-2). It is in this fibre beam splitter that the HOM interference takes places.

The idler photon was used as a reference wave packet to interfere with the modulated-signal photon. It is collimated using a variable collimation package (Thorlabs, CFC-11X-B, focal length, $f = 11.0$ mm, AR for 650-1050 nm) as it exits the original collection fibre. It is then fibre-coupled into an input arm of the second fibre beam splitter (PMFBS-2). This input arm is mounted on a linear, translation stage. This allows one to introduce a temporal delay, τ, into this arm as required for HOM interference, see subsection 3.4.4.

The modulated-signal and reference-idler wave packets are interfered in the fibre beam splitter. The output arms of the fibre beam splitter were connected to two APDs, labelled 1 and 2 in Figure 5.8, and both singles, R_1 and R_2, and coincidence counts, R_{CC}, were

monitored using an FPGA with a coincidence window of 8 ns.

Data Collection

The SPDC single-photon source was established with single count rates of approximately $R_{\mathrm{s}} = 300$ ks^{-1} and $R_{\mathrm{i}} = 520$ ks^{-1} for the signal and idler photons respectively and a coincidence count rate of $R_{\mathrm{CC}} = 42$ ks^{-1} resulting in heralding efficiencies of approximately 14% and 8%, respectively. Following transmission through the experimental set up, coincidence rates on the order of $R_{\mathrm{CC}} = 15$ s^{-1} were measured between APDs 1 and 2 at the output of the interferometer.

The HOM interference measurement was taken as follows: coincidence counts, R_{CC}, were measured as the temporal delay, τ, in arm B was scanned from approximately -2 ps relative to perfect temporal overlap of the wave packets to $+2$ ps. Coincidence count rates were measured at a total of 71 equally spaced temporal delay locations in between this range. This data was collected for a measurement time of $T = 60$ s for each data point. This was to ensure counting uncertainties on the order of 10% at the minima regions of the dip and that the experimental run was completed in an appropriate time frame. The total experimental run time for one HOM interference measurement thus took seventy-one minutes. The HOM interference was then repeated five times.

HOM Interference Background Measurement and Dark Counts

To correct for any possible higher photon number states created in the SPDC single-photon source, coincidence count background measurements were taken. Consider a two-photon idler photon state being created by the SPDC source. As it propagates through the HOM interference set up, it may probabilistically split at the fibre beam splitter (PMFBS-2) and cause a coincidence event to be registered on the output. This could be interpreted, falsely, as a coincidence event between the signal and idler photons. Since the APDs are not photon number resolving, during the HOM interference measurement one cannot

identify these higher-order contributions. Therefore, by blocking the optical input arm to the interferometer for each of the signal and idler in turn, and measuring coincidences, one can determine the average contribution rate of coincidences to the interference data and correct for this.

A total of 29 (19) background data points were measured following the five HOM interference measurements to determine higher-order contributions from the signal (idler) optical arm. Coincidence counts were measured for 60 seconds. Average background coincidence counts of $\langle R_{\mathrm{BG,i}} \rangle = (0.7 \pm 0.2)\ \mathrm{s}^{-1}$ and $\langle R_{\mathrm{BG,\ s}} \rangle = (0.2 \pm 0.1)\ \mathrm{s}^{-1}$ were measured by blocking the signal and idler optical paths, respectively. The measured coincidence data was then corrected similarly as in Equation 3.30,

$$R_{\mathrm{CC,BG}} = R_{\mathrm{CC}} - (\langle R_{\mathrm{BG,s}} \rangle + \langle R_{\mathrm{BG,i}} \rangle)\,. \tag{5.4}$$

The errors on the background count rates were also propagated through to determine the error for $R_{\mathrm{CC,BG}}$ using Equation 3.31. Note, that this assumes a time-stationary source. However, drifting in the singles count rates was seen. Since the HOM interference data took much longer than the time period of the drift, on the order of tens of minutes, it was not possible to take background data that would accurately represent the source throughout. Nonetheless, since the background data discussed above were taken following the long HOM measurement, they recorded smaller count rates from the source than during the interference measurements. Hence, the contribution of background coincidence counts are likely to be underestimated.

Spectral Intensity Measurement

It was not possible to perform a heralded single-photon spectral measurement during the HOM interference measurement. Therefore, despite observing spectral components not originating from the single photon source in previous non-heralded spectral measurements,

see subsection 3.4.2, the signal wave packet spectral intensities were measured intermittently throughout the HOM measurement using the spectrometer and CCD. This was achieved by connecting the fibre beam splitter included in arm A of the interferometer (PMFBS-1) to the spectrometer. Despite not accurately representing the single-photon source, these spectra allowed one to monitor any drifts in the spectral properties of the non-heralded wave packet, which is also undergoing temporal phase modulation. This would highlight if the drifting resulted from the EOM itself. An integration time of 120 s was used to measure the data at two minute intervals throughout the interference measurement. Further details on the measurement process and data analysis are described in section 3.4.1.

The idler wave packet's spectra was also measured using the spectrometer and CCD at the start and end of the HOM interference data run by connecting one output of the fibre beam splitter (PMFBS-2) in Figure 5.8 to the fibre input of the spectrometer. A measurement was taken for 120 s.

Background spectral measurements were taken at the start and end of the HOM interference measurement to correct the intensity spectra for any scattered light in the laboratory which would add noise to the data. This was done by blocking the optical input to the spectrometer, keeping all other variables constant, and measuring for the same time as the intensity spectral measurement. The background spectrum was then subtracted off the measured intensity spectra, using Equation 3.13.

Both the idler and signal wave packets are plotted in Figure 5.9. Two sets are plotted: with the signal intensity wave packet measured at the start of the data run, Figure 5.9(a), with central wavelength and bandwidth labelled, $\lambda_{0,\mathrm{s,start}}$ and $\Delta\lambda_{\mathrm{s,start}}$ respectively, and at the end, Figure 5.9(b), with central wavelength and bandwidth labelled, $\lambda_{0,\mathrm{s,end}}$ and

$\Delta\lambda_{\mathrm{s,end}}$ respectively. This was done to highlight any variation in the spectral amplitude due to drifting as seen in data in previous chapters due to the temporal jitter associated with the EOM.

Owing to the spectral filtering, the spectra do not resemble Gaussian functions. This was also seen previously in the HOM interference measurement in subsection 3.4.4. Nonetheless, a Gaussian function, of the same form as in Equation 3.12, was fitted to each spectra to extract the central wavelength. The fit was weighted by the error on each data point of the spectra, where a photon count of N has an error given by $\sqrt{N}$. Central wavelengths of $\lambda_{0,\mathrm{i}} = (829.7 \pm 0.2)$ nm, $\lambda_{0,\mathrm{s,start}} = (829.0 \pm 0.2)$ nm, and $\lambda_{0,\mathrm{s,end}} = (829.2 \pm 0.2)$ nm were extracted. The bandwidths were determined by identifying the width of the spectrum at half the intensity maximum, also as done in subsection 3.4.4, returning values of $\Delta\lambda_{\mathrm{i}} = (2.4 \pm 0.3)$ nm, $\Delta\lambda_{\mathrm{s,start}} = (2.2 \pm 0.3)$ nm and $\Delta\lambda_{\mathrm{s,end}} = (2.2 \pm 0.3)$ nm.

The same Gaussian fits were also performed on all of the signal photon spectra measured every two minutes throughout the HOM interference measurement. For each of the measured spectral intensities, a central wavelength was extracted from the Gaussian fit and the bandwidth was calculated using Equation 3.10. A plot of these spectral parameters versus the experiment run-time is given in Figure 5.10. The integrated signal, $\int \tilde{S}(\lambda)$, is also plotted. The integrated signal was included to demonstrate if there was long-term drifting of the optical power. Finally, a plot of the five subsequent HOM interference data is also aligned with the plotted spectral properties to demonstrate the oscillation of the spectral fit properties is of the same order as the experimental run time.

Unfortunately, data was only recorded for the first half of the experimental run time. Nonetheless, clear variations of the central wavelength are seen varying over 0.4 nm, almost a quarter of the idler bandwidth. The optical power is also seen to fluctuate with

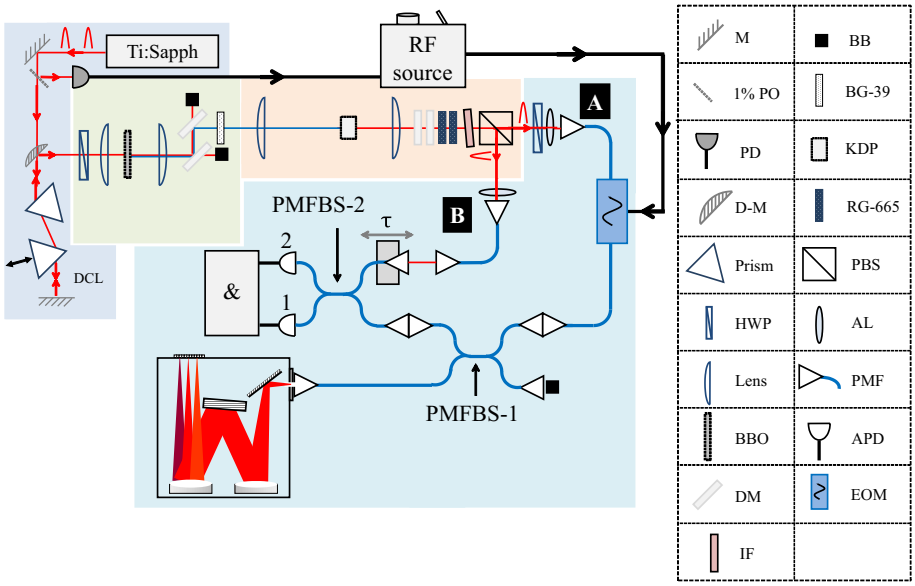

Figure 5.8: The experimental set up for the quantum wave packet interference in a Hong-Ou-Mandel type interferometer is shown. The single-photon source was set up as described previously. Both wave packets are spectrally filtered (IF) before being spatially separated by the polarizing beam splitter. The signal photon wave packet is sent into arm A of the interferometer. It is transmitted through the EOM, which is driven by the RF source. The idler photon wave packet is sent into arm B which is comprised of a mounted linear translation stage to induce a temporal delay, τ. The two arms are brought together to interfere the wave packets in the polarizing-maintaining fibre beam splitter (PMFBS-2). A half wave plate (HWP) is included in arm A to match the polarizations. The outputs of the interferometer are connected to APDs. The APD signals are sent to an FPGA, &, to monitor the coincidence events, R_{CC}. The output of arm A has an extra fibre beam splitter (PMFBS-1) inserted. This is connected to the spectrometer with CCD on the output to monitor the spectrum of the signal wave packet throughout the data run.

the same oscillation pattern as the spectral bandwidth. The central wavelength follows a different pattern. This could be an indication of two causes of instability: 1. an optical alignment instability, causing the bandwidth to drift as the optical path alignment with the interference filter (IF) changes and 2. an instability in the linear temporal phase modulation, likely due to the temporal jitter that is suspected to be in the system.

5.4.2 Results and Data Analysis

The five background-correct HOM interference dips are shown, superimposed, in Figure 5.9(c). They are also shown in subsequent order in Figure 5.10(d). Drifting in the singles rates was seen. If this is a result of drifting of alignment within the single-photon source, itself,

it may have an effect on the data. The HOM interference data was corrected for these drifts by normalizing the singles data to the smallest rate outside of the interference region. The data was corrected for the drifts in the singles count rates by:

$$R_{\mathrm{CC,BG,cor}} = \frac{R_{\mathrm{CC,BG}}}{\sqrt{R_1 R_2}}. \tag{5.5}$$

The data in Figure 5.9(c) have had this correction performed.

HOM Interference Visibility

Following all data correction, an inverted Gaussian was fitted to each HOM dip as described in subsection 3.4.4. The fits for each of the five sets of data are plotted in Figure 5.9(c) and allowed for the interference visibility to be extracted. A summary of the extracted visibilities is given in Table 5.2. A mean of $V_{\mathrm{HOM}} = (88 \pm 2)\%$ was determined using all five results. The error on this average was propagated through, and calculated in a similar manner to that in Equation 5.3.

Spectral Overlap Calculation

The spectral overlap was calculated using two methods as described in subsection 3.4.4, section "Spectral Overlap Calculation":

1. The first method used the spectral intensity data directly. Equation 3.37 was used to determine expressions for the wave packets and the overlap calculated using Equation 2.18.

2. A second method used the Gaussian fit parameters to simulate spectral amplitudes and perform a Monte Carlo-type algorithm calculation.

For the signal spectra measured at the start of the experimental run, shown in Figure 5.9(a), the square of the spectral overlap calculated by the two methods are 1. 86% and 2. $(85 \pm 1)\%$, respectively. For the signal spectra measured at the end of the data run, the

Repeat No.	V_{HOM} (%)
1	89 (6)
2	87 (6)
3	90 (6)
4	90 (5)
5	85 (4)
Mean (%)	88 (2)

Time of Spectrum Measurement	$\lvert\langle\psi_{\mathrm{s}}\lvert\psi_{\mathrm{i}}\rangle\rvert^2$ (%)	
	Monte Carlo	Data
Start	85(1)	86
End	93(1)	91

Table 5.2: Table of HOM interference extracted visibilities V_{HOM} for each of the five HOM interference measurements. The spectral overlap, $\lvert\langle\psi_{\mathrm{s}}\lvert\psi_{\mathrm{i}}\rangle\rvert^2$, calculated in two ways using the Monte Carlo method, described in the text, and using the data are also given for the spectra measured at the start and the end of the long HOM interference measurement.

square of the spectral overlap was calculated to be 1. 91% and 2. (93 ± 1)% using the two methods, respectively. These are summarized in Table 5.2 for comparison with the interference visibility,

5.4.3 Summary of HOM Interference of Modulated Wave Packets

To verify that the temporal-phase modulation method introduced here preserves the coherence of the wave packet, HOM interference was performed between a temporally-phase modulated wave packet and a spectrally-similar reference wave packet. If the method did indeed preserve the wave packet, it was expected that the HOM interference visibility would agree with the square of the spectral overlap, $V_{\mathrm{HOM}} = \lvert\langle\psi_{\mathrm{s}}\lvert\psi_{\mathrm{i}}\rangle\rvert^2$. The extracted interference visibility and calculated spectral overlap and summarized in Table 5.2.

The central wavelength of the modulated signal wave packet's intensity spectrum was seen to drift to a higher wavelength, becoming more spectrally overlapped with the idler reference, throughout the HOM interference measurement which took over one hour to

complete. This accounts for the increase in calculated spectral overlap extracted for the spectra measured at the end of the experimental run. Five repeats of the interference measurement were taken subsequently to identify if this drifting had a long-term effect on the HOM interference visibility. As one can observe from the summary of the extracted visibilities in Table 5.2, the visibilities appear to be scattered around the average value, calculated as $\langle V_{\mathrm{HOM}} \rangle = (88 \pm 2)\%$.

The spectral overlap was calculated using both the measured intensity spectra and the Gaussian fits. However, due to the spectral filtering of the spectra, the Gaussian fits may not accurately represent the data which have been seen to have a flat spectrum. Furthermore, the spectral measurements were not heralded. Therefore, they may contain components not originating from the bi-photon source. Nonetheless, this calculation allowed for an estimate of the overlap to be extracted with an error. For the intensity spectra measured at the beginning of the data run, plotted in Figure 5.9(a), the two spectral overlaps that were calculated using the different two methods, are seen to agree within error: $(85 \pm 1)\%$ and 86%. For the set of spectra measured at the end of the data run, plotted in Figure 5.9(b), the two spectral overlaps calculated using the two different methods do not agree. The spectral overlaps disagree by two standard deviations. However, the spectral data taken at the end of the HOM measurement had a much larger signal-to-noise ratio (SNR), with a SNR = 63% compared to a value of SNR = 34% for the set taken at the start. This is a result of the decreased count rates at the end of the HOM experiment.

The calculated average of the HOM interference visibilities, $\langle V_{\mathrm{HOM}} \rangle = (88 \pm 2)\%$, agrees, within error, with the square of the spectral overlaps calculated using the intensity spectra measured at the start of the interference measurement: $|\langle \psi_{\mathrm{s}} | \psi_{\mathrm{i}} \rangle|^2 = (85 \pm 1)\%$ and 86%. The average HOM interference visibility, however, does not agree with the spectral overlaps calculated with the spectral intensity data taken at the end of the HOM measurement.

The visibility lies two standard deviations away from the overlap calculated for the spectra at the end of the measurement, however this data had a significant SNR, so may not represent the actual spectra as well. Furthermore, all spectral overlaps were calculated using the non-heralded spectral measurements which may contain spectral components that do not originate from the bi-photon source. Therefore, these spectral overlaps can only provide an estimate.

5.5 Chapter Summary

In this chapter successful demonstration of spectral shifting and expansion for quantum wave packets of light was shown. The photon-number statistics before and following temporal-phase modulation for spectral wave packet modification were measured. These measurements demonstrated that the single-photon source was non-classical and that no significant photon noise was added during the phase-modulation. Finally, Hong-Ou-Mandel interference was successfully performed between two single-photon wave packets from a down-conversion source and with one photon undergoing phase modulation.

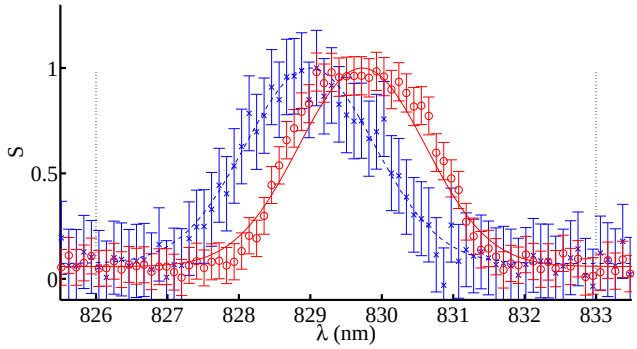

(a) Start

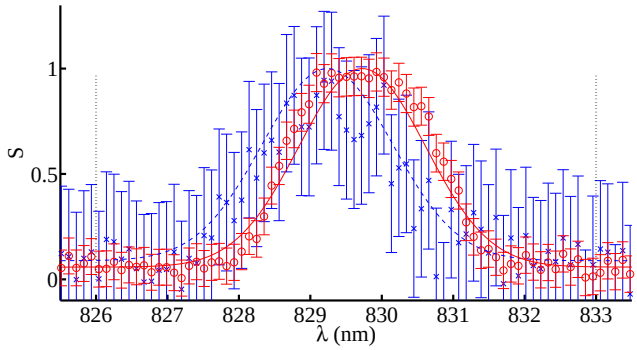

(b) End

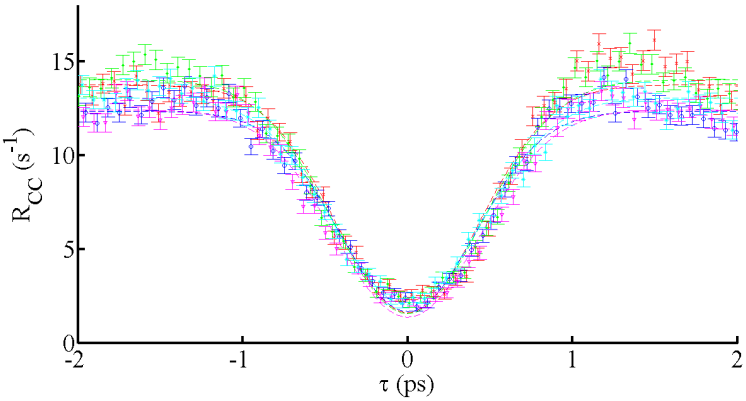

(c) HOM Interference

Figure 5.9: In (a) and (b), the signal (blue crosses) and idler (red circles) wave packet intensity spectra and their Gaussian fits are shown. In both plots, the rescaled intensity measurement has been plotted: $S = R_{\mathrm{CC}}/R_{\mathrm{CC,\,max}}$ where $R_{\mathrm{CC,\,max}}$ is the maximum of the data, for easy comparison. (a) Shows the spectra measured before the HOM interference measurement and (b) shows the data measured following. Both plots have black dotted vertical lines indicating the region between which the data was used to calculate the spectral overlap. In (c) the five repeat HOM interference measurements, with the coincidence events, R_{CC}, plotted versus the relative temporal delay, τ of the two arms. The plotted data have been corrected for background, beam splitter and polarization extinction ratios as well as drifting of the singles count rates. An average visibility of $\langle V_{\mathrm{HOM}}\rangle = (88 \pm 2)\%$ was determined.

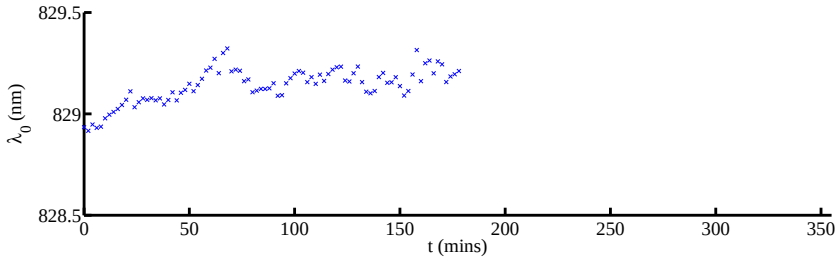

(a) λ_0 vs. Experiment Run Time

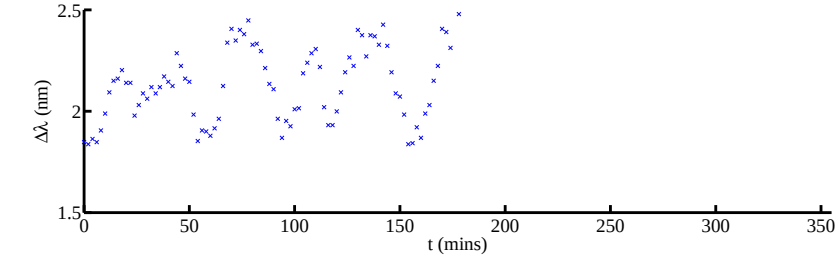

(b) $\Delta\lambda$ vs. Experiment Run Time

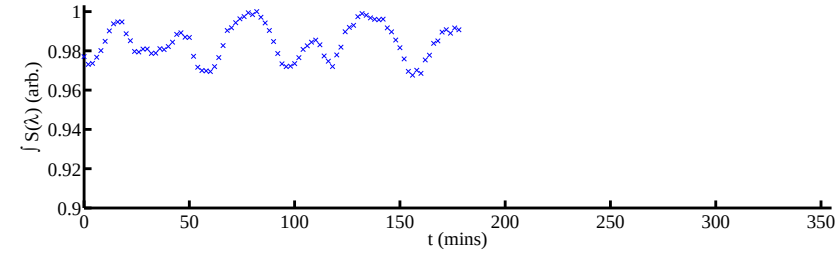

(c) $\int \tilde{S}(\lambda)$ vs. Experiment Run Time

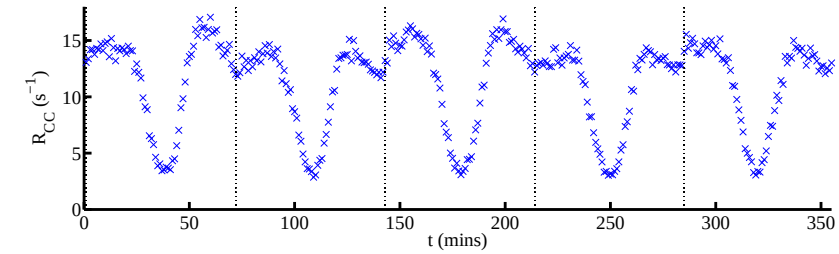

(d) HOM Interference

Figure 5.10: The spectral properties of the non-heralded, signal spectral measurement are plotted as a function of experimental run-time. The central wavelength, λ_0, (a), was extracted from the Gaussian fit to the measured spectra data. The spectral bandwidth, $\Delta\lambda$, (b), was determined using the wavelengths where the signal had dropped to half the maximum value. In both (a) and (b) and range of 1 nm has been used as a scale on the y-axis. The sum of the measured signal, $\int \tilde{S}(\lambda)$, is also included in (c) to highlight any optical power drifting. These data have been normalized to the maximum such that $\int \tilde{S}(\lambda)/S_{\max}$ is plotted where $S_{\max}$ is the maximum of all $\int \tilde{S}$. The variation in power is less than 4% These are all compared with the five subsequent HOM interference coincidence count data, R_{CC}, (d). Only the first half of the spectral data was recorded. The full run-time corresponding to the HOM interference data is shown.

Chapter 6

Conclusions and Future Directions

6.1 What Has Been Done Here?

In this work, a method for pulse shaping of single-photon wave packets in the spectral degree of freedom has been experimentally demonstrated. This method applies a linear or quadratic temporal phase to the wave packet to produce a spectral shift or expansion, respectively. The phase is induced using an electro-optic modulator (EOM) which is driven by a 40 GHz signal which is phase locked to the single-photon wave packet pulse train. The method was demonstrated here on a pulsed, heralded single-photon source with central wavelength (831.58 ± 0.1) nm and spectral bandwidth of (0.95 ± 0.2) nm. A total spectral shift of (0.90 ± 0.1) nm was achieved and a spectral expansion of the bandwidth to (1.64 ± 0.1) nm was also measured. It is believed that this is the first demonstration of an EOM for deterministic control of the spectral-temporal mode structure of quantum light pulses.

The method was shown to conserve the photon-number statistics of the single-photon source. A second order correlation of $g_{\mathrm{H}}^{(2)}(0) = (0.038 \pm 0.001)$ was measured for the heralded single-photon demonstrating non-classical photon-number statistics. Following temporal-phase modulation to achieve spectral amplitude manipulation, a value of $g_{\mathrm{H}}^{(2)}(0) =$

(0.040 ± 0.001) was measured. This demonstrated that significant noise was not added to the single-photon state during the pulse shaping technique.

The method presented here operates at 80 MHz, and up to 40 GHz. It is also deterministic: if the wave packet is transmitted through the EOM, it *will* be frequency converted. It also allows some freedom in tuning the desired spectral shift and bandwidth expansion. This method is noise-free, however, is a victim of marked optical losses, with an optical insertion loss of 5 dB from the EOM itself. This method could also be improved with better developed wave-guiding technology and if one works in telecom wavelengths. The author also believes that, to date, this is the fastest operation of an EOM applied to both classical and non-classical wave packets of light. The largest RF frequency applied to an EOM in the literature is 35 GHz [199] and higher speed devices are currently under development [200].

In principle, this method can be applied to a variety of spectral frequencies and bandwidths. The implementation would require a change of EOM and driving source. Nonetheless, the theoretical procedure has the potential to for allow arbitrary temporal phase to be applied, by applying different function forms to the modulator. This has recently been demonstrated using classical wave packets [201]. Furthermore, if this method is coupled with a wave packet sorting method, such as that described in [78], and by making use of an array of multiple EOM and RF source combinations, suited for different ranges of optical frequencies, this method has the potential to be an integral part of an ideal quantum pulse shaper.

Overall, preliminary development and measurements in this work support the large potential that this method holds for arbitrary pulse shaping of wave packets with a large scope for further development and testing.

6.2 Applications of this Work

During this work, useful applications of this pulse-shaping method were both proposed and their implementation begun. Unfortunately, these applications were not at an appropriate stage to comment on in the main body of this thesis. Nonetheless, they are described here for the next generation to take on.

6.2.1 Complete Quantum State Tomography of the Spectral-Temporal Domain

When there is a fixed number of photons, n, occupying a mode then one can introduce an n-photon wave function which can be used to describe the evolution of the state for when the photon number is preserved[202,203]. The complete characterization of this wave function in all degrees of freedom is one of the main goals of research into single-photon states[174]. Complete state characterization has been demonstrated in the polarization[204] and spatial[205] degrees of freedom and, most commonly, the number state with quadrature amplitudes extracted[174,206]. However, to date, a method has yet to be experimentally demonstrated. This requires extracting both the spectral-temporal profile and the phase of the state.

Methods have been proposed[207] and demonstrated[208–210], for partial and complete characterization of the spectral-temporal states. However, these methods often require the ability to prepare a reference pulse in many different wave packet modes that are spectrally overlapped with the non-classical light source. This is challenging to implement, and also limits the spectral range where characterization can be performed to where known reference pulses are available.

A method for complete spectral-temporal characterization was proposed which makes use of the quantum pulse-shaping technique demonstrated in this thesis. This method is self-

referencing, requiring no additionally prepared reference pulse. As part of this method, one is required to apply a spectral shift, on the order of the pulse bandwidth, to the wave packet being characterized. The work in this thesis is therefore an essential step towards establishing this full state characterization method. The theory of the proposed full state characterization method is presented in Appendix B. A protocol for experimentally extracting the form of the spectral-temporal modes of classical and non-classical wave packets of light is also described.

The protocol is based on electro-optic shearing interferometry (EOSI) and involves sending the wave packet for characterization into an interferometer. In one path of the interferometer the wave packet amplitude undergoes a temporal delay. In the other arm, the wave packet undergoes a spectral shift, implemented using the pulse-shaping method presented here. The delayed and spectrally sheared wave packet amplitudes interfere and the spectral fringes are detected on the output. One is thus measuring the temporal interference of adjacent parts of the spectral profile. One can manipulate the measured fringes to extract the phase relationship between these separated frequencies. By scanning the implemented spectral shear over the full spectral width of the pulse, and measuring fringes for each shear, one can extract the phase relationship across the pulse. For further details the reader can refer to Appendix B and [72].

The components of this set up have been prepared and preliminary testing of the experimental method have proved promising. However, it has previously been shown that any temporal instability in the system directly affects the result of SSI [211]. Thus, before the spectral shear by temporal phase modulation can be incorporated into this full state characterization, the temporal jitter inferred to be present in the system, must be carefully accounted for.

6.2.2 Quantum Key Distribution

A second useful application of the pulse shaping method demonstrated in this work, is as part of a quantum key distribution (QKD) scheme. Quantum key distribution is the process whereby a secret key is established between two authorized partners connected by a quantum, and a classical authenticated, channel. The key's security, assuming perfect single-photon sources and detectors, is guaranteed by quantum mechanics. QKD remains one of the few, successful quantum enhanced technologies that is currently commercially available[212] yet still remains open to improvement in the form of increasing bit rates and measurement efficiencies.

QKD was first demonstrated in the polarization basis[213], and encoding in the phase[214] was also popular. In recent years, however, encoding in the spectral-temporal modes has gained large interest[43,46,215–217]. The spectral-temporal modes offer a large Hilbert space for increased information encoding when compared to the polarization states, for example. Furthermore, photons with information encoded in the spectral-temporal modes are tolerant to de-coherence for long distance propagation and are not affected by cross-talk as necessary for quantum networks. Therefore, the spectral-temporal modes offer a highly desirable option for high-bit rate QKD.

One such protocol of time-frequency encoding QKD is proposed in[47]. In this protocol spectral measurements are performed only. Spectral measurements allow for high efficiency, large bin number and high bit rate when compared to temporally-resolved measurements, this is attributed to the availability of entangled photon sources and single-photon detector arrays placed at the output of the spectrometer. Therefore, a time-to-frequency conversion is used to measure the temporal correlations. The spectral modification technique developed in this thesis is a key part of the time-to-frequency conversion.

Full details of this QKD protocol and how the temporal phase modulation method developed in this work can be found in the literature[47].

6.3 The Next Generation

Throughout this seminal work, designing and building the quantum pulse shaping method, improvements to the procedure were identified by the author. The most essential modifications of the system are proposed below.

6.3.1 Tackling the Jitter

The results of the pulse shaping method revealed the presence of a temporal jitter between the RF driving signal and optical pulse. The jitter was seen to affect the spectral shaping capabilities, with the pulse shaping method only stable on the order of a few picoseconds.

During data acquisition, different photodiodes were tested and with the optical reference signal from the Ti:Sapph pulse train sampled at different locations throughout the optical set up. However, this did not eradicate the jitter. Following indirect analysis of the effect of the jitter, section 4.5, it was suggested the cause may be due to the detuning of the Ti:Sapph oscillator's repetition rate, at $R_L = 79.997$ MHz, from 80 MHz. This 80 MHz was the specified reference input of the phase-locked dielectric resonator oscillator, from which the 40 GHz signal originated. One suggested experiment is to perform multiple spectral shifting and expansion measurements for different laser cavity lengths, hence different values of R_L. By analysing the effects on the spectral results, one should be able to determined if there is a relationship between the laser repetition rate and the extent of the temporal jitter.

6.3.2 Efficient RF Signals

The 40 GHz RF signal is a sinusoidal signal of high power and was found to give off substantial heat during operation. It was also found that the EOM required a couple of minutes to reach a stable temperature. Furthermore, the sinusoidal signal oscillates 500 times in between each interaction with the 80 MHz optical pulse, as indicated pictorially in Figure 6.1(a). The oscillations in between two interactions with an optical pulse are therefore essentially wasted. Of course, if a higher optical repetition rate was used, the number of unused oscillations would decrease.

For the 80 MHz case here, a more efficient method type of driving signal might look like that proposed Figure 6.1(b). This saw-tooth type driving signal displays a very sharp voltage gradient every 12.5 ns, when temporally aligned with the 80 MHz optical pulse. In the regions between the 80 MHz pulses, there is no fast driving voltage, hence a more efficient operation. Following consultation with Aspen Electronics (who assisted with the design and build the 40GHz source), it has been verified that this alternative driving signal is feasible. This would be a useful route to explore, and may also help to probe further the problem of temporal jitter in the system as discussed above.

Another alternative to achieving a larger spectral shift and expansion capability would be using a lower driving frequency and higher voltage driving source for the EOM, recalling that the spectral shift is directly proportional to the driving voltage, V_{D}, and driving frequency, ω_{D}, as given in Equation 4.6. Voltages on the order of kV have been reported for MHz sources[218–221]. In this case, the reduction in driving frequency is balanced by the increase in voltage, hence there is no real advantage for using such a high power source. Furthermore, the frequency separation of sidebands, when operated with a continuous wave laser, would be very challenging to resolve.

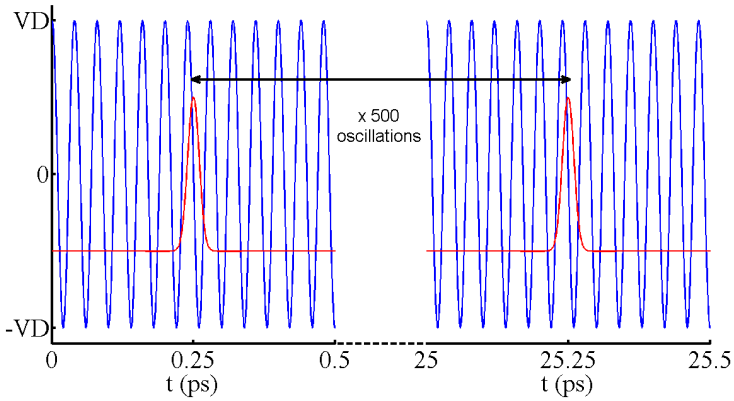

(a) 80 MHz with 40 GHz Sinusoidal Driving Signal

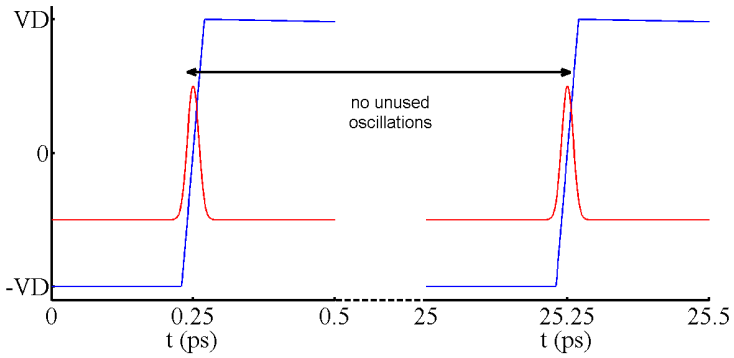

(b) 80 MHz with 80 MHz Saw-Tooth

Figure 6.1: The current temporal alignment of the 40 GHz driving signal source with the optical pulse (a) and a proposed alternative profile of the driving signal (b) is shown. (a) Shows the current temporal alignment of the optical pulse (red Gaussian) with the sinusoidally varying driving signal (blue) due to the 40 GHz sinusoidal oscillation compared with the laser repetition rate of 80 MHz. One possible alternative, to create a more power-efficient device, is using a saw tooth-type driving signal which has one large spike every 12.5 ns to temporally align with the optical pulse.

6.3.3 Arbitrary and Multiple RF Signals

It has been recently proposed that applying multiple sinusoidal RF signals can lead to boundless phase application[222] and waveform shaping[201,223]. This spectral amplitude manipulation method presented here allows for multiple applications of phase modulation. These can be applied subsequently to the single-photon wave packet using multiple EOM devices. One disadvantage of this, however, would be the decreased count rates due to cumulative optical transmission losses. This author suggests modelling of applying multiple RF signals to single-photon wave packets for arbitrary spectral shaping, be performed to

determine the feasibility of this approach.

6.3.4 Calibration of the Variable Attenuator

As part of the design for the RF source, the variable attenuator, for controlling the strength of the driving signal, was integrated with an electronically-controlled stepper-motor with a USB interface for computer control and automation. This function has yet to be properly calibrated and automated. This would allow for precise control and automation of the spectral shift and expansion. This could be combined into a feed-back circuit, once a detection has been made, to change the spectral shaping applied based on another result. The author therefore recommends that this calibration is also pursued. This would also allow for further parameters of the RF source to be tested to investigate the temporal jitter in the system.

6.4 Implications of this Work

The work presented in this thesis will impact greatly on those interested in a compact procedure to deterministically modify the spectral-temporal modes of single-photon wave packets by small, precisely-controllable amounts. The principle of temporal phase modulation can be applied to a range of frequencies, laser repetition rates and a selection of bandwidths. It is hoped that this work will inspire others to develop their own tailored temporal-phase modulation system. Further down the line, the applications of this work, as discussed above, represent two major advancements to the field of quantum communication in the spectral-temporal domain. Both of these applications rely heavily on the work presented in this thesis. As has been demonstrated within the spatial-momentum domain [104], it is also hoped that this work contributes to the quest of establishing a method to combine temporal phase control with the well-studied spectral phase control methods for complete control over the quantum optical spectral-temporal state.

6.5 To End

It has been a wonderful experience witnessing effects of quantum theory in real time in a standard laboratory environment at room-temperature, built from scratch and using mostly off-the-shelf components and with very few people. The field of quantum optics currently has enormous and diverse potential for real-life applications to improve on existing technologies. It also inspiring to have been part of such a wonderful international community of quantum optical researchers who are consistently interesting in learning from and collaborating with each other for the greater goal of developing the area of research. Being able to contribute to this field of research has been an honour and a wholesome experience and one the author looks forward to sharing with the wider world in my new pursuits as an educator.

Appendix A

Pulse Expansion for Gaussian: Derivation

A.1 Derivation of Pulse Broadening

In this appendix, the form of the pulse broadening for a Gaussian pulse, as presented in Equation 2.31, chapter 2, is derived. Assume a wave packet with temporal form given by,

$$\psi(t) = N\mathrm{e}^{-\frac{t^2}{T^2}}\mathrm{e}^{-i\omega_0 t}, \tag{A.1}$$

The spectral form is found by performing an IFT:

$$\tilde{\psi}_(\omega) = \mathcal{F}^{-1}\left[\psi(t)\right], \tag{A.2}$$

$$= \tilde{N}\mathrm{e}^{-\frac{1}{4}T^2(\omega-\omega_0)^2}, \tag{A.3}$$

$$= \tilde{N}\mathrm{e}^{-\frac{(\omega-\omega_0)^2}{2\sigma^2}}, \tag{A.4}$$

where $\sigma^2 = \frac{2}{T^2}$. This wave packet is now modulated by a quadratically varying temporal phase,

$$\psi_{\mathrm{mod}}(t) = \psi(t)\mathrm{e}^{i\phi(t)} = N\mathrm{e}^{-\frac{t^2}{T^2}}\mathrm{e}^{-i\omega_0 t}\mathrm{e}^{-i\beta t^2}, \tag{A.5}$$

The effect in the spectral degree of freedom is,

$$\begin{aligned}
\tilde{\psi}_{\mathrm{mod}}(\omega)/N &= \mathcal{F}^{-1}\left[\psi_{\mathrm{mod}}(t)\right], \\
&= \mathrm{e}^{-\frac{1}{4}\frac{iT^2(\omega-\omega_0)^2}{(i+\beta T^2)}}, \\
&= \mathrm{e}^{-\frac{1}{4}\frac{iT^2(\omega-\omega_0)^2(i-\beta T^2)}{(i+\beta T^2)(i-\beta T^2)}}, \\
&= \mathrm{e}^{-\frac{1}{4}\frac{i^2T^2(\omega-\omega_0)^2-i\beta T^4(\omega-\omega_0)^2}{(i^2-\beta^2T^4)}}, \\
&= \mathrm{e}^{-\frac{1}{4}\frac{-T^2(\omega-\omega_0)^2}{(-1-\beta^2T^4)}}\mathrm{e}^{-\frac{1}{4}\frac{-i\beta T^4(\omega-\omega_0)^2}{(-1-\beta^2T^4)}}, \\
&= \mathrm{e}^{-\frac{(\omega-\omega_0)^2}{2\left[\frac{2}{T^2}(1+\beta^2T^4)\right]}}\mathrm{e}^{-\frac{i\beta T^2(\omega-\omega_0)^2}{2\left[\frac{2}{T^2}(1+\beta^2T^4)\right]}}, \\
&= \mathrm{e}^{-\frac{(\omega-\omega_0)^2}{2\sigma^2_{\mathrm{mod}}}}\mathrm{e}^{-\frac{i\beta T^2(\omega-\omega_0)^2}{2\sigma^2_{\mathrm{mod}}}}.
\end{aligned}$$

Hence a new Gaussian form of the spectral amplitude is given by, $\mathrm{e}^{-\frac{(\omega-\omega_0)^2}{2\gamma^2}}$, where,

$$\begin{aligned}
\sigma^2_{\mathrm{mod}} &= \frac{2}{T^2}(1+\beta^2T^4), \\
&= \sigma^2(1+\beta^2\frac{4}{\sigma^2}).
\end{aligned}$$

Thus, the wave packet's spectral bandwidth, $\Delta\lambda$, has increased by a factor of $\sqrt{1+\beta^2T^4}$.

$$\Delta\lambda_{E,\mathrm{mod}} = \sqrt{1+\beta^2T^4}\Delta\lambda_E. \tag{A.6}$$

Appendix B

Quantum State Tomography of the Spectral-Temporal Modes: A Proposal

B.1 Complete Wave Packet Characterization Methods

There exist a number of complete wave packet characterization methods for electric fields in their spectral-temporal modes such as frequency-resolved optical gating method (FROG)[224], where one measures a two-dimensional function of time and frequency and extract the electric field through iterative algorithms and the robust spectral phase interferometry for direct electric field reconstruction (SPIDER)[225] and its many iterations. For a detailed review of all of these methods, the reader can refer to in-depth reviews[72].

The complete wave packet characterization method for state characterization proposed here is a derivative of the *interferometric* group of techniques. In interferometric techniques the spectral phase difference is directly measured between different frequencies in the pulse. This is typically a result of frequency shifting one copy of the pulse, interfering the two and measuring the interference fringes. Many classical approaches make use of nonlinear interactions to induce the frequency shift between two field copies. These approaches rely on high optical intensities. When working with wave packets of light occu-

pied by a single photon, these methods fall short. In the interferometric approach proposed here, the spectral shear is achieved using the spectral shifting method by temporal phase modulation, demonstrated in this thesis.

B.1.1 Method: Interferometric Characterization

The approach to the interferometric pulse characterization technique employed here is more commonly known as spectral shearing interferometry (SSI). Two copies of the wave packet for characterization are generated by impinging the wave packed onto a beam splitter. One copy undergoes a linear shift in frequency, a spectral shear and the other is temporally delay. These two copies are then recombined. Temporal interference thus occurs between two adjacent frequencies in the original pulse spectrum, separated by the spectral shear. A spectrally-resolved measurement of the interference is then performed and the spectral fringes are extracted. From the measured fringes, one can extract the density matrix of the state. This is done by first extracting the two-frequency correlation function, $\tilde{\tilde{C}}(\omega, \omega')$ which is a statistical measure between two frequencies. From the two-frequency correlation function, one can determine the Wigner distribution, an alternative representation of the quantum state, as described below.

B.1.2 The Wigner Quasi-Probability Distribution

The Wigner distribution is a useful representation of a quantum state[226]. It graphically provides intuition into how the complimentary degrees of freedom relate to each other. It is defined, in terms of the density matrix, $\hat{\rho}$, as,

$$W(\omega, t) = \frac{1}{\pi\hbar} \int_{-\infty}^{\infty} \langle \omega + \omega' | \hat{\rho} | \omega - \omega' \rangle \, \mathrm{e}^{-2it\omega'/\hbar} d\omega', \tag{B.1}$$

$$= \frac{1}{\pi\hbar} \int_{-\infty}^{\infty} \left\langle \tilde{\psi}^*(\omega + \omega') \tilde{\psi}(\omega - \omega') \right\rangle \mathrm{e}^{-2it\omega'/\hbar} d\omega'. \tag{B.2}$$

The Wigner function is symmetric such that the same result comes from defining the state in its complex conjugate, $\psi(t)$, integrating over a temporal variable instead.

Extracting the Wigner Function from the Two-Frequency Correlation

Correlation functions are a useful method to determine the nature of both classical and quantum electric fields and can be extracted from interferometric measurements. The two-time correlation function was introduced in chapter 2 . A more general definition is used here,

$$C(t,t') = \langle \psi(t)\psi^*(t') \rangle \,, \tag{B.3}$$

where angular brackets indicate an ensemble average over repeated measurements. An equivalent definition exists for the two-frequency correlation function determined by a double Fourier transform of $C(t,t')$,

$$\tilde{\tilde{C}}(\omega,\omega') = \left\langle \tilde{\psi}(\omega)\tilde{\psi}^*(\omega') \right\rangle . \tag{B.4}$$

Both $C(t,t')$ and $\tilde{\tilde{C}}(\omega,\omega')$ on their own do not provide a direct insight into any existing time-frequency correlations. Nonetheless, the Wigner function can be extracted via a transform of coordinates and a Fourier Transform

First, note that the product the integral in the Wigner function is similar to the definition of the two-frequency correlation function. A coordinate transformation allows one to rewrite the Wigner function in terms of the measured two-frequency correlation function. The following transform is made using the sum, $\omega_c = (\omega + \omega')/2$, and difference, $\Delta\omega = (\omega - \omega')$, coordinates. One can then rewrite the two-frequency correlation function,

$$\tilde{\tilde{C}}(\Delta\omega,\omega_c) = \left\langle \tilde{\psi}(\omega_c + \Delta\omega/2)\tilde{\psi}^*(\omega_c - \Delta\omega/2) \right\rangle \tag{B.5}$$

Substituting ω' in the Wigner function, Equation B.2, with the difference frequency, $\Delta\omega/2$, this gives,

$$\begin{aligned} W(\omega,t) &= \frac{1}{\pi\hbar}\int \left\langle \tilde{\psi}(\omega_c+\Delta\omega/2)\tilde{\psi}^*(\omega_c-\Delta\omega/2)\right\rangle \mathrm{e}^{-it\Delta\omega/\hbar}d\Delta\omega, \\ &= \frac{1}{\pi\hbar}\int \left\langle \tilde{\tilde{C}}(\Delta\omega,\omega_c)\right\rangle \mathrm{e}^{-it\Delta\omega/\hbar}d\Delta\omega. \end{aligned} \tag{B.6}$$

Thus if one can measure the two-frequency correlation function then the Wigner function, and hence density matrix of the quantum state in the spectral-temporal degree of freedom, can be extracted.

B.1.3 Measuring the Two-Frequency Correlation

As mentioned previously, the two frequency correlation function can be extracted from spectral interference fringes. During the SSI procedure described above, the wave packet undergoing characterization, defined as $\tilde{\psi}(\omega) = \tilde{\psi}_0(\omega)\mathrm{e}^{i\phi(\omega)}$, is split into two equal copies, $\tilde{\psi}_{\frac{1}{2}}(\omega) = \frac{1}{2}\tilde{\psi}(\omega)$. One half is temporally delayed by τ, introducing a factor of $\mathrm{e}^{i\omega\tau}$. The other copy undergoes a spectral shear such that the field is transformed from $\tilde{\psi}_{\frac{1}{2}}(\omega) \rightarrow \tilde{\psi}_{\frac{1}{2}}(\omega+\Omega)$. This spectral shift is achieved using the pulse shaping technique presented and experimentally verified in this work.

The two copies are then recombined for interference and the summed field on the output spectrally-resolved. The intensity measured is given by,

$$\begin{aligned} \tilde{I}(\omega) &= \left\langle |\tilde{\psi}_{\frac{1}{2}}(\omega+\Omega)+\tilde{\psi}_{\frac{1}{2}}(\omega)\mathrm{e}^{i\omega\tau}|^2\right\rangle, \\ &= |\tilde{\psi}_{\frac{1}{2}}(\omega+\Omega)|^2+|\tilde{\psi}_{\frac{1}{2}}(\omega)|^2+\tilde{\psi}_{\frac{1}{2}}(\omega+\Omega)\tilde{\psi}^*_{\frac{1}{2}}(\omega)\mathrm{e}^{-i\omega\tau}+\text{c.c.}, \end{aligned} \tag{B.7}$$

where c.c. is the complex conjugate of the third term. The measurement is assumed to be taken over a long integration time such that the ensemble average is measured. The first two terms in the second line are the spectral intensities of the pulse in the individual

arms $\tilde{I}_{\frac{1}{2}}(\omega+\Omega)$ and $\tilde{I}_{\frac{1}{2}}(\omega)$ which can be measured separately and subtracted. The last two terms describe the interference fringes and contain the desired phase information about the wave packet.

B.1.4 Extracting Information from the Interference Fringes

The two-frequency correlation can be extracted from the interference fringes. Once again, the difference and sum frequency coordinates are used, now defining $\omega_c = (\omega + \Omega/2)$ and $\Delta\omega = \Omega$. The term containing the fringes in Equation B.7, is rewritten as,

$$\begin{aligned}\tilde{I}_{\text{fringes}}(\omega_c;\Delta\omega) &= 2\Re\left[\tilde{\psi}^*_{\frac{1}{2}}(\omega_c+\Delta\omega/2)\tilde{\psi}_{\frac{1}{2}}(\omega_c-\Delta\omega/2)\mathrm{e}^{-i(\omega_c-\Delta\omega/2)\tau}\right], \\ &= |\tilde{\tilde{C}}(\Delta\omega,\omega_c)|\cos\Big(\arg[\tilde{\tilde{C}}(\Delta\omega,\omega_c)]+(\omega_c-\Delta\omega/2)\tau\Big). \qquad \text{(B.8)}\end{aligned}$$

The spectrally-resolved measurement thus picks out a line of $\tilde{\tilde{C}}(\Delta\omega,\omega_c)$ along $\omega=\omega_c$ since $\Delta\omega=\Omega$ remains constant throughout the measurement. For an arbitrary pulse, Ω must then scanned, and the fringes measured, over the full spectral support of the wave packet. However, for a pure state, with no correlations between the temporal and spectral domain, only two measurements are required to completely determine the quantum state.

B.1.5 Experimental Method

A fibre-based Sagnac interferometer is proposed to achieve a same-path, phase-stable propagation of the wave packet through the interferometer. A schematic representation of this is shown in Figure B.1(a). The single-photon wave packet is launched along the slow axis of an input arm of a polarization maintaining fibre beam splitter. This provides the necessary equal splitting of wave packet amplitude in two modes which have well-defined spatial and polarization modes.

The upper arm of the Sagnac interferometer, labelled **A** in Figure B.1(a), contains the electro-optical modulator (EOM) used to apply a linear temporal phase and spectrally

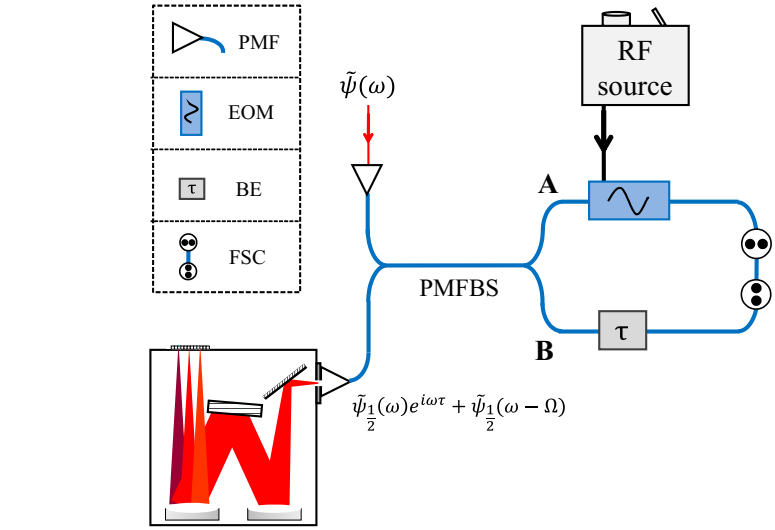

(a) Proposed Fibre-Based Sagnac Interferometer

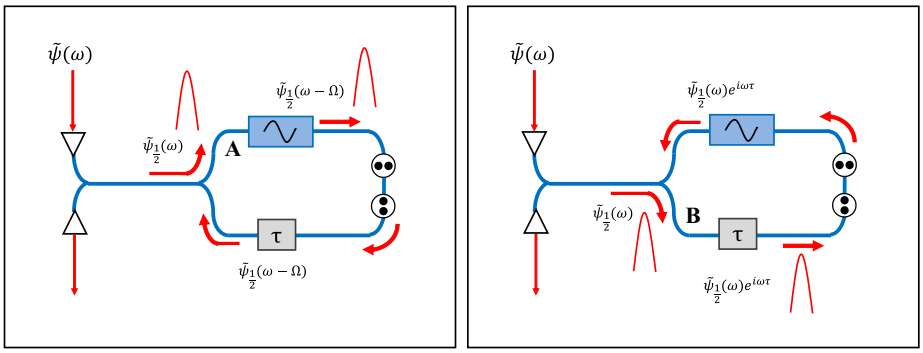

(b) Upper Arm Path, **A**, Spectral Shear **(c)** Lower Arm Path**B**, Temporal Delay

Figure B.1: (a) The proposed experimental set up for full state characterization of the spectral-temporal modes. The wave packet for characterization, $\tilde{\psi}(\omega)$, is propagated into the input arm of the polarization-maintaining fibre beam-splitter (PMFBS). A Sagnac interferometer is used so that the pulses propagate along the same optical path. The two copies of the spectral amplitude, $\tilde{\psi}_{\frac{1}{2}}(\omega)$, are produced by the fibre-beam splitter. These pass through distinct arms A and B, respectively. The wave packet amplitude in arm A first passes through the RF signal driven electro-optic modulator (EOM) and undergoes spectral shift due to temporal phase modulation, $\tilde{\psi}_{\frac{1}{2}}(\omega-\Omega)$. It then passes through the fast-to-slow (FSC) converter and becomes aligned with the slow axis of the polarization maintaining fibre. It finally passes through the birefringent element (BE), on the slow axis, and exits through the second "input arm" of the PMFBS. The wave packet amplitude passing through arm B first passes through the BE on the fast axis, thus experiences a temporal delay, τ, relative to the wave packet that first passes in arm A such that it gains additional phase, $\tilde{\psi}_{\frac{1}{2}}(\omega)e^{i\omega\tau}$. The temporally delayed wave packet then passes through the FSC and becomes aligned with the slow axis. It then passes through the EOM without acquiring any temporal phase. The wave packet exits the interferometer through the second "input" arm of the PM FBS. The output of the fibre beam splitter is connected to a spectrometer for temporally resolved measurement of the interference fringes. In figures (b) and (c), these paths are shown specifically.

shift the wave packet amplitude. The sheared wave packet, $\tilde{\psi}_{\frac{1}{2}}(\omega-\Omega)$, then passes into a fast-to-slow converter (FSC) (OzOptics, PMJ-3S3S-850-5/125-1-0.4-1,2-SP). This adiabatically[227] transforms the polarization to the fast axis of the fibre by propagation through twisted polarization-maintaining fibre. The FSC marks the point where the arm labelling switches from the upper, **A**, to the lower, **B**, arm. The lower arm contains a birefringent element with first-order dispersion, $\phi'(\omega)$, such that a wave packet travelling along the slow axis experiences a temporal delay, τ. However, the wave packet that underwent the spectral shear, $\tilde{\psi}_{\frac{1}{2}}(\omega-\Omega)$, is now aligned to the fast axis, owing to its passage through the fast-to-slow converter. It therefore passes through without accumulating any additional phase.

The second half of the spectral wave packet propagates through the interferometer starting in the lower arm, **B**. This wave packet, being aligned to the slow axis, thus experiences a temporal delay when passing through the birefringent element becoming $\tilde{\psi}_{\frac{1}{2}}(\omega)\mathrm{e}^{i\omega\tau}$. After passing through the fast-to-slow converter the wave packet becomes aligned to the fast axis. As it passes through the upper arm it is unaffected by the EOM since this is also birefringent. The wave packets are then recombined at the beginning of the interferometer, where they were first split. A spectrally-resolved measurement is performed by connecting the output fibre of the Sagnac interferometer to the input of the spectrometer and CCD.

Bibliography

[1] Euclid. *Optica*. 330 BC.

[2] Harry Edwin Burton. The optics of euclid. *J. Opt. Soc. Am.*, 35(5):357–357, May 1945.

[3] R. Descartes. *La dioptrique*. 1637.

[4] C Huygens. *Traité de la lumière où sont expliquées les causes de ce qui lui arrive dans la réflexion, et dans la réfraction*. 1690.

[5] I Newton. *Opticks: or a treatise of the reflections, refractions, inflections and colours of light*. 1704.

[6] Thomas Young. The bakerian lecture: Experiments and calculations relative to physical optics. *Philosophical Transactions of the Royal Society of London*, 94:1–16, 1804.

[7] A. Fresnel. Mémoire sur la double réfraction. *Mémoires de l'Académie des Sciences de l'Institut de France*, 7:45Ű176, 1827.

[8] J. Clerk Maxwell. A dynamical theory of the electromagnetic field. *Philosophical Transactions of the Royal Society of London*, 155:459–512, 1865.

[9] A. Einstein. Über einen die erzeugung und verwandlung des lichtes betreffenden heuristischen gesichtspunkt. *Annalen der Physik*, 322(6):132–148, 1905.

[10] A Einstein and Translation into English. Concerning an heuristic point of view toward the emission and transformation of light. *American Journal of Physics*, 33(5):367, 1965.

[11] Arthur H. Compton. A quantum theory of the scattering of x-rays by light elements. *Phys. Rev.*, 21:483–502, May 1923.

[12] R. A. Millikan. A direct photoelectric determination of planck's "h". *Phys. Rev.*, 7:355–388, Mar 1916.

[13] P. A. M. Dirac. The fundamental equations of quantum mechanics. *Proceedings of the Royal Society of London. Series A*, 109(752):642–653, 1925.

[14] M. Born and P Jordan. Zur quantenmechanik. *Zeitschrift für Physik*, 34:858–888, 1925.

[15] J. R. Oppenheimer. Note on light quanta and the electromagnetic field. *Phys. Rev.*, 38:725–746, Aug 1931.

[16] Gilbert N Lewis. The nature of light. *Proceedings of the National Academy of Science*, (12):22–29, 1926.

[17] D von der Linde, K Sokolowski-Tinten, and J Bialkowski. LaserŰsolid interaction in the femtosecond time regime. *Applied Surface Science*, 109Ű110(0):1 – 10, 1997.

[18] Markus Drescher, Michael Hentschel, R Kienberger, Matthias Uiberacker, Vladislav Yakovlev, Armin Scrinzi, Th Westerwalbesloh, U Kleineberg, Ulrich Heinzmann, and Ferenc Krausz. Time-resolved atomic inner-shell spectroscopy. *Nature*, 419(6909):803–807, 2002.

[19] M Hentschel, R Kienberger, Ch Spielmann, Georg A Reider, N Milosevic, Thomas Brabec, Paul Corkum, Ulrich Heinzmann, Markus Drescher, and Ferenc Krausz. Attosecond metrology. *Nature*, 414(6863):509–513, 2001.

[20] Jennifer P. Ogilvie, Emmanuel Beaurepaire, Antigoni Alexandrou, and Manuel Joffre. Fourier-transform coherent anti-stokes raman scattering microscopy. *Opt. Lett.*, 31(4):480–482, Feb 2006.

[21] Jerome Mertz. Nonlinear microscopy: new techniques and applications. *Current opinion in neurobiology*, 14(5):610–616, 2004.

[22] S. A. Diddams, Th. Udem, J. C. Bergquist, E. A. Curtis, R. E. Drullinger, L. Hollberg, W. M. Itano, W. D. Lee, C. W. Oates, K. R. Vogel, and D. J. Wineland. An optical clock based on a single trapped 199hg+ ion. *Science*, 293(5531):825–828, 2001.

[23] P.W. Shor. Algorithms for quantum computation: discrete logarithms and factoring. In *Foundations of Computer Science, 1994 Proceedings., 35th Annual Symposium on*, pages 124–134, Nov 1994.

[24] Charles H Bennett and Gilles Brassard. Quantum cryptography: Public key distribution and coin tossing. In *Proceedings of International Conference on Computers, Systems and Signal Processing*, volume 175, pages 175–179, 1984.

[25] Thomas Jennewein, Ulrich Achleitner, Gregor Weihs, Harald Weinfurter, and Anton Zeilinger. A fast and compact quantum random number generator. *Review of Scientific Instruments*, 71(4):1675–1680, 2000.

[26] Martin Fürst, Henning Weier, Sebastian Nauerth, Davide G. Marangon, Christian Kurtsiefer, and Harald Weinfurter. High speed optical quantum random number generation. *Opt. Express*, 18(12):13029–13037, Jun 2010.

[27] Min Xiao, Ling-An Wu, and H. Kimble. Precision measurement beyond the shot-noise limit. *Phys. Rev. Lett.*, 59:278–281, Jul 1987.

[28] Jaewoo Joo, William J. Munro, and Timothy P. Spiller. Quantum metrology with entangled coherent states. *Phys. Rev. Lett.*, 107:083601, Aug 2011.

[29] J.L. O'Brien, A. Furusawa, and J. Vučković. Photonic quantum technologies. *Nature Photonics*, 3:687–695, December 2009.

[30] Yoshihisa Yamamoto, C Santori, G Solomon, J Vuckovic, D Fattal, E Waks, and E Diamanti. Single photons for quantum information systems. *Prog. Informatics*, 1:5–37, 2005.

[31] Gabriel F. Calvo and Antonio Picón. Manipulation of single-photon states encoded in transverse spatial modes: Possible and impossible tasks. *Phys. Rev. A*, 77:012302, Jan 2008.

[32] Damien Bonneau, Mirko Lobino, Pisu Jiang, Chandra M. Natarajan, Michael G. Tanner, Robert H. Hadfield, Sanders N. Dorenbos, Val Zwiller, Mark G. Thompson, and Jeremy L. O'Brien. Fast path and polarization manipulation of telecom wavelength single photons in lithium niobate waveguide devices. *Phys. Rev. Lett.*, 108:053601, Jan 2012.

[33] E. Nagali, F. Sciarrino, F. De Martini, B. Piccirillo, E. Karimi, L. Marrucci, and E. Santamato. Polarization control of single photon quantum orbital angular momentum states. *Opt. Express*, 17(21):18745–18759, Oct 2009.

[34] Samuel L. Braunstein and Peter van Loock. Quantum information with continuous variables. *Rev. Mod. Phys.*, 77(2):513–577, Jun 2005.

[35] Alex Hayat, Xingxing Xing, Amir Feizpour, and Aephraim M. Steinberg. Multidimensional quantum information based on single-photon temporal wavepackets. *Opt. Express*, 20(28):29174–29184, Dec 2012.

[36] Julia Fekete, Daniel Rieländer, Matteo Cristiani, and Hugues de Riedmatten. Ultranarrowband photon-pair source compatible with solid state quantum memories and telecommunication networks. *Phys. Rev. Lett.*, 110:220502, May 2013.

[37] J. S. Neergaard-Nielsen, B. M. Nielsen, H. Takahashi, A. I. Vistnes, and E. S. Polzik. High purity bright single photon source. *Opt. Express*, 15(13):7940–7949, Jun 2007.

[38] L.-M. Duan, M. D. Lukin, J. I. Cirac, and P. Zoller. Long-distance quantum communication with atomic ensembles and linear optics. *Nature*, 414(6862):413–418, November 2001.

[39] Thomas Legero, Tatjana Wilk, Markus Hennrich, Gerhard Rempe, and Axel Kuhn. Quantum beat of two single photons. *Phys. Rev. Lett.*, 93:070503, Aug 2004.

[40] Peter P. Rohde, Timothy C. Ralph, and Michael A. Nielsen. Optimal photons for quantum-information processing. *Phys. Rev. A*, 72:052332, Nov 2005.

[41] Ayman F. Abouraddy, Magued B. Nasr, Bahaa E. A. Saleh, Alexander V. Sergienko, and Malvin C. Teich. Quantum-optical coherence tomography with dispersion cancellation. *Phys. Rev. A*, 65:053817, May 2002.

[42] Matthieu Bloch, Steven W. McLaughlin, Jean-Marc Merolla, and Frédéric Patois. Frequency-coded quantum key distribution. *Opt. Lett.*, 32(3):301–303, Feb 2007.

[43] Jacob Mower, Zheshen Zhang, Pierre Desjardins, Catherine Lee, Jeffrey H. Shapiro, and Dirk Englund. High-dimensional quantum key distribution using dispersive optics. *Phys. Rev. A*, 87:062322, Jun 2013.

[44] Daniel Gauthier, Hannah Guilbert, Yunhui Zhu, Meizhen Shi, Kevin McCusker, Bradley Christensen, Paul Kwiat, Thomas Brougham, Stephen M. Barnett, and Venkat Chandar. Quantum key distribution using hyperentanglement. In *Research in Optical Sciences*, page QT4A.2. Optical Society of America, 2012.

[45] Catherine Lee, Zheshen Zhang, Jacob C. Mower, Greg Steinbrecher, Hongchao Zhou, Ligong Wang, Xiaolong Hu, Robert Horansky, Varun B. Verma, Michael Allman, Adriana Lita, Richard P. Mirin, Francesco Marsili, Andrew D. Beyer, Matthew Shaw, Sae Woo Nam, Gregory Wornell, Franco Wong, Jeffrey H. Shapiro, and Dirk Englund. High-dimensional time-energy entanglement-based quantum key distribution using dispersive optics. In *CLEO: 2014*, page FM4A.3. Optical Society of America, 2014.

[46] Bing Qi. Single-photon continuous-variable quantum key distribution based on the energy-time uncertainty relation. *Opt. Lett.*, 31(18):2795–2797, Sep 2006.

[47] J. Nunn, L. J. Wright, C. Söller, L. Zhang, I. A. Walmsley, and B. J. Smith. Large-alphabet time-frequency entangled quantum key distribution by means of time-to-frequency conversion. *Opt. Express*, 21(13):15959–15973, Jul 2013.

[48] L. Olislager, J. Cussey, A. T. Nguyen, P. Emplit, S. Massar, J.-M. Merolla, and K. Phan Huy. Frequency-bin entangled photons. *Phys. Rev. A*, 82:013804, Jul 2010.

[49] Marissa Giustina, Alexandra Mech, Sven Ramelow, Bernhard Wittmann, Johannes Kofler, Jörn Beyer, Adriana Lita, Brice Calkins, Thomas Gerrits, Sae Woo Nam, et al. Bell violation using entangled photons without the fair-sampling assumption. *Nature*, 497(7448):227–230, 2013.

[50] Robert H. Hadfield. Single-photon detectors for optical quantum information applications. *Nat Photon*, 3(12):696–705, December 2009.

[51] Sebastian Zaske, Andreas Lenhard, and Christoph Becher. Efficient frequency downconversion at the single photon level from the red spectral range to the telecommunications c-band. *Optics Express*, 19(13):12825, Jun 2011.

[52] Marius A. Albota and FrancoN. C. Wong. Efficient single-photon counting at 1.55 μm by means of frequency upconversion. *Opt. Lett.*, 29(13):1449–1451, Jul 2004.

[53] Aaron P Vandevender and Paul G Kwiat. High efficiency single photon detection via frequency up-conversion. *Journal of Modern Optics*, 51(9-10):1433–1445, 2004.

[54] Carsten Langrock, Eleni Diamanti, Rostislav V. Roussev, Yoshihisa Yamamoto, M. M. Fejer, and Hiroki Takesue. Highly efficient single-photon detection at communication wavelengths by use of upconversion in reverse-proton-exchanged periodically poled linbo3 waveguides. *Opt. Lett.*, 30(13):1725–1727, Jul 2005.

[55] Lijun Ma, Oliver Slattery, and Xiao Tang. Single photon frequency up-conversion and its applications. *Physics Reports*, 521(2):69 – 94, 2012. Single photon frequency up-conversion and its applications.

[56] E. Knill, R. Laflamme, and G. J. Milburn. A scheme for efficient quantum computation with linear optics. *Nature*, 409(6816):46–52, January 2001.

[57] Pieter Kok, W. J. Munro, Kae Nemoto, T. C. Ralph, Jonathan P. Dowling, and G. J. Milburn. Linear optical quantum computing with photonic qubits. *Rev. Mod. Phys.*, 79:135–174, Jan 2007.

[58] Alessandro Zavatta, Marco Bellini, Pier Luigi Ramazza, Francesco Marin, and Fortunato Tito Arecchi. Time-domain analysis of quantum states of light: noise characterization and homodyne tomography. *J. Opt. Soc. Am. B*, 19(5):1189–1194, May 2002.

[59] A. I. Lvovsky, H. Hansen, T. Aichele, O. Benson, J. Mlynek, and S. Schiller. Quantum state reconstruction of the single-photon fock state. *Phys. Rev. Lett.*, 87:050402, Jul 2001.

[60] Guillaume Labroille, Olivier Pinel, Nicolas Treps, and Manuel Joffre. Pulse shaping with birefringent crystals: a tool for quantum metrology. *Opt. Express*, 21(19):21889–21896, Sep 2013.

[61] H_J Kimble. The quantum internet. *Nature*, 453(7198):1023–1030, 2008.

[62] M Wallquist, K Hammerer, P Rabl, M Lukin, and P Zoller. Hybrid quantum devices and quantum engineering. *Physica Scripta*, 2009(T137):014001, 2009.

[63] Michael G. Raymer and Kartik Srinivasan. Manipulating the color and shape of single photons. *Phys. Today*, 65(11):32, 2012.

[64] Xavier Fernandez-Gonzalvo, Giacomo Corrielli, Boris Albrecht, Marcel.li Grimau, Matteo Cristiani, and Hugues de Riedmatten. Quantum frequency conversion of quantum memory compatible photons to telecommunication wavelengths. *Opt. Express*, 21(17):19473–19487, Aug 2013.

[65] Boris Albrecht, Pau Farrera, Xavier Fernandez-Gonzalvo, Matteo Cristiani, and Hugues de Riedmatten. A waveguide frequency converter connecting rubidium-based quantum memories to the telecom c-band. *Nature communications*, 5, 2014.

[66] Matthew Eisaman. Quantum nonlinear optics: Tailored single photons. *Nature Photon*, 7(5):345?346, Mar 2013.

[67] Thomas Volz, Andreas Reinhard, Martin Winger, Antonio Badolato, Kevin J Hennessy, Evelyn L Hu, and Ataç Imamoğlu. Ultrafast all-optical switching by single photons. *Nature Photonics*, 6(9):605–609, 2012.

[68] Xu Fang, Ming Lun Tseng, Jun-Yu Ou, Kevin F. MacDonald, Din Ping Tsai, and Nikolay I. Zheludev. Ultrafast all-optical switching via coherent modulation of metamaterial absorption. *Applied Physics Letters*, 104(14):–, 2014.

[69] A. L. Schawlow and C. H. Townes. Infrared and optical masers. *Phys. Rev.*, 112:1940–1949, Dec 1958.

[70] T.H. Maiman. Stimulated optical radiation in ruby. *Nature*, 187, 1960. cited By (since 1996)4.

[71] Andrew M. Weiner. Ultrafast optical pulse shaping: A tutorial review. *Optics Communications*, 284(15):3669 – 3692, 2011. Special Issue on Optical Pulse Shaping, Arbitrary Waveform Generation, and Pulse Characterization.

[72] Ian A. Walmsley and Christophe Dorrer. Characterization of ultrashort electromagnetic pulses. *Adv. Opt. Photon.*, 1(2):308–437, Apr 2009.

[73] Antoine Monmayrant, Sébastien Weber, and Béatrice Chatel. A newcomer's guide to ultrashort pulse shaping and characterization. *Journal of Physics B: Atomic, Molecular and Optical Physics*, 43(10):103001, 2010.

[74] J. P. Heritage, A. M. Weiner, and R. N. Thurston. Picosecond pulse shaping by spectral phase and amplitude manipulation. *Opt. Lett.*, 10(12):609–611, Dec 1985.

[75] Barak Dayan, Yaron Bromberg, Itai Afek, and Yaron Silberberg. Spectral polarization and spectral phase control of time-energy entangled photons. *Phys. Rev. A*, 75:043804, Apr 2007.

[76] D. Meshulach and Y. Silberberg. Coherent quantum control of two-photo transitions by a femtosecond laser pulse. *Nature*, 396(6708):239–242, 1998. cited By (since 1996)512.

[77] Susanne Blum, G. A. Olivares-Renterìa, Carlo Ottaviani, Christoph Becher, and Giovanna Morigi. Single-photon frequency conversion in nonlinear crystals. *Phys. Rev. A*, 88:053807, Nov 2013.

[78] D. V. Reddy, M. G. Raymer, and C. J. McKinstrie. Efficient sorting of quantum-optical wave packets by temporal-mode interferometry. *Opt. Lett.*, 39(10):2924–2927, May 2014.

[79] Karina Garay-Palmett, Raul Rangel-Rojo, and Alfred B. U'Ren. Tailored photon pair preparation relying on full group velocity matching in fiber-based spontaneous four-wave mixing. *Journal of Modern Optics*, 55(19-20):3121–3131, 2008.

[80] Shengwang Du, Jianming Wen, and Chinmay Belthangady. Temporally shaping biphoton wave packets with periodically modulated driving fields. *Phys. Rev. A*, 79:043811, Apr 2009.

[81] Genko S Vasilev, Daniel Ljunggren, and Axel Kuhn. Single photons made-to-measure. *New Journal of Physics*, 12(6):063024, 2010.

[82] M. D. Eisaman, L. Childress, A. André, F. Massou, A. S. Zibrov, and M. D. Lukin. Shaping quantum pulses of light via coherent atomic memory. *Phys. Rev. Lett.*, 93:233602, Nov 2004.

[83] Jeff T. Hill, Amir H. Safavi-Naeini, Jasper Chan, and Oskar Painter. Coherent optical wavelength conversion via cavity optomechanics. *Nature Communications*, 3:1196, Nov 2012.

[84] Serkan Ates, Imad Agha, Angelo Gulinatti, Ivan Rech, Matthew T. Rakher, Antonio Badolato, and Kartik Srinivasan. Two-photon interference using background-free quantum frequency conversion of single photons emitted by an inas quantum dot. *Phys. Rev. Lett.*, 109:147405, Oct 2012.

[85] Christophe Dorrer and Inuk Kang. Highly sensitive direct characterization of femtosecond pulses by electro-optic spectral shearing interferometry. *Opt. Lett.*, 28(6):477–479, Mar 2003.

[86] W. K. Wootters and W. H. Zurek. A single quantum cannot be cloned. *Nature*, 299(5886):802–803, October 1982.

[87] U. Leonhardt. *Essential Quantum Optics: From Quantum Measurements to Black Holes*. Cambridge University Press, 2010.

[88] R. Loudon. *The Quantum Theory of Light*. OUP Oxford, 2000.

[89] C. Gerry and P. Knight. *Introductory Quantum Optics*. Cambridge University Press, 2005.

[90] P. Grangier, G. Roger, and A. Aspect. Experimental evidence for a photon anticorrelation effect on a beam splitter: a new light on single-photon interferences. *Europhysics Letters*, pages 173–179, 1986.

[91] Leonard Mandel and Emil Wolf. *Optical coherence and quantum optics*. Cambridge university press, 1995.

[92] J.C. Diels and W. Rudolph. *Ultrashort Laser Pulse Phenomena: Fundamentals, Techniques, and Applications on a Femtosecond Time Scale*. Academic Press. Academic Press, 2006.

[93] R. L. Fork, B. I. Greene, and C. V. Shank. Generation of optical pulses shorter than 0.1 psec by colliding pulse mode locking. *Applied Physics Letters*, 38(9):671–672, 1981.

[94] D. E. Spence, P. N. Kean, and W. Sibbett. 60-fsec pulse generation from a self-mode-locked ti:sapphire laser. *Opt. Lett.*, 16(1):42–44, Jan 1991.

[95] Min Gu, Derryck Reid, and Adela Ben-Yakar. Ultrafast biophotonics. *Journal of Optics*, 12(8):080301, 2010.

[96] G. Andrew Antonelli, Bernard Perrin, Brian C. Daly, and David G. Cahill. Characterization of mechanical and thermal properties using ultrafast optical metrology. *MRS Bulletin*, 31:607–613, 8 2006.

[97] Roman Sobolewski. Ultrafast optoelectronic interface for digital superconducting electronics. *Superconductor Science and Technology*, 14(12):994, 2001.

[98] Osamu Wada. Femtosecond all-optical devices for ultrafast communication and signal processing. *New Journal of Physics*, 6(1):183, 2004.

[99] Jeremy C Hebden, Simon R Arridge, and David T Delpy. Optical imaging in medicine: I. experimental techniques. *Physics in medicine and biology*, 42(5):825, 1997.

[100] Erik Zeek, Kira Maginnis, Sterling Backus, Ulrich Russek, Margaret Murnane, Gérard Mourou, Henry Kapteyn, and Gleb Vdovin. Pulse compression by use of deformable mirrors. *Opt. Lett.*, 24(7):493–495, Apr 1999.

[101] Vadim V Lozovoy, Igor Pastirk, and Marcos Dantus. Multiphoton intrapulse interference. iv. ultrashort laser pulse spectral phase characterization and compensation. *Optics letters*, 29(7):775–777, 2004.

[102] A.M. Weiner. Femtosecond optical pulse shaping and processing. *Progress in Quantum Electronics*, 19(3):161 – 237, 1995.

[103] Debabrata Goswami. Optical pulse shaping approaches to coherent control. *Physics Reports*, 374(6):385 – 481, 2003.

[104] Jean-François Morizur, Lachlan Nicholls, Pu Jian, Seiji Armstrong, Nicolas Treps, Boris Hage, Magnus Hsu, Warwick Bowen, Jiri Janousek, and Hans-A. Bachor. Programmable unitary spatial mode manipulation. *J. Opt. Soc. Am. A*, 27(11):2524–2531, Nov 2010.

[105] Brian H. Kolner and Moshe Nazarathy. Temporal imaging with a time lens. *Opt. Lett.*, 14(12):630–632, Jun 1989.

[106] D. Strickland and G. Mourou. Compression of amplified chirped optical pulses. *Optics Communications*, 56(3):219 – 221, 1985.

[107] IP Christov. Theory of a Śtime telescopeŠ. *Optical and quantum electronics*, 22(5):473–479, 1990.

[108] C. Froehly, B. Colombeau, and M. Vampouille. Ii shaping and analysis of picosecond light pulses. *Progress in Optics*, 20(C):63–153, 1983. cited By (since 1996)41.

[109] A. M. Weiner. Femtosecond pulse shaping using spatial light modulators. *Review of Scientific Instruments*, 71(5):1929–1960, 2000.

[110] T. Feurer, Joshua C. Vaughan, Richard M. Koehl, and Keith A. Nelson. Multidimensional control of femtosecond pulses by use of a programmable liquid-crystal matrix. *Opt. Lett.*, 27(8):652–654, Apr 2002.

[111] T. Brixner and G. Gerber. Femtosecond polarization pulse shaping. *Opt. Lett.*, 26(8):557–559, Apr 2001.

[112] Avi Pe'er, Barak Dayan, Asher A. Friesem, and Yaron Silberberg. Temporal shaping of entangled photons. *Phys. Rev. Lett.*, 94:073601, Feb 2005.

[113] Eric Yao, Sonja Franke-Arnold, Johannes Courtial, Miles J. Padgett, and Stephen M. Barnett. Observation of quantum entanglement using spatial light modulators. *Opt. Express*, 14(26):13089–13094, Dec 2006.

[114] T. Oksenhendler and N. Forget. *Pulse-Shaping Techniques Theory and Experimental Implementations for Femtosecond Pulses*. INTECH Open Access Publisher, 2010.

[115] Klaus Mattle, Harald Weinfurter, Paul G. Kwiat, and Anton Zeilinger. Dense coding in experimental quantum communication. *Phys. Rev. Lett.*, 76:4656–4659, Jun 1996.

[116] D. Bouwmeester, J.-W. Pan, K. Mattle, M. Eibl, H. Weinfurter, and A. Zeilinger. Experimental quantum teleportation. *Nature*, 390(6660):575–579, 1997. cited By (since 1996)2495.

[117] H. P. Specht, J. Bochmann, M. Mücke, B. Weber, E. Figueroa, D. L. Moehring, and G. Rempe. Phase shaping of single-photon wave packets. *Nature Photon*, 3(8):469?472, Aug 2009.

[118] C. Polycarpou, K. N. Cassemiro, G. Venturi, A. Zavatta, and M. Bellini. Adaptive detection of arbitrarily shaped ultrashort quantum light states. *Phys. Rev. Lett.*, 109:053602, Aug 2012.

[119] Prem Kumar. Quantum frequency conversion. *Opt. Lett.*, 15(24):1476–1478, Dec 1990.

[120] Jianming Huang and Prem Kumar. Observation of quantum frequency conversion. *Phys. Rev. Lett.*, 68:2153–2156, Apr 1992.

[121] Aihong Tan, Xiaojun Jia, and Changde Xie. Frequency conversion of an entangled state. *Phys. Rev. A*, 73:033817, Mar 2006.

[122] Lijun Ma, Matthew T. Rakher, Martin J. Stevens, Oliver Slattery, Kartik Srinivasan, and Xiao Tang. Temporal correlation of photons following frequency up-conversion. *Opt. Express*, 19(11):10501–10510, May 2011.

[123] Christina E. Vollmer, Christoph Baune, Aiko Samblowski, Tobias Eberle, Vitus Händchen, Jaromír Fiurasek, and Roman Schnabel. Quantum up-conversion of squeezed vacuum states from 1550 to 532 nm. *Phys. Rev. Lett.*, 112:073602, Feb 2014.

[124] Dehuan Kong, Zongyang Li, Shaofeng Wang, Xuyang Wang, and Yongmin Li. Quantum frequency down-conversion of bright amplitude-squeezed states. *Opt. Express*, 22(20):24192–24201, Oct 2014.

[125] Christoph Baune, Axel Schönbeck, Aiko Samblowski, Jaromír Fiurášek, and Roman Schnabel. Quantum non-gaussianity of frequency up-converted single photons. *Opt. Express*, 22(19):22808–22816, Sep 2014.

[126] Paulina S. Kuo, Jason S. Pelc, Oliver Slattery, Yong-Su Kim, M. M. Fejer, and Xiao Tang. Reducing noise in single-photon-level frequency conversion. *Opt. Lett.*, 38(8):1310–1312, Apr 2013.

[127] Alejandra Valencia, Maria V. Chekhova, Alexei Trifonov, and Yanhua Shih. Entangled two-photon wave packet in a dispersive medium. *Phys. Rev. Lett.*, 88:183601, Apr 2002.

[128] M. Bellini, F. Marin, S. Viciani, A. Zavatta, and F. T. Arecchi. Nonlocal pulse shaping with entangled photon pairs. *Phys. Rev. Lett.*, 90:043602, Jan 2003.

[129] Silvia Viciani, Alessandro Zavatta, and Marco Bellini. Nonlocal modulations on the temporal and spectral profiles of an entangled photon pair. *Phys. Rev. A*, 69:053801, May 2004.

[130] So-Young Baek, Osung Kwon, and Yoon-Ho Kim. Temporal shaping of a heralded single-photon wave packet. *Phys. Rev. A*, 77:013829, Jan 2008.

[131] B. C. Buchler, M. Hosseini, G. Hétet, B. M. Sparkes, and P. K. Lam. Precision spectral manipulation of optical pulses using a coherent photon echo memory. *Opt. Lett.*, 35(7):1091–1093, Apr 2010.

[132] C. McKinstrie, J. Harvey, S. Radic, and M. Raymer. Translation of quantum states by four-wave mixing in fibers. *Opt. Express*, 13(22):9131–9142, Oct 2005.

[133] H. J. McGuinness, M. G. Raymer, C. J. McKinstrie, and S. Radic. Quantum frequency translation of single-photon states in a photonic crystal fiber. *Physical Review Letters*, 105(9), Aug 2010.

[134] J. Lavoie, J. M. Donohue, L. G. Wright, A. Fedrizzi, and K. J. Resch. Spectral compression of single photons. *Nature Photon*, 7(5):363?366, Mar 2013.

[135] Matthew T. Rakher, Lijun Ma, Marcelo Davanço, Oliver Slattery, Xiao Tang, and Kartik Srinivasan. Simultaneous wavelength translation and amplitude modulation of single photons from a quantum dot. *Physical Review Letters*, 107(8), Aug 2011.

[136] Matthew T. Rakher and Kartik Srinivasan. Subnanosecond electro-optic modulation of triggered single photons from a quantum dot. *Applied Physics Letters*, 98(21):–, 2011.

[137] Matthew Bradford, Kenechukwu C. Obi, and Jung-Tsung Shen. Efficient single-photon frequency conversion using a sagnac interferometer. *Phys. Rev. Lett.*, 108:103902, Mar 2012.

[138] Dmitry V Strekalov, Abijith S Kowligy, Yu-Ping Huang, and Prem Kumar. Optical sum-frequency generation in a whispering-gallery-mode resonator. *New Journal of Physics*, 16(5):053025, 2014.

[139] Abijith S. Kowligy, Paritosh Manurkar, Neil V. Corzo, Vesselin G. Velev, Michael Silver, Ryan P. Scott, S. J. B. Yoo, Prem Kumar, Gregory S. Kanter, and Yu-Ping Huang. Quantum optical arbitrary waveform manipulation and measurement in real time. *Opt. Express*, 22(23):27942–27957, Nov 2014.

[140] Andreas Eckstein, Benjamin Brecht, and Christine Silberhorn. A quantum pulse gate based on spectrally engineered sum frequency generation. *Opt. Express*, 19(15):13770–13778, Jul 2011.

[141] Yu-Ping Huang and Prem Kumar. Mode-resolved photon counting via cascaded quantum frequency conversion. *Opt. Lett.*, 38(4):468–470, Feb 2013.

[142] Valentin A. Averchenko, Valérian Thiel, and Nicolas Treps. Nonlinear photon subtraction from a multimode quantum field. *Phys. Rev. A*, 89:063808, Jun 2014.

[143] Benjamin Brecht, Andreas Eckstein, Raimund Ricken, Viktor Quiring, Hubertus Suche, Linda Sansoni, and Christine Silberhorn. Demonstration of coherent time-frequency schmidt mode selection using dispersion-engineered frequency conversion. *Phys. Rev. A*, 90:030302, Sep 2014.

[144] Yoon-Ho Kim, Sergei P. Kulik, and Yanhua Shih. Quantum teleportation of a polarization state with a complete bell state measurement. *Phys. Rev. Lett.*, 86:1370–1373, Feb 2001.

[145] Rikizo Ikuta, Yoshiaki Kusaka, Tsuyoshi Kitano, Hiroshi Kato, Takashi Yamamoto, Masato Koashi, and Nobuyuki Imoto. Wide-band quantum interface for visible-to-telecommunication wavelength conversion. *Nature Communications*, 2:1544, Nov 2011.

[146] S. Ramelow, A. Fedrizzi, A. Poppe, N. K. Langford, and A. Zeilinger. Polarization-entanglement-conserving frequency conversion of photons. *Phys. Rev. A*, 85:013845, Jan 2012.

[147] B. M. Sparkes, M. Hosseini, C. Cairns, D. Higginbottom, G. T. Campbell, P. K. Lam, and B. C. Buchler. Precision spectral manipulation: A demonstration using a coherent optical memory. *Phys. Rev. X*, 2:021011, Jun 2012.

[148] Stefan Preble, Liang Cao, Ali Elshaari, Abdelsalam Aboketaf, and Donald Adams. Single photon adiabatic wavelength conversion. *Applied Physics Letters*, 101(17):–, 2012.

[149] M. D. Eisaman, J. Fan, A. Migdall, and S. V. Polyakov. Invited review article: Single-photon sources and detectors. *Review of Scientific Instruments*, 82(7):–, 2011.

[150] Brahim Lounis and Michel Orrit. Single-photon sources. *Reports on Progress in Physics*, 68(5):1129, 2005.

[151] Andrew J Shields. Semiconductor quantum light sources. *Nature photonics*, 1(4):215–223, 2007.

[152] Martin Mücke, Joerg Bochmann, Carolin Hahn, Andreas Neuzner, Christian Nölleke, Andreas Reiserer, Gerhard Rempe, and Stephan Ritter. Generation of single photons from an atom-cavity system. *Phys. Rev. A*, 87:063805, Jun 2013.

[153] C. W. Chou, S. V. Polyakov, A. Kuzmich, and H. J. Kimble. Single-photon generation from stored excitation in an atomic ensemble. *Phys. Rev. Lett.*, 92:213601, May 2004.

[154] Christian Kurtsiefer, Sonja Mayer, Patrick Zarda, and Harald Weinfurter. Stable solid-state source of single photons. *Phys. Rev. Lett.*, 85:290–293, Jul 2000.

[155] Paul G. Kwiat, Klaus Mattle, Harald Weinfurter, Anton Zeilinger, Alexander V. Sergienko, and Yanhua Shih. New high-intensity source of polarization-entangled photon pairs. *Phys. Rev. Lett.*, 75:4337–4341, Dec 1995.

[156] Paul G. Kwiat, Edo Waks, Andrew G. White, Ian Appelbaum, and Philippe H. Eberhard. Ultrabright source of polarization-entangled photons. *Phys. Rev. A*, 60:R773–R776, Aug 1999.

[157] Jun Chen, Aaron J Pearlman, Alexander Ling, Jingyun Fan, and Alan L Migdall. A versatile waveguide source of photon pairs for chip-scale quantum information processing. *Optics express*, 17(8):6727–6740, 2009.

[158] Justin B. Spring, Patrick S. Salter, Benjamin J. Metcalf, Peter C. Humphreys, Merritt Moore, Nicholas Thomas-Peter, Marco Barbieri, Xian-Min Jin, Nathan K. Langford, W. Steven Kolthammer, Martin J. Booth, and Ian A. Walmsley. On-chip low loss heralded source of pure single photons. *Opt. Express*, 21(11):13522–13532, Jun 2013.

[159] LJ Wang, CK Hong, and SR Friberg. Generation of correlated photons via four-wave mixing in optical fibres. *Journal of optics B: Quantum and semiclassical optics*, 3(5):346, 2001.

[160] Jérémie Fulconis, Olivier Alibart, Jeremy L. O'Brien, William J. Wadsworth, and John G. Rarity. Nonclassical interference and entanglement generation using a photonic crystal fiber pair photon source. *Phys. Rev. Lett.*, 99:120501, Sep 2007.

[161] P. J. Mosley, J. S. Lundeen, B. J. Smith, and I. A. Walmsley. Conditional preparation of single photons using parametric downconversion: a recipe for purity. *New J. Phys.*, 10(9):23589–23602, 2008.

[162] Morton H. Rubin, David N. Klyshko, Y. H. Shih, and A. V. Sergienko. Theory of two-photon entanglement in type-ii optical parametric down-conversion. *Phys. Rev. A*, 50:5122–5133, Dec 1994.

[163] W. P. Grice and I. A. Walmsley. Spectral information and distinguishability in type-ii down-conversion with a broadband pump. *Phys. Rev. A*, 56:1627–1634, Aug 1997.

[164] O. E. Martinez, J. P. Gordon, and R. L. Fork. Negative group-velocity dispersion using refraction. *J. Opt. Soc. Am. A*, 1(10):1003–1006, Oct 1984.

[165] David Nikolaevich Klyshko. *Photons Nonlinear Optics*. CRC Press, 1988.

[166] Peter J. Mosley. *Generation of Heralded Single Photons in Pure Quantum States*. PhD thesis, Department of Atomic and Laser Physics, University of Oxford, Trinity Term 2007.

[167] Merlin Cooper, Laura J. Wright, Christoph Söller, and Brian J. Smith. Experimental generation of multi-photon Fock states. *Opt. Express*, 21(5):5309–5317, Mar 2013.

[168] ANDOR. idus 401 series specifications, 2015. SiDus401SS 0215 R1.

[169] Aaron L. Stancik and Eric B. Brauns. A simple asymmetric lineshape for fitting infrared absorption spectra. *Vibrational Spectroscopy*, 47(1):66 – 69, 2008.

[170] MATLAB. *version 7.10.0 (R2013b)*. The MathWorks Inc., Natick, Massachusetts, 2010.

[171] C. K. Law, I. A. Walmsley, and J. H. Eberly. Continuous frequency entanglement: Effective finite hilbert space and entropy control. *Phys. Rev. Lett.*, 84:5304–5307, Jun 2000.

[172] R Grobe, K Rzazewski, and J H Eberly. Measure of electron-electron correlation in atomic physics. *Journal of Physics B: Atomic, Molecular and Optical Physics*, 27(16):L503, 1994.

[173] J.H. Eberly. Schmidt analysis of pure-state entanglement. *Laser Physics*, 16(6):921–926, 2006.

[174] A. I. Lvovsky and M. G. Raymer. Continuous-variable optical quantum-state tomography. *Rev. Mod. Phys.*, 81:299–332, Mar 2009.

[175] G.H. Golub and C.F. Van Loan. *Matrix Computations*. Johns Hopkins Studies in the Mathematical Sciences. Johns Hopkins University Press, 2012.

[176] C. Hong, Z. Ou, and L. Mandel. Measurement of subpicosecond time intervals between two photons by interference. *Phys. Rev. Lett.*, 59:2044–2046, Nov 1987.

[177] Katiúscia N Cassemiro, Kaisa Laiho, and Christine Silberhorn. Accessing the purity of a single photon by the width of the hongŰouŰmandel interference. *New Journal of Physics*, 12(11):113052, 2010.

[178] T. Gerrits, F. Marsili, V. B. Verma, L. K. Shalm, M. Shaw, R. P. Mirin, and S. W. Nam. Spectral correlation measurements at the hong-ou-mandel interference dip. *Phys. Rev. A*, 91:013830, Jan 2015.

[179] Megan Ray and S. van Enk. Verifying entanglement in the hong-ou-mandel dip. *Phys. Rev. A*, 83:042318, Apr 2011.

[180] L. Mejling, C. J. McKinstrie, M. G. Raymer, and K. Rottwitt. Quantum frequency translation by four-wave mixing in a fiber: low-conversion regime. *Opt. Express*, 20(8):8367–8396, Apr 2012.

[181] C. J. McKinstrie, L. Mejling, M. G. Raymer, and K. Rottwitt. Quantum-state-preserving optical frequency conversion and pulse reshaping by four-wave mixing. *Phys. Rev. A*, 85:053829, May 2012.

[182] Laurent Olislager, Ismaël Mbodji, Erik Woodhead, Johann Cussey, Luca Furfaro, Philippe Emplit, Serge Massar, Kien Phan Huy, and Jean-Marc Merolla. Implementing two-photon interference in the frequency domain with electro-optic phase modulators. *New Journal of Physics*, 14(4):043015, 2012.

[183] K. G. Katamadze, A. V. Paterova, E. G. Yakimova, K. A. Balygin, and S. P. Kulik. Control of the frequency spectrum of a biphoton field due to the electro-optical effect. *Jetp Lett.*, 94(4):262?265, Oct 2011.

[184] Pavel Kolchin, Chinmay Belthangady, Shengwang Du, G. Y. Yin, and S. E. Harris. Electro-optic modulation of single photons. *Phys. Rev. Lett.*, 101:103601, Sep 2008.

[185] B.E.A. Saleh and M.C. Teich. *Fundamentals of Photonics*. Wiley Series in Pure and Applied Optics. Wiley, 2007.

[186] Nufern. Data provided by nufern. Nufern, 7 Airport Park Road, East Granby, CT 06026, USA, April 2015.

[187] David E. Zelmon, David L. Small, and Dieter Jundt. Infrared corrected sellmeier coefficients for congruently grown lithium niobate and 5 mol.% magnesium oxide –doped lithium niobate. *J. Opt. Soc. Am. B*, 14(12):3319–3322, Dec 1997.

[188] Juejun Hu, Hongtao Lin, O. Ogbuu, Jifeng Liu, Lin Zhang, and J. Michel. Breaking the energy-bandwidth limit of electro-optic modulators: Theory and a device proposal. In *Optical Interconnects Conference, 2013 IEEE*, pages 23–24, May 2013.

[189] R.P. Scott. *Design and Applications of Resonant Electro-optic Time Lenses*. University of California, Los Angeles, 1995.

[190] EoSpace Inc. http://www.eospace.com/. 6222 185th AVE NE, Suite 100, Redmond, WA 98052-5034, April 2015.

[191] Photline Technologies. http://www.photline.com. 16 rue Jouchoux, 25000 Besancon, France., April 2015.

[192] JENOPTIK AG. http://www.jenoptik.com. Carl-ZeiSS-StraSSe 1, 07743 Jena, Germany, April 2005.

[193] Aspen electronics ltd. 1-3 Kildare Close, Eastcote, Ruislip, Middlesex HA4 9UR, April 2015.

[194] Christophe Dorrer and Inuk Kang. Complete temporal characterization of short optical pulses by simplified chronocyclic tomography. *Opt. Lett.*, 28(16):1481–1483, August 2003.

[195] S. Brady. *rack mount 77 Success Secrets - 77 Most Asked Questions On rack mount - What You Need To Know*. Emereo Publishing, 2014.

[196] D.A. Ellerbruch. Uhf and microwave phase-shift measurements. *Proc. IEEE*, 55(6):960–969, 1967. cited By (since 1996)5.

[197] C D Cantrell. *Modern Mathematical Methods for Physicists and Engineers*, volume 12. Cambridge University Press, 2001.

[198] M. Beck. Comparing measurements of g(2)(0) performed with different coincidence detection techniques. *J. Opt. Soc. Am. B*, 24(12):2972–2978, Dec 2007.

[199] Yongwoo Park, Tae-Jung Ahn, and José Aza na. Real-time complex temporal response measurements of ultrahigh-speed optical modulators. *Opt. Express*, 17(3):1734–1745, Feb 2009.

[200] Press release, joint effort with fujikura (company and institute of micro-electronics, agency for science, technology and research (a*star), singapore. `http://www.fujikura.co.jp/eng/newsrelease/2037592_3501.html`.

[201] Christophe Dorrer, Richard Roides, Robert Cuffney, Andrey V Okishev, Wade A Bittle, Gregory Balonek, Albert Consentino, Elizabeth Hill, and Jonathan D Zuegel. Fiber front end with multiple phase modulations and high-bandwidth pulse shaping for high-energy laser-beam smoothing. *Selected Topics in Quantum Electronics, IEEE Journal of*, 19(6):219–230, 2013.

[202] J. Sipe. Photon wave functions. *Phys. Rev. A*, 52:1875–1883, Sep 1995.

[203] I. Bialynicki-Birula. *Progress in Optics*. Amsterdam, 1996.

[204] Andrew G. White, Daniel F. V. James, Philippe H. Eberhard, and Paul G. Kwiat. Non-maximally entangled states: Production, characterization, and utilization. *Phys. Rev. Lett.*, 83:3103–3107, Oct 1999.

[205] Brian J. Smith, Bryan Killett, M. G. Raymer, I. A. Walmsley, and K. Banaszek. Measurement of the transverse spatial quantum state of light at the single-photon level. *Opt. Lett.*, 30(24):3365–3367, Dec 2005.

[206] D. T. Smithey, M. Beck, M. G. Raymer, and A. Faridani. Measurement of the wigner distribution and the density matrix of a light mode using optical homodyne tomography: Application to squeezed states and the vacuum. *Phys. Rev. Lett.*, 70:1244–1247, Mar 1993.

[207] Peter P. Rohde. Quantum state tomography of single photons in the spectral degree of freedom. September 2006.

[208] A Zavatta, S Viciani, and M Bellini. Non-classical field characterization by high-frequency, time-domain quantum homodyne tomography. *Laser Physics Letters*, 3(1):3–16, 2006.

[209] Wojciech Wasilewski, Piotr Kolenderski, and Robert Frankowski. Spectral density matrix of a single photon measured. *Phys. Rev. Lett.*, 99(12):123601, September 2007.

[210] F. A. S. Barbosa, A. S. Coelho, K. N. Cassemiro, P. Nussenzveig, C. Fabre, M. Martinelli, and A. S. Villar. Beyond spectral homodyne detection: Complete quantum measurement of spectral modes of light. *Phys. Rev. Lett.*, 111:200402, Nov 2013.

[211] C. Dorrer. Effect of jitter on linear pulse-characterization techniques. *Opt. Express*, 16(9):6567–6578, Apr 2008.

[212] Idquantique, magiq, quintessencelabs smart quantum and toshiba commercial qkd systems. www.idquantique.com, www.magiqtech.com, www.qlabsusa.com, www.smartquantum.com, www.toshiba-europe.com/research/crl/qig/quantumkeyserver.html.

[213] CharlesH. Bennett, François Bessette, Gilles Brassard, Louis Salvail, and John Smolin. Experimental quantum cryptography. *Journal of Cryptology*, 5(1):3–28, 1992.

[214] Christophe Marand and Paul D. Townsend. Quantum key distribution over distances as long as 30 km. *Opt. Lett.*, 20(16):1695–1697, Aug 1995.

[215] Catherine Lee, Zheshen Zhang, Gregory R. Steinbrecher, Hongchao Zhou, Jacob Mower, Tian Zhong, Ligong Wang, Xiaolong Hu, Robert D. Horansky, Varun B. Verma, Adriana E. Lita, Richard P. Mirin, Francesco Marsili, Matthew D. Shaw, Sae Woo Nam, Gregory W. Wornell, Franco N. C. Wong, Jeffrey H. Shapiro, and Dirk Englund. Entanglement-based quantum communication secured by nonlocal dispersion cancellation. *Phys. Rev. A*, 90:062331, Dec 2014.

[216] Zheshen Zhang, Jacob Mower, Dirk Englund, C. Wong, Franco N. and Jeffrey H. Shapiro. Unconditional security of time-energy entanglement quantum key distribution using dual-basis interferometry. *Phys. Rev. Lett.*, 112:120506, Mar 2014.

[217] Zhu Chang-Hua, Pei Chang-Xing, Quan Dong-Xiao, Gao Jing-Liang, Chen Nan, and Yi Yun-Hui. A new quantum key distribution scheme based on frequency and time coding. *Chinese Physics Letters*, 27(9):090301, 2010.

[218] W. Mulligan, G. Bekefi, S.C. Chen, B.G. Danly, and R.J. Temkin. A high-voltage modulator for high-power rf source research. In *Power Modulator Symposium, 1990., IEEE Conference Record of the 1990 Nineteenth*, pages 514–518, Jun 1990.

[219] Peter B OŠConnor, Catherine E Costello, and William E Earle. A high voltage {RF} oscillator for driving multipole ion guides. *Journal of the American Society for Mass Spectrometry*, 13(12):1370 – 1375, 2002.

[220] Ronald M. Jones and Scott L. Anderson. Simplified radio-frequency generator for driving ion guides, traps, and other capacitive loads. *Review of Scientific Instruments*, 71(11):4335–4337, 2000.

[221] Y.-Y. Jau, F. M. Benito, H. Partner, and P. D. D. Schwindt. Low power high-performance radio frequency oscillator for driving ion traps. *Review of Scientific Instruments*, 82(2):–, 2011.

[222] Christi K. Madsen. Boundless-range optical phase modulator for high-speed frequency-shift and heterodyne applications. *J. Lightwave Technol.*, 24(7):2760, Jul 2006.

[223] Christophe Dorrer. Spectral and temporal properties of optical signals with multiple sinusoidal phase modulations. In *CLEO: 2014*, page STu3F.5. Optical Society of America, 2014.

[224] D.J. Kane and R. Trebino. Characterization of arbitrary femtosecond pulses using frequency-resolved optical gating. *Quantum Electronics, IEEE Journal of*, 29(2):571 –579, feb 1993.

[225] C. Iaconis and I.A. Walmsley. Spectral phase interferometry for direct electric-field reconstruction of ultrashort optical pulses. *Opt. Lett.*, 23(10):792–794, May 1998.

[226] E. Wigner. On the quantum correction for thermodynamic equilibrium. *Phys. Rev.*, 40:749–759, Jun 1932.

[227] M. Born and V. Fock. Beweis des adiabatensatzes. *Zeitschrift für Physik*, 51(3-4):165–180, 1928.